ROTATION AND NON-OBERBECK–BOUSSINESQ EFFECTS IN TURBULENT RAYLEIGH–BÉNARD CONVECTION

DISSERTATION

zur Erlangung des mathematisch-naturwissenschaftlichen Doktorgrades
"Doctor rerum naturalium"
der Georg-August-Universität Göttingen

im Promotionsprogramm ProPhys
der Georg-August University School of Science (GAUSS)

vorgelegt von
Susanne Horn
aus Schleiz
Göttingen 2014

Betreuungsausschuss

Prof. Dr. Andreas Tilgner
Institut für Geophysik, Georg-August-Universität Göttingen

Prof. Dr. Detlef Lohse
Department of Physics of Fluids, University of Twente

PD Dr. habil. Olga Shishkina
Laboratory for Fluid Dynamics, Pattern Formation and Biocomplexity,
Max-Planck-Institut für Dynamik und Selbstorganisation

Mitglieder der Prüfungskommission

Referent: Prof. Dr. Andreas Tilgner
Institut für Geophysik, Georg-August-Universität Göttingen

Koreferent: Prof. Dr. Detlef Lohse
Department of Physics of Fluids, University of Twente

2\. Koreferentin: PD Dr. habil. Olga Shishkina
Laboratory for Fluid Dynamics, Pattern Formation and Biocomplexity,
Max-Planck-Institut für Dynamik und Selbstorganisation

Weitere Mitglieder der Prüfungskommission

Prof. Dr. Dominik Schleicher
Institut für Astrophysik, Georg-August-Universität Göttingen

Prof. Dr. Gert Lube
Institut für Numerische und Angewandte Mathematik,
Georg-August-Universität Göttingen

Prof. Dr. Ulrich Parlitz
Biomedical Physics Group,
Max-Planck-Institut für Dynamik und Selbstorganisation

Prof. Dr. Laurent Gizon
Department Solar and Stellar Interiors,
Max-Planck-Institut für Sonnensystemforschung

Tag der mündlichen Prüfung: 30. September 2014

ROTATION AND NON-OBERBECK–BOUSSINESQ EFFECTS IN TURBULENT RAYLEIGH–BÉNARD CONVECTION

CONTENTS

INTRODUCTION

Rayleigh–Bénard convection is one of the standard model systems studied in turbulence research. Despite the simple setup, i.e. a fluid layer confined between a heating-plate at the bottom and a cooling-plate at the top, it is a useful tool to understand the complex flows occurring in nature and technology. A small selection of examples is depicted in figure 1.1. It is an idealised description of the flow in the outer layer of the Sun, the large scale structures in the Earth's atmosphere and oceans, a main ingredient for the dynamo model in the Earth's core and plate tectonics via mantle convection, for the thermal comfort in aircraft cabins, and even everyday life, when cooking. Understanding this fundamental problem is, thus, not only utterly important for geo- and astrophysics, but also in industry.

Classically, Rayleigh–Bénard convection has been studied with either infinite lateral extension or confined within simple geometries, like cubes or cylinders with small diameter-to-height aspect ratios, and by employing the so-called Oberbeck–Boussinesq approximation (Boussinesq, 1903; Oberbeck, 1879). First and foremost, this means that all properties are assumed to be constant with temperature and pressure. Furthermore, the parameter ranges in terms of the Rayleigh and Prandtl number, are rather limited, i.e. $\mathrm{Ra} \lesssim 10^{15}$ and $\mathrm{Pr} \approx \mathcal{O}(1)$ (cf. recent reviews, e.g. Ahlers et al., 2009; Chillà and Schumacher, 2012). The Rayleigh number is the ratio of buoyancy to dissipation, hence, being a measure for the thermal forcing and the grade of turbulence. The Prandtl number is the ratio of the viscous to the thermal time scale and is characteristic for every fluid.

However, all of the examples mentioned above are complicated by certain peculiarities making at least one of these conditions not applicable. Amongst others, in solar convection rotation and magnetic fields are expected to play an important role, the Prandtl number is very low, $\mathrm{Pr} \approx 10^{-4}$ and the Rayleigh number is very high, $\mathrm{Ra} \approx 10^{23}$. In the Earth's atmosphere the Prandtl number is not crucial with $\mathrm{Pr} \approx 0.7$. But again the Rayleigh number is high, being around 10^{20}, and moreover, one has to deal with rotation, very large aspect ratios, the stratification and the occurrence of clouds. In aircraft cabins, the geometry is complex, with passengers and electrical devices being the heat sources opposing the forced cooling by the air conditioning, thus, it is more accurate to talk about mixed convection. In the Earth's interior there is rotating metal core, which has a very small Prandtl number, and is the source of magnetic fields. On the contrary, in the Earth's mantle the Prandtl number is very high, and furthermore the fluid there shows a strongly temperature-dependent viscosity, which ultimately leads to a stagnant lid. And when cooking, the material properties are usually temperature-dependent, and when boiling there are additionally phase transitions.

Including all of these effects at once would not be very expedient. Here I primarily focus on two important issues, rotation and non-Oberbeck–Boussinesq effects. Accordingly, the main objective of this work is to improve the understanding of rotating Rayleigh–Bénard convection and to investigate the consequences of temperature-dependent material properties in liquids in the rotating and in the non-rotating case. Furthermore, I touch on the topic of the importance of the Prandtl number, i.e. in what way a very small or a very large Prandtl number affects the flow, and I also deal with the issue of high Rayleigh numbers.

1.1 Non-Oberbeck–Boussinesq effects [*]

The Oberbeck-Boussinesq (OB) approximation is the well-established and most commonly used method to study Rayleigh–Bénard convection from a mathematical and numerical point of view. Put very simply, it means, that all material properties are constant with pressure and with temperature, except the density within the buoyancy term, which is allowed to vary linearly with temperature therein. However, depending on the employed temperature difference and the height of the considered container, it is intuitively clear, that if either one of them or both are too large, this assumption cannot be fulfilled. A rigorous deduction for the range of validity of this approach was given by Gray and Giorgini (1976) and the method will be briefly summarised in section 2.2.5. Deviations due to the violation of the OB assumption are referred to as non-Oberbeck-Boussinesq (NOB) effects.

NOB effects have been studied theoretically by Busse (1967b) in a Rayleigh number range close to the onset of convection. For higher Rayleigh numbers, and in particular in the turbulent regime, experiments have been conducted with gases at low temperature or close to the critical point, for example, in helium by Wu and Libchaber (1991), in ethane by Ahlers et al. (2007), and in sulfur hexa-fluoride by Burnishev et al. (2010). There the compressibility and the pressure dependence of the material properties play the most important role for NOB effects.

On the other hand, NOB effects in liquids almost solely originate from the temperature dependence of the material properties. And that is what I am going to focus on. As the starting point of my investigations I use the work by Ahlers et al. (2006). They have not only conducted experiments in water, but also made some hypothetical predictions for glycerol. Later, their research was complemented by 2D simulations in water and glycerol by Sugiyama et al. (2007, 2009).

However, the reliability of two-dimensional simulations to predict three-dimensional properties is debatable. Schmalzl et al. (2004) have investigated the difference between two- and three-dimensional simulations for a moderate Rayleigh number of $\mathrm{Ra} = 10^6$ and $\mathrm{Pr} \in [0.001, 100]$. They found that, e.g., the discrepancy in the Nusselt number Nu and the maximal horizontal root mean square (rms) velocity is about 80% for $\mathrm{Pr} = 0.025$. In comparison to that, the calculations for $\mathrm{Pr} = 100$ seemed to yield similar results in the two- and three-dimensional simulations. Nonetheless, the deviation in the Nusselt numbers and the maximal horizontal rms velocity was larger than 20%.

---

[*] Partly adopted from HORN, S., SHISHKINA, O. AND WAGNER, C., On non-Oberbeck–Boussinesq effects in three-dimensional Rayleigh–Bénard convection in glycerol, *J. Fluid Mech. 724* (2013), 175–202.

The main objective of the current work concerning NOB effects is to study the influence of temperature-dependent material properties in liquids by means of three-dimensional Direct Numerical Simulations (DNS) for low-, moderate- and high-Prandtl-number fluids on three examples, namely mercury, water and glycerol. This is a step in the direction to predict the flow behaviour of realistic fluids.

1.2 Rotating Rayleigh–Bénard convection

Rotation is known to be able to change the flow completely and leads to effects that are suprising, not only at first sight. Thus, also in Rayleigh–Bénard convection, the Coriolis force can significantly influence the shape of the large scale structures and the efficiency of heat transport.

The parameter space spanned by the aspect ratio, the Prandtl number and the Rayleigh number is now enlarged by a fourth parameter, expressing the importance of rotation. Depending on the context, convenient choices can be the Ekman, the Rossby or the Taylor number. The full exploration of this larger parameter space is still an unfinished endeavour, and has led to lots of new insights into the nature of turbulent convection. Furthermore, another, so far unanswered question is, how NOB effects influence rotating convection in a confined geometry at relatively high Rayleigh numbers.

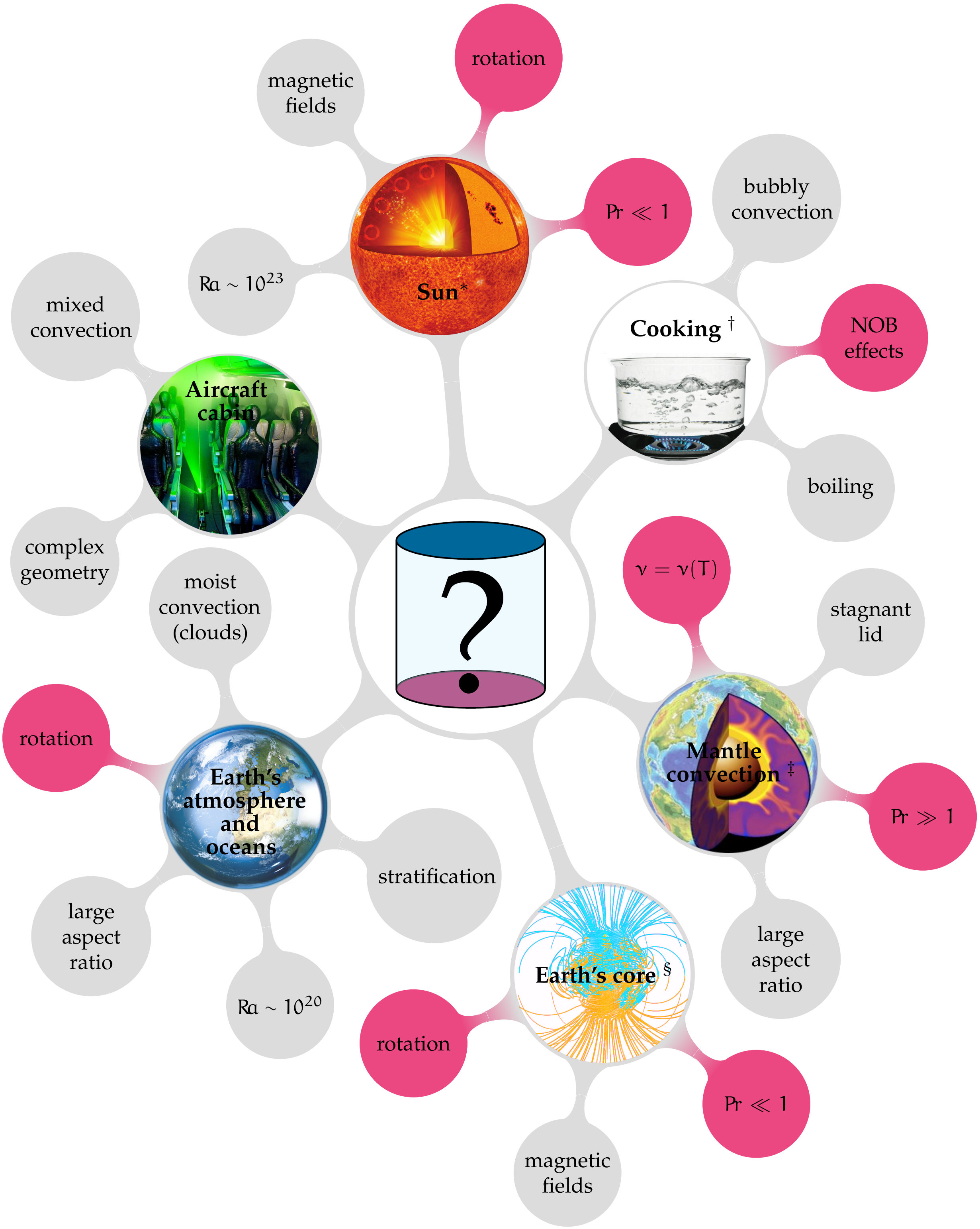

FIGURE 1.1: Diagram to visualise a few examples, said to be describable by Rayleigh–Bénard convection, but exhibiting certain peculiarities not covered by the standard model. The peculiarities investigated in the current work are highlighted in pink.

---

[1] Image credit: NASA/Jenny Mottar

[2] Image credit: Magnascan/iStockphoto

[3] Image credit: http://earth.yale.edu/solid-earth-geophysics

[4] Image credit: http://www.es.ucsc.edu/~glatz/geodynamo.html

THEORETICAL BACKGROUND

2.1 The basic concept of Rayleigh–Bénard convection

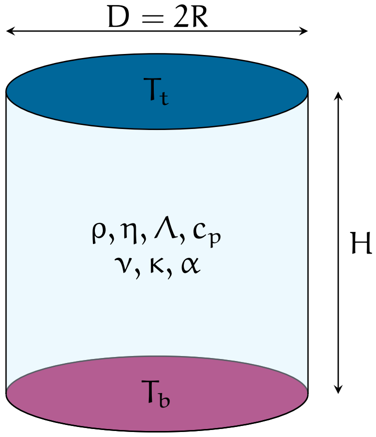

FIGURE 2.1: Sketch of the used geometry.

The fundamental Rayleigh–Bénard setup is constituted of a fluid heated from below and cooled from above. In the current work, I restrict myself to cylindrical geometries, as sketched in figure 2.1. This means, the fluid is confined by an impermeable, adiabatic side-wall and isothermal top and bottom plates, with temperatures T_t and T_b, respectively. This geometry defines a diameter-to-height aspect ratio $\Gamma = D/H$, and, introduced for later convenience, a radius-to-height aspect ratio $\gamma = R/H$. In general, the acceleration due to gravity is $\mathbf{g} = -g\mathbf{e}_z$, where $\mathbf{e}_z$ is the unit vector pointing in vertical direction, i.e. $\mathbf{g} = (0, 0, g)$.

The fluid itself is characterised by its primary thermophysical properties, density ρ, dynamic viscosity η, thermal conductivity Λ and isobaric specific heat capacity c_p. Other relevant derivable thermodynamic and transport coefficients are the kinematic viscosity $\nu = \eta/\rho$, the thermal diffusivity $\kappa = \Lambda/(\rho c_p)$ and the isobaric thermal expansion coefficient $\alpha = -1/\rho\, \partial_T \rho|_{P=\mathrm{const}}$. The ratio of viscosity and thermal diffusivity, defines the Prandtl number

$$Pr = \frac{\nu}{\kappa}, \tag{2.1.1}$$

which is a pure material function. The Prandtl number of liquid metals is very low, $Pr \ll 1$, while gases have $Pr \simeq 1$, the Prandtl number in water varies between $Pr = 1.75$ at $T = 100\,^\circ\mathrm{C}$ and $Pr = 13.5$ at $T = 0\,^\circ\mathrm{C}$, and finally oils and alcohols have $10 \lesssim Pr \lesssim 40\,000$.

The imposed adverse temperature difference $\Delta = T_b - T_t$ and, consequently, the buoyancy is a source of constant energy supply. In case of a positive expansion coefficient α, which almost all fluids possess under normal conditions – an exception is water around its critical point – the hot fluid at the bottom will be lighter than the cold fluid at the top. This is a potential source of instability, but with the viscosity of the fluid working against it. Naturally, if Δ exceeds a certain value the system is expected to become unstable. First experiments on this matter were performed by Bénard (1900), who found out that above a critical Δ_{crit} convection sets in and a regular pattern of hexagons forms, when looking on the fluid layer from above. Rayleigh (1916) laid the foundations of the problem by identifying the ratio of buoyancy force to viscous and thermal dissipation as the crucial control parameter for the onset of thermal instability,

$$\mathrm{Ra} = \frac{\alpha g H^3 \Delta}{\kappa \nu}. \tag{2.1.2}$$

In his honour this quantity was named Rayleigh number afterwards. As shown, for example, by Chandrasekhar (1961), for a laterally infinite system and free boundaries at the top and bottom the critical Rayleigh number and its corresponding critical wavelength are

$$\mathrm{Ra}_{\mathrm{crit}} = \frac{27}{4}\pi^4 = 657.11, \qquad k_{\mathrm{crit}} = \sqrt{\frac{\pi^2}{2}} = 2.2214; \tag{2.1.3}$$

and for two rigid bounding surfaces, their values are given by,

$$\mathrm{Ra}_{\mathrm{crit}} = 1707.662, \qquad k_{\mathrm{crit}} = 3.117. \tag{2.1.4}$$

These values do not depend on the Prandtl number. However, Pr is crucially affecting the secondary instabilities, discussed in more detail in 2.9. In the current work, Ra is generally chosen to be well above $\mathrm{Ra}_{\mathrm{crit}}$.

2.2 The governing equations

The equations governing Rayleigh–Bénard convection are the continuity equation, describing mass conservation, the Navier–Stokes equations, describing momentum conservation and the equation of heat transfer, describing energy conservation. In the following, they will be introduced in Cartesian tensor notation and using the usual summation convention (Batchelor, 1967; Chandrasekhar, 1961; Landau and Lifschitz, 2007).

2.2.1 The continuity equation

Let x_j $(j = 1, 2, 3)$ denote the position, u_j the velocity components and ∂_j the partial derivative with respect to the coordinate x_j. The mass conservation of a fluid is then expressed as

$$\partial_t \rho + \partial_j (\rho u_j) = 0. \tag{2.2.1}$$

In the case of an incompressible fluid this simplifies to

$$\partial_j u_j = 0, \tag{2.2.2}$$

therefore the velocity field is solenoidal. There are two sufficient conditions when this assumption is reasonable. For one thing, the flow speed u must be much less than the speed of sound c_s, i.e. the local Mach number $\mathrm{Ma} = u/c_s$ must be much less than one. For another thing, the typical time scale τ in which the flow significantly varies must be much bigger than the time a sound signal needs to cover a typical length scale l, i.e. $\tau \gg l/c_s$ (see e.g. Chorin and Marsden, 2000; Landau and Lifschitz, 2007).

2.2.2 The Navier–Stokes equations

The equations of motion, guaranteeing momentum conservation, read

$$\rho\partial_t u_i + \rho u_j \partial_j u_i = -\partial_i P + \partial_j \tau_{ij} + f_i. \tag{2.2.3}$$

Here, P is the pressure, τ_{ij} the deviatoric stress tensor, defined as

$$\tau_{ij} = \eta \left(\partial_j u_i + \partial_i u_j - \tfrac{2}{3}\delta_{ij}\partial_k u_k\right), \tag{2.2.4}$$

which in the incompressible case simplifies to

$$\tau_{ij} = \eta \left(\partial_j u_i + \partial_i u_j\right), \tag{2.2.5}$$

and f_i is an arbitrary external force. For convection problems, one external force is the buoyancy force,

$$f_b = -\rho g \delta_{i3}. \tag{2.2.6}$$

Another relevant example is the Coriolis force

$$f_c = -2\rho\epsilon_{ijk}\Omega_j u_k, \tag{2.2.7}$$

where Ω_j is the angular velocity component.
Assuming, furthermore, a constant dynamic viscosity η, equation (2.2.3) simplifies to the original form of the Navier–Stokes equations:

$$\rho\partial_t u_i + \rho u_j \partial_j u_i = -\partial_i P + \eta\nabla^2 u_i + f_i. \tag{2.2.8}$$

It is also often convenient to split the pressure into a hydrostatic pressure P_0 and a reduced pressure p, $P = P_0 + p$. The derivative of P_0 is $\partial_i P_0 = -\rho_0 g \delta_{i3}$, with ρ_0 being the reference density in static equilibrium. Thus, the Navier–Stokes equations for Rayleigh–Bénard convection without additional forces read

$$\rho\partial_t u_i + \rho u_j \partial_j u_i = -\partial_i p + \partial_j \tau_{ij} + (\rho_0 - \rho) g \delta_{i3}. \tag{2.2.9}$$

2.2.3 The equation of heat transfer

The equation expressing the conservation of energy can be obtained by starting with the equation for the entropy S,

$$\rho T \left(\partial_t S + u_j \partial_j S\right) = \partial_j \left(\Lambda \partial_j T\right) + \rho\Phi, \tag{2.2.10}$$

where Φ is the dissipation due to viscosity, given by

$$\Phi = \frac{1}{2\rho}\tau_{ij}\left(\partial_j u_i + \partial_i u_j\right), \tag{2.2.11}$$

and in the incompressible case, respectively,

$$\Phi = \frac{\nu}{2}\left(\partial_j u_i + \partial_i u_j\right)^2. \tag{2.2.12}$$

In natural convection, however, the viscous dissipation is negligible (see e.g. Landau and Lifschitz, 2007). As a next step the differential 1-form of S,

$$dS = \partial_T S|_p dT + \partial_p S|_T dp, \tag{2.2.13}$$

is rewritten using several thermodynamic relations, namely, one of the Maxwell identities,

$$\partial_p S|_T = -\partial_T V|_p, \tag{2.2.14}$$

with V being the volume, the definition of the isobaric specific heat capacity

$$c_p \equiv T\partial_T S|_p, \tag{2.2.15}$$

and the isobaric expansion coefficient

$$\alpha \equiv \frac{1}{V}\partial_T V|_p = -\frac{1}{\rho}\partial_T \rho|_p. \tag{2.2.16}$$

This yields

$$dS = \frac{c_p}{T}\, dT - \alpha\rho\, dp. \tag{2.2.17}$$

In case of an incompressible fluid, p can be considered to be constant at the differentiation of thermodynamic quantities (see e.g. Landau and Lifschitz, 2007), thus the last term of equation (2.2.17) can be neglected. Hence, the general equation (2.2.10) reduces to

$$\rho c_p \partial_t \left(T + u_j \partial_j T\right) = \partial_j \left(\Lambda \partial_j T\right). \tag{2.2.18}$$

2.2.4 The Oberbeck-Boussinesq approximation

In Rayleigh–Bénard convection, commonly, the general set of equations (2.2.2), (2.2.9) and (2.2.18) is further reduced to the so-called Oberbeck–Boussinesq (OB) approximation, which was first independently applied by Oberbeck (1879) and Boussinesq (1903).

The main idea behind it is that in many circumstances, density variations and compressibility effects can be justifiably neglected. The only exception is the density variation in the buoyancy term, where naturally it must be of significance.

The four main assumptions to obtain the governing equations in the OB approximation are as follows. First, the density ρ is constant everywhere, except within the buoyancy term. Second, in the buoyancy term a Taylor expansion for the density around a reference temperature $T = T_0$ is performed where ρ_0 is the density at this reference temperature leading to

$$\rho = \rho_0 + \partial_T \rho|_{T=T_0}(T - T_0) + \mathcal{O}\big((T - T_0)^2\big). \tag{2.2.19}$$

With the definition of the isobaric thermal expansion coefficient α, given by equation (2.2.16), and dropping the higher order terms, this yields

$$\frac{\rho - \rho_0}{\rho_0} = -\alpha_0(T - T_0). \tag{2.2.20}$$

Third, all other material properties are independent of pressure and temperature. Fourth, energy dissipation due to viscosity is neglected.
The final result are the *Oberbeck–Boussinesq equations*, expressed by additionally making use of the material derivative operator $D_t = \partial_t + u_j \partial_j$

$$\begin{aligned} \partial_j u_j &= 0, && (2.2.21) \\ D_t u_i &= -\frac{1}{\rho_0}\partial_i p + \nu \nabla^2 u_i + \alpha(T - T_0) g \delta_{i3}, && (2.2.22) \\ D_t T &= \kappa \nabla^2 T. && (2.2.23) \end{aligned}$$

2.2.5 Validity range of the Oberbeck–Boussinesq approximation *

Intuitively, it is evident that the OB approximation is not valid if the temperature difference Δ or the pressure difference, becomes too large, because naturally the material properties vary with temperature and with pressure.
Gray and Giorgini (1976) provided a mathematically straightforward way to explicitly calculate the validity range of the OB approximation. Their final result is a requirement on certain ε_i factors to be smaller than a requested accuracy. In this thesis I only focus on liquids, thus, only the temperature dependencies of the material properties are relevant. The ε factors are therefore given by

$$\begin{aligned} \varepsilon_1 &= \frac{\alpha_m\, g\, H\, T_m}{c_{p,m}\ \ \Delta}, & \varepsilon_2 &= \frac{\alpha_m\, g\, H\, \nu_m}{c_{p,m}\ \ \kappa_m}, & \varepsilon_3 &= -\frac{\Delta}{\rho_m}\left.\frac{\partial \rho}{\partial T}\right|_{T=T_m}, \\ \varepsilon_4 &= \frac{\Delta}{c_{p,m}}\left.\frac{\partial c_p}{\partial T}\right|_{T=T_m}, & \varepsilon_5 &= \frac{\Delta}{\rho_m \nu_m}\left.\frac{\partial(\rho\nu)}{\partial T}\right|_{T=T_m} & & \qquad (2.2.24) \\ \varepsilon_6 &= \frac{\Delta}{\Lambda_m}\left.\frac{\partial \Lambda}{\partial T}\right|_{T=T_m}, & \varepsilon_7 &= \frac{\Delta}{\alpha_m}\left.\frac{\partial \alpha}{\partial T}\right|_{T=T_m}. \end{aligned}$$

The index m here and in the following refers to the quantity at the arithmetic mean temperature between the heating and cooling plate

$$T_m = \frac{T_t + T_b}{2}. \qquad (2.2.25)$$

That means, that if $|\varepsilon_1| \dots |\varepsilon_7| \leqslant 0.1$, a residual error of at most 10 % is guaranteed. The factor ε_3 represents the common $\alpha\Delta \leqslant 0.1$ criterion which is often quoted as being a sufficient criterion (e.g. Chavanne et al., 2001).
Note that the Gray–Giorgini ansatz does not provide a criterion for a strong development of non-Oberbeck–Boussinesqness, which becomes visible already in such integral quantities like the Nusselt number or the centre temperature. As it was shown by Ahlers et al. (2006) and Sugiyama et al. (2007), these global parameters are affected mainly by higher order terms in the temperature dependences of the material parameters.

---

*Partly adopted from HORN, S., SHISHKINA, O. AND WAGNER, C., On non-Oberbeck–Boussinesq effects in three-dimensional Rayleigh–Bénard convection in glycerol, *J. Fluid Mech. 724* (2013), 175–202.

2.2.6 The non-Oberbeck–Boussinesq equations

Here, I only investigate the temperature-dependence of liquids, where not only the pressure dependence, but also the temperature dependence of c_p and ρ, except within the buoyancy term, is negligible. This will be elaborated further in chapter 5. The general set of equations used to describe liquids with temperature dependent material, i.e. under non-Oberbeck–Boussinesq (NOB) conditions, are given by

$$\partial_j u_j = 0, \tag{2.2.26}$$

$$D_t u_i = -\frac{1}{\rho_m}\partial_i p + \partial_j\big(\nu\left(\partial_j u_i + \partial_i u_j\right)\big) + \frac{\rho_m - \rho}{\rho_m} g\delta_{i3},, \tag{2.2.27}$$

$$\rho_m c_{p,m} D_t T = \partial_j\left(\Lambda \partial_j T\right). \tag{2.2.28}$$

They will be referred to as *non-Oberbeck–Boussinesq equations* in the following.

2.2.7 Governing equations in cylindrical coordinates

Throughout this thesis a cylindrical coordinate system is used, thus, for sake of clarity and comprehensibility, the two main sets of equations, (2.2.21)–(2.2.23) and (2.2.26)–(2.2.28), are also given here in terms of the radial, azimuthal and vertical coordinate (r, ϕ, z) and the respective velocity components (u_r, u_ϕ, u_z).
The OB equations are

$$\frac{1}{r}\partial_r\left(r u_r\right) + \frac{1}{r}\partial_\phi u_\phi + \partial_z u_z = 0 \tag{2.2.29}$$

$$D_t u_r - \frac{u_\phi^2}{r} + \frac{1}{\rho_m}\partial_r p = \nu_m\left(\nabla^2 u_r - \frac{u_r}{r^2} - \frac{2}{r^2}\partial_\phi u_\phi\right),$$

$$D_t u_\phi + \frac{u_r u_\phi}{r} + \frac{1}{\rho_m}\frac{1}{r}\partial_\phi p = \nu_m\left(\nabla^2 u_\phi - \frac{u_\phi}{r^2} + \frac{2}{r^2}\partial_\phi u_r\right) \tag{2.2.30}$$

$$D_t u_z + \frac{1}{\rho_m}\partial_z p = \nu_m \nabla^2 u_z + \alpha_m (T - T_0) g.$$

$$D_t T = \kappa_m \nabla^2 T. \tag{2.2.31}$$

The NOB equations read

$$\frac{1}{r}\partial_r\left(r u_r\right) + \frac{1}{r}\partial_\phi u_\phi + \partial_z u_z = 0, \tag{2.2.32}$$

$$D_t u_r - \frac{u_\phi^2}{r} + \frac{1}{\rho_m}\partial_r p = \frac{1}{r}\partial_r\left(r\nu\sigma_{rr}\right) + \frac{1}{r}\partial_\phi\left(\nu\sigma_{r\phi}\right) + \partial_z\left(\nu\sigma_{rz}\right) - \frac{1}{r}\nu\sigma_{\phi\phi},$$

$$D_t u_\phi + \frac{u_r u_\phi}{r} + \frac{1}{\rho_m}\frac{1}{r}\partial_\phi p = \frac{1}{r^2}\partial_r\left(r^2\nu\sigma_{\phi r}\right) + \frac{1}{r}\partial_\phi\left(\nu\sigma_{\phi\phi}\right) + \partial_z\left(\nu\sigma_{\phi z}\right), \tag{2.2.33}$$

$$D_t u_z + \frac{1}{\rho_m}\partial_z p = \frac{1}{r}\partial_r\left(r\nu\sigma_{zr}\right) + \frac{1}{r}\partial_\phi\left(\nu\sigma_{z\phi}\right) + \partial_z\left(\nu\sigma_{zz}\right) + \frac{\rho_m - \rho}{\rho_m} g,$$

$$\rho_m c_{p,m} D_t T = \frac{1}{r}\partial_r(\Lambda r \partial_r T) + \frac{1}{r^2}\partial_\phi(\Lambda \partial_\phi T) + \partial_z(\Lambda \partial_z T), \tag{2.2.34}$$

where the components of the symmetric tensor σ are given by

$$\begin{aligned}
\sigma_{rr} &= 2\partial_r u_r, & \sigma_{r\phi} &= \sigma_{\phi r} = \frac{1}{r}\partial_\phi u_r + \partial_r u_\phi - \frac{u_\phi}{r}, \\
\sigma_{\phi\phi} &= 2\left(\frac{1}{r}\partial_\phi u_\phi + \frac{u_r}{r}\right), & \sigma_{\phi z} &= \sigma_{z\phi} = \partial_z u_\phi + \frac{1}{r}\partial_\phi u_z, \\
\sigma_{zz} &= 2\partial_z u_z, & \sigma_{zr} &= \sigma_{zr} = \partial_z u_r + \partial_r u_z.
\end{aligned}$$

2.2.8 Dimensionless equations

It is more convenient to work with non-dimensional equations to study Rayleigh–Bénard convection. They are obtained by using the physical parameters radius R, temperature difference Δ, buoyancy velocity $\sqrt{g\alpha_m R\Delta}$, and the various material properties at the mean temperature, i.e. $\alpha_m, \nu_m, \Lambda_m, c_{p,m}\kappa, \rho_m$ as reference scales. In line with this, the reference time is given by $R/\sqrt{g\alpha_m R\Delta}$ and the reference pressure is $\rho_m g\alpha_m R\Delta$. Hence, the dimensionless quantities, denoted by a hat, are given by

$$\begin{aligned}
\hat{X} &= \frac{X}{X_m} \quad (X = \alpha, \nu, \Lambda, c_p, \kappa, \rho), & \hat{T} &= \frac{T - T_m}{\Delta} \\
\hat{u}_i &= \frac{u_i}{\sqrt{g\alpha_m R\Delta}}, & \hat{x}_i &= \frac{x_i}{R} \\
\hat{t} &= \frac{t}{R}\sqrt{g\alpha_m R\Delta}, & \hat{p} &= \frac{p}{\rho_m g\alpha_m R\Delta}.
\end{aligned}$$

Replacing the original variables in the OB equations (2.2.21)–(2.2.23) with their scaled counterparts reduces the problem to a dimensionless form:

$$\partial_{\hat{j}}\hat{u}_{\hat{j}} = 0, \tag{2.2.35}$$

$$D_{\hat{t}}\hat{u}_{\hat{i}} = -\partial_{\hat{i}}\hat{p} + Ra^{-\frac{1}{2}} Pr^{\frac{1}{2}} \gamma^{-\frac{3}{2}} \nabla^2 \hat{u}_{\hat{i}} + \hat{T}\delta_{\hat{i}3}, \tag{2.2.36}$$

$$D_{\hat{t}}\hat{T} = Ra^{-\frac{1}{2}} Pr^{-\frac{1}{2}} \gamma^{-\frac{3}{2}} \nabla^2 \hat{T}. \tag{2.2.37}$$

Similarly, after inserting them into the NOB equations (2.2.26)–(2.2.28), the non-dimensional NOB equations are:

$$\partial_{\hat{j}}\hat{u}_{\hat{j}} = 0, \tag{2.2.38}$$

$$D_{\hat{t}}\hat{u}_{\hat{i}} = -\partial_{\hat{i}}\hat{p} + Ra^{-\frac{1}{2}} Pr^{\frac{1}{2}} \gamma^{-\frac{3}{2}} \partial_{\hat{j}}\left(\hat{\nu}\left(\partial_{\hat{j}}\hat{u}_{\hat{i}} + \partial_{\hat{i}}\hat{u}_{\hat{j}}\right)\right) + (1 - \hat{\rho})\delta_{\hat{i}3}, \tag{2.2.39}$$

$$D_{\hat{t}}\hat{T} = Ra^{-\frac{1}{2}} Pr^{-\frac{1}{2}} \gamma^{-\frac{3}{2}} \partial_{\hat{j}}\left(\hat{\Lambda}\partial_{\hat{j}}\hat{T}\right). \tag{2.2.40}$$

Here, the classical control parameters Ra, Pr and γ appear, showing that only their ratios are important but not the actual physical quantities. The Rayleigh and the Prandtl number are defined at the mean temperature T_m,

$$Ra = Ra_m = \frac{\alpha_m g\Delta H^3}{\kappa_m \nu_m}, \tag{2.2.41}$$

$$Pr = Pr_m = \frac{\nu_m}{\kappa_m}. \tag{2.2.42}$$

The radius-to-height aspect ratio

$$\gamma = \frac{R}{H} \tag{2.2.43}$$

characterises the confinement, (cf. section 2.1). Of course, different choices for the reference scales are possible. The hat on the dimensionless quantities is dropped for clarity furtheron.

Two convective flows having different physical dimensions but being scaled in the same way are called similar. Under OB conditions, this means that Ra, Pr and Γ are to be identical. Under NOB conditions, the functional dependence of the material properties must also be the same to yield a similar flow. Since these dependencies are in general very specific for every fluid, however, dimensions are implicitly fixed.

2.3 The Nusselt and the Reynolds number

The key response parameters in Rayleigh–Bénard convection are the Nusselt number Nu, characterising the mean heat transport, and the Reynolds number Re, characterising the turbulence level in the flow. Their dependence on Ra and Pr is one of the primary questions eagerly demanding an answer in turbulent convection research.

The Nusselt number is defined as

$$Nu = \frac{qH}{\Lambda_m \Delta} = \frac{(q_{conv} + q_{cond})H}{\Lambda_m \Delta} = \frac{(\langle \rho c_p u_z T \rangle_{A,t} + \langle \Lambda \partial_z T \rangle_{A,t})H}{\Lambda_m \Delta}, \tag{2.3.1}$$

i.e. the ratio of the total heat flux q normalised by the heat flux without convection. The total heat flux is the sum of the conductive and convective heat flux, $q = q_{cond} + q_{conv}$. Here, $\langle \cdot \rangle_{A,t}$ denotes avering over any horizontal plane and in time. Per definition in the conduction state, i.e. when Ra is below the critical value Ra_c, the Nusselt number equals one.

The Reynolds number, however, is not uniquely defined. Formally, it is given by

$$Re = \frac{U}{\nu L}, \tag{2.3.2}$$

with a characteristic velocity U, a characteristic length L and a characteristic viscosity scale ν. All of them can be chosen differently and thereby significantly influence the actual value of Re.

Finding a universal equation that describes how Re and Nu depend on the dimensionless control parameters Ra, Pr and Γ is one of the key questions sought to be solved in convection research. Recently, the Grossmann–Lohse theory is the most established theory in this respect and will be discussed in section 2.9.

2.4 Statistical moments and their relevance for turbulent flows

Most quantities in turbulent thermal convection cannot be predicted in their detailed behaviour, but only in a statistical sense. However, certain statistical quanti-

ties are reproducible, making the statistical desription a very succesful tool in the characterisation of turbulent flows. Most versatile for this purpose are the classical statistical moments mean, variance, skewness and kurtosis.
The first, and probably most important, moment is the mean value. For a certain quantity χ it is given by

$$\langle\chi\rangle = \int\limits_{-\infty}^{\infty} \chi p(\chi)\, d\chi, \tag{2.4.1}$$

where $p(\chi)$ is the probability density function (pdf) of the variable χ with

$$\int\limits_{-\infty}^{\infty} p(\chi)\, d\chi = 1. \tag{2.4.2}$$

The brackets mark a suitable averaging operation. In fluid dynamics usually an averaging in space and/or in time is performed. Furthermore, ergodicity is assumed, implying that time averages and ensemble averages are equivalent. Thus, both temporal and spatial averages are utterly important.
An instantaneous and/or local flow quantity can be decomposed into its mean $\langle\chi\rangle$ and a perturbation, or fluctuating, part χ',

$$\chi = \langle\chi\rangle + \chi' \tag{2.4.3}$$

This is known as Reynolds decomposition.
The second moment of χ' is the variance

$$\sigma^2 = \left\langle \chi'^2 \right\rangle = \int\limits_{-\infty}^{\infty} \left(\chi - \langle\chi\rangle\right)^2 p(\chi)\, d\chi. \tag{2.4.4}$$

It is closely related to the root-mean-square (rms) of the fluctuations

$$\chi_{rms} = \sqrt{\left\langle \left(\chi - \langle\chi\rangle\right)^2 \right\rangle} = \sqrt{\langle\chi^2\rangle - \langle\chi\rangle^2}. \tag{2.4.5}$$

It is a measure for the strength of the turbulent fluctuations. In the case of the velocity components, these quantities are referred to as turbulence intensities. The specific turbulent kinetic energy is a combined quantity of them and is given by

$$e_{tk} = \tfrac{1}{2}\left(u_{z,rms}^2 + u_{\phi,rms}^2 + u_{r,rms}^2\right). \tag{2.4.6}$$

The skewness is the third normalised moment of χ' and a measure of the asymmetry of a distribution. In the case of thermal convection usually of the asymmetry of the temperature and the velocity fluctuations is considered. It is defined as

$$S(\chi) = \frac{\left\langle (\chi - \langle\chi\rangle)^3 \right\rangle}{\chi_{rms}^3} = \frac{\langle\chi^3\rangle - 3\langle\chi^2\rangle\langle\chi\rangle + 2\langle\chi\rangle^3}{\left(\langle\chi^2\rangle - \langle\chi\rangle^2\right)^{3/2}}. \tag{2.4.7}$$

If a distribution is symmetric, than $S = 0$. If it is positive, than large positive values are more likely than large negatives ones. The analogue is true for a negative skewness, there large negative values are more likely than large positive ones.
The flatness, also called kurtosis, is another measure to characterise a turbulent flow and is given by[†]

$$F(\chi) = \frac{\left\langle (\chi - \langle\chi\rangle)^4 \right\rangle}{\chi_{rms}^4} = \frac{\langle\chi^4\rangle - 4\langle\chi^3\rangle\langle\chi\rangle + 6\langle\chi^2\rangle\langle\chi\rangle^2 - 3\langle\chi\rangle^4}{\left(\langle\chi^2\rangle - \langle\chi\rangle^2\right)^2}. \tag{2.4.8}$$

For high values of the flatness, strong positive or negative fluctuations are likely. Thus it indicates high amplitude and intermittency episodes in a time series. If the flatness is low, then most values are clustered around the mean value.

2.5 Thermal and viscous boundary layers

In a confined system boundary layers form at the solid walls. In a cylindrical Rayleigh–Bénard cell, as considered in this thesis, viscous boundary layers form at the top and bottom and the lateral sidewall since the fluid at the walls has zero velocity relative to the wall. Thermal boundary layers occur only at the isothermal top and bottom plates, but not on the lateral wall due to the assumed adiabaticity. Their thickness depends on the viscosity and the diffusivity and, thus, their relative thickness depends on the Prandtl number. For $Pr \gg 1$, the thermal boundary layer is nested within the viscous one and for $Pr \ll 1$ the viscous boundary layer is nested within the thermal one. In a confined Rayleigh–Bénard cell, the actual ratio of both boundary layer thicknesses also depends strongly on the angle of the wind attacking the boundary layer. This will be further elaborated below in section 2.8.
The boundary layer thicknesses can be defined by different criteria. The ones used here, and probably the most common ones, are the slope and the rms criterion. According to the slope criterion, the thicknesses of the boundary layers are determined by the point where the tangent of the profile at the plate intersects with either the centre temperature, in the case of thermal boundary layers, or with the maxima of the radial velocity, in the case of viscous boundary layers. Mathematically expressed, the thermal top and bottom boundary layer thicknesses are given by

$$\lambda_t^\theta = \frac{T_t - T_c}{\partial_z \langle T\rangle_{r,\phi,t}\big|_{z=H}}, \qquad \lambda_b^\theta = \frac{T_c - T_b}{\partial_z \langle T\rangle_{r,\phi,t}\big|_{z=0}}, \tag{2.5.1}$$

and similarly the viscous ones are given by,

$$\lambda_t^u = -\frac{u_r^{max_t}}{\partial_z \langle u_r\rangle_{r,\phi,t}\big|_{z=H}}, \qquad \lambda_b^u = \frac{u_r^{max_b}}{\partial_z \langle u_r\rangle_{r,\phi,t}\big|_{z=0}}, \tag{2.5.2}$$

where $u_r^{max_t}$ and $u_r^{max_b}$ are the first maxima of the radial velocity profile close to the top and bottom plate, respectively. Because of the intrinsic symmetry of Rayleigh–Bénard convection under OB conditions, the top and bottom boundary layers have

---

[†] sometimes the kurtosis is not defined as the fourth moment, but the fourth cumulant divided by the square of the second cumulant, i.e. a factor 3 is subtracted

the same thickness,

$$\lambda_{OB} = \lambda_t = \lambda_b. \tag{2.5.3}$$

The Boundary layer thickness based on rms-value is defined as the vertical distance from the top and bottom plate, respectively, where the temperature rms, T_{rms}, or radial velocity rms, $u_{r,rms}$ profile reaches the first maximum:

$$\delta_t^\theta = \max\left(z|_{\partial_z \langle u_{r,rms} \rangle = 0} \right), \qquad \delta_b^\theta = \min\left(z|_{\partial_z \langle u_{r,rms} \rangle = 0} \right), \tag{2.5.4}$$

$$\delta_t^u = \max\left(z|_{\partial_z \langle T_{rms} \rangle = 0} \right), \qquad \delta_b^u = \min\left(z|_{\partial_z \langle T_{rms} \rangle = 0} \right). \tag{2.5.5}$$

2.6 Flow structures in thermal convection: Plumes and the large-scale circulation (LSC)

The large-scale circulation (LSC), also called "wind" is a coherent flow structure in turbulent convection along the walls of the Rayleigh–Bénard cell. It has an elliptical shape and usually fills the whole container. Hence, there is a wind almost parallel to the bottom plate and a wind in the opposite direction along the top plate. The circulation is closed by an up- and down-welling flow along the lateral wall(s). In Cartesian geometries, the LSC is confined between two opposite corners, trying to fill most of the space, while in cylindrical containers its azimuthal orientation is random and can vary with time (Brown and Ahlers, 2006).

Since its first detection by Krishnamurti and Howard (1981), it has become subject of intensive research and is a major ingredient in the theories attempting to predict and explain the relation between the Nusselt, Reynolds, Rayleigh and Prandtl number, as for example in the Grossmann–Lohse theory, which will be discussed in more detail in section 2.9. The origin of the LSC in the first place is not completely certain. There are essentially two different opinions. The first one assumes, that the rolls that develop close to the onset of convection continue to exist at even the highest Ra, but only in an averaged sense (Fitzjarrald, 1976). The second one, proposed by Krishnamurti and Howard (1981), considers the LSC as a high Rayleigh number effect, where the plumes detaching from the boundary layers interact with the mean shear. This results in tilted plumes generating a Reynolds stress to maintain a shear against dissipation.

The appearance of the LSC, such as its geometrical features and its dynamics, strongly depend on the aspect ratio Γ and the inherent symmetry of the Rayleigh–Bénard cell (Ahlers et al., 2009). If the aspect ratio equals one, a large-scale convection roll in a vertical plane and two smaller counter-rotating rolls in the corners occur. In the plane perpendicular to it four equally-sized rolls are observed (Horn et al., 2013b). According to Ahlers et al. (2009) an LSC can be described by a unique turnover time τ and a typical length scale L. Therewith a Reynolds number can be defined by

$$Re^{LSC} \equiv \frac{2L^2}{\tau\nu}. \tag{2.6.1}$$

The driving mechanism of the LSC is on the one hand conduction across the boundary layers to the adjacent fluid and on the other hand hot plumes ascending from the bottom plate and cold plumes descending from the top plate. These thermal plumes are another coherent mode of heat transport (Siggia, 1994). They can be understood as detached boundary layers (Grossmann and Lohse, 2004) or interior layers (Shishkina and Wagner, 2007a). Consequently, thermal plumes and the thermal boundary layers have the same characteristic length scale, namely the thickness of the thermal boundary layer. The thermal plumes are extended in the direction in which they are advected.

2.7 Useful analytical relations

There are a few analytical relations that come handy in the investigation of Rayleigh–Bénard convection.

The heat flux, and hence, the Nusselt number is constant in vertical direction, also under NOB conditions. This can be proven by averaging the energy equation (2.2.28) in time,

$$\left\langle \rho_m c_{p,m} \left(\partial_t T + u_i \partial_i T \right) \right\rangle_t - \left\langle \partial_i \left(\Lambda \partial_i T \right) \right\rangle_t = 0. \tag{2.7.1}$$

The temporal average of a time derivative is zero,

$$\left\langle \partial_t T \right\rangle_t = 0 \tag{2.7.2}$$

and the second term can be rewritten using the continuity equation (2.2.26),

$$\partial_i \left(u_i T \right) = T \partial_i u_i + u_i \partial_i T = u_i \partial_i T, \tag{2.7.3}$$

yielding

$$\rho_m c_{p,m} \partial_i \left\langle (u_i T) \right\rangle_t - \partial_i \left\langle (\Lambda \partial_i T) \right\rangle_t = 0. \tag{2.7.4}$$

Averaging over a whole horizontal cross section $S = \{0 \leqslant r \leqslant R, 0 \leqslant \phi \leqslant \pi, z\}$ at an arbitrary height z gives

$$\rho_m c_{p,m} \left\langle u_z T \right\rangle_{t,S} - \left\langle \Lambda \partial_z T \right\rangle_{t,S} = \text{const}. \tag{2.7.5}$$

Hence, the Nusselt number Nu (eq. (2.3.1)) is constant. Other rigorous analytical relations for the heat flux involve the kinetic dissipation rate

$$\epsilon_u(x,t) = \nu \left(\partial_i u_j(x,t) \right)^2 \tag{2.7.6}$$

and the thermal dissipation rate

$$\epsilon_\theta(x,t) = \kappa \left(\partial_i T(x,t) \right)^2. \tag{2.7.7}$$

Global averaging over the whole volume gives (Siggia, 1994)

$$\langle \epsilon_u(x,t) \rangle_V = \frac{\nu^3}{H^4} (\mathrm{Nu} - 1) \mathrm{Ra} \mathrm{Pr}^{-2}, \tag{2.7.8}$$

$$\langle \epsilon_\theta(x,t) \rangle_V = \kappa \frac{\Delta^2}{H^2} \mathrm{Nu}. \tag{2.7.9}$$

2.8 Falkner–Skan boundary layer approximation[‡]

In many theoretical considerations of Rayleigh–Bénard convection it is assumed that the large-scale wind blows parallel along the plates and is constant leading to a zero pressure gradient with respect to the wind direction. This results in an approximate description of the boundary layer dynamics based on a classical Prandtl–Blasius ansatz (Schlichting and Gersten, 2006).

In contrast to this, direct numerical simulations (DNS) of turbulent convection in different fluids showed that, first, the time-averaged pressure gradient does not vanish (Shi et al., 2012); second, the wind is non-constant along its path and, third, the ratio of the thicknesses of the thermal and viscous boundary layers, although being almost constant along the wind, is approximately two times larger (Wagner et al., 2012) than that predicted by the Prandtl–Blasius equations.

In order to account for the influence of the non-constant wind, the Falkner–Skan approximation of the boundary layers can be used, which can be interpreted as an extension of the Prandtl–Blasius ansatz to a non-zero pressure change along the wind. This approach, compared to a Prandtl–Blasius one, leads to more reliable predictions of some integrated quantities related to the thicknesses of the thermal and viscous boundary layers.

The laminar boundary layer equations in this case are given by

$$
\begin{aligned}
\tilde{u}\partial_{\tilde{x}}\tilde{u} + \tilde{v}\partial_{\tilde{y}}\tilde{u} &= \tilde{\nu}\partial_{\tilde{y}\tilde{y}}\tilde{u} - \partial_{\tilde{x}}\tilde{p}/\tilde{\rho} &\quad (2.8.1)\\
0 &= -\partial_{\tilde{y}}\tilde{p}/\tilde{\rho}, &\quad (2.8.2)\\
\tilde{u}\partial_{\tilde{x}}\tilde{T} + \tilde{v}\partial_{\tilde{y}}\tilde{T} &= \tilde{\kappa}\partial_{\tilde{y}\tilde{y}}\tilde{T}. &\quad (2.8.3)
\end{aligned}
$$

Here $\tilde{\mathbf{u}} \equiv (\tilde{u}, \tilde{v}, \tilde{w})^T$ is the velocity vector-function in the Cartesian coordinate system $\tilde{\mathbf{x}} = (\tilde{x}, \tilde{y}, \tilde{z})$, $\tilde{y}$ is the vertical direction, $\tilde{x}$ and $\tilde{z}$ are horizontal directions and $\tilde{x}$ is along the wind. Since the considered boundary layer flow is two-dimensional and incompressible, (2.8.1), (2.8.3) can be rewritten in terms of the streamfunction $\tilde{\Psi}$, which satisfies

$$\tilde{u} = \partial_{\tilde{y}}\tilde{\Psi}, \qquad \tilde{v} = -\partial_{\tilde{x}}\tilde{\Psi}. \tag{2.8.4}$$

If a similarity solution is sought under the assumption that $\tilde{\Psi}$ and the similarity variable ξ are representable in the forms

$$\tilde{\Psi} = \tilde{\nu}\Psi(\xi)\, g(x), \quad \xi = y\, f(x), \tag{2.8.5}$$

and for the wind at the edge of the viscous boundary layer holds $\tilde{U} = \tilde{U}(\tilde{x})$, then the similarity solution exists only if g_x/f is constant and g is either exponential or a power function of x. Here $x \equiv \tilde{x}/\tilde{L}$ and $y \equiv \tilde{y}/\tilde{L}$ are the dimensionless spatial coordinates and the functions g and f depend on x alone.

[‡] This section has partly been adopted from SHISHKINA, O., HORN, S. AND WAGNER, S., Falkner–Skan boundary layer approximation in Rayleigh–Bénard convection, *J. Fluid. Mech. 730* (2013), 442–463; and SHISHKINA, O., WAGNER, S. AND HORN, S., Influence of the angle between the wind and the isothermal surfaces on the boundary layer structures in turbulent thermal convection, *Phys. Rev. E 89* (2014), 033014.

The case in which g is exponential describes a decreasing boundary layer thickness along the wind, while if g is a power function, the boundary layer thickness increases. The latter case is in good agreement with DNS results by Wagner et al. (2012), which showed that near the horizontal plate, after the stagnation point, the boundary layer thickness grows together with the wind magnitude.
Thus, for Rayleigh–Bénard convection this case is relevant and solely considered in the following. It leads to a boundary layer of Falkner–Skan type (Falkner and Skan, 1931), which develops for a corner flow with angle β along the corners' sides, sketched in figure 2.2. The core flow (or wind) above the boundary layer and the pressure term within the BL equal, respectively,

$$\begin{aligned} \widetilde{U} &= \widetilde{U}_0 \, x^{-1+\pi/\beta}, && (2.8.6)\\ -\widetilde{p}_{\widetilde{x}}/\widetilde{\rho} &= (\pi/\beta - 1)\, x^{-3+2\pi/\beta}\, \widetilde{U}_0^2/\widetilde{L}, && (2.8.7) \end{aligned}$$

where $\widetilde{U}_0$ is a constant velocity magnitude. If the wind is parallel to the horizontal plate, i.e. $\beta = \pi$, the Falkner–Skan BL is reduced to the Prandtl–Blasius one.
Thus, one obtains the following system of the dimensionless boundary layer equations for the momentum (Falkner–Skan)

$$\begin{aligned} \partial_{\xi\xi\xi}\Psi + \Psi\partial_{\xi\xi}\Psi + (2-\gamma)\left(1 - (\partial_\xi\Psi)^2\right) &= 0, && (2.8.8)\\ \Psi(0) = 0, \quad \partial_\xi\Psi(0) = 0, \quad \partial_\xi\Psi(\infty) &= 1, && (2.8.9) \end{aligned}$$

and the energy

$$\begin{aligned} \partial_{\xi\xi}\Theta + \mathrm{Pr}\,\Psi\partial_\xi\Theta &= 0, && (2.8.10)\\ \Theta(0) = 0, \quad \Theta(\infty) &= 1. && (2.8.11) \end{aligned}$$

For the similarity variable ξ, the stream function Ψ and the dimensionless tempera-

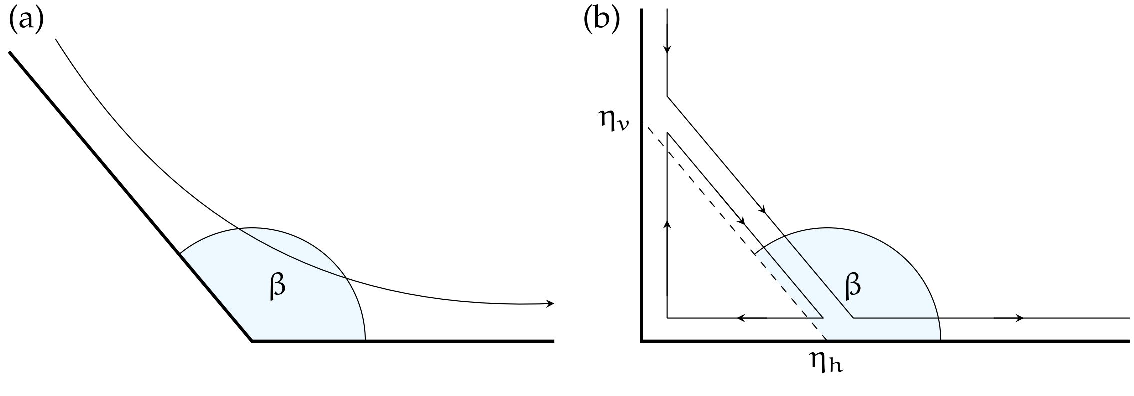

FIGURE 2.2: (a) Sketch of the corner flow with opening angle β in the Falkner–Skan sense. (b) Sketch of the LSC and the secondary roll within the LSC-plane. Here η_v and η_h are the distances from the corner to the locations, where the wall shear stress equals zero, and β is the angle at which the LSC attacks the heated bottom plate.

ture Θ the following expressions hold

$$\xi \equiv \gamma^{-1/2}\, \mathrm{Re}_0^{1/2} y\, x^{-1+1/\gamma}, \tag{2.8.12}$$

$$\Psi \equiv \gamma^{-1/2}\, \mathrm{Re}_0^{-1/2} x^{-1/\gamma}\, \widetilde{\nu}^{-1}\, \widetilde{\Psi}, \tag{2.8.13}$$

$$\Theta \equiv 2(\widetilde{T}_b - \widetilde{T})/\widetilde{\Delta}. \tag{2.8.14}$$

Here, $\mathrm{Re}_0 \equiv \widetilde{L}\widetilde{U}_0/\widetilde{\nu}$ is the Reynolds number based on the wind magnitude and

$$\gamma \equiv 2\beta/\pi. \tag{2.8.15}$$

With respect to the similarity variable ξ, the thickness of the viscous BL equals

$$\delta = \left(\partial_\xi \Psi|_{\xi=0}\right)^{-1} \tag{2.8.16}$$

and can be determined by solutions of the system (2.8.8), (2.8.9). δ depends on γ and, hence, on the angle β. Taking $\xi = \delta$, $y = \widetilde{\delta}_u/\widetilde{L}$, where $\widetilde{\delta}_u$ is the thickness of the viscous boundary layer in physical space, from (2.8.12) one obtains

$$\widetilde{\delta}_u/\widetilde{L} = \delta\, \gamma^{1/2}\, \mathrm{Re}_0^{-1/2} x^{1-1/\gamma}. \tag{2.8.17}$$

From (2.8.6), (2.8.15) and (2.8.16) it follows that

$$\widetilde{\delta}_u/\widetilde{L} \sim \sqrt{x/\mathrm{Re}}, \tag{2.8.18}$$

where the Reynolds number Re is based on the wind $\widetilde{U}$ (2.8.6). Relation (2.8.18) holds for general Falkner–Skan BLs and thus also for the special case of Prandtl–Blasius boundary layers, i.e. $\gamma = 2$. The proportionality of the relative thickness of the boundary layer and the inverse square-root of the Reynolds number, commonly known as Prandtl–formula, is one of the basic assumptions in the Grossmann–Lohse theory (see the following section 2.9), for the case of non-turbulent BLs.

The dependence of the viscous boundary layer δ on γ is obtained by solving numerically the system of Falkner–Skan equations (2.8.8) and (2.8.9) for $0 \leqslant \gamma \leqslant 2$; i.e., for all angles $0 \leqslant \beta \leqslant \pi$. It can be well approximated by

$$\delta \approx \delta_{\mathrm{appr}} \equiv C_1 (C_2 - \gamma)^{-1/2} \tag{2.8.19}$$

with $C_1 \approx 0.88$, $C_2 \approx 2.17$.

The temperature distributions within the boundary layers, i.e. the solution of (2.8.10), (2.8.11) does not only depend on γ, but also on Pr. The temperature profiles for the limiting cases $\mathrm{Pr} \ll 1$ and $\mathrm{Pr} \gg 1$ which satisfy the boundary conditions

$$\Theta|_{\zeta=0} = 0, \quad \partial_\zeta \Theta|_{\zeta=0} = 1, \quad \Theta|_{\zeta=\infty} = 1. \tag{2.8.20}$$

Thus, for the similarity variable

$$\zeta = C_3(\mathrm{Pr})\gamma^{-1/2}\mathrm{Re}_0^{1/2} y x^{1/\gamma - 1} \tag{2.8.21}$$

with

$$C_3(\mathrm{Pr}) = \begin{cases} 2^{1/2}\,\pi^{-1/2}\,\mathrm{Pr}^{1/2}, & \mathrm{Pr} \ll 1, \\ 6^{-1/3}[\Gamma(4/3)]^{-1}\delta^{-1/3}\mathrm{Pr}^{1/3}, & \mathrm{Pr} \gg 1, \end{cases}$$

the limiting energy boundary layer equations

$$\begin{aligned} \partial_{\zeta\zeta}\Theta + (\pi/2)\zeta\partial_{\zeta}\Theta = 0, &\qquad \mathrm{Pr} \ll 1, \\ \partial_{\zeta\zeta}\Theta + 3\Gamma^3(4/3)\zeta^2\partial_{\zeta}\Theta = 0, &\qquad \mathrm{Pr} \gg 1, \end{aligned} \tag{2.8.22}$$

have the following solution

$$\Theta(\zeta) = \int_0^{\zeta} \exp(-B\chi^{\omega})\,d\chi, \tag{2.8.23}$$

with B and ω being constants defined as follows:

$$\begin{aligned} \omega = 2, \quad B = \pi/4, &\qquad \mathrm{Pr} \ll 1, \\ \omega = 3, \quad B = \Gamma^3(4/3) \approx 0.71, &\qquad \mathrm{Pr} \gg 1, \end{aligned} \tag{2.8.24}$$

and Γ being the gamma function. The limiting profiles (2.8.23), (2.8.24) are independent of the angle β, i.e. they are the same as in the Prandtl–Blasius case for all β. Further, from the equations (2.8.20) and (2.8.21) one obtaines for the thermal boundary layer thickness

$$\widetilde{\delta}_\theta/\widetilde{L} = C_3^{-1}\,\gamma^{1/2}\,\mathrm{Re}_0^{-1/2}x^{1-1/\gamma}. \tag{2.8.25}$$

The relations (2.8.17) and (2.8.25) give the ratio of the thermal to viscous boundary layers in the limiting cases $\mathrm{Pr} \ll 1$ and $\mathrm{Pr} \gg 1$, which depends only on the angle β and Prandtl number as

$$\begin{aligned} \widetilde{\delta}_\theta/\widetilde{\delta}_u &= [C_3(\mathrm{Pr})\delta]^{-1} \\ &= \begin{cases} 2^{-1/2}\,\pi^{1/2}\,\mathrm{Pr}^{-1/2}\delta^{-1}, & \mathrm{Pr} \ll 1, \\ 6^{1/3}\Gamma(4/3)\mathrm{Pr}^{-1/3}\delta^{-2/3}, & \mathrm{Pr} \gg 1. \end{cases} \end{aligned} \tag{2.8.26}$$

Inserting the approximation (2.8.19), δ_{appr}, into the ratio (2.8.26), yields

$$\widetilde{\delta}_\theta/\widetilde{\delta}_u \approx C_4(\mathrm{Pr})(C_2 - \gamma)^{1/\omega}\mathrm{Pr}^{-1/\omega} \tag{2.8.27}$$

with

$$\begin{aligned} \omega = 2, \quad C_4 \approx 1.43, &\qquad \mathrm{Pr} \ll 1, \\ \omega = 3, \quad C_4 \approx 1.77, &\qquad \mathrm{Pr} \gg 1. \end{aligned} \tag{2.8.28}$$

The change of the regime from $\mathrm{Pr}^{-1/2}$ ($\mathrm{Pr} \ll 1$) to $\mathrm{Pr}^{-1/3}$ ($\mathrm{Pr} \gg 1$) in (2.8.26) corresponds to the critical Pr^*, where the two asymptotes intersect. It can be approximated by

$$\mathrm{Pr}^* \approx 0.596 - 0.275\gamma. \tag{2.8.29}$$

DNS for $\mathrm{Pr} \in \{0.1, 0.786, 1, 4.38, 10\}$ and Ra up to 10^8 have shown that β is always around 0.7β, or equivalently, that $\gamma = 1.4$. Hence,

$$\frac{\widetilde{\delta}_\theta}{\widetilde{\delta}_u} \approx \begin{cases} 1.25\mathrm{Pr}^{-1/2}, & \mathrm{Pr} < 10^{-4}, \\ 1.75\mathrm{Pr}^{-0.395+0.017\log\mathrm{Pr}}, & 10^{-4} \leqslant \mathrm{Pr} \leqslant 10^3, \\ 1.62\mathrm{Pr}^{-1/3}, & 10^3 < \mathrm{Pr}. \end{cases} \tag{2.8.30}$$

2.9 Regimes in turbulent thermal convection and the Grossmann–Lohse theory

Grossmann & Lohse provided in a series of papers (Grossmann and Lohse (2000, 2001, 2002, 2003, 2004, 2011); Stevens et al. (2013a), see also Ahlers et al. (2009)) a "unifying theory" of the scaling of the Nusselt and the Reynolds number in turbulent thermal convection. Their theory is referred to as Grossmann–Lohse (GL) theory. It classifies different regimes based on whether the system is dominated by the thermal or viscous dissipation rate in the bulk and in the boundary layers and the relative thickness of the thermal and viscous boundary layers.
The theory assumes a coherent large-scale convection roll or LSC, or in other words, a wind along the walls. The LSC stirs the bulk fluid and all velocity fluctuations are a consequence of it. Thus, the Reynolds number Re used in the GL theory is based on the LSC velocity, rather than on fluctuations because it is expected to be more appropriate to describe bulk turbulence. Consequently, if no LSC exists, one of the main assumptions is not met and the Re can not be defined accordingly. However, even if without an LSC and considering local velocities to define Re, the Grossmann–Lohse theory predicts decently the Nusselt and Reynolds number an their dependence on Ra (see e.g. section 5.2).
At all walls a shear layer, i.e. a viscous boundary layer develops which is driven by the large-scale wind. At the heating and cooling plate a thermal boundary layer builds up and additionally the plumes are considered as interior layers. The main idea is to use the exact relations for the global viscous and thermal dissipation rates, (2.7.8) and (2.7.9), and split them into a bulk and a boundary layer contribution,

$$\langle \epsilon_u(\mathbf{x}, t) \rangle_V = \epsilon_u = \epsilon_{u,\mathrm{bulk}} + \epsilon_{u,\mathrm{BL}} \tag{2.9.1}$$

and a background and a plumes with boundary layers contribution, respectively,

$$\langle \epsilon_\theta(\mathbf{x}, t) \rangle_V = \epsilon_\theta = \epsilon_{\theta,\mathrm{bg}} + \epsilon_{u,\mathrm{pl}}. \tag{2.9.2}$$

The thermal and the viscous boundary layer are assumed to be given by

$$\lambda_\theta = \frac{H}{2\mathrm{Nu}} \qquad \text{and} \qquad \lambda_u = \frac{aH}{\sqrt{\mathrm{Re}}}. \tag{2.9.3}$$

The first relation is exact, as long as the thermal boundary layer thickness is based on the slope criterion, the latter is only valid when a Falkner–Skan type boundary layer is considered. The Prandtl–Blasius type boundary layer is a special case of it (Shishkina et al., 2013, 2014). The constant a is a coefficient that needs to be determined by experiments or numerical simulations.
Hence, there a basically four possible regimes spanning the parameter space of Rayleigh and Prandtl numbers, depicted in figure 2.3. In regime I, ϵ_u and ϵ_θ are dominated by their boundary layer and plume contribution, respectively. This means, that Ra is relatively small, since then the boundary layers are thickest and the plumes are large. In regime II, ϵ_θ is dominated by $\epsilon_{\theta,\mathrm{pl}}$ and ϵ_u is dominated

by $\epsilon_{u,\text{bulk}}$. This is true for small Pr, since then $\lambda_u \ll \lambda_\theta$. In regime III, ϵ_u is dominated by $\epsilon_{u,BL}$ and ϵ_θ is dominated by $\epsilon_{\theta,bg}$, which is the case for large Pr, since the $\lambda_u \gg \lambda_\theta$. Finally, in regime IV, ϵ_u and ϵ_θ are dominated by their bulk and background contribution, respectively. In this regime, Ra has to be relatively large, since then the boundary layers are very thin. Additionally, these regimes are distinguished between an upper and lower sub-regime. When the thermal boundary layer is thicker than the viscous one, the regime is marked by the index l, and analogues, when the viscous boundary layer is thicker than the thermal one the regime is marked by the index u. Thus, the crossovers between upper and lower regimes are each determined by the line

$$\frac{2a\mathrm{Nu}}{\sqrt{\mathrm{Re}}} = 1. \tag{2.9.4}$$

Furthermore, for very large Prandtl numbers the flow is suppressed by the high viscosity and for too small Re the distinction between the bulk and the boundary layer is no longer meaningful. But the viscous boundary layer cannot increase limitless because they cannot become thicker than $H/2$. The critical Reynolds number Re_c for this case, determined by the demand that

$$\lambda_u = \frac{aH}{\sqrt{\mathrm{Re}_c}} = \frac{H}{2}, \tag{2.9.5}$$

is fixed for a given a. The Nusselt number becomes independent of Pr and those regimes are marked by the index ∞.

When only taking the dominating contributions of the bulk and the boundary layer into account, pure scaling laws for all four major regimes can be obtained. These results are summarised in table 2.1 and allow for a quick estimation of Nu and Re. The phase diagram is also shown in figure 2.3. However, these scalings are not to be expected to be observed since the pure scaling laws are usually spoiled by the neighbouring regimes.

More accurately, Nu and Re in the whole parameter range are given by the following two equations

$$(\mathrm{Nu}-1)\,\mathrm{Ra}\,\mathrm{Pr}^{-2} = c_1 \frac{\mathrm{Re}^2}{g\left(\sqrt{\frac{\mathrm{Re}_c}{\mathrm{Re}}}\right)} + c_2 \mathrm{Re}^3, \tag{2.9.6}$$

$$\mathrm{Nu}-1 = c_3 \mathrm{Re}^{1/2}\mathrm{Pr}^{1/2}\left[f\left(\frac{2a\mathrm{Nu}}{\sqrt{\mathrm{Re}_c}}g\left(\sqrt{\frac{\mathrm{Re}_c}{\mathrm{Re}}}\right)\right)\right]^{1/2} + c_4 \mathrm{Pr}\,\mathrm{Re}\, f\left(\frac{2a\mathrm{Nu}}{\sqrt{\mathrm{Re}_c}}g\left(\sqrt{\frac{\mathrm{Re}_c}{\mathrm{Re}}}\right)\right) \tag{2.9.7}$$

with the crossover functions

$$f(x) = (1+x^n)^{-1/n} \quad \text{and} \quad g(x) = x\,(1+x^n)^{-1/n} \quad (n=4). \tag{2.9.8}$$

Similarly, as the factor a the other prefactors c_i were obtained by fitting experimental and numerical data. The results for all prefactors are not universal and depend

regime	dominance of	boundary layers	Nu	Re
I_l	$\epsilon_{u,BL}$, $\epsilon_{\theta,BL}$	$\lambda_u < \lambda_\theta$	$0.22Ra^{1/4}Pr^{1/8}$	$0.765Ra^{1/2}Pr^{-3/4}$
I_u		$\lambda_u > \lambda_\theta$	$0.31Ra^{1/4}Pr^{-1/12}$	$0.887Ra^{1/2}Pr^{-5/6}$
I_∞		$\lambda_u = \frac{aH}{\sqrt{Re_c}} > \lambda_\theta$	$0.35Ra^{1/5}$	$0.656Ra^{3/5}Pr^{-1}$
II_l	$\epsilon_{u,bulk}$, $\epsilon_{\theta,pl}$	$\lambda_u < \lambda_\theta$	$0.37Ra^{1/5}Pr^{1/5}$	$2.064Ra^{2/5}Pr^{-3/5}$
II_u		$\lambda_u > \lambda_\theta$	$0.51Ra^{1/5}$	$2.307Ra^{2/5}Pr^{-2/3}$
III_u	$\epsilon_{u,BL}$, $\epsilon_{\theta,bg}$	$\lambda_u > \lambda_\theta$	$0.018Ra^{3/7}Pr^{-1/7}$	$0.279Ra^{4/7}Pr^{-6/7}$
III_∞		$\lambda_u = \frac{aH}{\sqrt{Re_c}} > \lambda_\theta$	$0.027Ra^{1/3}$	$0.182Ra^{2/3}\,Pr^{-1}$
IV_l	$\epsilon_{u,bulk}$, $\epsilon_{\theta,bg}$	$\lambda_u < \lambda_\theta$	$0.0012Ra^{1/2}Pr^{1/2}$	$0.304Ra^{1/2}Pr^{-1/2}$
IV_u		$\lambda_u > \lambda_\theta$	$0.050Ra^{1/3}$	$1.069Ra^{4/9}Pr^{-2/3}$

TABLE 2.1: Pure power laws for Nu and Ra for the whole Ra-Pr parameter space (adopted from Grossmann and Lohse (2001, 2002); Stevens et al. (2013a))

on the aspect ratio. For $\Gamma = 1$ the prefactors, updated by Stevens et al. (2013a), are

$$c_1 = 8.05,\ c_2 = 1.38,\ c_3 = 0.487,\ c_4 = 0.0252,\ a = 0.922,\ Re_c = (2a)^2. \tag{2.9.9}$$

The equations (2.9.6) and (2.9.7) are invariant under the rescaling transformation

$$\begin{aligned} &Re \to \alpha Re, && Re_c \to \alpha Re_c, && a \to \alpha^{1/2} a, && \\ &c_1 \to c_1/\alpha^2, && c_2 \to c_2/\alpha^3, && c_3 \to c_3/\alpha^{1/2}, && c_4 \to c_4/\alpha. \end{aligned}$$

By determining one exact value of $Re(Ra, Pr)$ for a certain numerical or experimental set-up and comparing it to the original GL theory one can calculate new prefactors. Thus, the prefactors of the GL theory can be adopted to different aspect-ratios etc. For very high Ra the laminar boundary layers eventually become turbulent, thus the Rayleigh–Bénard system reaches the so-called "ultimate regime". In figure 2.3 these regimes are marked with a prime. The regime IV_l' was observed by He et al. (2012).

2.10 Rotating Rayleigh–Bénard convection

In rotating Rayleigh–Bénard convection the Coriolis force (2.2.7) appears in the Navier–Stokes equations (2.2.22). In Cartesian tensor notation and in the co-rotating frame of reference they read

$$D_t u_i = -\frac{1}{\rho_0}\partial_i p + \nu\nabla^2 u_i + \alpha(T - T_0)g\delta_{i3} + 2\epsilon_{ijk}\Omega_j u_k. \tag{2.10.1}$$

Consequently, an additional control parameter apart from the aspect ratio, Rayleigh number and Prandtl number is needed to characterise the importance of rotation.

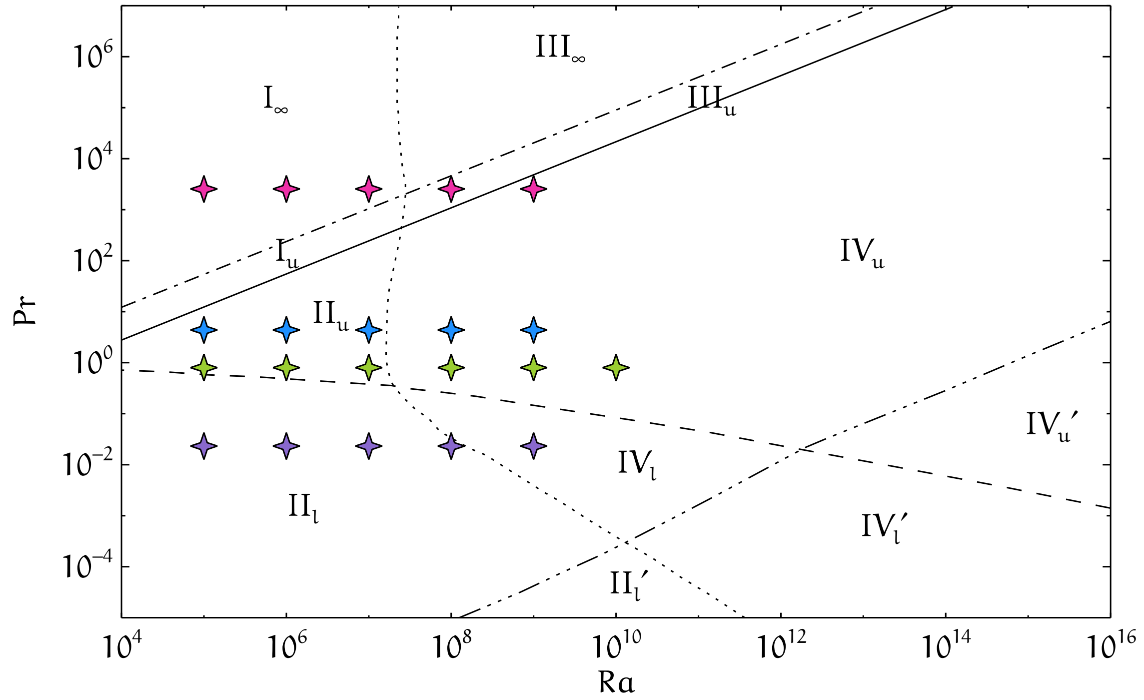

FIGURE 2.3: Phase diagram of the different regimes according to the Grossmann–Lohse theory for a Rayleigh–Bénard cell with $\Gamma = 1$, adopted from Stevens et al. (2013a). The dot dashed line corresponds to $Re = 1$; the solid line to $\epsilon_{u,bulk} = \epsilon_{u,BL}$; the dashed line is $\lambda_u = \lambda_\theta$; the dotted line is $\epsilon_{\theta,bg} = \epsilon_{\theta,pl}$ and the triple-dot dashed line marks the transition to the ultimate regime. The stars mark the simulations that I performed. The pink stars denote $Pr = 2547.9$ (glycerol) and the blue stars $Pr = 4.38$ (water), discussed in more detail in chapter 3 and 5. The green stars stand for $Pr = 0.8$ (SF_6), although an aspect ratio of $\Gamma = 0.5$ was considered in that case, discussed in chapter 4. The purple stars mark simulations in $Pr = 0.0232$ (mercury), discussed in chapter 3.

There are several possibilities for it. Depending on what is to be investigated, one or another proves to be the most convenient one. From a classical force balance between inertia and Coriolis force, one obtains the Rossby number

$$Ro = \frac{(\alpha_m g \Delta H)^{1/2}}{2\Omega H}. \tag{2.10.2}$$

If $Ro \ll 1$ the flow is dominated by the Coriolis force, if $Ro \gg 1$ the flow is dominated by inertial forces, i.e. the flow should behave as in the non-rotating case.
In dimensionless form and using Ro, eq. (2.10.1) becomes

$$D_{\hat{t}}\hat{u}_{\hat{i}} = -\partial_{\hat{i}}\hat{p} + Ra^{-\frac{1}{2}}Pr^{\frac{1}{2}}\gamma^{-\frac{3}{2}}\nabla^2\hat{u}_{\hat{i}} + \hat{T}\delta_{\hat{i}3} + Ro^{-1}\gamma^{1/2}\epsilon_{\hat{i}\hat{j}\hat{k}}\hat{e}_{\hat{j}}\hat{u}_{\hat{k}} \tag{2.10.3}$$

The same term can be added to the NOB equations (2.2.38)–(2.2.40).
Other dimensionless rotation rates are for example the Taylor number Ta and the Ekman number Ek. The Taylor number is usually used for stability analysis (e.g.

Chandrasekhar, 1961) and is given by

$$\mathrm{Ta} = \left(\frac{2\Omega H^2}{\nu_m}\right)^2 = \frac{\mathrm{Ra}}{\mathrm{Pr}\,\mathrm{Ro}^2}. \tag{2.10.4}$$

For the investigation of boundary layers the Ekman number is the most adequate choice (Greenspan, 1968),

$$\mathrm{Ek} = \frac{\nu_m}{\Omega H^2} = \frac{2\mathrm{Ro}\,\mathrm{Pr}^{1/2}}{\mathrm{Ra}^{1/2}} = \frac{2}{\mathrm{Ta}^{1/2}}, \tag{2.10.5}$$

since this has proven to be a convenient dimensionless number in the boundary layer analysis of rotating flows, sometimes defined with an extra factor of one half (Julien et al., 2012; King et al., 2012). The Ekman number compares the viscous force to the Coriolis force, and is essentially the inverse Reynolds number.
As pointed out by Chandrasekhar (1961), "the role of viscosity [...] is reverted", i.e., instead of preventing instability, a higher viscosity inhibits the stabilising effect of rotation and thereby aids instability.

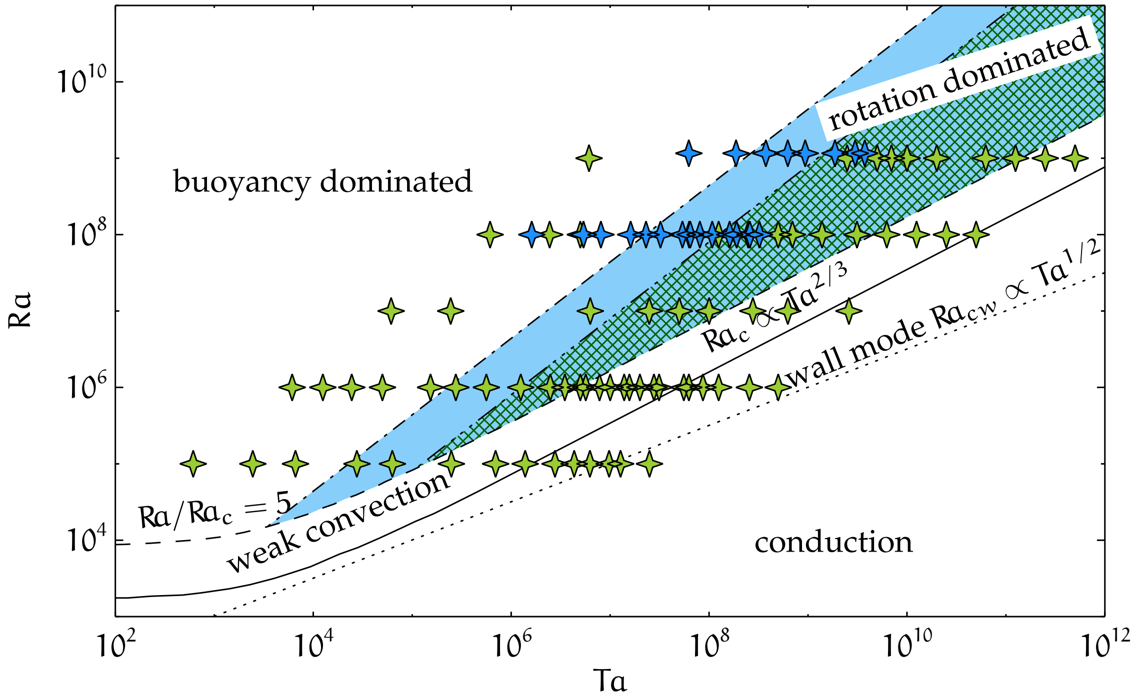

FIGURE 2.4: Phase diagram of rotating convection, adopted from Ecke (2012). The solid line marks the critical Rayleigh number $\mathrm{Ra}_c \propto \mathrm{Ta}^{2/3}$ for an infinite lateral extent according to Chandrasekhar (1961). The dotted line shows the boundary for wall mode convection in case of lateral confinement with $\mathrm{Ra}_{cw} \propto \mathrm{Ta}^{1/2}$ (Herrmann and Busse, 1993). The dashed line marks $\mathrm{Ra}/\mathrm{Ra}_c = 5$, below convection is expected to be relatively weak. The blue shaded area shows the rotation dominated regime for water with $\mathrm{Pr} = 4.38$ and the dark green hatched area shows the rotation dominated regime for SF_6 with $\mathrm{Pr} = 0.8$, where the upper boundary is given by $\mathrm{Ra} = \mathrm{Pr}\mathrm{Ta}$ and is denoted by a dot dashed line and a triple dotted dashed line, respectively. Above the system is dominated by buoyancy. The blue stars mark the simulations of rotating convection in water ($\mathrm{Pr} = 4.38$), discussed in more detail in chapter 6 and the green stars stand for the simulations of SF_6 discussed in chapter 4.

For free surfaces and a laterally infinite fluid layer (and for $\mathrm{Pr} > 0.677$ and no oscillating over-stability), the critical Rayleigh number is given by

$$\mathrm{Ra}_{\mathrm{crit}} = 3\pi^4\left(\tfrac{1}{4} + \cosh\left(\tfrac{1}{3}\phi\right) + \cosh^2\left(\tfrac{1}{3}\phi\right)\right), \qquad \phi = \cosh^{-1}\left(1 + \tfrac{2}{\pi^4}\mathrm{Ta}\right) \tag{2.10.6}$$

(Chandrasekhar, 1961; Nakagawa and Frenzen, 1955). The corresponding critical wavelength is given by

$$k_{\mathrm{crit}} = \sqrt{\pi^2 \cosh\left(\tfrac{1}{3}\phi\right) - \tfrac{1}{3}\pi^2}. \tag{2.10.7}$$

For $\mathrm{Ta} = 0$, i.e. the non-rotating case, the result is identical to equation (2.1.3). Since $\mathrm{Ta} \propto \nu^{-1/2}$ and $\mathrm{Ra} \propto \mathrm{Ta}^{2/3}$, viscosity indeed aids instability.

For high Taylor numbers ($\mathrm{Ta} \gtrsim 10^6$) the following asymptotic behaviour is obtained,

$$\begin{aligned} \mathrm{Ra}_{\mathrm{crit}} &\to 3\left(\tfrac{1}{2}\pi^2\mathrm{Ta}\right)^{2/3}, & (2.10.8) \\ k_{\mathrm{crit}} &\to \left(\tfrac{1}{2}\pi^2\mathrm{Ta}\right)^{1/6}. & (2.10.9) \end{aligned}$$

These results are modified when considering rigid walls. The solution of this case can be obtained by a variational method given by (Chandrasekhar, 1961), and it shows a similar asymptotic $\mathrm{Ta}^{2/3}$-behaviour for large Ta.

However, for a fluid confined by cylindrical sidewalls the critical Rayleigh number is lower. The dependence of $\mathrm{Ra}_{\mathrm{crit}}$ on the aspect ratio for low and moderate rotation rates was first predicted by Buell and Catton (1983). While the actual value was sufficiently accurate, they assumed that the onset was time-independent. However, as was shown later on experimentally and theoretically, the onset is time-dependent (Ecke et al., 1992; Goldstein et al., 1994, 1993; Herrmann and Busse, 1993; Kuo and Cross, 1993; Zhong et al., 1991a,c, 1993), which means that wall-modes in the form of travelling waves develop. For large enough rotation rates and insulating walls, the asymptotic critical Rayleigh number Ra_{cw} is given by

$$\mathrm{Ra}_{cw} \to \pi^2(6\sqrt{3})^{1/2}\mathrm{Ta}^{1/2} \tag{2.10.10}$$

(Herrmann and Busse, 1993).

Similar as in non-rotating Rayleigh–Bénard convection, there are several attempts to characterise different regimes in rotating Rayleigh–Bénard convection. Several combinations of the control parameters and flow quantities have been proposed to determine whether turbulent thermal convection is rotation or buoyancy dominated (Ecke and Niemela, 2014; Julien et al., 2012; King et al., 2012, 2009; Rossby, 1969; Schmitz and Tilgner, 2009, 2010; Stevens et al., 2013b, 2009). Most interest here is drawn to the regime of geostrophic turbulence. Figure 2.4 depicts the suggestion for different regimes by Ecke (2012). Different approaches are detailed in chapter 4 and 6. In chapter 4 I propose another way to characterise transitions based on the toroidal and poloidal energy.

Moreover, there is a point, when the rotation is so fast, that the centrifugal buoyancy (Hart and Ohlsen, 1999; Homsy and Hudson, 1969; Lopez and Marques, 2009;

Marques et al., 2007; Rossby, 1969) becomes important. This point can be estimated by calculating the Froude number,

$$\mathrm{Fr} = \frac{\Omega^2 D}{2g} = \frac{\alpha_m \Delta\Gamma}{8\mathrm{Ro}^2}. \tag{2.10.11}$$

If $\mathrm{Fr} \ll 1$ then centrifugal buoyancy is negligible. Therefore, in experiments it is usually attempted to keep Fr as small as possible, i.e. around 0.05 and lower (Zhong et al., 2009). However, $\mathrm{Fr} \neq 0$ can lead to an additional source of breaking the symmetry about the mid plane (Hart and Ohlsen, 1999) and it would be hard to decouple centrifugal buoyancy and NOB effects. Since the investigation of NOB effects is one of the major objectives of this thesis, I deliberately set $\mathrm{Fr} \equiv 0$ everywhere.

2.10.1 Taylor–Proudman theorem and thermal wind balance

The Taylor–Proudman theorem (Proudman, 1916; Taylor, 1921) is very often invoked to explain the behaviour of a flow under the influence of rapid rotation. However, strictly speaking, it is only valid for a steady, time-independent flow without any additional forcing Chandrasekhar (1961).

It is most conveniently derived by considering the Navier–Stokes equations in OB approximation in vector notation and assuming a constant angular velocity (Greenspan, 1968). They are given by

$$\partial_t \mathbf{u} + (\mathbf{u} \cdot \boldsymbol{\nabla})\mathbf{u} + 2\boldsymbol{\Omega} \times \mathbf{u} = -\boldsymbol{\nabla} \mathbf{p} + \nu \boldsymbol{\nabla}^2 \mathbf{u}. \tag{2.10.12}$$

The variables $\mathbf{r}$, t, $\mathbf{u}$, $\boldsymbol{\Omega}$, p are substituted by their scaled counterparts $H\mathbf{r}$, $\Omega^{-1}t$, $(\alpha_m g \Delta H)^{1/2}\mathbf{u}$, $\Omega\mathbf{k}$, $\rho\Omega(\alpha_m g \Delta H)^{1/2} Hp$, with $\mathbf{k}$ being a unit vector parallel to the rotation axis. Hence, the following dimensionless form of the previous equation (2.10.12) is obtained

$$\partial_{\hat{t}} \hat{\mathbf{u}} + \mathrm{Ro}(\hat{\mathbf{u}} \cdot \boldsymbol{\nabla})\hat{\mathbf{u}} + 2\mathbf{k} \times \hat{\mathbf{u}} = -\boldsymbol{\nabla}\hat{\mathbf{p}} + \mathrm{Ek}\boldsymbol{\nabla}^2 \hat{\mathbf{u}}. \tag{2.10.13}$$

Assuming that the flow is steady, thus, time-independent, the temporal derivative is dropped, i.e. $\partial_{\hat{t}} \hat{\mathbf{u}} = 0$. In the case of very rapid rotation, it is $\mathrm{Ro} \ll 1$ and $\mathrm{Ek} \ll 1$. Thus, the viscous forces and the convective acceleration are small compared to the Coriolis force and are neglected. This yields

$$2\mathbf{k} \times \hat{\mathbf{u}} = -\boldsymbol{\nabla}\hat{\mathbf{p}}. \tag{2.10.14}$$

Taking the curl of equation (2.10.14) and using the imcompressible continuity equation gives the Taylor–Proudman theorem

$$(\mathbf{k} \cdot \boldsymbol{\nabla})\hat{\mathbf{u}} = 0. \tag{2.10.15}$$

If the rotation axis is assumed to be the vertical axis, it can be written as

$$\partial_{\hat{z}} \hat{\mathbf{u}} = 0. \tag{2.10.16}$$

This means that no motion varying in the direction of $\boldsymbol{\Omega}$ is allowed. Or alternatively, that every motion is necessarily two-dimensional.
In rotating convection, the thermal wind balance is a more adequate approximation. In this case, also the buoyancy force is taken into account. The result is

$$\partial_{\hat{z}}\hat{\mathbf{u}} = \mathrm{Ro}\hat{T}\boldsymbol{e}_{\hat{z}}. \tag{2.10.17}$$

Clearly, in turbulent rotating convection the key assumption of a steady, inviscid and slow-moving (compared to the rotational speed) flow are never met. However, the tendency to a two-dimensional flow can still be found, which is sometimes referred to as Taylor–Proudman effect. The best example are the columnar vortex structures observed. But, since there the "viscosity lifts away" the constraints by the Taylor–Proudman theorem (Boubnov and Golitsyn, 1986), heat can be transported in vertical direction as long as the Rayleigh number is above $\mathrm{Ra}_{\mathrm{crit}}$. Below, the Taylor–Proudman effect finally leads to the complete supression of the convective heat transport parallel to the axis of rotation.

NUMERICAL METHODOLOGY

To study Rayleigh–Bénard convection, the dimensionless governing equations discussed before in section 2.2, are solved numerically. For the investigation of Rayleigh–Bénard convection under OB conditions I performed DNS and LES with the well-tested finite volume code `flowsi` for cylindrical domains. In opposite to finite difference schemes, finite volume schemes have the advantage to be essentially conservative.
The code is based on a `fortran77` DNS code for turbulent pipe flow problems originally developed by Schmitt and Friedrich (1988). The three-dimensional Navier–Stokes equations are solved following an ansatz proposed by Chorin (1967). The equations are solved on staggered grids and the volume balance procedure motivated by Schumann (1975) is used.
Later on, it was completely rewritten and advanced. The spatial integration scheme was changed to be fourth order accurate (Shishkina and Wagner, 2007b) and furthermore, the simulation of Rayleigh–Bénard convection was made possible (Shishkina and Wagner, 2005). Eventually, in the course of this work, it was parallelised and modernised to the `fortran90/95/2003` standard (Horn et al., 2013b).

3.1 The basic Oberbeck–Boussinesq code `flowsi`

The governing equations are solved for finite volumes $V = V(z_i, \phi_j, r_k)$ shaped liked "cake slices" with a cut off tip, as sketched in figure 3.1. The volume cell is associated with the coordinates of its centre (z_i, ϕ_j, r_k) and has the dimensions Δr_k, $r_k \Delta\phi_j$ and Δz_i. It is bounded by the cell surfaces

$$\begin{array}{rclllll} A_z^{\pm} &=& A_z\,(z_i \pm \frac{\Delta z_i}{2}, & \phi_j, & r_k &), \\ A_\phi^{\pm} &=& A_\phi\,(z_i, & \phi_j \pm \frac{\Delta\phi_j}{2}, & r_k &), \\ A_r^{\pm} &=& A_r\,(z_i, & \phi_j, & r_k \pm \frac{\Delta r_k}{2} &). \end{array} \tag{3.1.1}$$

Accordingly, the volume element and the surface elements written in a discretised forms yield

$$\Delta V = r_k \Delta r_k \Delta z_i \Delta\phi_j, \tag{3.1.2}$$

$$\Delta A_z = r_k \Delta r_k \Delta\phi_j, \tag{3.1.3}$$

$$\Delta A_\phi = \Delta r_k \Delta z_i, \tag{3.1.4}$$

$$\Delta A_r = r_k \Delta z_i \Delta\phi_j. \tag{3.1.5}$$

A velocity component u_α averaged over the finite volume V is given by

$$\overline{u_\alpha} = \frac{1}{\Delta V} \int_{\Delta V} u_\alpha dV, \tag{3.1.6}$$

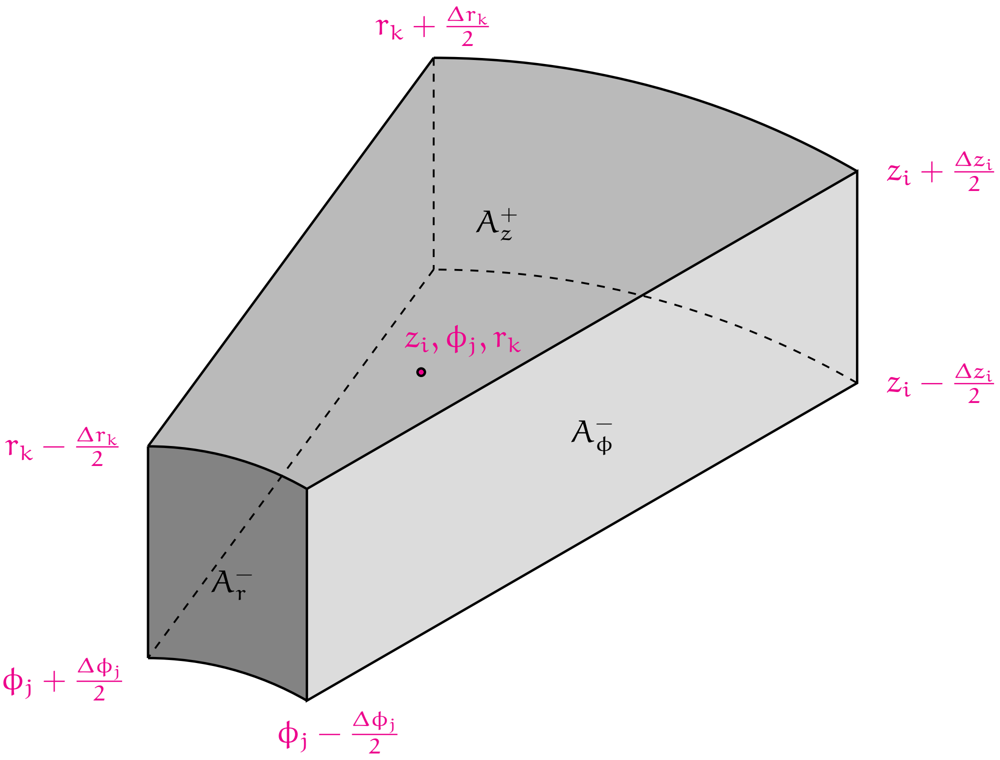

FIGURE 3.1: Sketch of an arbitrary finite volume element $V(z_i, \phi_j, r_k)$.

and a velocity component u_α averaged over the $A_\beta^\pm$ surface is given by

$$ {}^{\beta\pm}\overline{u_\alpha} = \frac{1}{\Delta A_\beta^\pm} \int_{\Delta A_\beta^\pm} u_\alpha dA_\beta^\pm, \tag{3.1.7}$$

where α and β is one of the coordinates r, ϕ or z, respectively.
The continuity (2.2.35) and the Navier–Stokes equations (2.2.36) integrated over such a finite volume read

$$\sum_\alpha (F_{\alpha^+} - F_{\alpha^-}) = 0, \tag{3.1.8}$$

$$\partial_t \overline{u_\alpha} + \sum_\beta (K_{\alpha\beta} - D_{\alpha\beta}) + P_\alpha - C_\alpha + B_\alpha = 0. \tag{3.1.9}$$

The single terms denote the momentum flux

$$F_{\alpha^\pm} = \Delta A_\alpha^\pm {}^{\alpha\pm}\overline{u_\alpha}, \tag{3.1.10}$$

the convective term

$$K_{\alpha\beta} = \frac{1}{\Delta V}\left(F_{\beta^+}{}^{\beta^+}\overline{u_\alpha} - F_{\beta^-}{}^{\beta^-}\overline{u_\alpha}\right), \tag{3.1.11}$$

the diffusive term

$$D_{\alpha\beta} = Ra^{-1/2} Pr^{1/2} \gamma^{-3/2} \frac{1}{\Delta V}\left(\Delta A_\beta^+ {}^{\beta^+}\overline{s_{\alpha\beta}} - \Delta A_\beta^- {}^{\beta^-}\overline{s_{\alpha\beta}}\right) \tag{3.1.12}$$

with the surface averaged deformation tensor

$$ {}^{\beta}\overline{s_{\alpha\beta}} = \begin{pmatrix} 2\partial_z{}^{z}\overline{u_z} & \frac{1}{r}\partial_\phi{}^{\phi}\overline{u_z} + \partial_z{}^{\phi}\overline{u_\phi} & \partial_r{}^{r}\overline{u_z} + \partial_z{}^{r}\overline{u_r} \\ \frac{1}{r}\partial_\phi{}^{\phi}\overline{u_z} + \partial_z{}^{\phi}\overline{u_\phi} & 2\frac{1}{r}\left(\partial_\phi{}^{\phi}\overline{u_\phi} + {}^{\phi}\overline{u_r}\right) & r\partial_r\left(\frac{1}{r}{}^{r}\overline{u_\phi}\right) + \frac{1}{r}\partial_\phi{}^{r}\overline{u_r} \\ \partial_r{}^{r}\overline{u_z} + \partial_z{}^{r}\overline{u_r} & r\partial_r\left(\frac{1}{r}{}^{r}\overline{u_\phi}\right) + \frac{1}{r}\partial_\phi{}^{r}\overline{u_r} & 2\partial_r{}^{r}\overline{u_r} \end{pmatrix}, $$

the pressure term

$$ P_\alpha = \frac{1}{\Delta V}\left(\Delta A_\alpha^{+\,\alpha^+}\overline{p} - \Delta A_\alpha^{-\,\alpha^-}\overline{p}\right) \tag{3.1.13} $$

the curvature terms

$$ \begin{aligned} C_z &= 0, && (3.1.14) \\ C_\phi &= \frac{\Delta\phi_j \Delta A_\phi}{\Delta V}\left(-{}^{\phi}\overline{u_\phi}{}^{\phi}\overline{u_r} + Ra^{-1/2}Pr^{1/2}\gamma^{-3/2}{}^{\phi}\overline{s_{\phi r}}\right), && (3.1.15) \\ C_r &= \frac{\Delta\phi_j \Delta A_\phi}{\Delta V}\left(({}^{\phi}\overline{u_\phi})^2 + {}^{\phi}\overline{p} - Ra^{-1/2}Pr^{1/2}\gamma^{-3/2}{}^{\phi}\overline{s_{\phi\phi}}\right), && (3.1.16) \end{aligned} $$

and an additional force term B_α, i.e. the buoyancy term and in case of rotating convection the Coriolis force term. The energy equation (2.2.37) can be written accordingly.

As time integration scheme, a hybrid explicit/semi-implicit Euler-Leapfrog method is employed. This means an explicit scheme is used almost everywhere, except for a small subdomain close to the cylinder axis where the convection and diffusion term are solved semi-implicitly for azimuthal component ϕ. The border between the semi-implicit and explicit scheme is determined by the empirical value of 10% of the nodes N_r in radial direction.

The explicit Leapfrog-Euler time integration scheme is given by

$$ \overline{u_\alpha^{n+1}} = f^{n_0}\overline{u_\alpha^{n-1}} + f^{n_1}\overline{u_\alpha^{n}} + \Delta t_l\Big(\sum_\beta (K_{\alpha\beta}^n - D_{\alpha\beta}^{n-1}) + P_\alpha^n - C_\alpha^n + B_\alpha^n\Big), \tag{3.1.17} $$

n is the number of the time step, f^{n_0} and f^{n_1} are prefactors that depend on the stage of the integration cycle and Δt_l is the time step Δt scaled with a factor, that depends on the stage of the integration cycle as well.

One time integration cycle consisty typically of $N = 50$ time steps. The cycle starts with an Euler step ($n = 1$) where the coefficients are given by

$$ f^{n_0} = 0,\ f^{n_1} = 1,\ \Delta t_l = 1\Delta t, \tag{3.1.18} $$

followed by leapfrog steps ($2 \leqslant n \leqslant N - 1$) with

$$ f^{n_0} = 1,\ f^{n_1} = 0,\ \Delta t_l = 2\Delta t, \tag{3.1.19} $$

and is closed by an averaging Leapfrog-Euler step ($n = N$)

$$ f^{n_0} = \tfrac{1}{2},\ f^{n_1} = \tfrac{1}{2},\ \Delta t_l = \tfrac{3}{2}\Delta t. \tag{3.1.20} $$

In case of a constant Δt the Euler step is only necessary for the very first time step of an simulation, in case of a variable time step the full cycle needs to be performed.

If a variable time stepping is used, Δt is essentially determined by means of the von-Neumann stability sufficient condition for fourth order schemes (Shishkina, 2007)

$$\Delta t \leqslant \left(\frac{3}{2} \sum_{\alpha} \frac{|U_\alpha|}{\Delta x_\alpha} + \frac{16}{3} \frac{Pr^{1/2}}{Ra^{1/2}\gamma^{3/2}} \sum_{\alpha} \frac{1}{\Delta x_\alpha^2} \right)^{-1},$$

with $\Delta x_\alpha = \Delta z,\ r\Delta\phi,\ \Delta r$.

The solution of (3.1.17) is based on the Chorin ansatz (Chorin, 1967) and is sketched here exemplary for the leapfrog part of the cycle, i.e. for

$$\frac{\mathbf{u}^{n+1} - \mathbf{u}^{n-1}}{2\Delta t} + \mathbf{u}^n \cdot \nabla \mathbf{u}^n + \nabla p^n = \frac{Pr^{1/2}}{Ra^{1/2}\gamma^{3/2}} \nabla^2 \mathbf{u}^{n-1} + T^n \mathbf{e}_z. \qquad (3.1.21)$$

Firstly, an auxilliary velocity field $\mathbf{u}^*$ is calculated by neglecting the pressure term,

$$\frac{\mathbf{u}^* - \mathbf{u}^{n-1}}{2\Delta t} + \mathbf{u}^n \cdot \nabla \mathbf{u}^n = \frac{Pr^{1/2}}{Ra^{1/2}\gamma^{3/2}} \Delta \mathbf{u}^{n-1} + T^n \mathbf{e}_z. \qquad (3.1.22)$$

Then, the Poisson equation for p^n is solved using $\mathbf{u}^*$,

$$\nabla^2 p^n = \frac{\nabla \cdot \mathbf{u}^*}{2\,\Delta t}, \qquad (3.1.23)$$

with the boundary condition

$$(\mathbf{n} \cdot \nabla p^n)|_{\partial\Upsilon} = 0 \qquad (3.1.24)$$

at the solid walls $\partial\Upsilon$. Then the velocity field is updated and the actual solution $\mathbf{u}^{n+1}$ is obtained

$$\mathbf{u}^{n+1} = \mathbf{u}^* - 2\,\Delta t\,\nabla p^n. \qquad (3.1.25)$$

Since the explicit time integration scheme demands a very tiny time step an implicit time integration scheme is employed in the azimuthal direction close to the cylinder axis. The semi-implicit scheme

$$\begin{aligned} &\frac{\mathbf{u}^{n+1} - \mathbf{u}^{n-1}}{2\Delta t} + \mathbf{u}^n \cdot \nabla \mathbf{u}^n + \nabla p^n \\ &\quad = \frac{Pr^{1/2}}{Ra^{1/2}\gamma^{3/2}} \left(\partial_\phi^2 \mathbf{u}^{n+1} + (\nabla^2 - \partial_\phi^2)\mathbf{u}^{n-1} \right) + T^n \mathbf{e}_z \end{aligned} \qquad (3.1.26)$$

is solved there. That means, at first, the auxilliary velocity field is obtained by computing

$$\frac{\mathbf{u}^* - \mathbf{u}^{n-1}}{2\Delta t} + \mathbf{u}^n \cdot \nabla \mathbf{u}^n = \frac{Pr^{1/2}}{Ra^{1/2}\gamma^{3/2}} \left(\partial_\phi^2 \mathbf{u}^* + (\nabla^2 - \partial_\phi^2)\mathbf{u}^{n-1} \right) + T^n \mathbf{e}_z. \qquad (3.1.27)$$

Secondly, the Poisson equation for Ψ,

$$\nabla^2 \Psi = \nabla \cdot \mathbf{u}^*, \qquad (3.1.28)$$

is solved with the boundary condition

$$(\mathbf{n}\cdot\nabla\Psi)|_{\partial\Upsilon}=0. \tag{3.1.29}$$

Finally, $\mathbf{u}^{n+1}$ and ∇p^n are computed,

$$\mathbf{u}^{n+1}=\mathbf{u}^*-\nabla\Psi,\quad \nabla p^n=\left(\frac{\mathbb{1}}{2\,\Delta t}-\frac{Pr^{1/2}}{Ra^{1/2}\gamma^{3/2}}\partial^2_\phi\right)\nabla\Psi. \tag{3.1.30}$$

The Navier–Stokes equations for every velocity component and for the temperature are solved on different, that is staggered meshes. The meshes are non-equidistant in radial and vertical direction and equidistant in azimuthal direction.
For example, in the radial direction the creation of the meshes starts with the mesh for the velocity $w=u_r$, i.e. for every point r^k_w the velocity $u_r(k)$ is defined as a surface averaged quantity. Originating from that, the corresponding pressure and temperature mesh r_p is created by

$$r^k_p=\frac{1}{2}\left(r^{k-1}_w+r^k_w\right). \tag{3.1.31}$$

Hence the points r^k_p define the centre of the radial velocity or w-cell, whereas the centre of the p-cell is defined by

$$r^k_{mi}=\frac{1}{2}\left(r^k_p+r^{k+1}_p\right). \tag{3.1.32}$$

Thus, the distance between the points on the w-mesh and p mesh are given by

$$\Delta r^k_p = r^k_w-r^{k-1}_w, \tag{3.1.33}$$

$$\Delta r^k_w = r^{k+1}_p-r^k_p, \tag{3.1.34}$$

respectively, see also figure 3.2. For the vertical and azimuthal direction the approach is similar, however, due to the equidistant mesh in azimuthal direction it is much simpler. The volumes for the p-cell, the green cell in fig. 3.2, and the w-cell, that is the cell of the radial velocity u_r, corresponding to the blue hatched cell in fig. 3.2, and accordingly the other velocity cells for the z and ϕ component, called u- and v-cell, are given by

$$V_p = r_p\Delta\phi\Delta r_p\Delta z_p, \tag{3.1.35}$$

$$V_z = r_p\Delta\phi\Delta r_p\Delta z_u, \tag{3.1.36}$$

$$V_\phi = V_p, \tag{3.1.37}$$

$$V_r = r_{mi}\Delta\phi\Delta r_w\Delta z_p. \tag{3.1.38}$$

The values of u_r, u_ϕ, u_z, T and deduced flow quantities presented in this thesis are given as volume avaraged value at centre of the p-cell. Thus, the velocity components are always interopolated to the p-mesh.

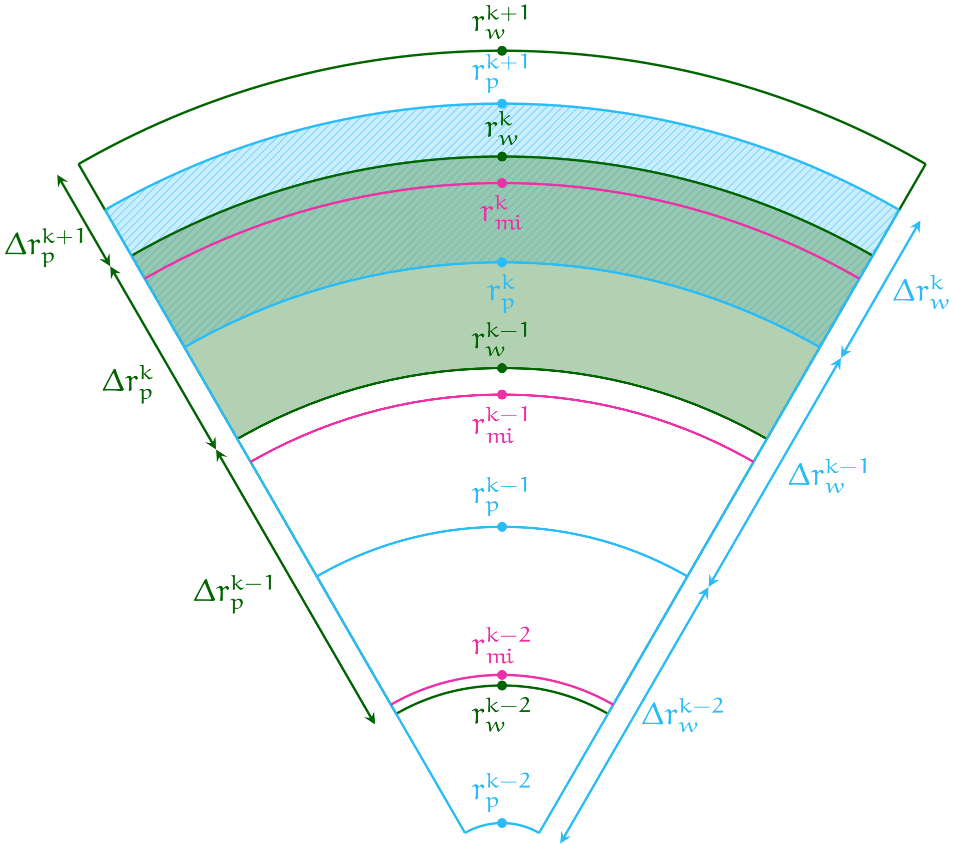

FIGURE 3.2: Sketch of the radial mesh.

3.2 Resolution requirements for numerical simulations of Rayleigh-Bénard convection

The numerical solution of the Navier–Stokes equations as discussed above is, however, only physical meaningful if the smallest scales of the flow problem are resolved. Numerical simulations without any additional model and the appropriate resolution are called direct numerical simulations (DNS). As I will show in the following, this can be a very challenging task with respect to the computational resources.
In Rayleigh–Bénard convection the smallest spatial scales, are the Kolmogorov and the Batchelor length scale

$$\eta_K = \left(\frac{\nu^3}{\epsilon_u}\right)^{1/4}, \tag{3.2.1}$$

$$\eta_B = \left(\frac{\nu\kappa^2}{\epsilon_u}\right)^{1/4} = \eta_K Pr^{-1/2}, \tag{3.2.2}$$

with the kinetic dissipation rate $\epsilon_u = \nu|\nabla \mathbf{u}|^2$. Hence, for fluids with $Pr < 1$ the

Kolmogorov length is crucial, whereas for fluids with $Pr > 1$ the Batchelor length is crucial. Using the exact relation

$$\langle \epsilon_u \rangle_{V,t} = \frac{\nu^3}{H^4}(Nu - 1)RaPr^{-2}, \tag{3.2.3}$$

a global mesh size h^{global} can be estimated (Shishkina et al., 2010), yielding

$$h^{global} \leqslant \begin{cases} \dfrac{Pr^{1/2}}{Ra^{1/4}\left(Nu-1\right)^{1/4}}H, & Pr \leqslant 1 \\ \dfrac{1}{Ra^{1/4}\left(Nu-1\right)^{1/4}}H, & Pr > 1 \end{cases} . \tag{3.2.4}$$

However, these relations only apply for the bulk, since the local Kolmogorov and Batchelor lengths are usually much smaller close to rigid walls. This allows to estimate the number of nodes in one dimension, i.e.

$$N^{global} = \frac{H}{h^{global}}. \tag{3.2.5}$$

In the thermal and viscous boundary layers more complicated relations for the mesh size h^{BL} apply. Based on the Prandtl–Blasius boundary layer theory Shishkina et al. (2010) provided the following criteria

$$h^{BL} \lesssim \begin{cases} 2^{-3/2}a^{-1}Nu^{-3/2}Pr^{3/4}A^{-3/2}\pi^{-3/4}H, & Pr < 3\times 10^{-4} \\ 2^{-3/2}a^{-1}Nu^{-3/2}Pr^{0.5355-0.033\log Pr}H, & 3\times 10^{-4} \leqslant Pr \leqslant 1 \\ 2^{-3/2}a^{-1}Nu^{-3/2}Pr^{0.0355-0.033\log Pr}H, & 1 < Pr \leqslant 3 \\ 2^{-3/2}a^{-1}Nu^{-3/2}E^{-3/2}H, & Pr > 3 \end{cases} \tag{3.2.6}$$

with $A \approx 0.332$, $E \approx 0.982$ and $a \approx 0.922$ [*]. This results in the following number of nodes in the thermal and viscous boundary layers, respectively

$$N^{\theta} \gtrsim \begin{cases} \sqrt{2}aNu^{-1/2}Pr^{-3/4}A^{3/2}\pi^{3/4}, & Pr < 3\times 10^{-4} \\ \sqrt{2}aNu^{-1/2}Pr^{-0.5355+0.033\log Pr}, & 3\times 10^{-4} \leqslant Pr \leqslant 1 \\ \sqrt{2}aNu^{-1/2}Pr^{-0.0355+0.033\log Pr}, & 1 < Pr \leqslant 3 \\ \sqrt{2}aNu^{-1/2}E^{3/2}, & Pr > 3 \end{cases} \tag{3.2.7}$$

$$N^{u} \gtrsim \begin{cases} \sqrt{2}aNu^{-1/2}Pr^{-1/4}A^{1/2}\pi^{1/4}, & Pr < 3\times 10^{-4} \\ \sqrt{2}aNu^{-1/2}Pr^{-0.1785+0.011\log Pr}H, & 3\times 10^{-4} \leqslant Pr \leqslant 1 \\ \sqrt{2}aNu^{-1/2}Pr^{0.3215+0.011\log Pr}H, & 1 < Pr \leqslant 3 \\ \sqrt{2}aNu^{-1/2}Pr^{1/3}E^{1/2}H, & Pr > 3 \end{cases} . \tag{3.2.8}$$

Thus, non-equidistant staggered grid with very fine resolution in the boundary layers are used. However, to use these criteria the Nusselt number Nu still needs to be known, which is actually an outcome of the simulations. To overcome this problem, the GL theory can be used which gives a good estimate of Nu.

---

[*] The factor a is the same as in the GL theory 2.9, i.e. $a \approx 0.922$ holds according to the updated prefactors by Stevens et al. (2013a). However, in most of the thesis $a \approx 0.482$ was used as in the original publication by Shishkina et al. (2010).

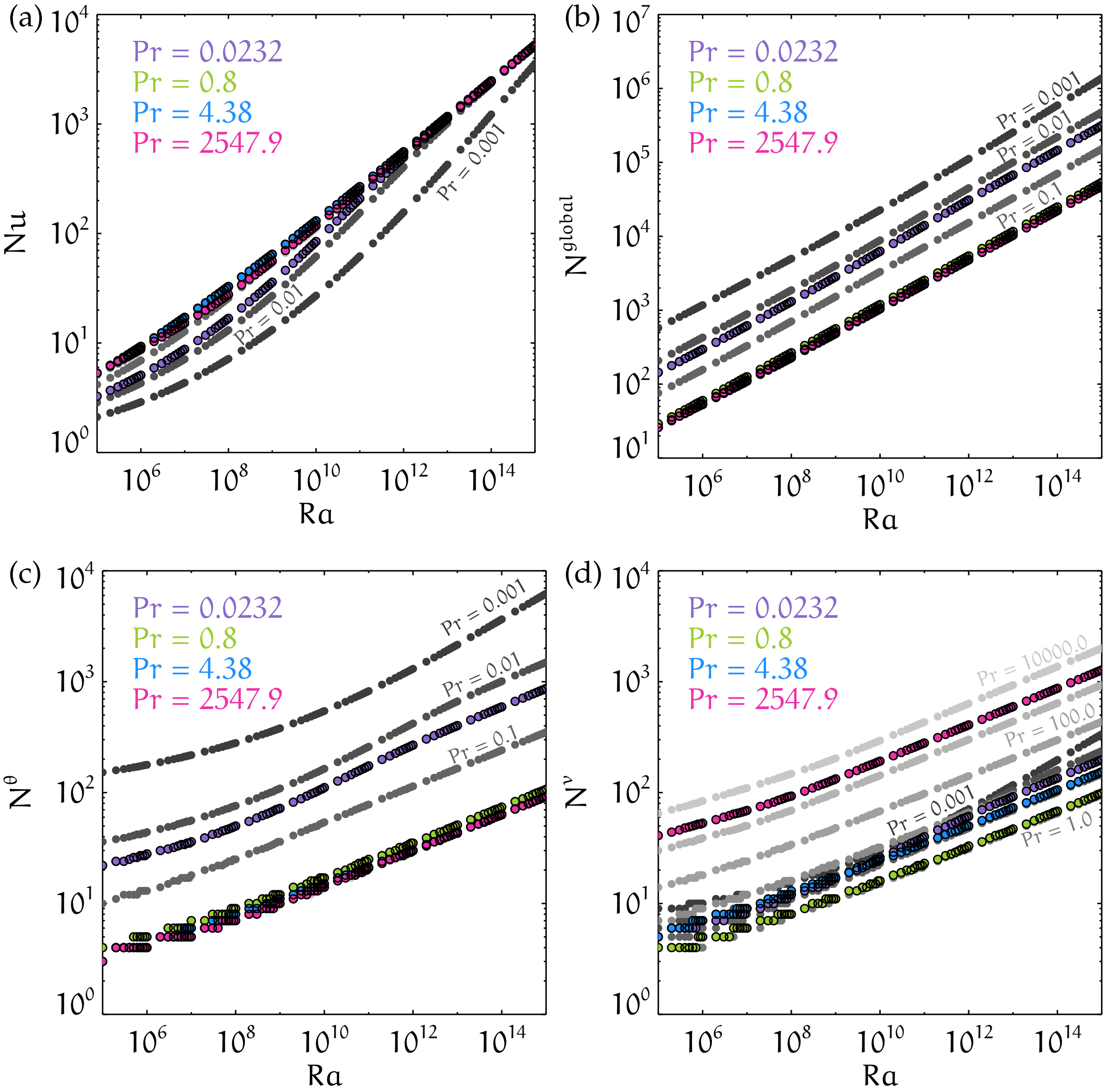

FIGURE 3.3: Estimation of the the Nusselt number Nu and the required mesh size for various Prandtl numbers. The purple circles mark $\mathrm{Pr} = 0.0232$ (mercury), the blue ones $\mathrm{Pr} = 4.38$ (water), the green ones $\mathrm{Pr} = 0.8$ (SF_6) and the pink ones $\mathrm{Pr} = 2547.9$ (glycerol). The grey circles show the generic Prandtl numbers $\mathrm{Pr} \in \{0.001, 0.01, 0.1, 1.0, 10.0, 100.0, 1000., 10000.0\}$, where the grey scale changes from dark to light grey with increasing Pr. (a) Nusselt number Nu according to the GL theory; (b) Global number of grid points in one dimension N^{global} given by eq. (3.2.5). (c) Number of nodes in the thermal boundary layer N^{θ} given by eq. (3.2.7); (d) Number of nodes in the viscous boundary layer N^{u} given by eq. (3.2.8).

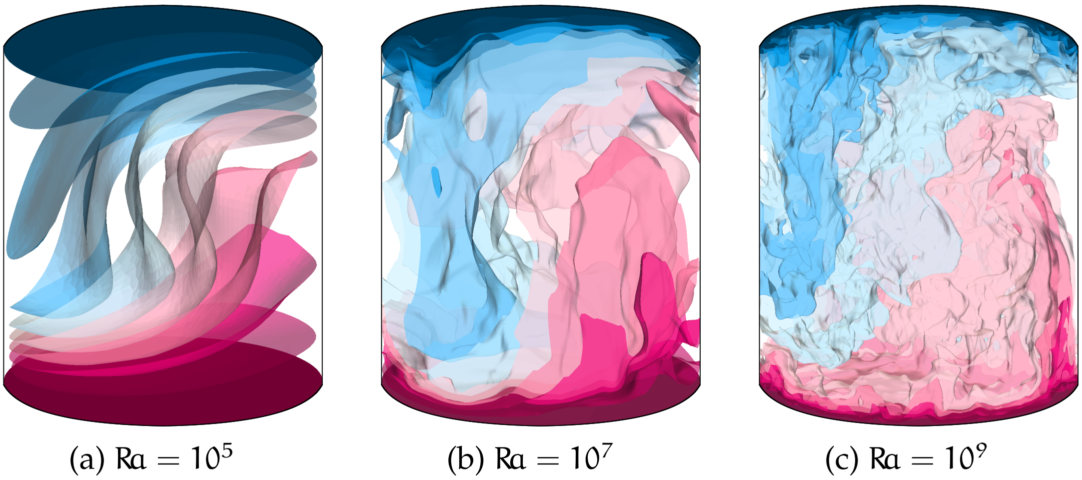
(a) $\mathrm{Ra} = 10^5$ (b) $\mathrm{Ra} = 10^7$ (c) $\mathrm{Ra} = 10^9$

FIGURE 3.4: Instantaneous temperature fields for mercury ($\mathrm{Pr} = 0.0232$) under OB conditions. Shown are isosurfaces for ten equidistantly distributed values between the top and bottom temperature for (a) $\mathrm{Ra} = 10^5$, (b) $\mathrm{Ra} = 10^7$, (c) $\mathrm{Ra} = 10^9$. Blue corresponds to temperatures below T_m, pink to temperatures above T_m.

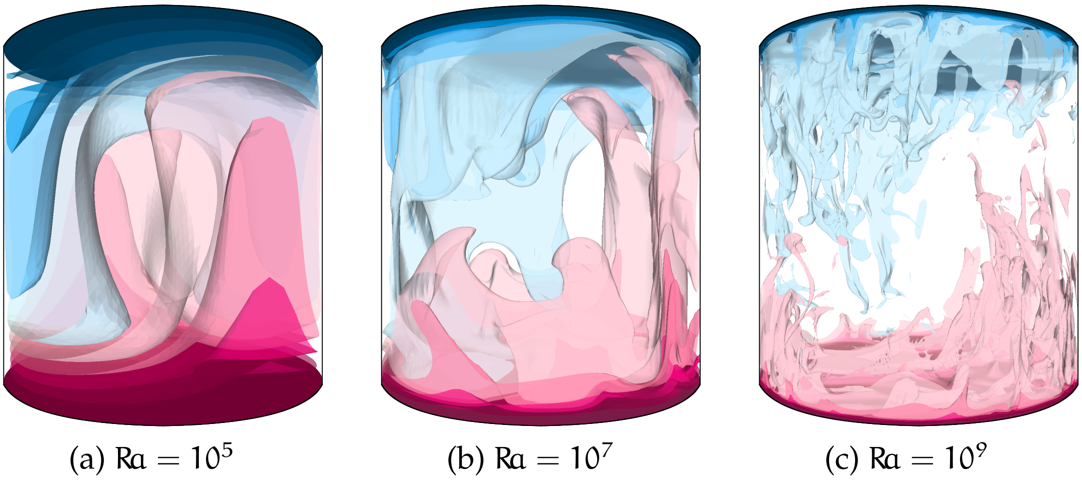
(a) $\mathrm{Ra} = 10^5$ (b) $\mathrm{Ra} = 10^7$ (c) $\mathrm{Ra} = 10^9$

FIGURE 3.5: Instantaneous temperature fields for water ($\mathrm{Pr} = 4.38$) under OB conditions. Shown are isosurfaces for ten equidistantly distributed values between the top and bottom temperature for (a) $\mathrm{Ra} = 10^5$, (b) $\mathrm{Ra} = 10^7$, (c) $\mathrm{Ra} = 10^9$. Blue corresponds to temperatures below T_m, pink to temperatures above T_m.

In figure 3.3 I present the predictions of the GL theory and the estimations of the global number of grid points N^{global} and the required number of grid points in the thermal and viscous boundary layers, N^{θ} and N^{ν}, for generic Prandtl numbers in terms of powers of 10 for $0.001 \leqslant \mathrm{Pr} \leqslant 10000.0$ and for the fluids investigation in one way or another in this thesis, i.e. mercury ($\mathrm{Pr} = 0.0232$), SF_6 ($\mathrm{Pr} = 0.8$), water ($\mathrm{Pr} = 4.38$) and glycerol $\mathrm{Pr} = 2547.9$. The Nusselt number Nu increases with Ra for all Pr, however, for very low Prandtl numbers, say $\mathrm{Pr} = 0.001$ or already for mercury with $\mathrm{Pr} = 0.0232$, the heat transfer is very inefficient compared to higher Prandtl numbers. Nonetheless, as seen in figure 3.3(b)–(d) the resolution is very

(a) $Ra = 10^5$ (b) $Ra = 10^7$ (c) $Ra = 10^9$

FIGURE 3.6: Instantaneous temperature fields for glycerol ($Pr = 2548$) under OB conditions. Shown are isosurfaces for ten equidistantly distributed values between the top and bottom temperature for (a) $Ra = 10^5$, (b) $Ra = 10^7$, (c) $Ra = 10^9$. Blue corresponds to temperatures below T_m, pink to temperatures above T_m.

demanding. In figure 3.4 instantaneous temperature fields are shown for mercury. These show that in opposite to fluids with $Pr = \mathcal{O}(1)$ as for example water, presented in figure 3.5, also in the bulk small structures occur, and not only plumes following the LSC along the walls, and hence, the resolution in the bulk needs to be finer. For $Pr \gtrsim 1$ the resolution in the bulk does no longer change significantly with Pr. However, as shown on the example of glycerol in figure 3.6, the convection is plume dominated, i.e. the assumption, that the dissipation rate within the bulk can be estimated in good approximation with the global value of it, might not apply. This will be detailed in chapter 5.

Probably most crucial about DNS is the resolution of the boundary layers. Not only the number of nodes that need to be placed in there increases tremendously, but both the viscous and thermal boundary layer thicknesses decrease. As a consequence of this the dimensions of the volume cells, i.e. the grid spacing, becomes much smaller with increasing Ra and so does the time step Δt. Numerical simulations of turbulent convection for high Ra are, hence, computational very expensive in many respects. The governing equations have to be solved for much more points and much more time steps per time unit. Moreover, also the files containing the flow fields require much more storage and memory. Generally, even below the ultimate regime, when the boundary layers turn turbulent, DNS for high Ra are not feasible. If high Ra are the main goal fluids with $Pr \approx 1$ are easiest to achieve.

The Rayleigh number range that is achievable with adequate costs with nowadays supercomputers is $Ra \lesssim 10^9$. This requires, of course an efficient parallelisation of the code, discussed below in section 3.3. Higher Ra are extremely expensive, and it might be more reasonable to conduct large eddy simulations (LES), see section 3.4. An estimation of the complexity of DNS shows that one can expect one additional order of magnitude in Ra about every four years.

3.3 Parallelisation

The parallelisation is implemented via a spatial domain decomposition in vertical direction to solve the temperature and velocity equations and via the distribution of the decoupled pressure source terms in azimuthal and horizontal direction to solve the Poisson equation. Both times making use of the Message Passing Interface (MPI).

To test the scalability of the code, simulations on the National Supercomputer HLRB-II SGI Altix 4700 at the Leibniz Computing Centre in Munich to study thermal convection in cylindrical domains were peformed. It is shown in figure 3.7 exhibiting a perfect, almost linear behaviour for up to 1024 CPUs. The simulations were performed using a cylindrical mesh of $N_z \times N_\phi \times N_r = 384 \times 512 \times 192$ nodes and 1000 time steps for 4 to 64 CPUs and $4096 \times 4096 \times 128$ nodes for 100 time steps for 64 to 1024 CPUs normalised to the value at 64 cores.

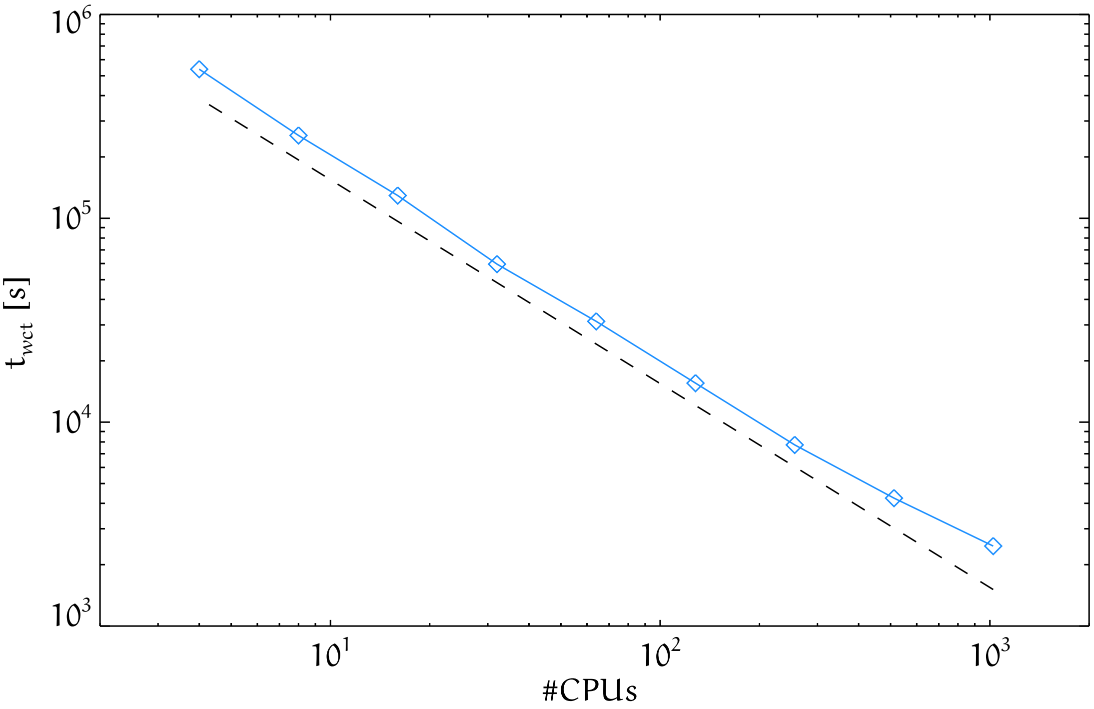

FIGURE 3.7: Scaling behaviour the OB code `flowsi` on the HLRB II Altix cluster. The diamonds show the obtained values of the wall clock time t_{wct} used for 1000 time steps and the blue line is a guide to the eye. For comparison the perfect scalability for an ideal code is plotted, i.e. wall clock time $t_{wct} \propto 1/\#$ CPUs is shown by the black dashed line.

3.4 Large Eddy Simulations

The i-th momentum equation of (3.1.21) averaged over a finite volume V is given by

$$\frac{1}{2\Delta t}\left(\left\langle u^{n+1}\right\rangle_V - \left\langle u_i^{n-1}\right\rangle_V\right) + \langle \mathbf{u}^n \cdot \nabla u_i^n\rangle_V + \langle \nabla p^n \cdot \mathbf{e}_i\rangle_V \tag{3.4.1}$$

$$= \frac{Pr^{1/2}}{Ra^{1/2}\gamma^{3/2}}\langle \Delta u_i^{n-1}\rangle_V + \langle T^n\rangle_V \mathbf{e}_z \cdot \mathbf{e}_i. \tag{3.4.2}$$

Its solution requires integrals over surfaces S, hence, the convective and diffusive term are rewritten using the Gauß–Ostrogradsky theorem and the continuity equation as follows

$$\begin{aligned}
\langle \mathbf{u}^n \cdot \nabla u_i^n\rangle_V &= \langle \nabla \cdot (u_i^n \mathbf{u}^n)\rangle_V - \langle u_i^n \nabla \cdot \mathbf{u}^n\rangle_V \\
&= \frac{1}{\Delta V}\oint_S \mathbf{n} \cdot (u_i^n \mathbf{u}^n)\, dS, && (3.4.3)\\
\frac{Pr^{1/2}}{Ra^{1/2}\gamma^{3/2}}\left\langle \nabla^2 u_i^{n-1}\right\rangle_V &= \frac{Pr^{1/2}}{Ra^{1/2}\gamma^{3/2}}\left\langle \nabla \cdot \nabla u_i^{n-1}\right\rangle_V \\
&= \frac{Pr^{1/2}}{Ra^{1/2}\gamma^{3/2}}\frac{1}{\Delta V}\oint_S \mathbf{n} \cdot \boldsymbol{\nabla} u_i^{n-1}\, dS, && (3.4.4)
\end{aligned}$$

The analogue is true for the temperature equation. Hence, in the numerical simulations the averaged products $\langle u_i u_j\rangle_S$ and $\langle T u_j\rangle_S$ are required. In DNS it is assumed, and actually demanded, that the resolution is fine enough so that the following

$$\langle u_i u_j\rangle_S \approx \langle u_i\rangle_S \langle u_j\rangle_S\,, \tag{3.4.5}$$

$$\langle T u_j\rangle_S \approx \langle T\rangle_S \langle u_j\rangle_S \tag{3.4.6}$$

is valid. If the mesh is too coarse, the above becomes less and less valid. The modelling of the so-called subgrid scale stress tensors

$$\begin{aligned}
\tau_{ij} &= \langle u_i u_j\rangle_S - \langle u_i\rangle_S \langle u_j\rangle_S\,,\\
\tau_{T_j} &= \langle T u_j\rangle_S - \langle T\rangle_S \langle u_j\rangle_S
\end{aligned}$$

is therefore one of the key problems in computational fluid dynamics. In simulations where these terms are modelled one speaks of large eddy simulations (LES). Here, I will present results of LES with a very simple approach: an approximation by the first term of the exact Fourier series expansions for filtered products according to the model by Leonard (1975) and Shishkina and Wagner (2007c),

$$\begin{aligned}
{}^{\beta}\overline{u_\alpha u_\beta} &= {}^{\beta}\overline{u_\alpha}\,{}^{\beta}\overline{u_\beta} + \frac{1}{12}\sum_{\gamma\neq\beta}(\Delta\gamma)^2 \frac{\partial\,{}^{\beta}\overline{u_\alpha}}{\partial\gamma}\frac{\partial\,{}^{\beta}\overline{u_\beta}}{\partial\gamma} + \mathcal{O}\big((\Delta\gamma)^4\big),\\
{}^{\beta}\overline{T u_\beta} &= {}^{\beta}\overline{T}\,{}^{\beta}\overline{u_\beta} + \frac{1}{12}\sum_{\gamma\neq\beta}(\Delta\gamma)^2 \frac{\partial\,{}^{\beta}\overline{T}}{\partial\gamma}\frac{\partial\,{}^{\beta}\overline{u_\beta}}{\partial\gamma} + \mathcal{O}\big((\Delta\gamma)^4\big).
\end{aligned}$$

It has the major adavantage that no empirical constants are required. It has proven to be quite successful in Rayleigh–Bénard convection for moderate Rayleigh numbers (Shishkina and Wagner, 2007c).

3.5 Implementation of temperature-dependent material properties into **`flowsi`**

To solve the non-Oberbeck–Boussinesq equations (2.2.38)–(2.2.40), I additionally included the temperature-dependent material properties ν, Λ and ρ in `flowsi`. The material properties of water and glycerol are given by polynomials of the temperature up to order i with certain prefactors a_i, i.e.

$$\frac{X - X_m}{X_m} = \sum_i a_i (T - T_m)^i \qquad X \in \{\rho, \nu, \Lambda\}.. \tag{3.5.1}$$

Values for a_i are given and also the functional dependency of mercury on the temperature are given in chapter 5.

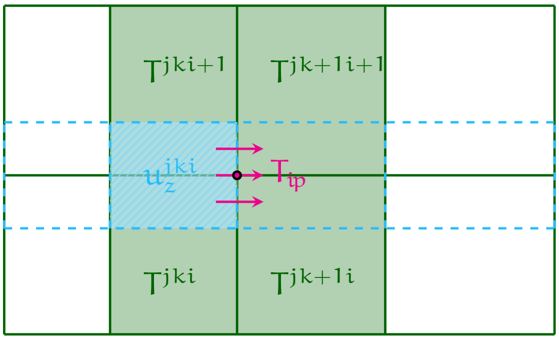

(a) radial direction r

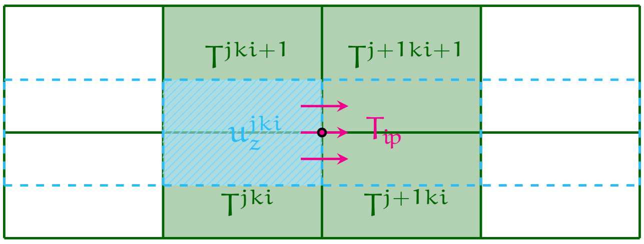

(b) azimuthal direction ϕ

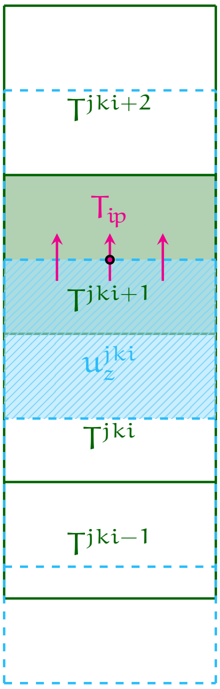

(c) vertical direction z

FIGURE 3.8: Sketch of how to interpolate the temperature for the calculation of the viscosity for solving the Navier–Stokes equation for the vertical velocity component u_z in radial, azimuthal and vertical direction.

The main issue from a numerical point of view now is, that the temperature and the velocity are calculated on different meshes. To solve the momentum equation the viscosity ν is needed at the surface of the velocity cells. But since ν is a function of the temperature T it needs to be interpolated. In a sufficient accuracy it is given by the weighted average value of the surrounding temperature cells. For clarity this is shown for the example of the vertical velocity u_z in fig. 3.8. In that case interopolated temperatures T_{ip} are given by

$$T_{ip} = \frac{V^{jki}\,T^{jk+1i} + V^{jki+1}\,T^{jk+1i+1} + V^{jk+1i}\,T^{jki} + V^{jk+1i+1}\,T^{jki+1}}{V^{jki} + V^{jki+1} + V^{jk+1i} + V^{jk+1i+1}} \tag{3.5.2}$$

in the radial direction r,

$$T_{ip} = \frac{V^{jki+1}\left(T^{jki} + T^{j+1ki}\right) + V^{jki}\left(T^{jki+1} + T^{j+1ki+1}\right)}{2V^{jki} + 2V^{jki+1}} \tag{3.5.3}$$

in the azimuthal direction ϕ, and

$$T_{ip} = T^{jki+1} \tag{3.5.4}$$

in the vertical direction z.

The calculation of the heat conductivity Λ required for solution of the temperature equation is simpler, no interpolation is needed.
In NOB simulations, the boundary layers at the top and bottom have different thicknesses, and can be thinner than in the OB case. How much thinner is not a priori known. To ensure that the NOB simulations are properly resolved twice as many nodes as required in the OB case were placed in the boundary layers. Furthermore, because of the temperature-dependent material properties, the time step Δt had to be reduced.

ROTATING RAYLEIGH–BÉNARD CONVECTION OF SF_6 IN A SLENDER CYLINDER*

This chapter is devoted to rotating Rayleigh–Bénard convection of a fluid with a low Prandtl number of $Pr = 0.8$, as is for air or SF_6. The fluid is confined in a slender cylinder with an aspect ratio of $\Gamma = 1/2$. Since this cuts down the needed number of grid points in the radial direction, higher Rayleigh numbers than for $\Gamma \geqslant 1$ can be achieved. Nonetheless, these simulations are expensive and to study the impact of rotation on the flow, a large range of rotation rates, i.e. inverse Rossby numbers $1/Ro$, has to be covered.

The ultimate objective would be to understand the influence of rotation on high Rayleigh number convection, e.g. occurring in stars such as our Sun or gaseous planets like Jupiter, Uranus and Neptune and the many recently found giant planets. Accordingly, it would be desirable to simulate Rayleigh numbers as high as $Ra \approx \mathcal{O}(10^{23})$, but these are far beyond reach, not only numerically but also experimentally. The Rayleigh numbers that can be achieved by experiments and DNS are magnitudes lower. Present experiments are limited to $Ra \approx 10^{15}$ (He et al., 2012) and DNS to $Ra \approx 10^{12}$ (Stevens et al., 2011). Studying convection at lower Ra might still help to understand the fundamental processes and some of the observed phenomena in geo- and astrophysics, since even then, there is a lack of knowledge about the actual influence of the other control parameters $1/Ro$, Pr and also Γ.

However, the geometry of the container, first and foremost the aspect ratio, plays an important role. The preferred geometry for rotating Rayleigh–Bénard convection is a cylinder, however, the preferred aspect ratio has changed over the years. Starting with large diameter-to-height aspect ratios, $\Gamma = D/H$, recent developments in numerical and experimental studies, rather go to smaller and smaller Γ of 0.5 (Ahlers et al., 2012; He et al., 2012) or even 0.23 (Stevens et al., 2011). Most of the earlier studies were about the onset of convection and pattern formation (Chandrasekhar, 1961), thus, the aim was to mimic an infinite lateral extent, where analytical relations are available. On the contrary, most of the current investigations focus on turbulent thermal convection, including the transition to the so-called "ultimate state" (Grossmann and Lohse, 2011), thus, the aim is to achieve high Ra and, hence, practical considerations demand a small Γ. The development to smaller Γ is true for both, "ordinary" and rotating convection (Ecke and Niemela, 2014; Oresta et al., 2007; Stevens et al., 2012). Yet, the finite size has serious implications for rotating Rayleigh–Bénard convection. Not only, does the destabilising effect of the lateral

---

*Parts of this chapter have been adopted from HORN, S. AND SHISHKINA, O., Toroidal and poloidal energy in rotating Rayleigh–Bénard convection, *J. Fluid Mech. 762* (2015), 232–255.

wall yield a lower critical Ra for the onset of convection at fast rotation rates (Buell and Catton, 1983) because of drifting wall modes (Ecke et al., 1992; Goldstein et al., 1994, 1993; Herrmann and Busse, 1993; Kuo and Cross, 1993; Zhong et al., 1991b), but Γ also determines the bifurcation point Ro_b, at which, for $\mathrm{Pr} \gtrsim 1$ and higher Ra, heat transfer enhancement sets in (Weiss and Ahlers, 2011b; Weiss et al., 2010).

The increased heat transport, expressed in terms of the Nusselt number Nu, is usually used as an indicator for the different turbulent states occurring in rotating turbulent thermal convection, suggesting a division into three regimes (Kunnen et al., 2011). In the weak rotation regime, Nu remains nearly constant, but as soon as $1/\mathrm{Ro}$ is increased to values above $1/\mathrm{Ro}_b$, after a sharp onset, a continuous increase of Nu is observed for moderate rotation rotates, which coincides with the generation of columnar vortex structures (Stevens et al., 2011; Weiss et al., 2010). After it has reached a peak, which marks the transition to the regime of strong rotation, it drops rapidly with the rotation rate due to the suppression of vertical velocity fluctuations (cf. also the recent review by Stevens et al., 2013b). However, this classification of regimes is only valid for fluids with $\mathrm{Pr} \gtrsim 1$; for $\mathrm{Pr} \lesssim 1$ no heat transfer enhancement is expected (Stevens et al., 2010b).

As the change of Nu is closely connected to the columnar vortices, the number of vortices serves as another criterion to determine the point where rotation dominates over buoyancy. However, extracting these vortices is relatively cumbersome, and involves a certain arbitrariness in choosing what constitutes a vortex. Furthermore, for $\mathrm{Pr} < 1$ the larger diffusivity results in only short vortices that dissipate quickly when they reach the bulk, which complicates matters. Conversely, one can also look at the large-scale circulation (LSC) or more specifically at the rotation rate when it breaks-down (Kunnen et al., 2008; Stevens et al., 2012; Weiss and Ahlers, 2011a). In experiments, this is frequently obtained by analysing the temperature signal at the sidewall. However, one has to be careful with two-vortex states or multiple-roll states occurring in Rayleigh–Bénard cells with small aspect ratios. Evidently, also the crossover of the boundary layer thicknesses (King et al., 2012, 2009; Rossby, 1969) cannot be applied to fluids with $\mathrm{Pr} < 1$, where the thermal boundary layer is thicker than the viscous one even without rotation.

Here, I offer an alternative method for the characterisation of the different regimes in rotating Rayleigh–Bénard convection. Motivated by the work by Breuer et al. (2004), who have shown, that the toroidal and poloidal energy are characteristic for the distinctive types of dynamics in low and high Prandtl number flows in non-rotating convection, namely, that the toroidal energy is highest for fluids with $\mathrm{Pr} \lesssim 1$ (Breuer et al., 2004), and vanishes for $\mathrm{Pr} = \infty$ (Busse, 1967a), I analyse the contribution of the toroidal and poloidal energy in rotating convection. This is a very natural approach. The poloidal energy is the energy contained in cellular or roll motion, such as the LSC or double-roll states, i.e. the dominant motion without rotation. The toroidal energy, on the other hand, is contained in swirling motion in the horizontal plane, i.e. with a vertical vorticity (Olson and Bercovici, 1991), which is the dominant motion in rotating convection. This means, it is possible to distinguish different regimes of rotating convection based on global quantities, namely the time and volume averaged toroidal and poloidal energy without a restriction to certain Prandtl numbers or aspect ratios.

4.1 Parameter space

All DNS results presented in this chapter were performed for a fluid with $Pr = 0.8$, corresponding to SF_6 or air, in a slender cylinder with $\Gamma = 1/2$ for $Ra \in [10^5, 10^9]$ and rotation rates $1/Ro \in [0, 20]$. In addition, also LES were performed, but the main focus lies on DNS.

The governing equations are the Navier–Stokes equations in Oberbeck–Boussinesq approximation with the Coriolis force as an additional force term. Thus, numerically the set of equations

$$\begin{aligned} \nabla \cdot \mathbf{u} &= 0, && (4.1.1)\\ D_t \mathbf{u} &= -\nabla p + Ra^{-1/2} Pr^{1/2} \gamma^{-3/2} \nabla^2 \mathbf{u} + Ro^{-1} \gamma^{1/2} \hat{\mathbf{e}}_z \times \mathbf{u} + T \hat{\mathbf{e}}_z, && (4.1.2)\\ D_t T &= Ra^{-1/2} Pr^{-1/2} \gamma^{-3/2} \nabla^2 T, && (4.1.3) \end{aligned}$$

is solved in cylindrical coordinates.

Any effects due to centrifugal buoyancy are neglected. Their importance can be estimated by calculating the Froude number

$$Fr = \frac{\Omega^2 D}{2g} = \frac{Ra\Gamma}{8Ro^2} \frac{\kappa\nu}{gH^3}. \tag{4.1.4}$$

Since numerically dimensionless equations are solved, I use the parameters of the High-Pressure Convection Facility (HPCF) at the Max Planck Institute for Dynamics and Self-Organization in Göttingen, Germany, to evaluate Fr. It is a cylindrical cell, with a height of $H = 2.24\,\text{m}$ and a diameter of $D = 1.12\,\text{m}$, i.e. $\Gamma = 1/2$, filled with sulfur hexafluoride (SF_6) at pressures between 2 bar and 19 bar (Ahlers et al., 2012; He et al., 2012). At a pressure of 2 bar, the viscosity of SF_6 is given by $\nu = 1.2 \times 10^{-6}\,\text{m}^2\text{s}^{-1}$ and its thermal diffusivity by $\kappa = 1.6 \times 10^{-6}\,\text{m}^2\text{s}^{-1}$, i.e. $Pr \approx 0.8$. The gravitational acceleration in Göttingen is approximately $9.81\,\text{m}\,\text{s}^{-2}$. Thus, for the highest Ra and $1/Ro$, namely 10^9 and 20, the Froude number is as low as $Fr = 4.4 \times 10^{-4}$. Hence, since $Fr \ll 1$ it is justifiable to set $Fr \equiv 0$ (Zhong et al., 2009). However, it should be noted, that the Rayleigh numbers in the HPFC are typically much larger than the ones that be can attained by DNS.

The resolution is chosen to fulfil the requirements by Shishkina et al. (2010). The meshes are non-equidistant in radial and vertical direction, with a clusterisation of grid points close to the walls. To guarantee enough points in the boundary layers, the grid points were denser clustered for smaller Ro, as it is well-known, that the viscous boundary layer becomes thinner as the rotation rate increases (e.g. Kunnen et al., 2008; Stevens et al., 2010a). This means, that in the Ekman type viscous boundary layer in the rotating case the same criterion for the number of grid points was applied as in the non-rotating case. The details of all simulation parameters and the numerical resolution can be found in table 4.1.

Ra	$1/Ro$	$N_r \times N_\phi \times N_z$
10^5	$\{0.0, 0.07, 0.14, 0.23, 0.47, 0.71, 1.41, 2.36, 3.33, 4.71, 5.89, 7.07, 8.84, 10.1, 14.14\}$	$11 \times 32 \times 34$
10^6	$\{0.0, 0.07, 0.1, 0.14, 0.2, 0.35, 0.47, 0.67, 1.0, 1.41, 1.67, 2.0, 2.13, 2.5, 2.83, 3.33, 3.54, 4.0, 4.71, 5.0, 6.67, 7.07, 8.33, 10.0, 14.29, 20.0\}$	$17 \times 64 \times 68$
10^7	$\{0.0, 0.07, 0.14, 0.71, 1.41, 2.0, 2.83, 4.71, 7.07, 14.14\}$	$33 \times 128 \times 132$
10^8	$\{0.0, 0.07, 0.14, 0.2, 0.71, 1.0, 1.41, 2.0, 2.36, 3.33, 5.0, 7.07, 10.0, 14.14, 20.0\}$	$80 \times 256 \times 320$
10^9	$\{0.0, 0.07, 1.41, 2.0, 2.36, 2.83, 4.0, 7.07, 10.0, 14.14, 20.0\}$	$192 \times 512 \times 768$

TABLE 4.1: Parameters used in the DNS for rotating Rayleigh–Bénard convection in SF$_6$ with $Pr = 0.8$ and $\Gamma = 1/2$, including the computational mesh size $N_r \times N_\phi \times N_z$.

4.2 Rayleigh number dependence of the flow structures in the non-rotating case

Firstly, the flow structures in the non-rotating case are shown for $10^5 \leqslant Ra \leqslant 10^{10}$. They are best seen in the temperature distribution, thus, in figure 4.1 instantaneous temperature iso-surfaces are presented, which are equidistantly distributed between the top and bottom temperature. The results for $10^5 \leqslant Ra \leqslant 10^9$ were obtained by DNS, for $Ra = 10^{10}$ by LES.

They visualise the dramatic change of the flow structures and the flow behaviour with increasing Ra. For the smallest Ra the flow is steady and one large convection roll fills the whole cylinder. With increasing Ra the flow becomes unsteady until it eventually enters the turbulent regime for $Ra \gtrsim 10^7$ and the single structures become gradually smaller. While for moderate Ra the LSC is clearly recognisable in the instantaneous flow fields, i.e. there are cold plume descending on one side and warm plumes ascending on the opposite side, this becomes hardly possible for higher Ra. But the LSC can be recovered in the sufficiently long temporal averaged flow fields; its break-down is not expected until $Ra \gtrsim 10^{13}$ (He et al., 2012).

But not only a change in the Rayleigh number Ra can be responsible for a tremendous alteration of the flow structure, but also a change in the inverse Rossby number $1/Ro$. Here, also different regimes depending on the rotation rate can be found, this will be discussed in the following. I propose, that the toroidal and poloidal energy can be used to universally capture these transitions in rotating Rayleigh–Bénard convection.

4.3 Decomposition of the velocity field

In the DNS the Navier–Stokes equations (4.1.1)–(4.1.3) are solved in primitive variables. Hence, in order to obtain the toroidal and poloidal energy, instantaneous

(a) $Ra = 10^5$ (b) $Ra = 10^6$ (c) $Ra = 10^7$

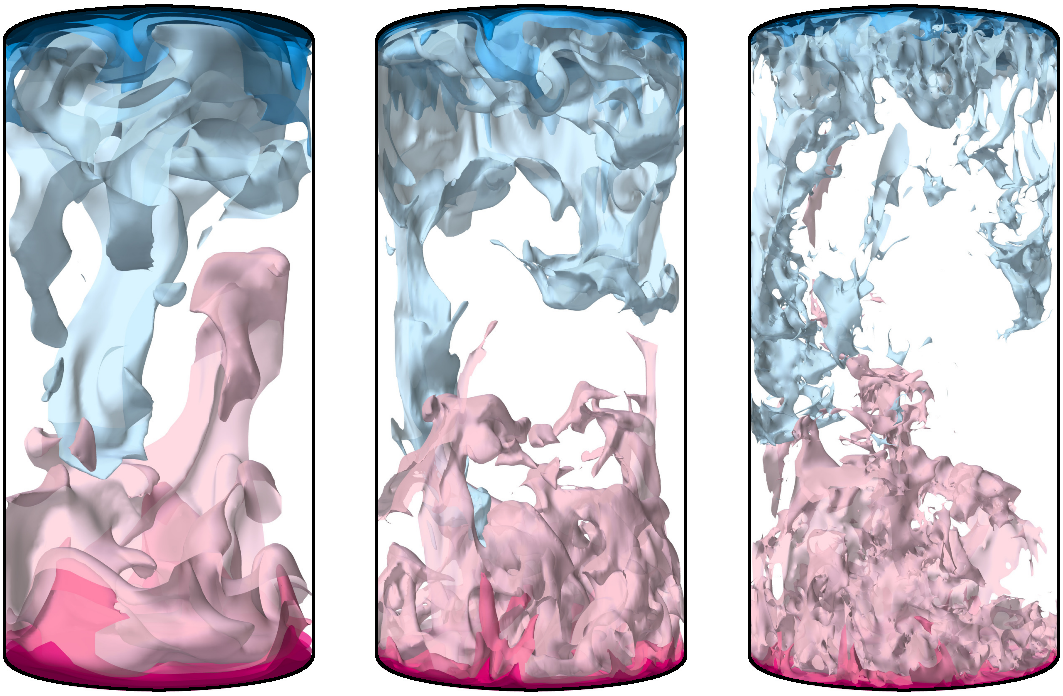

(d) $Ra = 10^8$ (e) $Ra = 10^9$ (f) $Ra = 10^{10}$

FIGURE 4.1: Temperature iso-surfaces, equidistantly distributed between the top and bottom temperature in the non-rotating case, i.e. $1/Ro = 0$, obtained by DNS for $Ra \in [10^5, 10^9]$ and LES for $Ra = 10^{10}$, respectively.

velocity fields are analysed every half dimensionless time unit. That means, the solenoidal velocity field $\mathbf{u}$ is decomposed into a poloidal field $\boldsymbol{\pi}$ and a toroidal field $\boldsymbol{\tau}$ with the defining scalars ξ and ψ, respectively, (Breuer et al., 2004; Chandrasekhar, 1961)

$$\mathbf{u} = \boldsymbol{\pi} + \boldsymbol{\tau} = \boldsymbol{\nabla} \times \boldsymbol{\nabla} \times (\xi \hat{\mathbf{e}}_z) + \boldsymbol{\nabla} \times (\psi \hat{\mathbf{e}}_z). \tag{4.3.1}$$

This decomposition is also called Mie decomposition or Mie representation of the vector field $\mathbf{u}$ (Backus, 1986). In cylindrical component notation, equation (4.3.1) reads

$$u_r = \pi_r + \tau_r = \partial_r \partial_z \xi + \tfrac{1}{r} \partial_\phi \psi, \tag{4.3.2}$$

$$u_\phi = \pi_\phi + \tau_\phi = \tfrac{1}{r} \partial_\phi \partial_z \xi - \partial_r \psi, \tag{4.3.3}$$

$$u_z = \pi_z + \tau_z = -\tfrac{1}{r} \partial_r (r \partial_r \xi) - \tfrac{1}{r^2} \partial_\phi \partial_\phi \xi. \tag{4.3.4}$$

The equations (4.3.2) and (4.3.3) can be combined, and expressed in terms of the vertical component of the vorticity $\boldsymbol{\omega} = \boldsymbol{\nabla} \times \mathbf{u}$,

$$\omega_z = -\tfrac{1}{r} \left(\partial_r \left(r u_\phi \right) - \partial_\phi u_r \right) = -\tfrac{1}{r} \partial_r (r \partial_r \psi) - \tfrac{1}{r^2} \partial_\phi \partial_\phi \psi. \tag{4.3.5}$$

The operator $-\frac{1}{r}\partial_r(r\partial_r) - \frac{1}{r^2}\partial_\phi\partial_\phi \equiv \Delta_{r\phi}$ is the horizontal Laplacian. The equations (4.3.4) and (4.3.5) are thus two-dimensional Poisson equations

$$\Delta_{r\phi} \xi + u_z = 0, \tag{4.3.6}$$

$$\Delta_{r\phi} \psi + \omega_z = 0. \tag{4.3.7}$$

Therefore, these scalars are also called velocity potentials, in analogy to, e.g., electrodynamics. However, the scalars ξ and ψ are not uniquely defined. In fact, to the toroidal potential ψ an arbitrary horizontal harmonic function, i.e. any solution of the corresponding Laplace equation, can be added. The poloidal potential ξ is only determined up to an arbitrary function of z (see e.g. Marques et al., 1993). Thus, there is a gauge freedom for the boundary conditions. The most simple and commonly used gauge condition for ξ is

$$\xi|_{r=R} = 0 \tag{4.3.8}$$

(Boronski and Tuckerman, 2007; Marques et al., 1993). This gauge in combination with (4.3.2) and the no-slip condition on the velocity, $u_r|_{r=R} = 0$, yields

$$\partial_\phi \psi = 0. \tag{4.3.9}$$

Hence, ψ needs to be constant along the contour $r = R$ for a constant z and can also be set consistently to

$$\psi|_{r=R} = 0. \tag{4.3.10}$$

Furthermore, it is

$$\xi|_{z=0} = \xi|_{z=H} = 0 \text{ and } \psi|_{z=0} = \psi|_{z=H} = 0 \tag{4.3.11}$$

(Marques et al., 1993). This choice of gauge is the most convenient one, because it implies Dirichlet boundary conditions on $r = R$ on the two equations (4.3.6) and (4.3.7). Hence, the problem of solving these two Poisson equations becomes well-posed, and the unique solutions for the poloidal and toroidal scalar field are given by

$$\xi(r, \phi, z) = \int_0^{2\pi}\int_0^{R} u_z(\zeta, \eta, z) G(r, \phi, \zeta, \eta)\zeta d\zeta d\eta, \qquad (4.3.12)$$

$$\psi(r, \phi, z) = \int_0^{2\pi}\int_0^{R} \omega_z(\zeta, \eta, z) G(r, \phi, \zeta, \eta)\zeta d\zeta d\eta, \qquad (4.3.13)$$

where ζ and η are integration variables and $G(r, \phi, \zeta, \eta)$ is the Green's function

$$G(r, \phi, \zeta, \eta) = \frac{1}{4\pi} \ln\left(\frac{r^2\zeta^2 - 2R^2 r\zeta\cos(\phi - \eta) + R^4}{R^2(r^2 - 2r\zeta\cos(\phi - \eta) + \zeta^2)}\right).$$

Albeit the fact, that this solution is analytically exact, the large mesh size of the numerically obtained flow fields makes the solving computationally expensive and for higher Ra, i.e. $Ra \gtrsim 10^8$, infeasible. Numerically, it is more efficient to solve the Poisson equations directly. This was done by adapting the well-tested `fishpack90` (Swarztrauber and Sweet, 1975) solver to double precision and to non-equidistant meshes. The solver is based on the generalized Buneman algorithm. Special care is also required at the cylinder axis where in cylindrical coordinates one always faces the problem of the mathematical, but not physical singularity, caused by terms involving $1/r$. But this can be elegantly overcome by calculating (4.3.12) and (4.3.13) at $r = 0$ directly, utilizing that the Green's function in this case simplifies to

$$G(0, \phi, \zeta, \eta) = \frac{1}{2\pi} \ln\left(\frac{R}{\zeta}\right). \qquad (4.3.14)$$

Thus, by prescribing the analytical solution at $r = 0$ as numerical boundary condition, a smooth scalar field is guaranteed. It is worth noting, that this does not impose any additional physical boundary or gauge condition, but is a direct consequence of the Dirichlet boundary conditions (4.3.8) and (4.3.10) and is, hence, merely a numerical trick. Eventually, it is possible to calculate the total kinetic energy e_{kin}, the poloidal energy e_{pol} and the toroidal energy e_{tor}, defined by

$$\begin{aligned} e_{kin} &= \langle u_r^2 + u_\phi^2 + u_z^2 \rangle_{V,t}, & (4.3.15)\\ e_{pol} &= \langle \pi_r^2 + \pi_\phi^2 + \pi_z^2 \rangle_{V,t}, & (4.3.16)\\ e_{tor} &= \langle \tau_r^2 + \tau_\phi^2 + \tau_z^2 \rangle_{V,t}, & (4.3.17) \end{aligned}$$

where $\langle \cdot \rangle_{V,t}$ denotes averaging in time t and over the whole volume V.

4.4 Nusselt number and characteristic flow properties

Most of the recent experiments and numerical simulations on rotating Rayleigh–Bénard convection were conducted in water with $3 \lesssim Pr \lesssim 7$ (King et al., 2009; Kunnen et al., 2010; Stevens et al., 2009; Weiss and Ahlers, 2011a; Zhong and Ahlers, 2010). One of the reasons for this might be, that only for fluids with $Pr > 1$ columnar vortex structures, sometimes called Ekman vortices (Stevens et al., 2010b; Weiss et al., 2010), occur that extend from one horizontal wall to the other (Horn et al., 2011b). Via Ekman pumping, the vortices are able to significantly enhance the heat transport compared to the non-rotating case, where the heat flux is usually expressed in terms of the Nusselt number,

$$Nu = (Ra Pr \gamma)^{1/2} \langle u_z T \rangle - \gamma^{-1} \langle \partial_z T \rangle . \tag{4.4.1}$$

But for fluids with $Pr < 1$, these vortices are much shorter, and do not form a regular grid. The reason is, that the thermal diffusivity is larger than the kinematic viscosity, thus, heat can spread in the bulk, making Ekman pumping less effective (Stevens et al., 2010b). Stevens et al. (2010b) found no heat transfer enhancement at all for $Pr = 0.7$, $Ra = 10^8$, $0.1 \leqslant 1/Ro \leqslant 10.0$ and $\Gamma = 1.0$, however, Oresta et al. (2007) found a slightly higher Nu for very similar simulation parameters, $Pr = 0.7$, $Ra = 2 \times 10^8$, $0.1 \leqslant 1/Ro \leqslant 33.3$ but $\Gamma = 0.5$, which they attributed to Ekman pumping. Figure 4.2(a) shows the Nusselt number for the rotating case normalized by the one in the non-rotating case, Nu/Nu^0, for the DNS for $10^5 \leqslant Ra \leqslant 10^9$ and $0.07 \leqslant 1/Ro \leqslant 20.0$. In addition, experimental results by Ecke and Niemela (2014) for $Ra = 6.2 \times 10^9$ in a cylindrical convection cell with $\Gamma = 0.5$ and helium with $Pr = 0.7$ are shown for comparison. The Nusselt number Nu is also presented in figure 4.2(b), but as function of the Taylor number.

For $Ra = 10^5$, convection is steady for all Rossby numbers considered, except for $1/Ro = 14.1$, where convection is completely suppressed due to rotation and heat is transported by conduction alone. For $Ra = 10^6$, convection is chaotic and unsteady for $1/Ro \lesssim 1.67$, for $1.67 \gtrsim 1/Ro \gtrsim 2.5$ oscillatory convection is found and for even faster rotation rates, i.e. $1/Ro \gtrsim 2.5$, convection is steady. For $Ra = 10^7$, there is turbulent convection for low rotation rates, but again, however, for even faster rotation rates, i.e. $1/Ro = 14.1$ steady convection is observed. Finally, for $Ra = 10^8$ and $Ra = 10^9$ the applied rotation was never rapid enough to completely suppress turbulent fluctuations.

The general behaviour of Nu with increasing rotation rate is very similar for all Ra, i.e. it is almost constant for slow rotation and then drops rapidly at a certain rotation rate. There is also a very slightly increased Nu for $1/Ro \lesssim 2$, which is due to the stabilizing effect of rotation, which suppresses reversals and changes from a one-roll state to a double-roll state, that occur more frequently for $\Gamma = 0.5$ than for $\Gamma = 1.0$. For $Ra = 10^6$ there is more switching between these different states than for the other Ra which is a possible explanation for the evident deviation of the behaviour of the Nusselt number for that particular Rayleigh number. It was also found by Oresta et al. (2007), in numerical simulations with parameters very similar to that at $Ra = 9 \times 10^5$ and $Pr = 0.7$. The continuous decrease of Nu

with increasingly high rotation rate is expected from the Taylor–Proudman theorem (Proudman, 1916; Taylor, 1921). It predicts the suppression of flow variations along the axis of rotation. Although strictly speaking it is not designated to the highly non-linear and time-dependent case of rotating Rayleigh–Bénard convection, the reduced heat transport can be understood with it. In figure 4.2(a) also the prediction by Weiss et al. (2010) and Weiss and Ahlers (2011b) based on a phenomenological Ginzburg–Landau model is shown. They have shown, that for fluids with $Pr \gtrsim 1$, at

$$\frac{1}{Ro_b} = \frac{a}{\Gamma}\left(1+\frac{b}{\Gamma}\right), \; a = 0.381, \; b = 0.061 \tag{4.4.2}$$

a bifurcation corresponding to the onset of Ekman vortex formation and Nusselt number enhancement occurs. This bifurcation is a finite-size effect, and gives $1/Ro_b = 0.86$ for $\Gamma = 0.5$. For $Pr = 0.8$ and $Ra = 10^5$ and $Ra = 10^7$ the Nusselt number starts to decrease at the point $1/Ro_b$, but no columnar vortices were observed. However, for $Ra = 10^8$ and $Ra = 10^9$, short columnar vortices are found and the Nusselt number also appears to increase slightly and then drops at a critical inverse Rossby number $2.36 \lesssim 1/Ro_{crit} \lesssim 3.33$. When Nu is plotted against Ta as in figure 4.2 (b), the vertex of the curve, marked with filled symbols, seems to match all Ra. In figure 4.2 (a) the same rotation rate is indicated by a grey shaded area. The transition at $1/Ro_{crit}$ is consistent with the one found empirically by Ecke and Niemela (2014) at $1/Ro_1 \approx 2.86$. Furthermore, Ecke and Niemela (2014) suggested that after this initial decrease a more rapid decrease occurs after $1/Ro_2 \approx 8.33$. An accurate identification of Ro_{crit} solely based on the Nusselt number is nonetheless difficult.

That a transition in the flow occurs is also visible in other important flow characteristics as the radial velocity component u_r, the temperature T, the rms temperature T_{rms} or the skewness of the temperature S_T. The temporally, radially and azimuthally averaged profiles of these quantities are presented in figure 4.3 for five representative rotation rates, $1/Ro \in \{0.0, 2.0, 3.3, 10.0, 20.0\}$. To rule out the sidewall effects (Kunnen et al., 2013), the radial averaging was performed for $0 \leqslant r \leqslant 0.9R$ (Stevens et al., 2010a). All of them, but in particular the radial velocity and the skewness of the temperature, reveal a significant flow change for $1/Ro \gtrsim 3.3$.

The radial velocity u_r as function of the vertical coordinate z, figure 4.3(a), nicely demonstrates the Taylor–Proudman effect. Variations of the flow in vertical direction are inhibited and as a consequence roll-like structures such as the LSC are not permitted. Hence, while the u_r mean profiles at low rotation rates still show the typical shape reflecting these structures, they show no variation in the bulk any more as soon as these structures break down. The first three moments of the temperature, presented in figure 4.3(b)–(d), reflect the impact of the generated columnar vortices. The mean temperature profiles exhibit a non-zero gradient in the bulk increasing with $1/Ro$ and strongest close to the plates. It is usually attributed to vortex merger (Julien et al., 1996). However, even without rotation a small non-vanishing temperature gradient is present that is assumed to be due to the small aspect ratio. The rms temperature also varies significantly with the rotation rate. It is almost constant without rotation, showing a crescent-shaped profile up to $1/Ro \approx 10.0$. For $1/Ro = 20.0$, the crescent-shape is dented in the midplane and bent in the opposite

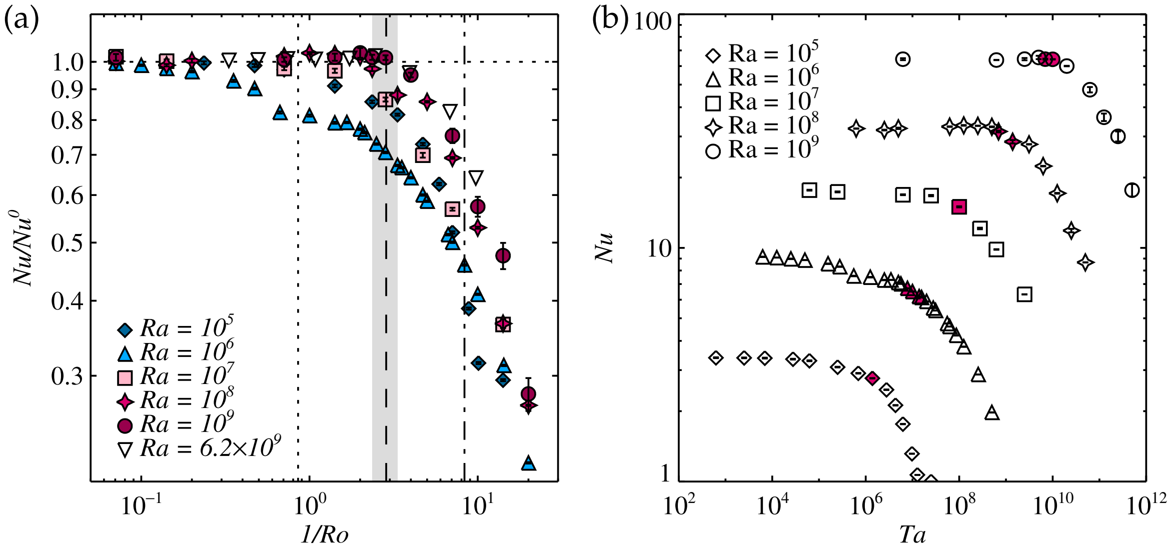

FIGURE 4.2: (a) Nusselt number for the rotating case normalized by the one in the non-rotating case Nu/Nu^0 as function of the inverse Rossby number $1/Ro$ for $Ra \in \{10^5, 10^6, 10^7, 10^8, 10^9\}$ obtained by DNS; experimental data by Ecke and Niemela (2014) for $Ra = 6.2 \times 10^9$ and $Pr = 0.7$ are shown for comparison. The vertical dotted line shows the prediction by Weiss and Ahlers (2011b); Weiss et al. (2010), $1/Ro_b = 0.86$, the vertical long-dashed and dashed-dotted line mark the proposed transition by Ecke and Niemela (2014) at $1/Ro_1 \approx 2.83$ and $1/Ro_2 \approx 8.33$, respectively. The grey shaded area shows where $e_{pol} \approx e_{tor}$ at $2.36 \lesssim 1/Ro_{crit} \lesssim 3.33$. (b) Nusselt number Nu as function of the Taylor number Ta. The filled (pink) symbols show where $e_{pol} \approx e_{tor}$ and are the same as marked by the grey shaded area in figure (a).

direction. The skewness of the temperature also exhibits signs of a fundamental change in the flow, in particular close to the vicinity of the top and bottom plates: with increasing $1/Ro$, S_T abruptly changes sign at $1/Ro \approx 10.0$. A similar change of behaviour was also reported by Kunnen et al. (2006, 2009) for the skewness of the vertical velocity S_{u_z} and of the rms vorticity S_{ω_z}, obtained by simulations in a periodic domain, $Pr = 1$ and $Ra = 2.5 \times 10^6$.

4.5 Toroidal and poloidal potential and energy

In the following, I show how to connect the different flow behaviour with the toroidal and poloidal potential and energy. It will allow to effectively identify the transitions between different regimes in rotating Rayleigh–Bénard based on the global quantities e_{tor} and e_{pol}.

In the figures 4.4–4.8 instantaneous flow quantities are presented for the same representative rotation rates $1/Ro \in \{0.0, 2.0, 3.3, 10.0, 20.0\}$ at $Ra = 10^8$ as before. I refrained from showing averaged flow fields, since the precession motion of the flow might distort their interpretation.

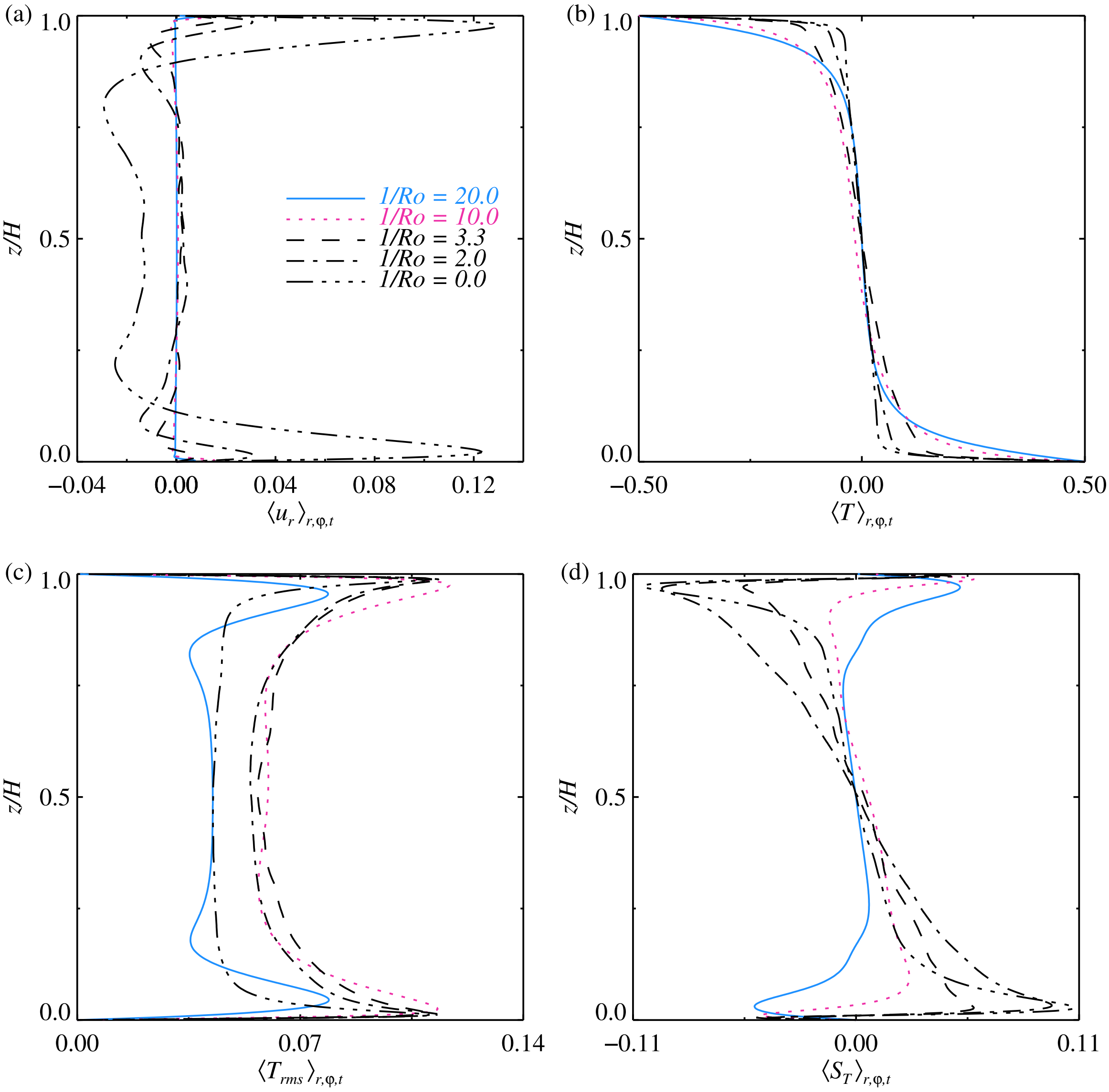

FIGURE 4.3: Temporally, radially and azimuthally averaged profiles of (a) the radial velocity component u_r, (b) the temperature T, (c) the rms temperature T_{rms} and (d) the skewness of the temperature S_T for $Ra = 10^8$. The radial averaging was performed for $0 \leqslant r \leqslant 0.9R$. In all figures $1/Ro = 20.0$ is indicated by a blue solid line, $1/Ro = 10.0$ by a dotted pink line, $1/Ro = 3.3$ by a short-dashed black line, $1/Ro = 2.0$ by a dash-dotted black line and $1/Ro = 0.0$ by dash-triple-dotted black line.

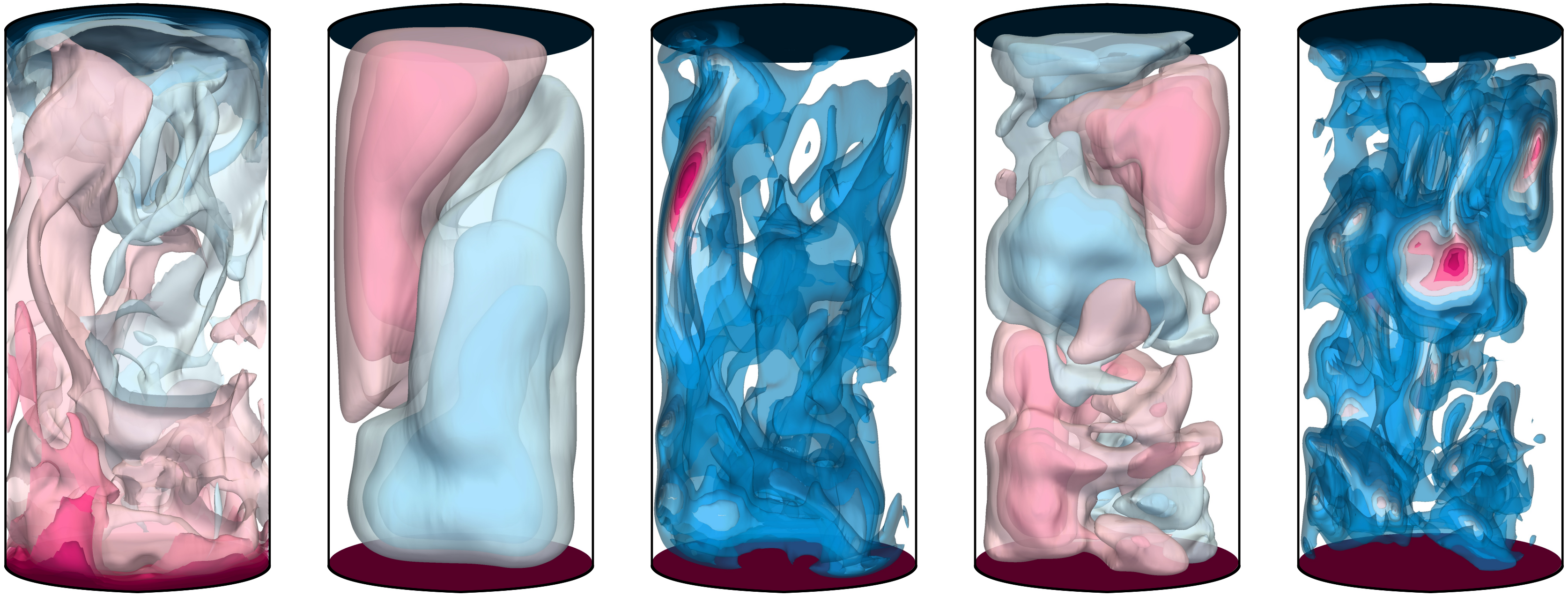

(a) T (b) ξ (c) e_{pol} (d) ψ (e) e_{tor}

FIGURE 4.4: Instantaneous flow structures for $Ra = 10^8$ and $1/Ro = 0$, i.e. without rotation. Shown are twelve isosurfaces that are equidistantly distributed between the interval boundaries. Colour scale ranges from blue (the smallest value) through white to pink (the largest value). (a) Temperature $T \in [-0.5, 0.5]$, (b) poloidal potential $\xi \in [-0.04, 0.04]$, (c) poloidal energy $e_{pol} \in [0, 0.76]$, (d) toroidal potential $\psi \in [-0.13, 0.13]$, (e) toroidal energy $e_{tor} \in [0, 0.27]$.

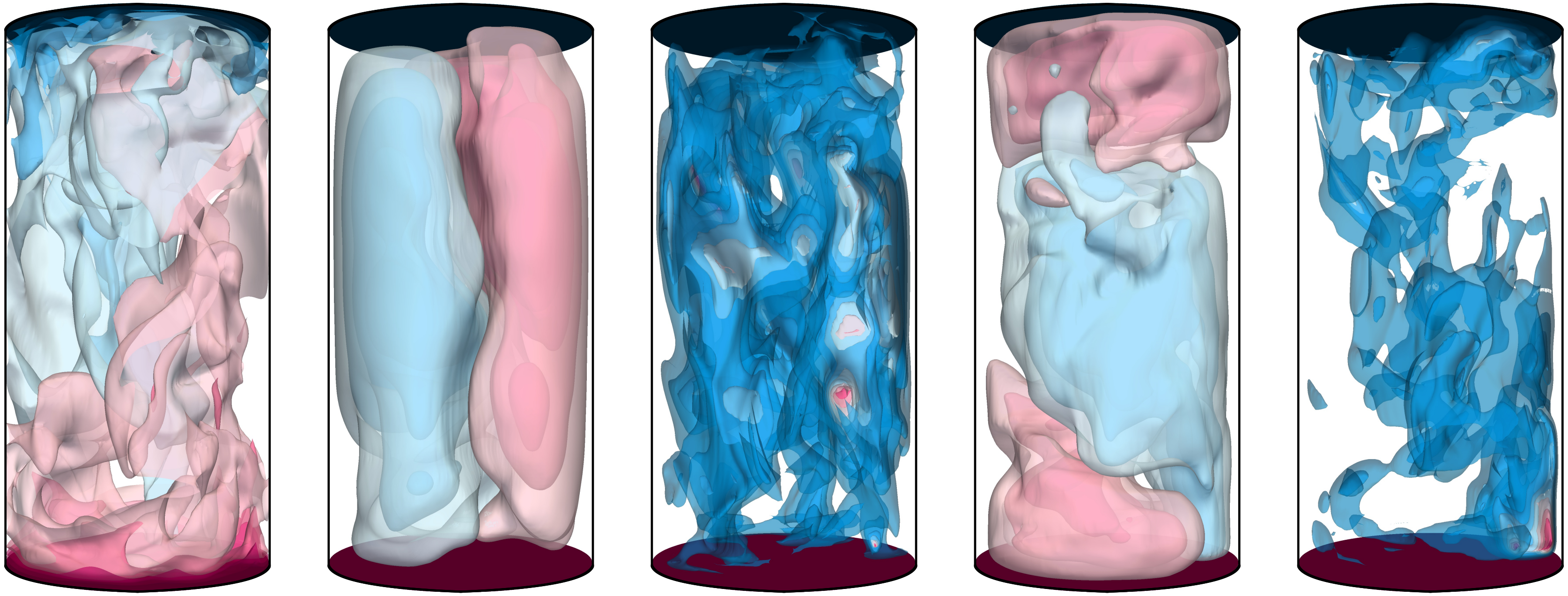

(a) T (b) ξ (c) e_{pol} (d) ψ (e) e_{tor}

FIGURE 4.5: As in figure 4.4, but for $1/Ro = 2.0$. (a) Temperature $T \in [-0.5, 0.5]$, (b) poloidal potential $\xi \in [-0.03, 0.03]$, (c) poloidal energy $e_{pol} \in [0, 0.70]$, (d) toroidal potential $\psi \in [-0.16, 0.16]$, (e) toroidal energy $e_{tor} \in [0, 0.74]$.

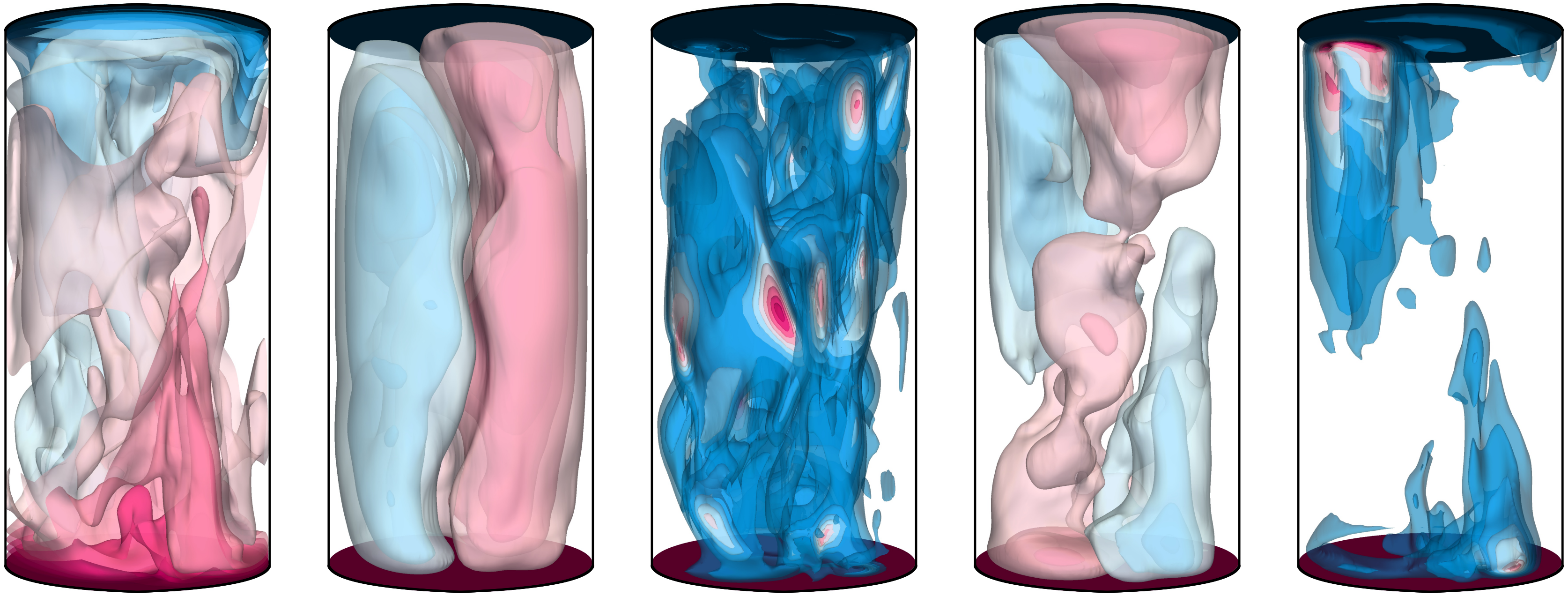

(a) T (b) ξ (c) e_{pol} (d) ψ (e) e_{tor}

FIGURE 4.6: As in figure 4.4, but for $1/\mathrm{Ro} = 3.3$. (a) Temperature $T \in [-0.5, 0.5]$, (b) poloidal potential $\xi \in [-0.02, 0.02]$, (c) poloidal energy $e_{pol} \in [0, 0.27]$, (d) toroidal potential $\psi \in [-0.21, 0.21]$, (e) toroidal energy $e_{tor} \in [0, 0.77]$.

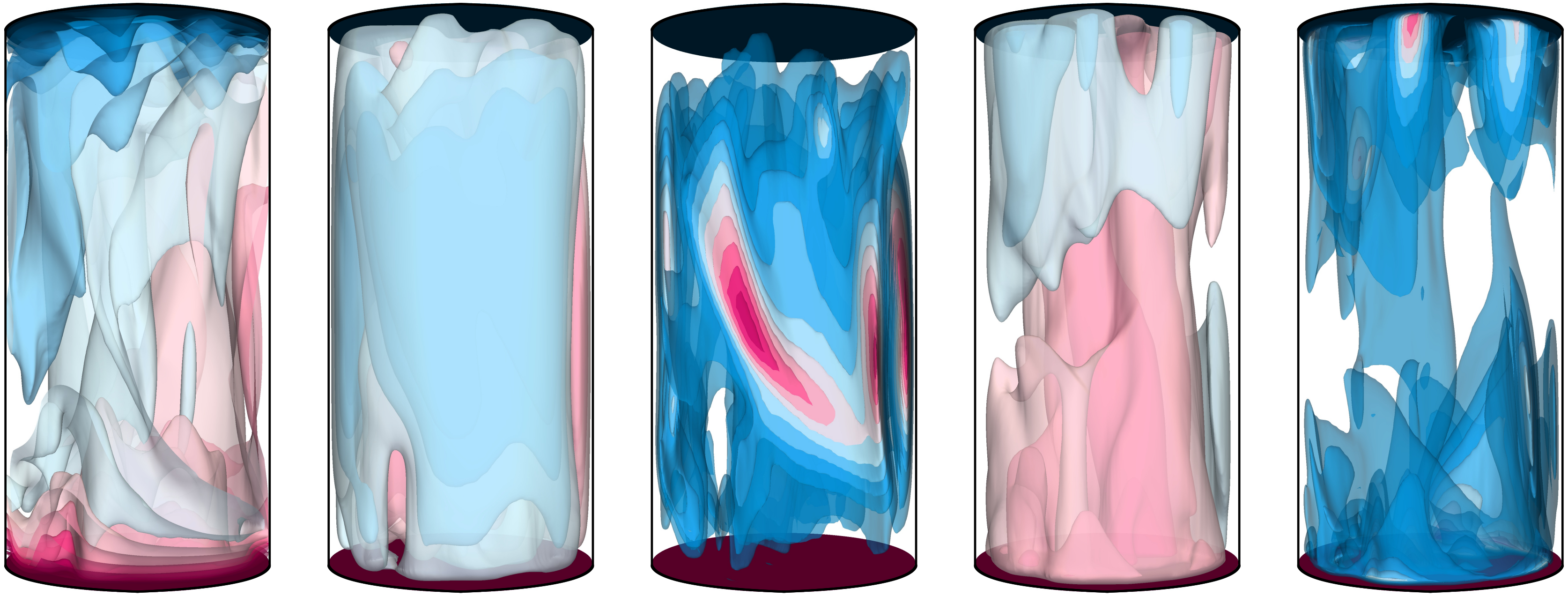

(a) T (b) ξ (c) e_{pol} (d) ψ (e) e_{tor}

FIGURE 4.7: As in figure 4.4, but for $1/Ro = 10.0$. (a) Temperature $T \in [-0.5, 0.5]$, (b) poloidal potential $\xi \in [-0.003, 0.003]$, (c) poloidal energy $e_{pol} \in [0, 0.12]$, (d) toroidal potential $\psi \in [-0.11, 0.11]$, (e) toroidal energy $e_{tor} \in [0, 0.22]$.

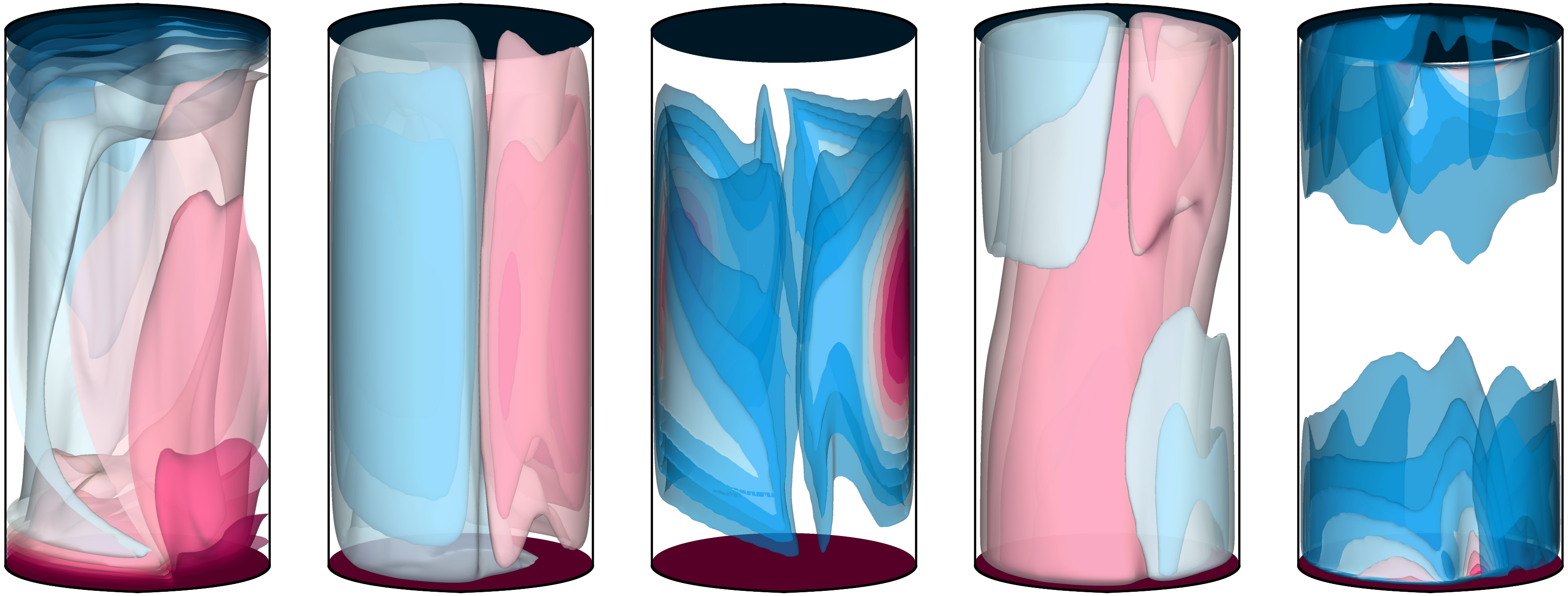

(a) T (b) ξ (c) e_{pol} (d) ψ (e) e_{tor}

FIGURE 4.8: As in figure 4.4, but for $1/Ro = 20.0$. (a) Temperature $T \in [-0.5, 0.5]$, (b) poloidal potential $\xi \in [-0.001, 0.001]$, (c) poloidal energy $e_{pol} \in [0, 0.05]$, (d) toroidal potential $\psi \in [-0.03, 0.03]$, (e) toroidal energy $e_{tor} \in [0, 0.09]$.

In the non-rotating case, $1/\mathrm{Ro} = 0.0$, the flow is most of the time organised in an LSC. This structure is not only visible in the temperature field T but also in the poloidal potential ξ and energy e_{pol}. The toroidal potential ψ shows a rather chaotic structure and the toroidal energy e_{tor} is concentrated in the bulk and of lower magnitude than e_{pol}. If the flow was two-dimensional and independent from one horizontal direction then it would be completely poloidal. However, since the toroidal energy is associated with the vortices in the flow, the toroidal field acts in a destabilising way on the flow and tears the plumes apart. On the other hand, when the convection cell is rotated, the toroidal field has a stabilising effect. With increasing rotation rate, as seen in the figures 4.5–4.8, the flow resembles a horizontally two-dimensional flow. But a two-dimensional flow independent from the vertical direction is fully toroidal. This means that with increasing $1/\mathrm{Ro}$ the toroidal energy increases and the poloidal energy decreases. Instead of an LSC, there are elongated flow structures emerging from the edge of the boundary layers, that are visible in the temperature field and in the toroidal potential ψ and energy e_{tor}. The highest toroidal energy is contained in these short columnar-like vortices seen in figure 4.6 and 4.7. For even more rapid rotation, at $1/\mathrm{Ro} = 20.0$, which is close to the onset of convection, wall modes dominate and both the poloidal and toroidal energy are highest close to the sidewall. Hence, the toroidal and poloidal energy can be used to characterize the different types of dynamics in rotating Rayleigh–Bénard convection.

In figure 4.9 also the temporal evolution of e_{kin}, e_{pol} and e_{tor} is shown. Indeed for $1/\mathrm{Ro} = 0.0$ and $1/\mathrm{Ro} = 2.0$ holds $e_{\mathrm{pol}} > e_{\mathrm{tor}}$ for all instances of time, while for $1/\mathrm{Ro} = 10.0$ and $1/\mathrm{Ro} = 20.0$ it is $e_{\mathrm{pol}} < e_{\mathrm{tor}}$. For $1/\mathrm{Ro} = 3.3$, e_{pol} and e_{tor} are of the same order. Furthermore, the oscillation frequency tends to decrease with increasing $1/\mathrm{Ro}$.

To analyse these observations quantitatively, the volume- and time-averaged energies are shown in figure 4.10 for all conducted simulations. Similar as in figure 4.2 (a), they are also compared with $1/\mathrm{Ro}_b$ suggested by Weiss et al. (2010) and Weiss and Ahlers (2011b) and the empirically found $1/\mathrm{Ro}_1$ and $1/\mathrm{Ro}_2$ by Ecke and Niemela (2014).

The DNS data share some common features for all Rayleigh numbers. All energies e_{kin}, e_{pol} and e_{tor} are independent of $1/\mathrm{Ro}$ up to approximately $1/\mathrm{Ro}_b = 0.86$. At this point, e_{kin} and e_{pol} decrease monotonically. On the contrary, e_{tor} increases at this point, then reaches a maximum and after that drops with increasing $1/\mathrm{Ro}$. It reaches the same value as in the non-rotating case at $1/\mathrm{Ro}_2 \approx 8.33$.

For the relatively low Rayleigh numbers $\mathrm{Ra} = 10^5$ and $\mathrm{Ra} = 10^6$, the toroidal energy is always lower than the poloidal energy, despite the fact that it can be up to about eight and three times higher, respectively, compared to the non-rotating case as it is recognizable in figure 4.10(a)–(d). As a consequence, the poloidal field is for all rotation rate able to sustain cellular-like flow structures. Since for $\mathrm{Ra} = 10^5$ convection is steady for all $1/\mathrm{Ro}$, the standard deviation σ is zero. For $\mathrm{Ra} = 10^6$, convection is unsteady for $0 \leqslant 1/\mathrm{Ro} \lesssim 1.67$ and due to the small computational mesh, DNS for several thousands of time units could be performed. Hence, the large error bars in figure 4.10(b) and (d) indicate physical variations and not a lack

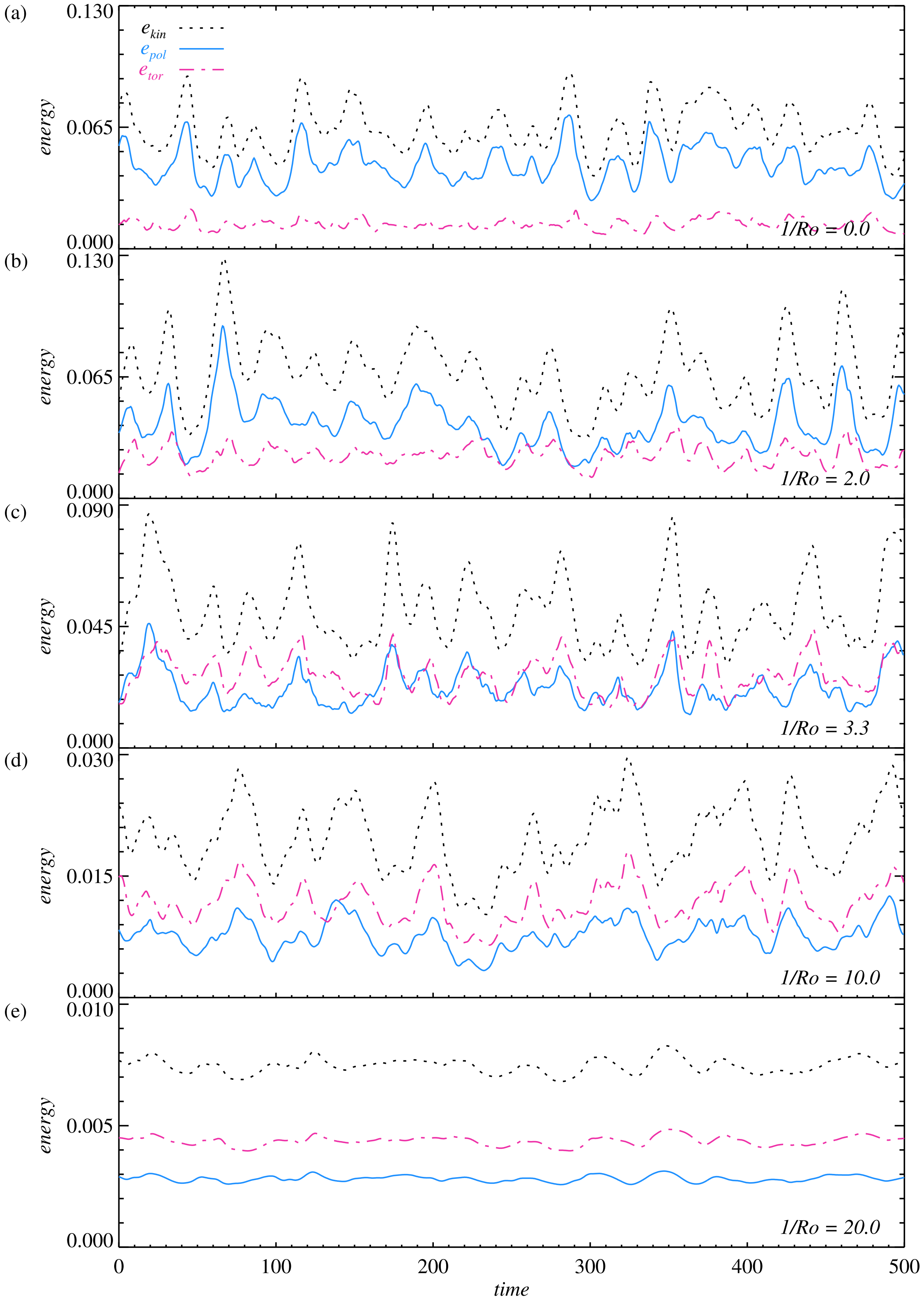

FIGURE 4.9: Times series of the volume-averaged kinetic energy e_{kin} (black dotted line), the poloidal energy e_{pol} (blue solid line) and the toroidal energy e_{tor} (pink dash-dotted line) for $Ra = 10^8$ and (a) $1/Ro = 0.0$, (b) $1/Ro = 2.0$, (c) $1/Ro = 3.3$, (d) $1/Ro = 10.0$, (e) $1/Ro = 20.0$.

The time is measured in dimensionless time-units (see main text), and all time series were deliberately set to zero at a point when statistical equilibrium was reached.

of statistics. In the range $1.67 \lesssim 1/Ro \lesssim 2.5$, when the convective heat transport is oscillatory, σ decreases with increasing $1/Ro$. The oscillatory behaviour is naturally present in the time series of e_{kin}, e_{pol} and e_{tor}. For even larger $1/Ro$, we found steady convection, in a sense that the Nusselt number does not change in time. Interestingly, at the transition between oscillatory and steady convection, there is a minimum in the toroidal energy and this point also coincides with $1/Ro_1$.

For $Ra = 10^7$ turbulent convection is observed for all considered $1/Ro$, except for the highest rotation rate $1/Ro = 14.1$, where convection is steady. But in this case, presented in 4.10(e) and (f), the toroidal energy is higher than the poloidal energy for $1/Ro$ being greater than a critical inverse Rossby number $1/Ro_{crit}$. This critical inverse Rossby number is hence determined by the condition

$$\frac{1}{Ro_{crit}} = \left.\frac{1}{Ro}\right|_{e_{pol}=e_{tor}} . \tag{4.5.1}$$

I argue, that only if toroidal motions are prevailing, i.e. $e_{tor} > e_{pol}$, one can speak of rotation dominated convection. If, on the other side, poloidal motions, i.e. $e_{tor} < e_{pol}$, are predominant then buoyancy is more important. If $e_{tor} > e_{pol}$, the LSC or other roll-like structures cease to exist and instead columnar vortices become apparent. Thus, this clarifies the change of behaviour, observed in the global flow properties presented in figure 4.3 and discussed in the previous section. Furthermore, these findings are also in agreement with those by other authors (Kunnen et al., 2008; Stevens et al., 2012, 2013b) that relate the breakdown of the large-scale circulation to the regime of rotation dominance. They also shed some more light on the fact, why not only the inverse Rossby number but also the Rayleigh number has to be sufficiently high to be in a rotation dominated regime (Ecke and Niemela, 2014; Julien et al., 2012). The behaviour of e_{kin}, e_{pol} and e_{tor} with $1/Ro$ at $Ra = 10^8$ and $Ra = 10^9$, displayed in figure 4.10(g)–(j), is very similar to that of $Ra = 10^7$, but the maximum relative enhancement of the toroidal energy compared to the non-rotating case is diminished with higher Ra. Nonetheless, in these cases the crossover of the poloidal and toroidal energy is more pronounced, in a sense that the difference between e_{tor} and e_{pol} is larger at rapid rotation.

To determine the transition point more accurately, the ratio of the toroidal to the total kinetic energy e_{tor}/e_{kin} and the ratio of the poloidal to the total kinetic energy e_{pol}/e_{kin} are shown in figure 4.11. Besides, the ratios e_{tor}/e_{kin} and e_{pol}/e_{kin} are known to be properties of the flow characterizing the different types of dynamics in non-rotating Rayleigh–Bénard convection (Breuer et al., 2004) and I argue that the same is true for rotating Rayleigh–Bénard convection.

Figure 4.11 reveals various information. First of all, the critical inverse Rossby number is about $1/Ro_{crit} \approx 3.0$ or more accurately it lies in the range $2.36 \lesssim 1/Ro_{crit} \lesssim 3.33$. At this point, both the poloidal and the toroidal energy are about 50% of the total kinetic energy. From the equations (4.3.2)–(4.3.4) and (4.3.15)–(4.3.17) it is obvious that not all of the kinetic energy is contained in the toroidal and poloidal part,

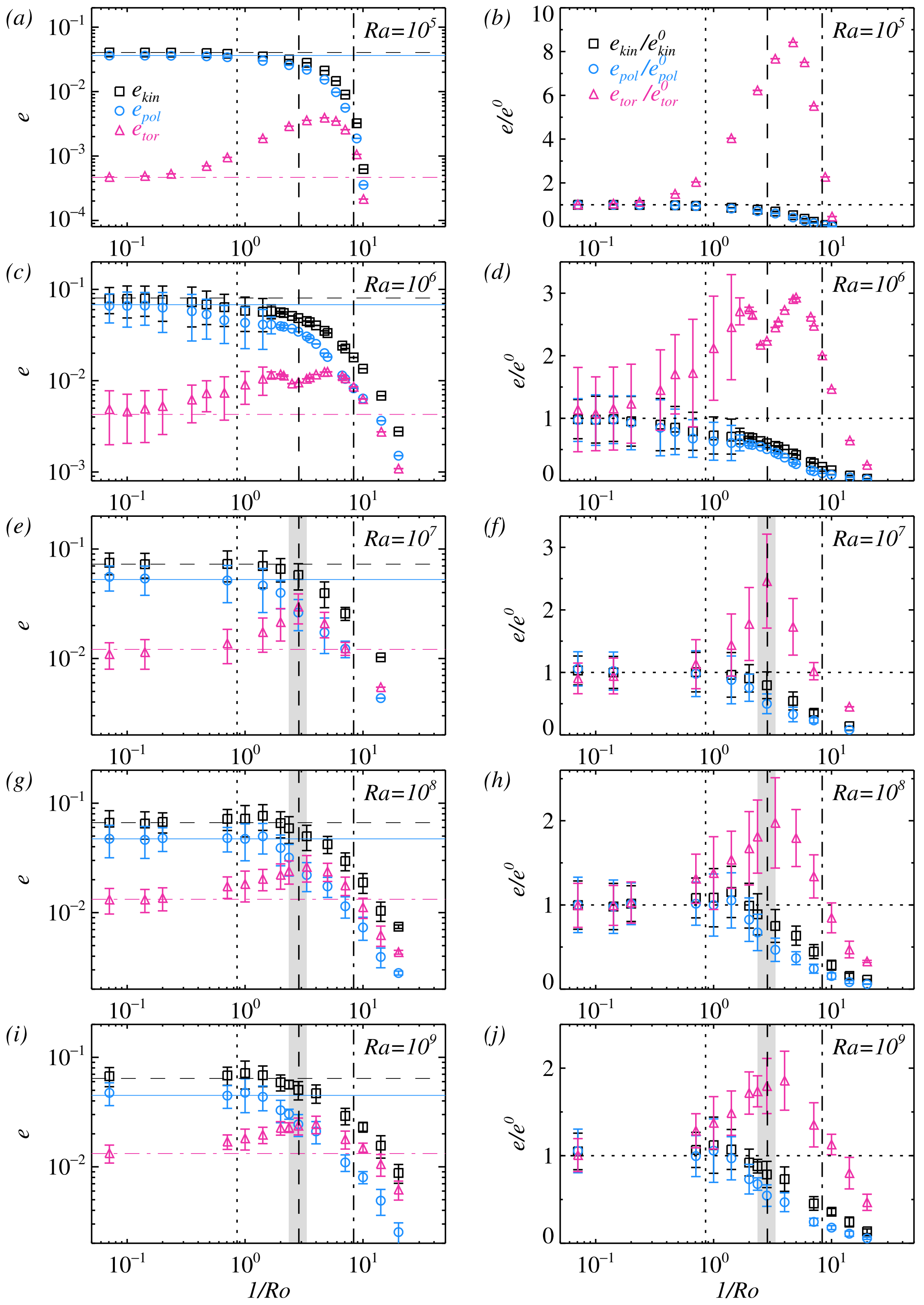

FIGURE 4.10: Left panel: Volume- and time-averaged kinetic energy e_{kin} (black squares and dashed line), poloidal energy e_{pol} (blue circles and solid line) and toroidal energy e_{tor} (pink triangles and dash-dotted line) as function of $1/Ro$. The horizontal lines indicate the value in the non-rotating case. Right panel: Volume- and time-averaged kinetic energies normalised

by their value in the non-rotating case. The vertical dotted line shows prediction by Weiss and Ahlers (2011b); Weiss et al. (2010), $1/\mathrm{Ro}_b = 0.86$, the vertical long-dashed and dashed-dotted line mark the proposed transition by Ecke and Niemela (2014) at $1/\mathrm{Ro}_1 \approx 2.86$ and $1/\mathrm{Ro}_2 \approx 8.33$, respectively. The grey shaded area indicates where $e_{pol} \approx e_{tor}$ at $2.36 \lesssim 1/\mathrm{Ro}_{crit} \lesssim 3.33$. The error bars show the standard deviation σ of the averaged values.

since

$$e_{kin} \neq e_{pol} + e_{tor}. \tag{4.5.2}$$

However, as can be readily seen from figure 4.11, the sum of e_{tor} and e_{pol} is for all cases about 90% of the total kinetic energy, indicating that the single components of the toroidal and poloidal field are almost uncorrelated.

At small inverse Rossby numbers, $1/\mathrm{Ro} \lesssim 1$ and also in non-rotating convection, the poloidal energy decreases, and the toroidal energy increases with the Rayleigh number. Without rotation, at $\mathrm{Ra} = 10^5$ about 90% of the kinetic energy is contained in the poloidal energy and only about 1% in the toroidal energy. At $\mathrm{Ra} = 10^9$ only about 70% of the kinetic energy is contained in the poloidal motion and 20% in the toroidal energy. This is not surprising, because the higher Ra the higher the number of plumes. Hence, there is an increased shearing and swirling in the flow that is associated with a vertical vorticity and a higher e_{tor}. Consequently, e_{pol} has to decrease. This is also related to the picture of a less strong LSC at higher Ra. With increasing $1/\mathrm{Ro}$ one has to distinguish between the steady cases $\mathrm{Ra} = 10^5$ and 10^6

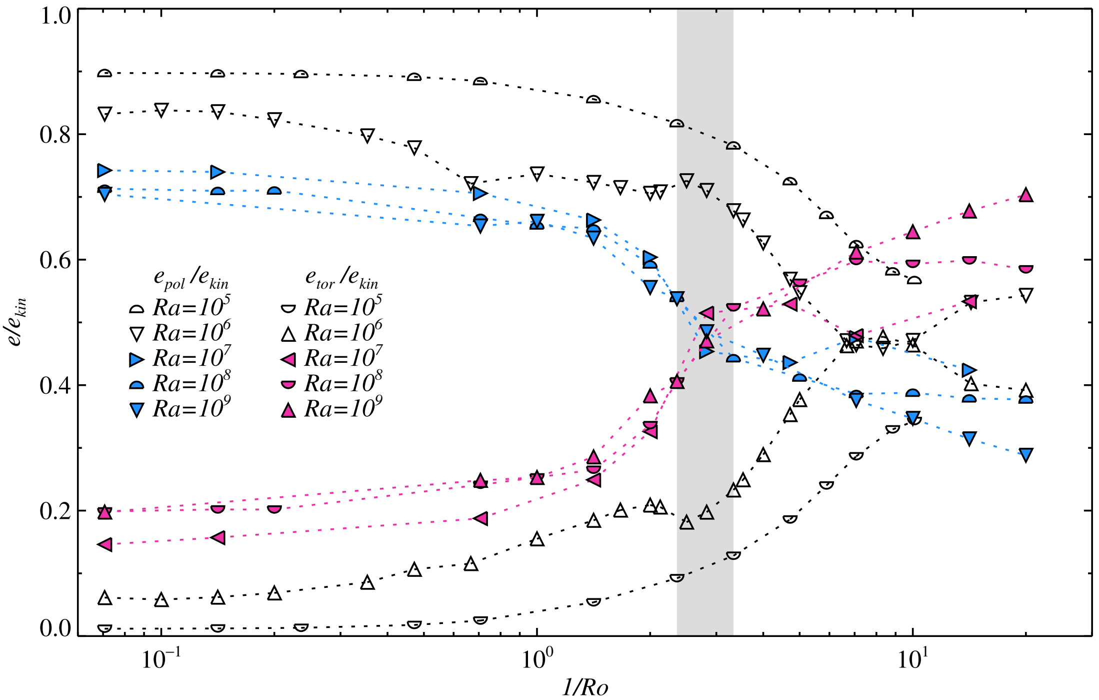

FIGURE 4.11: Poloidal and toroidal energy as fraction of the total kinetic energy versus $1/\mathrm{Ro}$. The grey shaded area shows the approximate range where $e_{pol} = e_{tor}$ at $2.4 \lesssim 1/\mathrm{Ro}_{crit} \lesssim 3.3$.

and the turbulent cases $10^7 \leqslant \mathrm{Ra} \leqslant 10^9$. At intermediate inverse Rossby numbers, $1 \lesssim 1/\mathrm{Ro} \lesssim 5$, $e_{\mathrm{tor}}/e_{\mathrm{kin}}$ and $e_{\mathrm{pol}}/e_{\mathrm{kin}}$ collapse at approximately the same value for $10^7 \leqslant \mathrm{Ra} \leqslant 10^9$, unlike for 10^5 and 10^6. Between $7 \lesssim 1/\mathrm{Ro} \lesssim 10$ the two data sets of $\mathrm{Ra} = 10^6$ and 10^7 cling to each other, however, for $\mathrm{Ra} = 10^6$, $e_{\mathrm{tor}}/e_{\mathrm{kin}}$ drops afterwards to a value of about 0.4 at $1/\mathrm{Ro} = 20.0$ and $e_{\mathrm{pol}}/e_{\mathrm{kin}}$ raises again to a value of about 0.55. On the contrary, $e_{\mathrm{tor}}/e_{\mathrm{kin}}$ increases further to 0.53 and $e_{\mathrm{pol}}/e_{\mathrm{kin}}$ decreases to 0.42 at $1/\mathrm{Ro} = 14.1$ for $\mathrm{Ra} = 10^7$. Thus, there is a clear distinction between non-turbulent and turbulent rotating Rayleigh–Bénard convection. Like this, at large inverse Rossby numbers, $1/\mathrm{Ro} \gtrsim 5$, the data show a larger spread depending on the Rayleigh number. At $1/\mathrm{Ro} \gtrsim 14$, $\mathrm{Ra} = 10^5$ is in the conducting state, hence e_{tor}, e_{pol} and e_{kin} are zero. The relative toroidal energy is highest for $\mathrm{Ra} = 10^9$, being about 70% of the kinetic energy and the poloidal energy is lowest for the very same Ra, being about 29% at $1/\mathrm{Ro} = 20.0$.

Another way of collapsing the data has been suggested by Ecke and Niemela (2014) choosing the quantity $\mathrm{Ra}\mathrm{Ek}^{7/4} = \mathrm{Ra}^{1/8}\mathrm{Pr}^{7/8}\mathrm{Ro}^{7/4}$ instead of $1/\mathrm{Ro}$. This implies a dependence on Ra and Pr, and indeed figure 2.4 (a) reveals that the collapse of the critical point where the toroidal and poloidal energy are equal is even better. The in this way determined crossover happens in the range $1 \leqslant \mathrm{Ra}\mathrm{Ek}^{7/4} \leqslant 2$ or at $\mathrm{Ra}\mathrm{Ek}^{7/4} \approx 1.5$, respectively. This quantity was also found to be a suitable scaling variable in water with $\mathrm{Pr} = 7$ (King et al., 2009), although it was corrected to $\mathrm{Ra}\mathrm{Ek}^{3/2}$ later on (King et al., 2012). However, the latter does not fit to the data. A better agreement of the Nu behaviour for all Ra (except for the particularities occurring at $\mathrm{Ra} = 10^6$) when plotted against $\mathrm{Ra}\mathrm{Ek}^{7/4}$ is also true and had already been found by Ecke and Niemela (2014). It is presented in figure 2.4 (b).

4.6 Summary

Rotating Rayleigh–Bénard convection of a fluid with a Prandtl number of $\mathrm{Pr} = 0.8$ in a slender cylinder with an aspect ratio of $\Gamma = 0.5$ was studied in the Rayleigh number range $10^5 \leqslant \mathrm{Ra} \leqslant 10^9$. The rotation rate was varied between the inverse Rossby numbers 0 and 20. Depending on the rotation rate, the general flow phenomenology changes, and with it certain flow characteristics, such as the temperature, the radial velocity, the rms temperature and the skewness of the temperature. These changes are not clearly present in the behaviour of the Nusselt number Nu even though also there different scalings depending on $1/\mathrm{Ro}$ are observed (Ecke and Niemela, 2014). To identify these regime transitions, I decomposed the velocity field into its toroidal and poloidal scalar field, and analysed the contribution of e_{tor} and e_{pol} to the total kinetic energy e_{kin}. Evaluating regime transitions by means of e_{tor} and e_{pol} has the advantage that it bases on global quantities which are characteristic for the flow in rotating and in non-rotating turbulent thermal convection. The poloidal energy is associated with all cellular-like structures, such as the LSC or multiple roll state, i.e. the flow typically observed in non-rotating convection. The toroidal energy is associated with the vertical vorticity and hence with columnar vortices, typical in rotating convection. Hence, this method is expected to work independently of the aspect ratio and of the Prandtl number and forthcoming studies with different Γ and Pr are to be conducted, to reinforce this idea.

In the present DNS four different regimes can be identified with the proposed method. As long as e_{tor} has the same value as in the non-rotating case, i.e. $e_{tor}/e^0_{tor} = 1$, the flow is completely dominated by buoyancy. As soon as the toroidal energy relative to the non-rotating case increases, $e_{tor}/e^0_{tor} > 1$, Rayleigh–Bénard convection is considered to be rotation influenced. This agrees well with the bifurcation point found by Weiss et al. (2010) and Weiss and Ahlers (2011b), which gives $1/Ro_b = 0.86$ for a cylindrical $\Gamma = 0.5$ cell. At a rotation rate where the toroidal energy is greater than the poloidal one, convection is rotation dominated and large-scale roll structures, such as the LSC, are expected to cease to exist and instead columnar vortex structures dominate the flow. To reach this regime, however, the Rayleigh number has to be at least about 10^7. The critical inverse Rossby number is thus determined by the condition $e_{pol} = e_{tor}$ which gives $1/Ro_{crit} = 1/Ro|_{e_{pol}=e_{tor}} \approx 3$ $(2.36 \lesssim 1/Ro_{crit} \lesssim 3.33)$ for the cases considered. Finally, when the toroidal energy drops below the value of the non-rotating case, $e_{tor}/e^0_{tor} < 1$ one reaches the regime of geostrophic turbulence. The last two in this way determined transitions agree well with the ones found by Ecke and Niemela (2014), who identify them by a different scaling behaviour of Nu, finding $1/Ro_1 \approx 2.86$ and $1/Ro_2 \approx 8.33$. An even better collapse of data for the Nusselt number and the toroidal and poloidal energy for all Ra considered can be obtained by using $RaEk^{7/4}$ instead of $1/Ro$ as scaling variable, yielding $1.0 \lesssim RaEk^{7/4}_{crit} \lesssim 2.0$ for the critical rotation rate where $e_{pol} \approx e_{tor}$.

NON-OBERBECK–BOUSSINESQ EFFECTS IN RAYLEIGH–BÉNARD CONVECTION OF LIQUIDS*

The influence of temperature-dependent material properties on Rayleigh–Bénard convection is investigated in three different liquids, ranging from a very small Prandtl number for mercury with $Pr = 0.0232$, over a moderate one for water with $Pr = 4.38$, to a very large one for glycerol with $Pr = 2547.9$. For this purpose, I performed three-dimensional DNS in a cylindrical cell with a unity aspect ratio. Local quantities such as the viscous and thermal boundary layer thicknesses, the centre temperature and the wind velocity show a breakdown of the top-bottom symmetry. One of the major objectives of NOB studies is to understand and quantify these asymmetries.

5.1 The validity range of the Oberbeck–Boussinesq approximation according to Gray & Giorgini on the example of mercury, glycerol and water

In the following, I exemplary apply the method by Gray and Giorgini (1976) to calculate the validity range of the OB approximation as introduced in section 2.2.5 to three particular fluids, which significantly distinguish themselves through their different Prandtl numbers. Namely, glycerol with $Pr = 2547.9$, water with $Pr = 4.38$ and mercury with $Pr = 0.232$, all at an arithmetic mean temperature of $T_m = 40\,^\circ\mathrm{C}$. The maximal requested residual error is 10 %, i.e. the absolute value of all ϵ_i is to be smaller than 0.1.

The material properties of glycerol and water were given in terms of polynomials of order i of the temperature by Ahlers et al. (2006). This means their functional dependency is described by

$$\frac{X - X_m}{X_m} = \sum_i a_i (T - T_m)^i, \qquad X \in \{\rho, \kappa, c_p, \nu, \alpha, \Lambda\} \tag{5.1.1}$$

---

*Parts of this chapter have been adopted from HORN, S., SHISHKINA, O. AND WAGNER, C., Non-Oberbeck–Boussinesq effects in Rayleigh–Bénard convection of liquids, *Turbulence and Interactions, Springer* (2014), 99–105; HORN, S., SHISHKINA, O. AND WAGNER, C., On non-Oberbeck–Boussinesq effects in three-dimensional Rayleigh–Bénard convection in glycerol, *J. Fluid Mech. 724* (2013), 175–202; and HORN, S. AND SHISHKINA, O., Rotating non-Oberbeck–Boussinesq Rayleigh–Bénard convection, *Phys. Fluids 26(5)* (2014), 055111.

with certain prefactors a_i. X stands for the various material properties, i.e. the density ρ, the heat diffusivity κ, the specific heat capacity c_p, the kinematic viscosity ν, the isobaric expansion coefficient α and the heat conductivity Λ. However, the given polynomial for ν was not sufficient, since it led to negative viscosities for $T \gtrsim 70$°C. Thus, I performed a least squares polynomial fit on the data from Segur and Oberstar (1951) ranging from 0 °C to 100 °C. The mean values at $T_m = 40\,$°C and the coefficients a_i were given in table 5.1 for glycerol and in table 5.2 for water, respectively. Mercury's material properties were taken from Bobkov et al. (2008):

$$\begin{aligned}
\rho\,[\mathrm{kg\,m^{-3}}] &= 13595.0\big(1.0 - 1.8144\times10^{-4}(T-T_0) \\
&\quad -7.016\times10^{-9}(T-T_0)^2 - 2.8625\times10^{-11}(T-T_0)^3 \\
&\quad -2.617\times10^{-14}(T-T_0)^4\big), && (5.1.2)\\
c_p\,[10^3\mathrm{J\,kg^{-1}\,K^{-1}}] &= 0.1508 - 6.630\times10^{-5}(T-T_0) + 6.4185\times10^{-8}(T-T_0)^2 \\
&\quad +0.8049(T-T_0)^{-1}, && (5.1.3)\\
\alpha\,[10^{-4}\mathrm{K^{-1}}] &= 1.8144 + 7.016\times10^{-5}T + 2.8625\times10^{-7}T^2 \\
&\quad +2.617\times10^{-10}T^3, && (5.1.4)\\
\Lambda\,[\mathrm{W\,m^{-1}\,K^{-1}}] &= 8.178 + 1.36\times10^{-2}T - 6.378\times10^{-6}T^2, && (5.1.5)\\
\kappa\,[\mathrm{m^2\,s^{-1}}] &= \frac{\Lambda}{\rho\,c_p}, && (5.1.6)\\
\nu\,[\mathrm{m^2\,s^{-1}}] &= \frac{0.31\times10^{-3}T^{0.07939} * \exp\left(\frac{341.13}{T}\right)}{\rho}, && (5.1.7)
\end{aligned}$$

where T is the temperature in Kelvin and $T_0 = 273.15\,$K.

The deviation of the material properties from their values at T_m is shown in figure 5.1(a) for glycerol, in figure 5.2(a) for water and in figure 5.3(a) for mercury the range between 0 °C and 80 °C.[†] By looking at the actual temperature dependencies of the material properties of the fluids it is intuitively clear, that the OB approximation is least applicable in the case of glycerol, and probably valid for a great range of temperatures in the case of mercury. This is especially evident for the variation of the viscosity ν, yielding the very different scales on the ordinate for the three fluids. But the aforementioned functional dependencies enables one to calculate the validity range of the OB approximation explicitly.

Glycerol only exhibits a strongly temperature-dependent viscosity, while all the other thermophysical properties are virtually constant. This suggests that NOB effects occur already at small Δ. Indeed, the validity range diagram according to Gray & Giorgini Gray and Giorgini (1976), presented in figure 5.1(b), confirms it, showing that the maximal admissible temperature difference is $\Delta = 0.044\,$K. It also shows that the maximal attainable Rayleigh number $\mathrm{Ra} = \alpha_m g \Delta H^3/(\kappa_m \nu_m)$ under OB conditions is 3.9×10^9. For water, the variation of the material properties is much weaker, however, the variation in ν and α is of the same strength, and also the variation in Λ and κ, respectively, is not negligible. The validity range presented

---

[†] Strictly speaking, the polynomials were not valid in the case of water for temperature values around 4 °C due to its density anomaly. Hence, I did not conduct water simulations for temperatures below 10 °C.

in figure 5.2(b) shows that OB conditions are limited to $\Delta < 0.268\,\mathrm{K}$. Finally, mercury has almost constant material properties, and thus NOB effects are only to be expected for larger Δ, as shown in figure 5.3(b). It should also be noted, than for none of the fluids, the $\alpha\Delta$ criterion is the crucial one.

	$\rho\,[10^3\,\mathrm{kg\,m^{-3}}]$	$c_p\,[10^3\,\mathrm{J\,kg^{-1}\,K^{-1}}]$	$\alpha\,[10^{-4}\,\mathrm{K^{-1}}]$	$\Lambda\,[10^{-1}\,\mathrm{W\,m^{-1}\,K^{-1}}]$	$\kappa\,[10^{-6}\,\mathrm{m^2\,s^{-1}}]$	$\nu\,[10^{-6}\,\mathrm{m^2\,s^{-1}}]$
X_m	1.2477	2.5108	4.7893	2.9351	0.0937	238.738
$a_1\,[10^{-4}\,\mathrm{K^{-1}}]$	−4.789	22.511	20.639	3.863	13.858	−771.27
$a_2\,[10^{-6}\,\mathrm{K^{-2}}]$	−0.3795	—	4.664	—	3.913	2746.4
$a_3\,[10^{-8}\,\mathrm{K^{-3}}]$	—	—	1.0757	—	−0.7577	−3257.1
$a_4\,[10^{-9}\,\mathrm{K^{-4}}]$	—	—	2.540	—	—	1513.2
$a_5\,[10^{-10}\,\mathrm{K^{-5}}]$	—	—	—	—	—	−1135.0
$a_6\,[10^{-11}\,\mathrm{K^{-6}}]$	—	—	—	—	—	261.07
$a_7\,[10^{-12}\,\mathrm{K^{-7}}]$	—	—	—	—	—	−18.682

TABLE 5.1: Material properties $X \in \{\rho, c_p, \alpha, \Lambda, \kappa, \nu\}$ of glycerol at a mean temperature of $T_m = 40\,^\circ\mathrm{C}$ and the coefficients of the polynomials (5.1.1). Adopted from Ahlers et al. (2006) and Segur and Oberstar (1951).

	$\rho\,[10^3\,\mathrm{kg\,m^{-3}}]$	$c_p\,[10^3\,\mathrm{J\,kg^{-1}\,K^{-1}}]$	$\alpha\,[10^{-4}\,\mathrm{K^{-1}}]$	$\Lambda\,[\mathrm{W\,m^{-1}\,K^{-1}}]$	$\kappa\,[10^{-6}\,\mathrm{m^2\,s^{-1}}]$	$\nu\,[10^{-6}\,\mathrm{m^2\,s^{-1}}]$
X_m	0.9922	4.1690	3.8810	0.6297	0.1528	0.6690
$a_1\,[10^{-4}\,\mathrm{K^{-1}}]$	−3.736	0.084	195.0	21.99	23.52	−175.9
$a_2\,[10^{-6}\,\mathrm{K^{-2}}]$	−3.98	4.60	−159.8	−17.8	−14.9	295.8
$a_3\,[10^{-8}\,\mathrm{K^{-3}}]$	—	—	207.0	—	—	−460.0

TABLE 5.2: Material properties $X \in \{\rho, c_p, \alpha, \Lambda, \kappa, \nu\}$ of water at a mean temperature of $T_m = 40\,^\circ\mathrm{C}$ and the coefficients of the polynomials (5.1.1). Adopted from Ahlers et al. (2006).

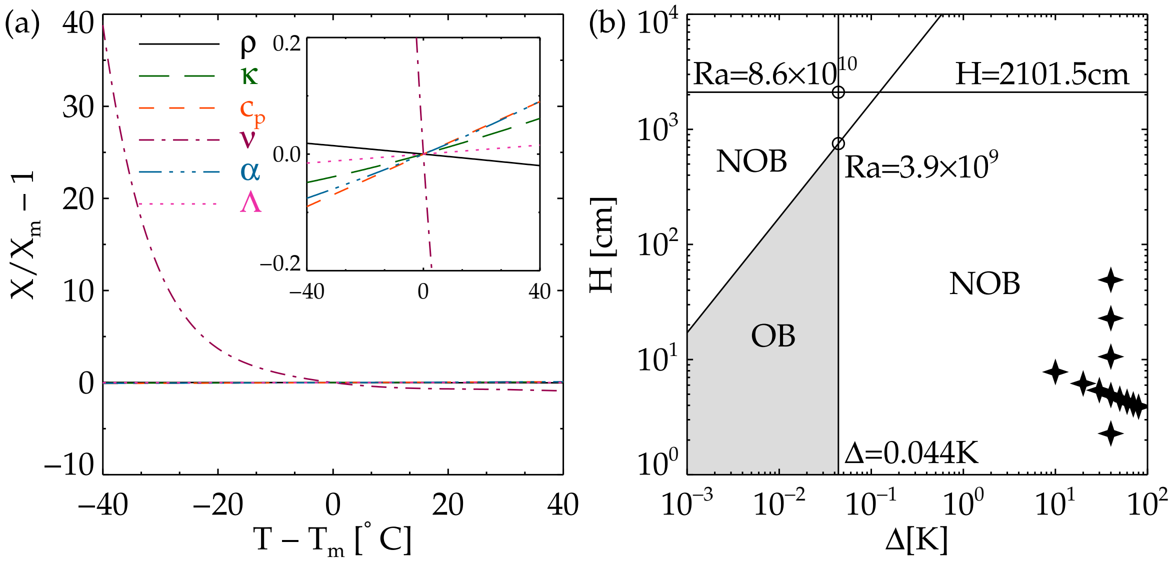

FIGURE 5.1: (a) Relative deviations of glycerol properties X from their values X_m at a mean temperature of $T_m = 40°$, according to Segur and Oberstar (1951) and Ahlers et al. (2006); black solid line: density ρ; green dashed line: thermal diffusivity κ; orange short dashed line: specific heat capacity c_p; purple dashed dotted line: kinematic viscosity ν; blue dashed triple-dotted line: expansion coefficient α; pink dotted line: thermal conductivity Λ. (b) Region of validity of the OB approximation for glycerol at $T_m = 40\,°C$, according to Gray and Giorgini (1976). The grey shaded area shows the parameter range where the OB approximation is valid within a residual error of 10%. The stars denote the NOB DNS data points.

For mercury, I only performed simulations under OB conditions because now significant differences under NOB conditions are to be expected. But the main objective of this work was the investigation of NOB effects, hence, I focused on DNS of Rayleigh–Bénard convection in glycerol and water.

5.2 Non-Oberbeck–Boussinesq effects in glycerol

Trying to understand the particular case of Rayleigh–Bénard convection in glycerol means facing two challenges at the same time. First of all, the standard approach of using the OB approximation is not appropriate here, and second, glycerol has a very high but finite Prandtl number of $Pr = 2547.9$. Thus the inertial forces are small but not negligible, while the momentum is very diffusive.

Thermal convection at large Pr exhibits very different characteristics compared to low and moderate Pr, even without NOB effects. But not much work has been devoted to this. Glycerol has been experimentally investigated by Zhang et al. (1997, 1998), but their experiments were conducted for a large range of Prandtl numbers ($600 \lesssim Pr \lesssim 8000$), a major shortcoming induced by the strongly varying viscosity. However, to draw quantitative conclusions, it is preferable to have a constant Pr. This can be achieved by means of numerical simulations, despite the fact that

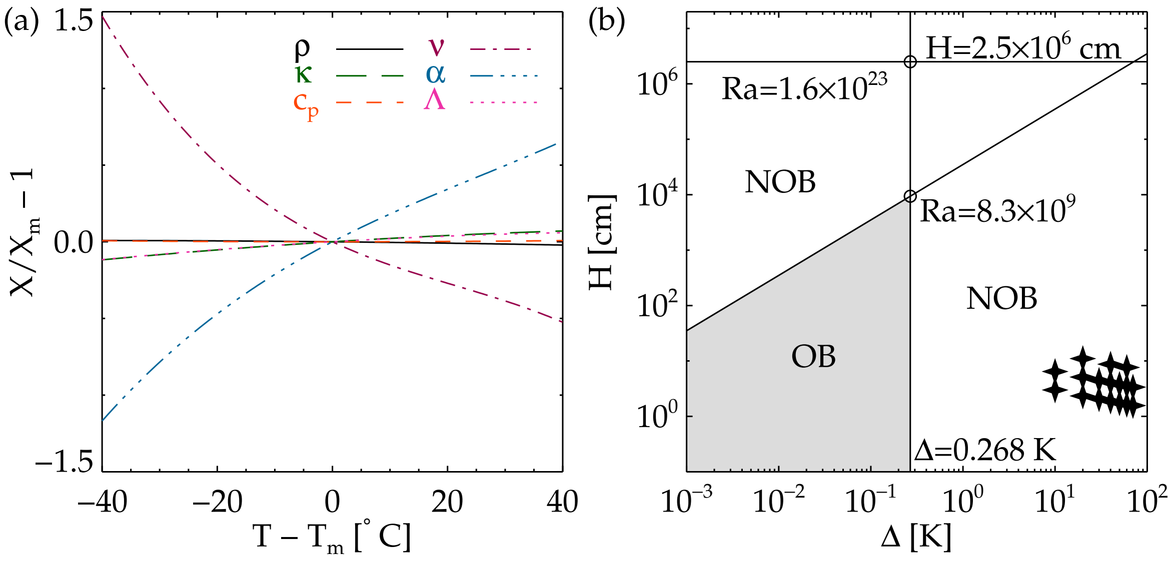

FIGURE 5.2: (a) Relative deviations of water properties X from their values X_m at a mean temperature of $T_m = 40°$, according to Ahlers et al. (2006); the lines are as in figure 5.1. (b) Region of validity of the OB approximation for water at $T_m = 40\,°C$, according to Gray and Giorgini (1976). The grey shaded area shows the parameter range where the OB approximation is valid within a residual error of 10%. The stars denote the NOB DNS data points.

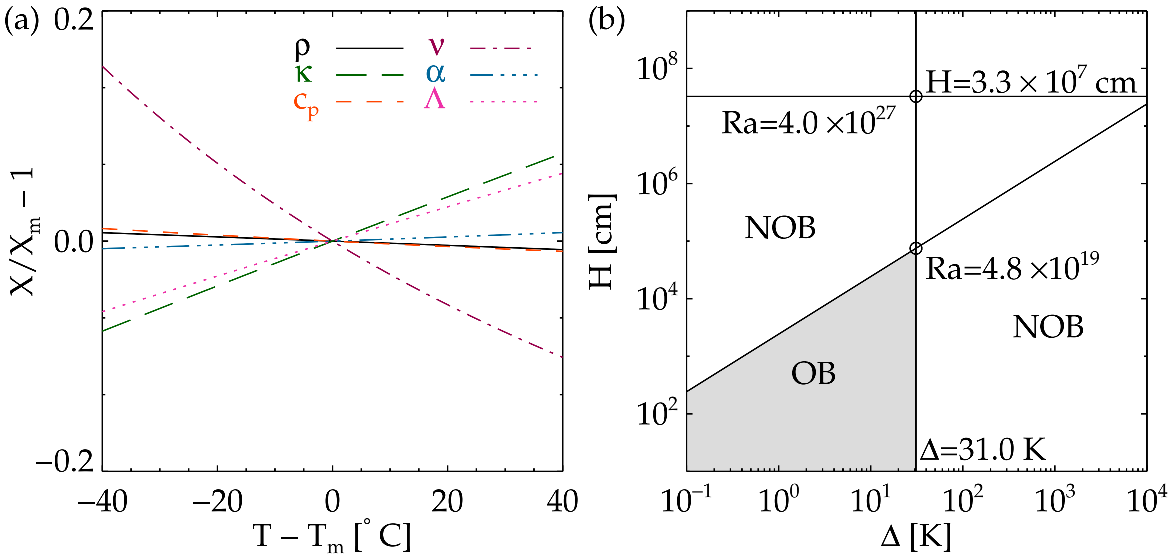

FIGURE 5.3: (a) Relative deviations of mercury properties X from their values X_m at a mean temperature of $T_m = 40°$, according to Ahlers et al. (2006); the lines are as in figure 5.1.(b) Region of validity of the OB approximation for mercury at $T_m = 40\,°C$, according to Gray and Giorgini (1976). The grey shaded area shows the parameter range where the OB approximation is valid within a residual error of 10%.

treating high Prandtl number fluids is very challenging due to the required mesh resolution. A recent example for a numerical study on fluids with large Prandtl numbers to mention here is the work by Silano et al. (2010). They performed numerical simulations for $\mathrm{Pr} = 1000$ and $\mathrm{Pr} = 10000$ for up to $\mathrm{Ra} = 10^9$ and up to $\mathrm{Ra} = 10^7$, respectively. Generally, instead of conducting simulations at high Pr, rather the limit as Pr goes to infinity has been used, as, for example, by Busse (1979) and Constantin and Doering (1999) under OB conditions and Christensen and Harder (1991); Ogawa et al. (1991) and Manga and Weeraratne (1999) with a temperature-dependent viscosity. While making analytical and numerical considerations simpler, this approach completely neglects effects induced by inertia.

Thus, the aim of studying Rayleigh–Bénard convection in glycerol was twofold: First, to provide an accurate and extensive set of data for a high Pr fluid under strict OB conditions – which is only possible by means of well-resolved three-dimensional DNS, because experiments are unavoidably spoiled by NOB effects at higher Ra (cf. e.g. Xia et al., 2002). Second, to also evaluate the influence of NOB effects for that case.

5.2.1 Resolution of the DNS and parameter range

The high Prandtl number of $\mathrm{Pr} = 2547.9$ puts severe constraints on the temporal and spatial resolution, making glycerol very challenging from a numerical point of view. First of all, the instabilities due to momentum diffusion are damped much faster than the instabilities in the temperature, and the system reacts almost instantaneously to temperature fluctuations. Thus, the temperature scales are much smaller than the velocity ones. As a result, the time to reach equilibrium and to gain reliable statistics is at least one order of magnitude longer, i.e., several thousand dimensionless time units.

Second, the system is known to be dominated by single plumes, also in the centre of the cell, which then occasionally cross the whole cell, as shown in figure 5.4. They also become thinner with increasing Ra, requiring a sufficient resolution not only in the boundary layers but also within the bulk. Furthermore, the viscous boundary layer becomes much thicker than the thermal one and eventually saturates at a certain value (Breuer et al., 2004; Grossmann and Lohse, 2001; Schmalzl et al., 2004). This cannot be described within the theory of mesh requirements proposed by Shishkina et al. (2010). I decided to take the criterion from Shishkina et al. (2010) for the mesh size in the Prandtl–Blasius type boundary layer and apply it to the whole domain and, moreover, I divided the required mesh size by a safety factor of 2 to consider NOB effects, i.e., all cells are smaller than

$$h^{\mathrm{BL}} = \frac{1}{2}\left[2^{-3/2}a^{-1}E^{-3/2}\mathrm{Nu}^{-3/2}H\right] \qquad (a \approx 0.482,\ E \approx 0.982). \tag{5.2.1}$$

The Nusselt number Nu was estimated using the scaling laws suggested by Ahlers et al. (2009); Grossmann and Lohse (2000, 2001, 2002) as the best available estimate. I refrained from using the experimental data by Zhang et al. (1997) because all of their measurements were made for strongly varying Prandtl numbers and only for a range between 8.2×10^6 and 6.1×10^8. The Nusselt number $\mathrm{Nu}_{\mathrm{GL}}$ calculated using

Ra	$\mathrm{Nu}_{\mathrm{GL}}$	h^{BL}/H	$\mathrm{Nu}_{\mathrm{OB}}^{\mathrm{DNS}}$	h/H	$\max(h_z/\eta_B)$	$N_r \times$	$N_\phi \times$	N_z
10^5	4.7	57.6×10^{-3}	3.88 ± 0.01	14.1×10^{-3}	0.41	$32\times$	$64\times$	64
10^6	7.6	19.9×10^{-3}	8.84 ± 0.02	12.3×10^{-3}	0.96	$32\times$	$64\times$	64
10^7	13.2	8.33×10^{-3}	17.62 ± 0.13	7.81×10^{-3}	1.04	$64\times$	$128\times$	128
10^8	25.6	3.00×10^{-3}	33.92 ± 0.61	2.60×10^{-3}	0.76	$192\times$	$512\times$	384
10^9	52.9	0.99×10^{-3}	65.38 ± 1.24	2.60×10^{-3}	1.60	$192\times$	$512\times$	384
10^9	52.9	0.99×10^{-3}	65.76 ± 0.74	1.30×10^{-3}	0.83	$384\times$	$1024\times$	768

TABLE 5.3: Rayleigh number Ra, the corresponding Nusselt number $\mathrm{Nu}_{\mathrm{GL}}$ according to the Grossmann–Lohse theory(Ahlers et al., 2009; Grossmann and Lohse, 2000, 2001, 2002), the Nusselt number for the OB cases obtained in the simulations $\mathrm{Nu}_{\mathrm{OB}}^{\mathrm{DNS}}$, the requested maximal cell size in the boundary layers h^{BL}/H, according to equation (5.2.1), and the actual one h/H, the maximal value of the ratio of the vertical mesh width to the Batchelor length $\max(h_z/\eta_B)$, and the number of nodes N_r, N_ϕ, N_z in the radial, azimuthal, and vertical direction, respectively, for $\mathrm{Pr} = 2547.9$.

the Grossmann–Lohse theory[‡], the herewith a priori requested resolution h^{BL}/H, and the number of nodes in the radial, azimuthal, and vertical direction, are given in table 5.3. In addition, also the actual maximal grid size in the boundary layers h/H is shown, as well as the Nusselt number obtained in the OB simulations $\mathrm{Nu}_{\mathrm{OB}}^{\mathrm{DNS}}$. Further details regarding the heat flux, including but not limited to the Nusselt number and its scaling, are discussed in section 5.2.8. Because of the very fine meshes, the nodes were distributed equidistantly for $\mathrm{Ra} = 10^7$, 10^8 and 10^9. For smaller Ra, non-equidistant meshes were used where the nodes were clustered in the vicinity of the walls.

For $\mathrm{Ra} = 10^9$, the maximal mesh size in the boundary layers is slightly smaller. However, a grid resolution study for the $\mathrm{Ra} = 10^9$ simulation was also conducted, and revealed that the $\mathrm{Nu}_{\mathrm{DNS}}$ obtained agrees well with the one obtained on a coarser grid with $192 \times 512 \times 384$ nodes (see table 5.3). The grid resolution was also verified with an a posteriori analysis, i.e., I checked that the vertical grid spacing h_z is everywhere smaller than the smallest relevant length scale, the (non-dimensional) Batchelor length

$$\eta_B = \gamma^{-9/8}\mathrm{Pr}^{-1/8}\mathrm{Ra}^{-3/8}\epsilon_u^{-1/4}, \tag{5.2.2}$$

with the dimensionless kinetic energy dissipation rate

$$\epsilon_u = \gamma^{-3/2}\mathrm{Pr}^{1/2}\mathrm{Ra}^{-1/2}|\nabla \mathbf{u}|^2. \tag{5.2.3}$$

The maximal value of the ratio h_z/η_B is also given in table 5.3. It is less than or equal to 1.0 for the whole computational domain and for all considered cases. These considerations show that the grid resolution has indeed been chosen properly.

Here, the results from a total of 17 simulations, that is, $\mathrm{Ra} \in \{10^5, 10^6, 10^7, 10^8, 10^9\}$, each under OB conditions and the NOB condition $\Delta = 40\,\mathrm{K}$ is discussed. For

---

[‡] The prefactors $a = 0.482$, $\mathrm{Re}_c = 1.041$, $c_1 = 8.685$, $c_2 = 1.441$, $c_3 = 0.462$, $c_4 = 0.013$ were used.

$Ra = 10^6$ I additionally performed NOB simulations for $\Delta \in \{10\,K, 20\,K, 30\,K, 50\,K, 60\,K, 70\,K, 80\,K\}$. For all simulations I started temporal averaging when the flow had statistically converged. As the criterion for this, I waited for the radial and azimuthal averaged Nusselt number to be constant along the vertical coordinate after an appropriate averaging time. In general, this meant at least five thousand time units, but rather typically ten thousand time units before initiating and several thousand time units of actual statistical averaging. Thus, the statistical data for the higher Δ, i.e. 60 K–80 K, and higher Ra, i.e., 10^8 and 10^9, were obtained within 1000 to 3000 time units, and for lower Δ and Ra, within more than 3000 and up to 10 000 time units.

5.2.2 Flow structures and plume dynamics

By looking at the instantaneous flow fields in figure 5.4, one can realise at first glance, that the flow in large Prandtl number fluids differs greatly from the flow at low and moderate Prandtl number fluids, for example, air ($Pr = 0.7$) and water ($Pr = 4.38$) at the same Rayleigh number (see e.g. Wagner et al., 2012). Following the classification by Busse (1978), Krishnamurti and Howard (1981), Getling (1998) and Manga and Weeraratne (1999), the flow behaviour in Rayleigh–Bénard convection can be distinguished into steady, unsteady, plume-dominated, transitional, and turbulent. Except for the fully turbulent case, my simulations covered all these flow regimes. The visualisation of the spatial structures can be used with relative ease as a method for distinguishing between the different states. Another criterion for categorising them is to use the probability density functions (PDFs), which will be discussed in section 5.2.5.

The instantaneous temperature fields for $Ra \in \{10^5, 10^6, 10^7, 10^8, 10^9\}$ are presented in figure 5.4, and in addition, the time averaged temperature and velocity fields for the representative cases of $Ra = 10^5$, 10^7, and 10^9 are shown in figure 5.5 under both OB and NOB conditions with $\Delta = 40\,K$.

For the lowest Rayleigh number, $Ra = 10^5$, and under OB conditions, a single convection roll is found. The time averaged 2D slices reveal a plane with one large roll and tiny counter-rotating secondary rolls at its edges. In the vertical plane perpendicular to it, four equally sized smaller convection rolls develop. The time averaged and the instantaneous flow fields are virtually the same. The temporal variation is only on a long time scale and we can speak of a three-dimensional flow with quasi-steady behaviour. A similar superposition of two roll patterns has been referred to as bimodal convection by Busse (1978), however, the sense of rotation of these patterns relative to each other is opposite to that reported by Busse (1979) for high Pr fluids. This disagreement might be an effect of the finite size of the cell. Under NOB conditions, the flow structures are similar, but the perfect top–bottom symmetry, typical for OB cases, is broken. Not only a clearly visible increase of the bulk temperature is obtained, but also a shifting of the large convection roll away from the centre. In the instantaneous flow field, one can also see that partially even the down-welling flow has a positive temperature, $T > 0$. Hence, the four rolls in the plane perpendicular to the large convection roll are arranged in a different manner.

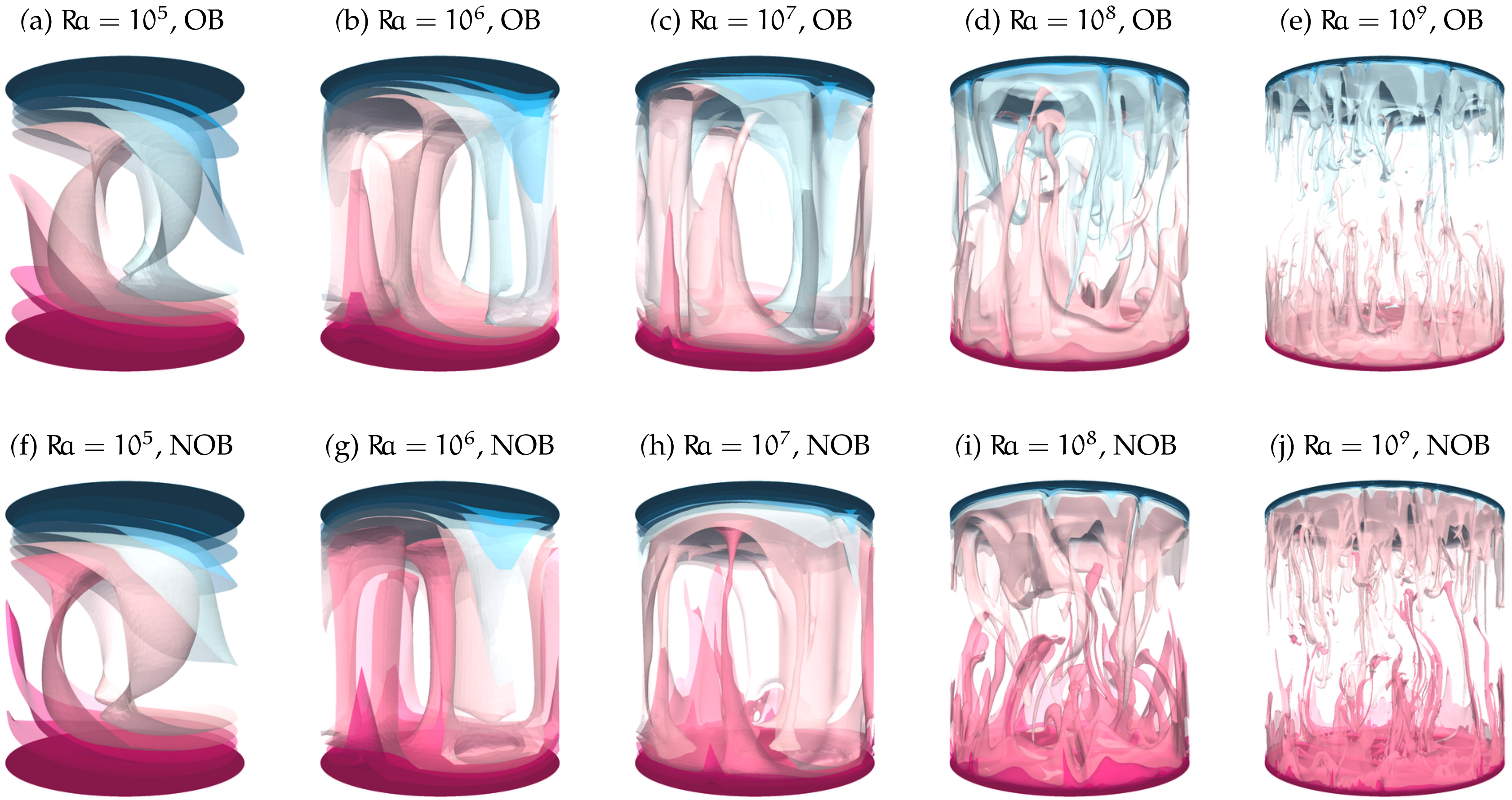

(a) $Ra = 10^5$, OB (b) $Ra = 10^6$, OB (c) $Ra = 10^7$, OB (d) $Ra = 10^8$, OB (e) $Ra = 10^9$, OB

(f) $Ra = 10^5$, NOB (g) $Ra = 10^6$, NOB (h) $Ra = 10^7$, NOB (i) $Ra = 10^8$, NOB (j) $Ra = 10^9$, NOB

FIGURE 5.4: Instantaneous temperature isosurfaces under OB (figures (a)–(e)) and NOB ($\Delta = 40\,\mathrm{K}$, figures (f)–(j)) conditions for $Ra \in \{10^5, 10^6, 10^7, 10^8, 10^9\}$. Shown are ten isosurfaces, evenly spaced between the minimal and maximal values, i.e., pink indicates (dimensionless) temperatures above zero and blue temperatures below zero.

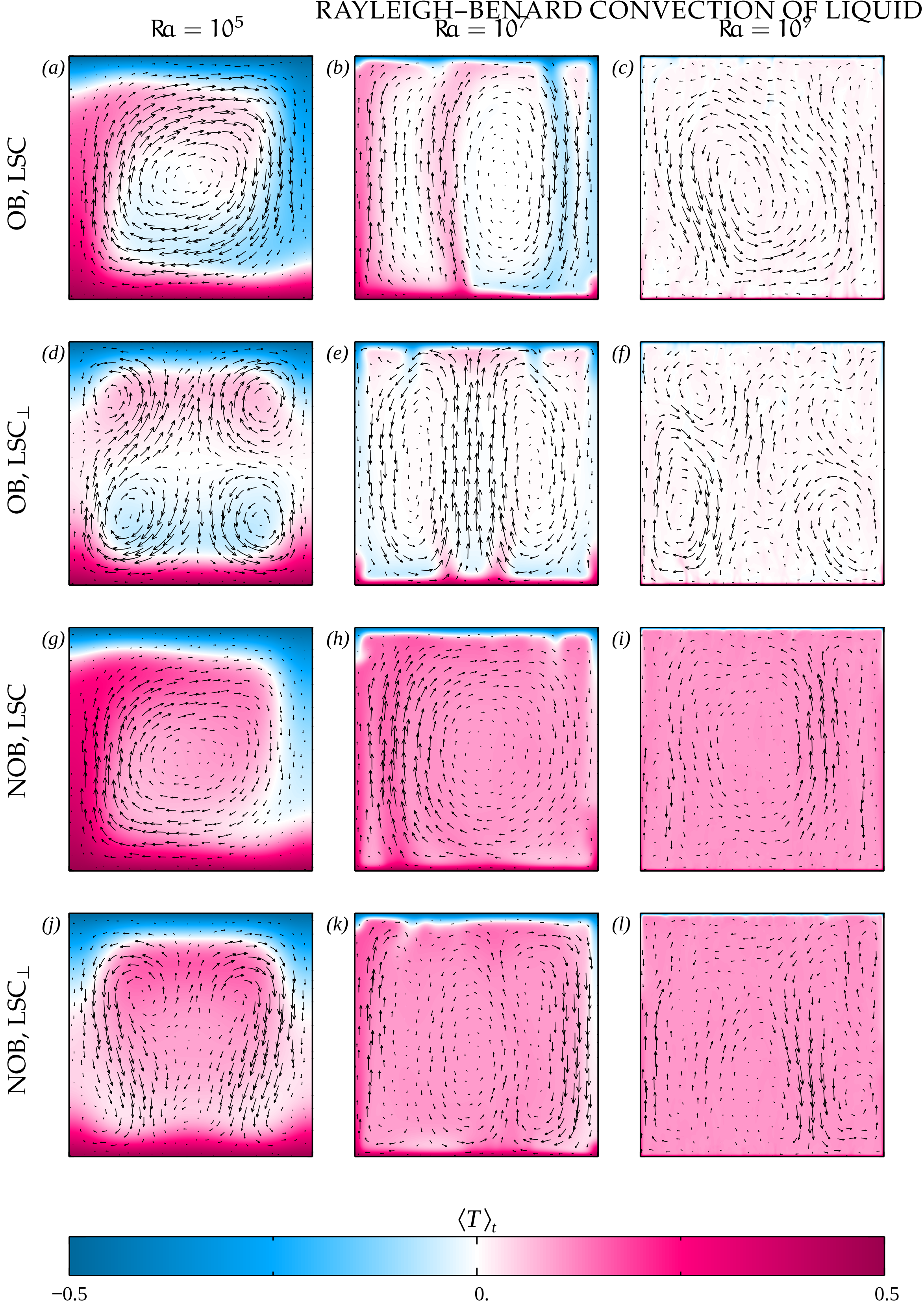

FIGURE 5.5: Time-averaged temperature fields with over-plotted velocity field for $\mathrm{Ra} = 10^5$ (first column), $\mathrm{Ra} = 10^7$ (second column) and $\mathrm{Ra} = 10^9$ (third column). The pictures

are arranged in the following manner: the first and second row show the OB case, (a)–(c) is the plane where one convection roll or large scale circulation, respectively, is found (abbreviated by LSC), (d)–(f) the central vertical plane perpendicular to it ($\mathrm{LSC}_{\perp}$); the third and the fourth row show the NOB case, again (g)–(i) is the plane of the LSC and (j)–(l) the plane $\mathrm{LSC}_{\perp}$.

The upper two rolls are less extended in size and their centres are shifted closer to the cylinder axis, while the lower rolls are situated closer to the walls.

With increasing Rayleigh number, the flow becomes gradually unsteady and plumes start to rise from the boundary layers. Generally, they keep on being connected to their boundary layers where they are formed, until they reach the opposite cold or hot wall. However, the plumes become thinner with increasing Ra and thus also the number of emitted plumes increases. Their persistency is attributed to the domination of the diffusion of momentum over the diffusion of heat.

For $\mathrm{Ra} = 10^6$ and 10^7, single isolated plumes emerge. In the OB case, time averaging reveals three lengthy rolls extending in the vertical direction with very small rolls between them at the top and bottom. This three roll structure resembles the flow developing at higher aspect ratios and lower Prandtl numbers. An example for $\mathrm{Pr} = 0.7$ and an aspect ratio of $\Gamma = 10$ was shown by Shishkina and Wagner (2006). A similar structure was also detected by Silano et al. (2010) for slightly different parameters, $\mathrm{Pr} = 10^3$, $\mathrm{Ra} = 10^8$ and $\Gamma = 0.5$. Under NOB conditions the flow is distorted similar to the case of $\mathrm{Ra} = 10^5$: again the centre temperature is higher, we find warm down going plumes, and the large scale structures are arranged asymmetrically. In fact, one of the three rolls is much larger than the other two. Therefore, one can find a plane where it resembles a typical large scale circulation (LSC). However, in the plane perpendicular to it ($\mathrm{LSC}_{\perp}$), the corresponding four-roll structure is missing. The 3D field confirms as well that the structure is more complex.

At $\mathrm{Ra} = 10^8$ and $\mathrm{Ra} = 10^9$, the highest Rayleigh numbers attained, I find a system where the velocity of the plumes and large-scale structures are comparable, leading to the impression that the flow is only governed by plumes, which cross the Rayleigh–Bénard cell almost unaffected. Thus, it seems reasonable to call this a plume-dominated regime. This was also described by Breuer et al. (2004) and Schmalzl et al. (2004). But even at $\mathrm{Ra} = 10^9$, the majority of plumes are still connected to their thermal boundary layers: only a few detach from them. While the instantaneous fields have very distinct features, as pictured in figure 5.4 for $\mathrm{Ra} = 10^8$ and 10^9, the time averaged flow fields are very similar to the ones obtained for lower Pr at the same Ra. They unambiguously show an LSC. Again in the NOB case the overall flow pattern within the cylinder is more complex, but the general feature, i.e. the LSC is still present. Apparently, this behaviour has not been found in the 2D simulations by Sugiyama et al. (2007), neither in the OB nor in the NOB case. Hence, 3D simulations are necessary to capture all the relevant flow structures, especially for NOB effects. These findings are also more consistent with the results of the experiments for $\mathrm{Ra} = 2.3 \times 10^8$ by Zhang et al. (1997), although all plumes stayed connected with their boundary layer and the LSC was easier to recognise in the experiments. The reason for this disagreement is probably the about half as large Pr in their case.

During averaging, neither reversals of the LSC nor any noticeable shifting of the azimuthal angle of the large scale structures were observed. While all the presented flow fields display a clearly chaotic behaviour, the transition range to a fully developed turbulent flow extends up to $Ra \approx 10^{12}$ when using the criterion based on the average Kolmogorov length as a typical length scale for the coherent structures.

Many of the asymmetries obtained in the NOB cases can be ascribed to the different viscosities in the cold top and hot bottom layers. That is, the lower viscosity at the warm bottom makes the plumes more prone to leave the bottom layer and they are also more mobile, i.e., faster. The cold plumes from the top have the exact opposite behaviour: they are very viscous and thus rather remain within the cold top boundary layer. Or alternatively, one could say that the plumes emanating from the cold top layer move more slowly and hence, they remain much longer in contact with the ambient medium in the bulk and heat up on their way down. These asymmetric plume dynamics have a significant influence on the entire flow behaviour and, in particular, on the boundary layers and the temperature profiles. This will be explained in more detail in the following sections.

5.2.3 Mean temperature profiles and thermal boundary layers

Figure 5.6 presents the time and r–ϕ plane averaged mean temperature profiles under OB and NOB conditions. Figure 5.6(a) shows the profiles for different Ra under OB and under NOB conditions, each time for $\Delta = 40\,\mathrm{K}$. In figure 5.6(b) the Rayleigh number is kept constant at $Ra = 10^6$ and various NOB conditions, i.e., Δ, are shown.

At the beginning of the simulations, all profiles exhibited an overshoot adjacent to the boundary layers. Schmalzl et al. (2004), amongst others, observed this feature already at $Pr = 100$ for $Ra = 10^6$, and suggested that this is a feature of the high Prandtl number. In my case, however, both under OB and NOB conditions, those overshoots disappeared in the course of the simulations. Thus, I think that this intermediate phenomenon is rather an indicator that the statistical equilibrium state has not been reached yet. Nonetheless, in the profiles for $Ra = 10^5$ and $Ra = 10^6$, seen in figure 5.6 (a)–(b), some non-monotonicity persists due to the occurring structures (cf. figure 5.12) in this still quasi-steady regime and is not expected to disappear after even longer averaging times.

The most prominent feature that distinguishes the NOB profiles from the OB ones is the higher temperature in the bulk. The deviation of the centre temperature T_c from the arithmetic mean temperature will be treated in detail in section 5.2.4. Furthermore, the NOB profiles always lie above the corresponding OB profiles, i.e., they bend more towards the plate temperature close to the top and further away from the plate temperature close to the bottom, in comparison to the OB profiles. It is more easily visible when looking at the second derivative where the profiles are normalised by the maximum absolute value of the second derivative of the corre-

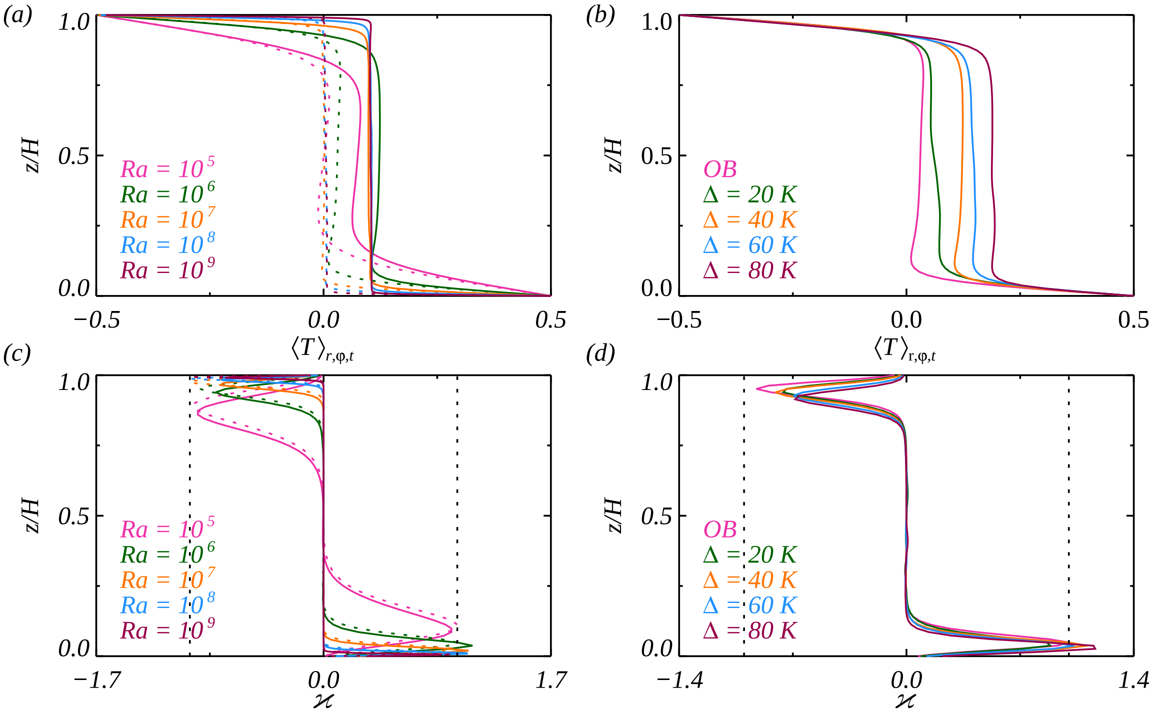

FIGURE 5.6: (a)–(b) Mean temperature profiles, i.e., the temperature averaged in time t and in every r–ϕ plane. (c)–(d) Curvature of the temperature profiles normalised to the OB value, as defined by equation (5.2.4). The black dashed vertical lines mark the points where $|\varkappa| = 1$. The left panels (a) and (c) correspond to varying Ra and the dashed lines indicate the OB case and the solid lines the NOB cases for $\Delta = 40\,\mathrm{K}$. The right panels (b) and (d) correspond to a constant $\mathrm{Ra} = 10^6$ and each time the OB case and various NOB conditions, i.e., $\Delta \in \{20\,\mathrm{K}, 40\,\mathrm{K}, 60\,\mathrm{K}, 80\,\mathrm{K}\}$.

sponding OB profile,

$$\varkappa = \frac{\langle \partial_z^2 T^2 \rangle_{r,\phi,t}}{\max|\varkappa_{\mathrm{OB}}|}, \tag{5.2.4}$$

seen in figures 5.6(c) and (d). Close to the top plate holds $|\varkappa| < 1$ and close the bottom one holds $|\varkappa| > 1$. This behaviour is enhanced with increasing Δ as well as with increasing Ra. A similar result was obtained for water by Ahlers et al. (2006). The reason lies in the larger heat conductivity Λ at the bottom and the smaller Λ at the top. Since the heat flux has to be same at both boundaries, the temperature profiles have to compensate for this.

Associated with the profiles are the different thicknesses of the boundary layer. The thermal boundary layer thicknesses λ_t^θ and λ_b^θ are defined by the slope criterion, i.e.

$$\lambda_t^\theta = \frac{T_t - T_c}{\partial_z \langle T \rangle_{r,\phi,t}|_{z=H}}, \qquad \lambda_b^\theta = \frac{T_c - T_b}{\partial_z \langle T \rangle_{r,\phi,t}|_{z=0}}. \tag{5.2.5}$$

The ratio of the top to bottom boundary layer thickness, $\chi_\lambda^\theta = \lambda_t^\theta / \lambda_b^\theta$, is given in figure 5.7. It is practically independent of Ra, but increases with increasing Δ, i.e., the top thermal boundary layer is always thicker than the bottom one, $\lambda_t^\theta > \lambda_b^\theta$. For

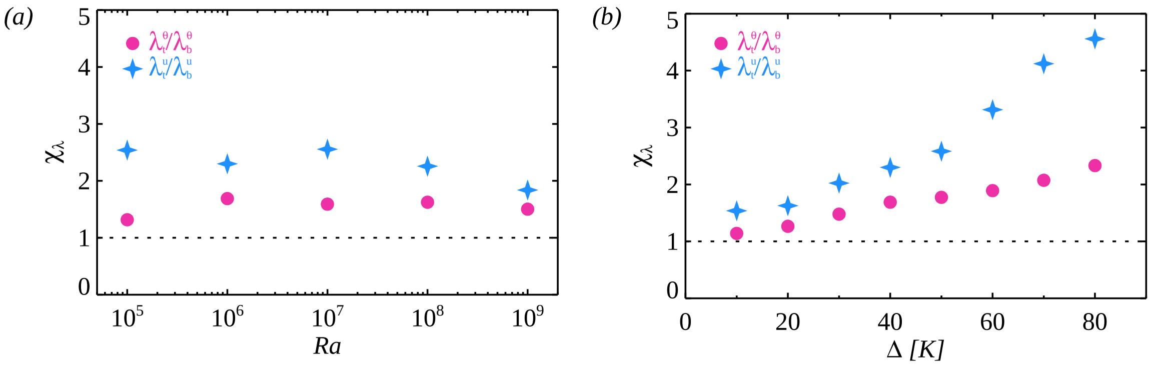

FIGURE 5.7: (a) Ratio of the top to bottom thermal (χ_λ^θ) and viscous (χ_λ^u) boundary layer thicknesses, for constant $\Delta = 40\,\mathrm{K}$, as functions of Ra. The dashed line indicates the point where the top and bottom boundary layer have the same thickness, i.e, $\chi_\lambda = 1$. (b) Similar to figure (a) but for constant $\mathrm{Ra} = 10^6$, as functions of Δ.

the highest considered temperature difference, $\Delta = 80\,\mathrm{K}$, the top boundary layer is about 2.5 times thicker.

5.2.4 Centre temperature T_c

One of the best known, and also best analysed, NOB phenomena is the deviation of the temperature in the centre T_c from the arithmetic mean temperature T_m. The three-dimensional DNS showed that for a temperature difference of $\Delta = 80\,\mathrm{K}$, the centre temperature can be up to 15 K higher than under OB conditions.
There exist several models to predict the change of T_c, amongst others there are the ones by Wu and Libchaber (1991), Manga and Weeraratne (1999), and Ahlers et al. (2006). The comparison of the model predictions to the DNS data is shown in figure 5.8. Most of the models considered here are essentially based on the following ideas. In the centre of the cell, the heat is almost solely transported by convection, but in the boundary layers by conduction, since there the velocity approaches zero. Because the total dimensionless heat flux, i.e., the Nusselt number Nu, is the sum of the convective and conductive heat fluxes, q_{conv} and q_{cond},

$$\mathrm{Nu} = q_{conv} + q_{cond} = \mathrm{Nu} = (\mathrm{Ra}\,\mathrm{Pr}\,\gamma)^{1/2}\,\langle u_z T\rangle - \gamma^{-1}\,\langle \Lambda \partial_z T\rangle\,, \tag{5.2.6}$$

it needs to be constant due to energy conservation. The temperature gradient is zero in the bulk, hence the mean temperature $\langle T\rangle_{r,\phi,t}$ only changes within the boundary layers, and thus the total temperature drop Δ is the sum of the temperature drops within the top and the bottom boundary layers:

$$\Delta = \Delta_t + \Delta_b. \tag{5.2.7}$$

Obviously, the ratio

$$\chi_\Delta = \frac{\Delta_t}{\Delta_b} \tag{5.2.8}$$

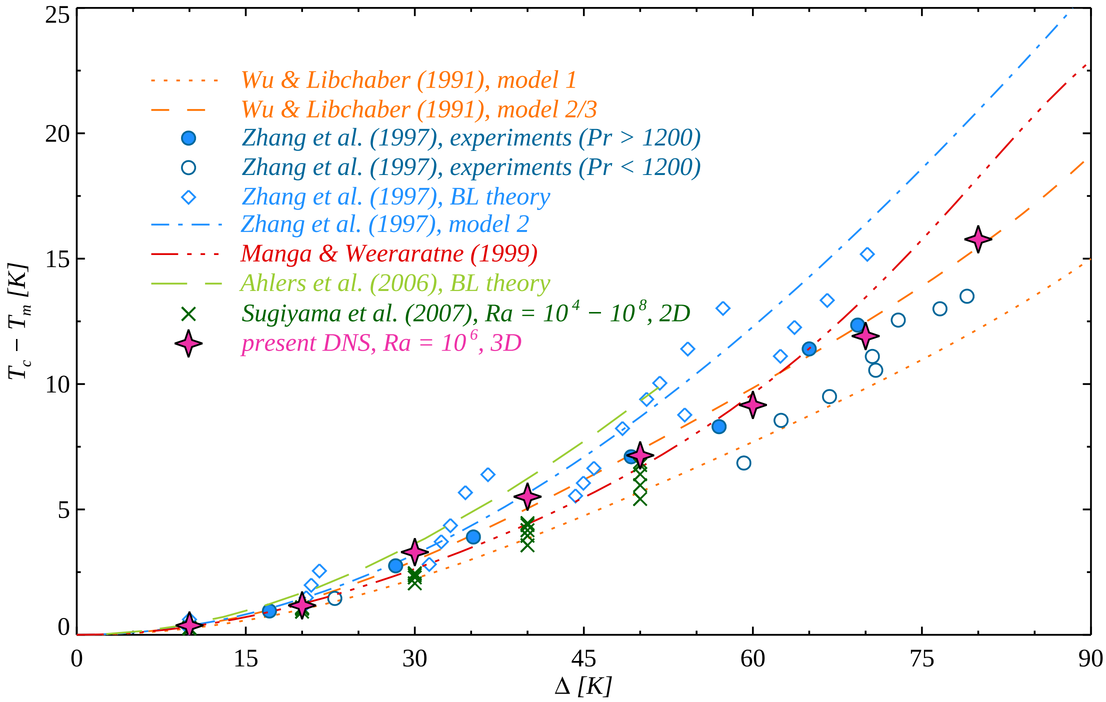

FIGURE 5.8: The centre temperature T_c versus. Δ for a fixed $Ra = 10^6$, the predictions from the models of Wu and Libchaber (1991), Zhang et al. (1997), Manga and Weeraratne (1999), and Ahlers et al. (2006), and the results from 2D simulations by Sugiyama et al. (2007) are plotted as well.

equals one under OB conditions, but in the NOB case this is no longer true. It will prove to be convenient to combine these two equations and express the two temperature drops as follows:

$$\Delta_t = \frac{\chi_\Delta}{1+\chi_\Delta}\Delta, \tag{5.2.9}$$

$$\Delta_b = \frac{1}{1+\chi_\Delta}\Delta. \tag{5.2.10}$$

In the thermal boundary layers the heat flux is given by conduction, hence

$$q_{cond} = \Lambda_{\bar{t}}\frac{\Delta_t}{\lambda_t^\theta} = \Lambda_{\bar{b}}\frac{\Delta_b}{\lambda_b^\theta} \quad \Rightarrow \quad \kappa_{\bar{t}}\frac{\Delta_t}{\lambda_t^\theta} = \kappa_{\bar{b}}\frac{\Delta_b}{\lambda_b^\theta}. \tag{5.2.11}$$

The indices $\bar{t}$ and $\bar{b}$ here and in the following denote that the quantity is taken at the interpolated temperatures $(T_t + T_c)/2$ and $(T_b + T_c)/2$. The latter equality in (5.2.11) results from the fact that ρ and c_p are assumed to be constant over the cell. In my opinion, a better prerequisite is the exact relation at the plates, i.e.,

$$q_{cond} = \Lambda_t\frac{\Delta_t}{\lambda_t^\theta} = \Lambda_b\frac{\Delta_b}{\lambda_b^\theta} \quad \Rightarrow \quad \kappa_t\frac{\Delta_t}{\lambda_t^\theta} = \kappa_b\frac{\Delta_b}{\lambda_b^\theta}. \tag{5.2.12}$$

Nonetheless, Wu and Libchaber (1991) used (5.2.11), since the latter equation (5.2.12) results in a greater deviation from their experimental data for all their T_c models. The same conclusion can be drawn with the DNS shown here.
In the first model, they assume that the boundary layer Rayleigh number is the same at the top and bottom,

$$\mathrm{Ra}_{\bar{t}} = \mathrm{Ra}_{\bar{b}} \qquad \Leftrightarrow \qquad \frac{\alpha_{\bar{t}} g \Delta_t \lambda_t^3}{\kappa_{\bar{t}} \nu_{\bar{t}}} = \frac{\alpha_{\bar{b}} g \Delta_b \lambda_b^3}{\kappa_{\bar{b}} \nu_{\bar{b}}}. \tag{5.2.13}$$

Their second proposed model follows the scaling model of Castaing et al. (1989) and assumes that the velocity scales w of the plumes are equal,

$$w_{\bar{t}} = w_{\bar{b}} \qquad \Leftrightarrow \qquad \frac{g \alpha_{\bar{t}} \Delta_t \lambda_t^2}{\nu_{\bar{t}}} = \frac{g \alpha_{\bar{b}} \Delta_b \lambda_b^2}{\nu_{\bar{b}}}. \tag{5.2.14}$$

These scales are based on the balance between the buoyancy force $g\alpha\Delta$ and the viscous force $\nu w/\lambda^2$. The third model will yield the same result, and is again based on the aforementioned scaling model, but this time assuming the same temperature scales Θ within the boundary layers,

$$\Theta_{\bar{t}} = \Theta_{\bar{b}} \qquad \Leftrightarrow \qquad \frac{\kappa_{\bar{t}} \nu_{\bar{t}}}{g \alpha_{\bar{t}} \lambda_t^3} = \frac{\kappa_{\bar{b}} \nu_{\bar{b}}}{g \alpha_{\bar{b}} \lambda_b^3}. \tag{5.2.15}$$

All these assumptions can be checked against the DNS data. Figure 5.9 presents the ratios

$$\chi_{\mathrm{Ra}} = \frac{\mathrm{Ra}_{\bar{t}}}{\mathrm{Ra}_{\bar{b}}}, \; \chi_w = \frac{w_{\bar{t}}}{w_{\bar{b}}} \; \text{ and } \; \chi_\Theta = \frac{\Theta_{\bar{t}}}{\Theta_{\bar{b}}}. \tag{5.2.16}$$

In the case of glycerol and the ranges of Ra and Δ I considered here, none of the assumptions is perfectly fulfilled. Wu and Libchaber (1991), however, found that at least the ratio χ_Θ of the third model was constant in their experiments conducted for low-temperature helium gas, while the assumptions for the first and second model did not hold.
Even though none of the required conditions are perfectly met, the models give a good prediction of the actual T_c for glycerol. One can complete equations (5.2.7) and (5.2.11) now with either equation (5.2.13), (5.2.14), or (5.2.15), and uniquely calculate the ratio χ_Δ,

$$\chi_{\Delta,1} = \left(\frac{\alpha_{\bar{b}} \nu_{\bar{t}}}{\alpha_{\bar{t}} \nu_{\bar{b}}}\right)^{1/4} \left(\frac{\kappa_{\bar{b}}}{\kappa_{\bar{t}}}\right)^{1/2}, \tag{5.2.17}$$

$$\chi_{\Delta,2/3} = \left(\frac{\alpha_{\bar{b}} \nu_{\bar{t}}}{\alpha_{\bar{t}} \nu_{\bar{b}}}\right)^{1/3} \left(\frac{\kappa_{\bar{b}}}{\kappa_{\bar{t}}}\right)^{2/3}. \tag{5.2.18}$$

All of the material properties still depend on χ_Δ, but with the help of the polynomial functions of the material properties these equations can be solved numerically. Herewith, and using equations (5.2.9) and (5.2.10), the centre temperature T_c can be calculated:

$$T_c = T_t + \Delta_t = T_b - \Delta_b. \tag{5.2.19}$$

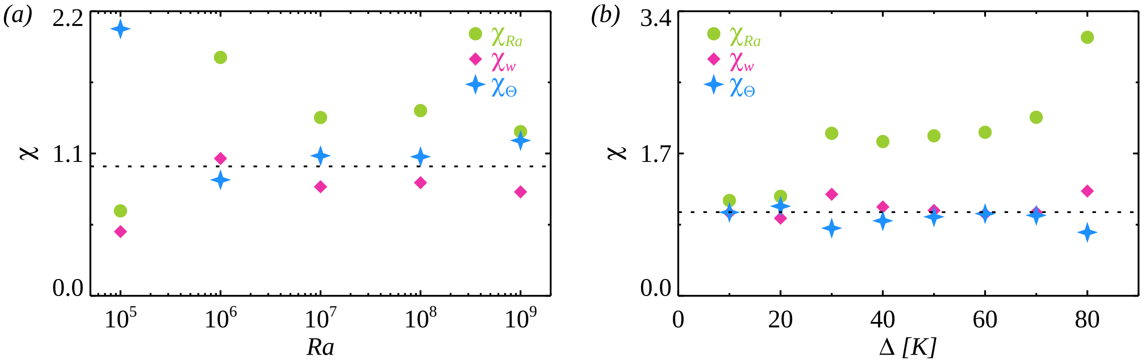

FIGURE 5.9: (a) The left panel shows different ratios of top to bottom quantities, the boundary layer Rayleigh numbers χ_{Ra}, the plume velocity scales χ_w, and the temperature scales χ_Θ as functions of Ra for the NOB simulations with $\Delta = 40\,K$. (b) The right panel shows the same quantities but as functions of Δ for fixed $Ra = 10^6$. The dashed line corresponds to $\chi = 1$ in each case.

The difference $T_c - T_m$ for the three models is shown for different Δ in figure 5.8. Zhang et al. (1997) used a two-dimensional steady-state boundary layer model with three main assumptions. First, the plumes transport not between the thermal top and bottom layer but only from the walls to the mixing region between the layers. Second, T_c is adjusted, so that the fluxes at the top and bottom are equal, and third, the viscous stress is constant within the thermal sub-layer. Then the laminar two-dimensional thermal boundary layer equation is solved numerically. The result yields T_c as a function of both T_t and T_b. However, they only took into account the temperature dependency of the viscosity and not the thermal diffusivity. Zhang et al. (1997) also gave another approximation for the third model of Wu and Libchaber (1991) consistent with their boundary layer theory. Using an exponential dependency of the viscosity, i.e., $\nu(T) \propto \exp(-cT)$, $c = 0.087$, and again leaving all the other material properties constant, they found the fit

$$T_c = \frac{\Delta}{2}\tanh(c\Delta/12). \tag{5.2.20}$$

They also conducted experiments and measured the centre temperature. Certain points for their boundary layer model, the tanh fit (5.2.20) and the experimental data are shown in figure 5.8 as well. In their experiments the mean temperature T_m varied strongly, between 24.55°C and 64.75°C, and hence, so did the Prandtl number, between approximately 600 and 8000. As consequence, the scatter of T_c is large. Thus, I distinguished between $Pr > 1200$ and $Pr < 1200$. The data points for higher Pr show a very good agreement with the three-dimensional DNS data. On the contrary, the lower Pr data yield a lower T_c.

Manga and Weeraratne (1999) investigated Rayleigh–Bénard convection in corn syrup which has a comparable high Prandtl number between $10^3 < Pr < 10^6$ and a similar temperature-dependent viscosity. By also considering an exponential dependency of the viscosity, assuming that Nu scales with the Péclet number $Pe = PrRe$ with $Nu \propto Pe^{-1/3}$ and that the temperature drop within the convecting region is

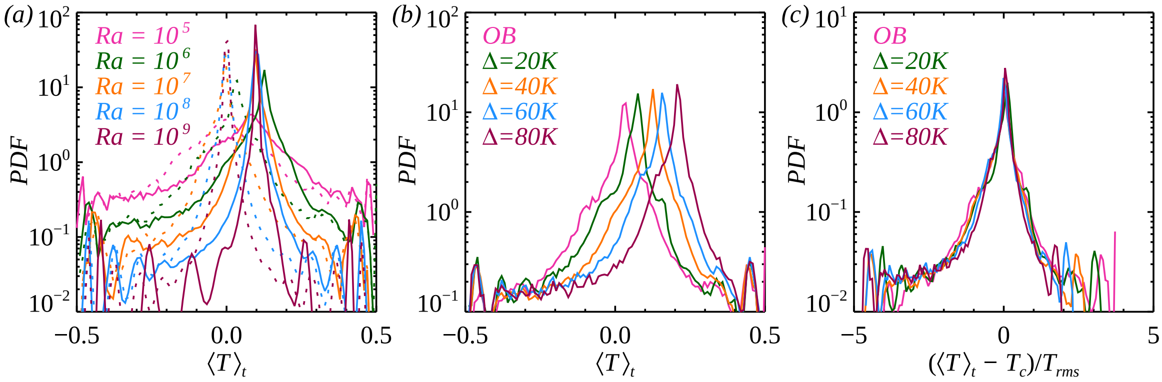

FIGURE 5.10: Probability density functions (PDFs) of the time averaged temperature for the whole volume. (a) Different Ra, the dashed line indicates the OB case, the solid line the NOB case with $\Delta = 40\,\mathrm{K}$. (b) Constant $\mathrm{Ra} = 10^6$, shown are the OB case and four different NOB cases.

$\Delta/2$ (which is equivalent to using $T_{\tilde{t}}$ and $T_{\tilde{b}}$), they found the following relation for the centre temperature,

$$T_c = \frac{\Delta}{1 + \left(\frac{\nu_t}{\nu_b}\right)^{-1/6}} + T_t, \tag{5.2.21}$$

also presented in figure 5.8.

Ahlers et al. (2006) used a similar approach to Zhang et al. (1997), but extended the Prandtl-Blasius boundary layer theory also for a temperature-dependent diffusivity κ. The comparison with the experimental and the DNS data revealed that the 2D boundary layer models overestimate the actual T_c. The rather poor agreement—at least in comparison to its very successful application in the case of water—can be explained easily. As already pointed out by Sugiyama et al. (2009) the main deviation is caused by plume emission. However, in the case of glycerol, this happens not only close to the walls, but indeed everywhere on the plates, making the Prandtl–Blasius boundary layer theory less applicable. The discrepancy gets worse due to the fact that the plumes stay connected to their boundary layers.

Finally, I also show in figure 5.8 the data from the two-dimensional simulations by Sugiyama et al. (2007). Their data are lower than mine, even though the Prandtl number is the same. Assuming that the scatter in the experimental data is indeed caused by different Pr, it seems hat two-dimensional simulations are insufficient for obtaining an accurate value of T_c.

In conclusion, the model of Wu and Libchaber (1991) based on the same velocity or temperature scale in the top and bottom boundary layer (equations (5.2.14)–(5.2.15)) predicts T_c the best out of all the considered models, with a standard deviation of $0.4\,\mathrm{K}$.

5.2.5 Probability density functions of the temperature

Figure 5.10(a) presents the volume-weighted probability density functions (PDFs) of the time averaged temperature for the whole cell. In the OB cases, the most likely temperature is the arithmetic mean temperature T_m, while in the NOB cases the most likely temperature is close to T_c. The change of the PDFs, i.e., the shift to the right, is also associated with the presence of thermal boundary layers with different thicknesses. Figure 5.10(b) shows the PDFs for a constant Ra but varying Δ; the PDFs become more asymmetric and the maximum peak is shifted to higher temperatures.

Following the classification of Manga and Weeraratne (1999), one can herewith also distinguish between the different styles of convection. If the distribution is Gaussian, then the flow is expected to be quasi-steady. If the distribution is exponential, then the flow is turbulent. However, for high Prandtl number fluids, these curves have superimposed on them a persisting peak caused by the plumes (cf. e.g. Manga and Weeraratne, 1999). Thus, for $Ra = 10^5$ the PDF is Gaussian, while with increasing Ra the plumes become more predominant, resulting in a more and more prominent peak. When Ra is increased further ($Ra \gtrsim 10^9$), the background starts to resemble an exponential distribution and the plume-induced peak starts to gradually vanish. For the fully developed turbulent regime, a completely exponential shape of the PDFs is to be expected.

5.2.6 Wind profiles and viscous boundary layers

The very distinct large scale structures occurring in glycerol can also be detected by looking at the profiles of the radial and vertical velocity components and the rms velocity fluctuations. The rms velocity fluctuations, or turbulence intensities, are defined by

$$u_{rms} = \left(\langle u^2\rangle_t - \langle u\rangle_t^2\right)^{1/2}, \tag{5.2.22}$$

where u denotes one of the three velocity components, u_r, u_ϕ or u_z.

The radial and vertical velocity profiles for $10^5 \leqslant Ra \leqslant 10^9$ under OB and the NOB condition $\Delta = 40\,\mathrm{K}$ are shown in figure 5.11(a), and likewise for $Ra = 10^6$ and various NOB conditions $\Delta = 20\,\mathrm{K}$, $40\,\mathrm{K}$, $60\,\mathrm{K}$ and $80\,\mathrm{K}$ in figure 5.11(b). The radial profiles are obtained by averaging $u_z(r, \phi, z)$ in time and along ϕ and z and are thus functions of the radial position, i.e., $\langle u_z\rangle_{\phi,z,t}(r)$. Similarly, the vertical profiles are obtained by averaging $u_r(r, \phi, z)$ in time and along r and ϕ and are thus functions of the vertical position, i.e., $\langle u_r\rangle_{r,\phi,t}(z)$. The radial profiles can generally be considered to be relevant for the wind along the plates, whereas the vertical profiles are relevant for the wind being parallel to the bottom and top plate.

However, the flow patterns for glycerol are more complex than just a single LSC with corner-flows, thus the profiles' appearance does not resemble the one detected at lower Pr. That means one cannot find small negative or positive values in the vicinity of the walls caused by corner-flows, but instead one finds several maxima in the vertical profiles, and not all the radial profiles are zero at the centre line of the cylinder. Furthermore, as can be seen in figure 5.4 and 5.5, there is an up-welling structure approximately in the centre of the cylinder for $10^6 \leqslant Ra \leqslant 10^8$, under both OB and NOB conditions. Thus, close to the bottom plate, the radial flow is direct inwards, i.e. $\langle u_r\rangle_{r,\phi,t} < 0$, feeding the central structures, and then when reaching the top, the flow is consequently, directed outwards, i.e., $\langle u_r\rangle_{r,\phi,t} > 0$.

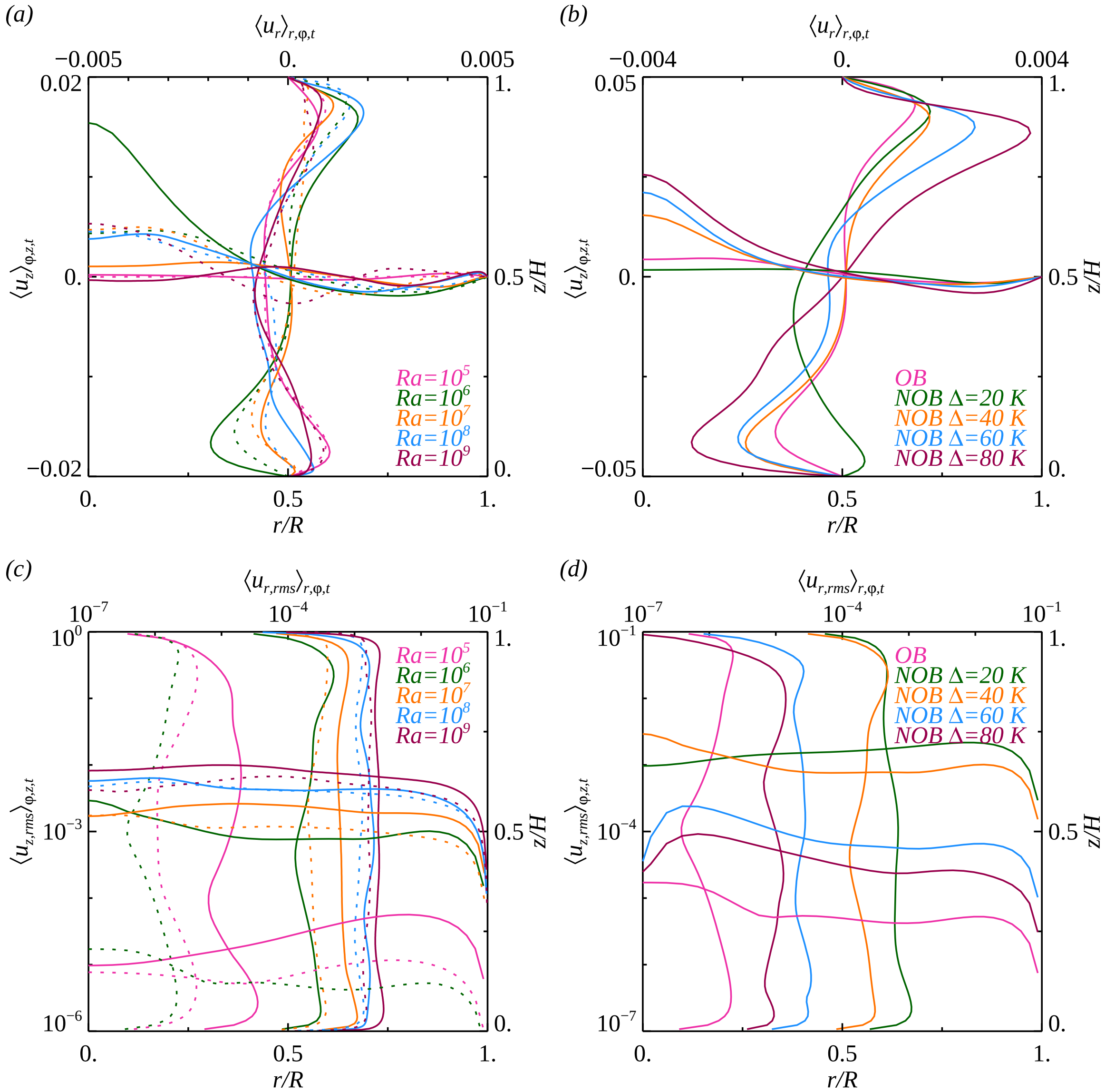

FIGURE 5.11: (a) Mean profiles of the radial velocity $u_r(z)$ and the vertical velocity $u_z(r)$ for different Ra. The dashed lines indicate the OB, the solid lines the NOB cases with $\Delta = 40\,\mathrm{K}$. (b) Similar to (a), but for constant $Ra = 10^6$ and different NOB cases, i.e., Δ, as well as under OB conditions. (c) Mean profiles of the radial rms velocity $u_{r,rms}(z)$ and the vertical rms velocity $u_{z,rms}(r)$ for different Ra. The dashed lines indicate the OB, the solid lines the NOB cases with $\Delta = 40\,\mathrm{K}$. (d) Similar to (d) but for $Ra = 10^6$ and different NOB cases, i.e., Δ, as well as under OB conditions.

The major difference in the NOB case is, that the vertical profiles are bent further away from the plate near the top, and closer towards it near the bottom compared to the OB profiles, i.e., exactly the opposite from the case for the temperature profiles. The reason is the different boundary layers, where also the largest variations of the material properties occur. But generally, there is no clear trend in which way the profiles are modified under NOB conditions. This is especially evident in the case of $Ra = 10^6$. For $\Delta = 20\,\mathrm{K}$ the velocity $\langle u_z \rangle_{\phi,z,t}(r = 0)$ is close to zero and lower than in the OB case, while for higher temperature differences Δ the velocity at the centre line is higher than in the OB case. The vertical profiles show a similar peculiar behaviour.

To understand this, I looked at the instantaneous temperature fields for OB conditions and various NOB conditions, figure 5.4(b), (g) and 5.12. Depending on the imposed Δ, a different number of cells develop, whose shapes are also clearly influenced by the cylinder wall. While for $\Delta = 20\,\mathrm{K}$ only two cells are present, a large one filling almost the whole cylinder and a very small one adjacent to it, the number of cells increases with Δ. Thus, there are three cells for $\Delta = 40\,\mathrm{K}$, four for $\Delta = 60\,\mathrm{K}$, and five for $\Delta = 80\,\mathrm{K}$. Remarkably, also under OB conditions, three cells develop, the same as for $\Delta = 40\,\mathrm{K}$. Except for $\Delta = 20\,\mathrm{K}$, there is always a coherent structure in the middle of the cell with a strong velocity component u_z directed upwards, explaining the different behaviours.

To further analyse why a different number of cells develops one needs to examine the viscous boundary layers. However, the slope criterion (e.g. Wagner et al., 2012) turned out to be inapplicable in the case of glycerol. Especially for higher Δ, the velocity profiles bend so much away from the top plate, as depicted in figure 5.11(b), that the top boundary layer thickness would be much thicker than $H/2$, which is not realistic. Thus, I decided to define the thickness of the viscous boundary layer as the vertical distance from the top and bottom plate, respectively, where the temporally averaged radial rms velocity profile $\langle u_{r,rms} \rangle_{r,\phi,t}$ reaches the first maximum,

$$\lambda_t^u = \max\left(z|_{\partial_z \langle u_{r,rms} \rangle = 0} \right), \tag{5.2.23}$$

$$\lambda_b^u = \min\left(z|_{\partial_z \langle u_{r,rms} \rangle = 0} \right). \tag{5.2.24}$$

The viscous boundary layers are thicker than the thermal ones, but show a similar asymmetry when NOB effects come into play. The reason for the asymmetry is that $\partial\nu/\partial T < 0$, and thus one has a thinner viscous boundary layer at the bottom and a thicker one at the top, which also induces correspondingly different thermal boundary layers. The ratios of top to bottom boundary layers, $\chi_\lambda^u = \lambda_t^u/\lambda_b^u$, as function of Ra and Δ are displayed in figure 5.7. χ_λ^u virtually does not depend on Ra, but increases with Δ, and reaches a maximum value of about 4.5 for $\Delta = 80\,\mathrm{K}$. The dependence of the ratio on Δ shows certain discontinuities, which agree with the points where one more cell appears, and thus implies a close connection. The increase of χ_λ means that the top boundary layer becomes thicker while the bottom one does not decrease in the same measure. I hypothesize, that this is the source of the different flow phenomenology, i.e., the different number of cells, occurring

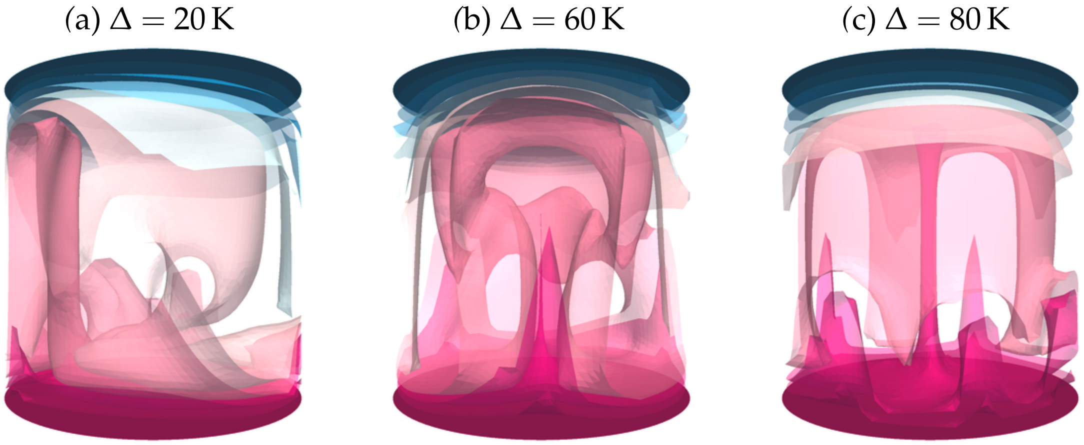

FIGURE 5.12: Instantaneous temperature isosurfaces for $\mathrm{Ra} = 10^6$ under various NOB conditions, (a) $\Delta = 20\,\mathrm{K}$, (b) $\Delta = 60\,\mathrm{K}$, (c) $\Delta = 80\,\mathrm{K}$. Shown are ten isosurfaces, evenly spaced between the minimal and maximal value, i.e. pink indicates (dimensionless) temperatures above zero and blue temperatures below zero. The corresponding temperature fields for OB conditions and $\Delta = 40\,\mathrm{K}$ can be seen in figure 5.4(b) and (g).

for different Δ: the effective volume where convection takes place and hence the effective aspect ratio is modified, and consequently the flow phenomenology.

Figure 5.11(c) and (d) show the rms profiles for the velocity components normal to the walls and parallel to it, $\langle u_{r,\mathrm{rms}} \rangle_{r,\phi,t}(z)$ and $\langle u_{z,\mathrm{rms}} \rangle_{r,\phi,t}(r)$, again for various Ra and under OB and NOB conditions and for $\mathrm{Ra} = 10^6$ and various Δ, respectively. In the OB case there is a jump of two orders of magnitude between 10^6 and 10^7 in both rms values, consistent with the qualitative observation that starting from $\mathrm{Ra} = 10^7$ plumes are emitted in a more random manner. Furthermore, the fluctuations in the velocity are higher in all NOB cases.

Alternatively, also wind profiles based on the specific kinetic energy can be introduced similar to Sugiyama et al. (2009),

$$U^E = \sqrt{\frac{1}{2}\left(u_r^2 + u_\phi^2 + u_z^2\right)}. \tag{5.2.25}$$

They are presented in figure 5.13. Since they combine all velocity components, these profiles are rather global and give a good overall impression. Hence they should be less sensitive to the actual developing flow modes, but still be sensitive to NOB effects. Indeed, the profiles have similar asymmetries to the ones presented in figure 5.11, but in figure 5.13(b) some of the peculiarities of the NOB case $\mathrm{Ra} = 10^6$ and $\Delta = 20\,\mathrm{K}$ disappear, i.e., the profiles at the top $z/H = 1$ are arranged in sequence with Δ away from the upper plate and the profiles at the bottom $z/H = 0$ are arranged in sequence closer to the lower plate.

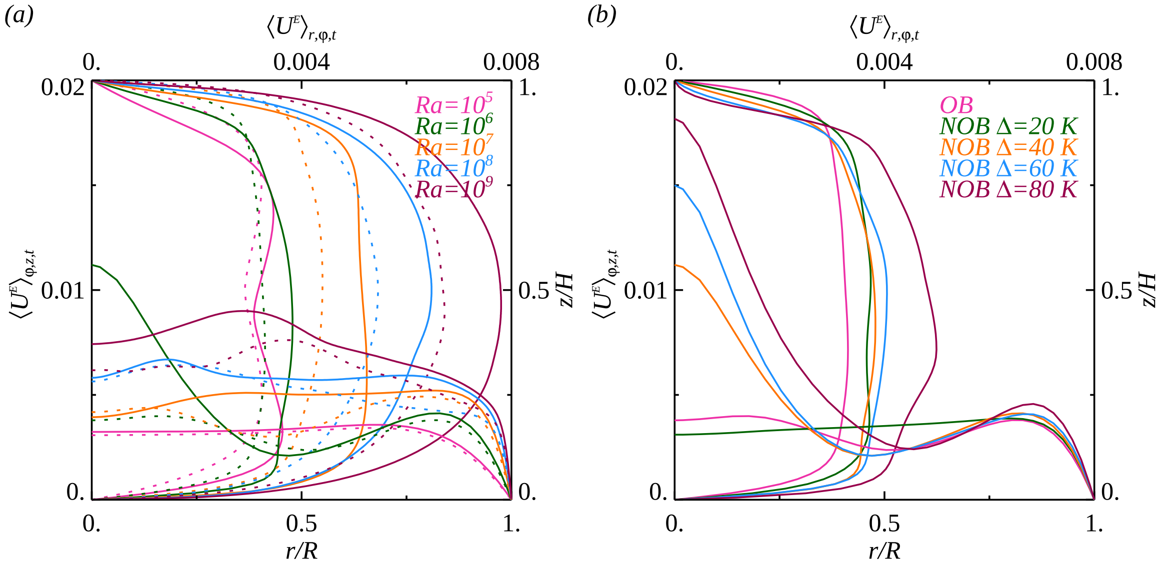

FIGURE 5.13: Energy based wind profiles as function of r and z. (a) For different Ra. The dashed lines indicate the OB, the solid lines the NOB cases with $\Delta = 40\,\mathrm{K}$. (b) Similar to (a), but for constant $\mathrm{Ra} = 10^6$ and different NOB cases, i.e., Δ, as well as under OB conditions.

5.2.7 Reynolds number

With the knowledge about the wind profiles, one can now analyse one important outcome parameter of Rayleigh–Bénard simulations, the Reynolds number Re. Its definition includes a characteristic velocity, length and viscosity scale. A reasonable choice for the characteristic length scale is the cylinder's height H, while the characteristic viscosity and the characteristic velocity are less evident and are to be determined. They can be chosen differently and thereby crucially influence the value of Re. The Reynolds number expressed within the chosen reference dimensions is

$$\mathrm{Re} = \frac{U\mathrm{Ra}^{1/2}\gamma^{1/2}}{\nu\mathrm{Pr}^{1/2}}. \tag{5.2.26}$$

I have analysed the Reynolds number Re^{pl}, based on the absolute peak value of the time averaged vertical velocity,

$$U = U^{pl} = \max|\langle u_z\rangle_t|, \tag{5.2.27}$$

representing a maximal plume speed, as suggested by Silano et al. (2010), and the Reynolds number Re^E, based on the volume averaged specific kinetic energy,

$$U = U^E_{\mathrm{tot}} = \sqrt{\left\langle \frac{1}{2}\left(u_r^2 + u_\phi^2 + u_z^2\right)\right\rangle_{V,t}}, \tag{5.2.28}$$

as was done by Sugiyama et al. (2009). Since the increased centre temperature leads to a smaller viscosity in the bulk, I also distinguish between Re_c defined with the viscosity ν_c and Re_m defined with the viscosity ν_m.

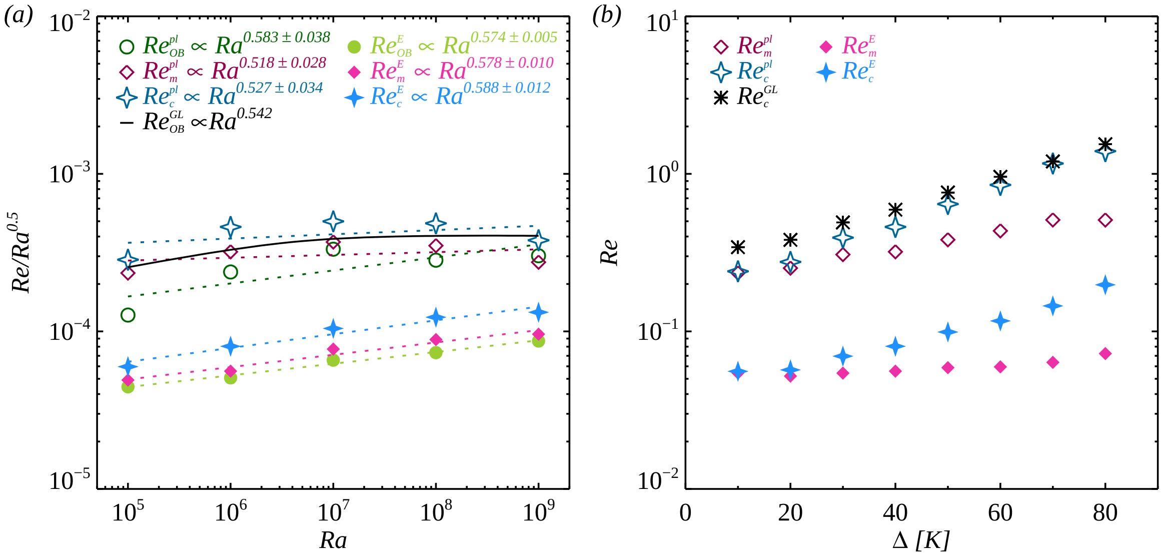

FIGURE 5.14: (a) Reduced Reynolds number $Re/Ra^{0.5}$ as function of Ra, based on the the maximal plume velocity Re^{pl} and the specific kinetic energy Re^{E}. Each defined in two ways: with the viscosity at T_m and with that at T_c, denoted by the index m and c, respectively. The dashed line shows the corresponding fitted power laws and the resulting scaling is shown in the legend. The black line shows the effective Grossmann–Lohse scaling for this range under OB conditions. (b) Similar to (a), showing Re^{pl} and Re^{E} under various NOB conditions as function of Δ for $Ra = 10^6$. The black asterisks show Re based on the Grossmann–Lohse theory evaluated for Pr_c and Ra_c.

As shown in figure 5.14 (b), the absolute value of Re^{pl} is always greater than Re^{E}. But there is only a minor influence of the different reference viscosities ν_m and ν_c for $\Delta = 40\,\mathrm{K}$ and the phenomenological behaviour is almost unaffected by it. However, Re^{pl} and Re^{E} differ not only in magnitude, but also in their scaling behaviour. I have performed power-law fits, $Re = cRe^{\gamma}$, in the range of $10^5 \leqslant Ra \leqslant 10^9$ for all defined Reynolds numbers and the results are shown in the legend of figure 5.14(a). The effective scaling in this range according to the Grossmann–Lohse theory (see esp. Ahlers et al., 2009; Grossmann and Lohse, 2002) under OB conditions is shown as well.

For Re^{E}, simple power laws are appropriate to capture the scaling of Re within the range of Ra considered. The 1-σ uncertainty estimates of the fit are at most 2% and there is no significant difference in the scaling exponents of Re^{E}_{OB}, Re^{E}_{m}, and Re^{E}_{c}. On the other hand, Re^{pl} does not obey a power law. One clearly sees that a linear fit on a double-logarithmic scale does not reflect the behaviour of Re^{pl} with Ra. Indeed, this is also obtained within the framework of the Grossmann–Lohse theory, which even yields the approximate magnitude. The corresponding scalings for Re^{pl}_{OB}, Re^{pl}_{m}, and Re^{pl}_{c} are given in figure 5.14(b), showing that here the 1-σ uncertainty estimates are about 7%. Remarkably, the NOB data agree much better, even within the uncertainty, with the Grossmann–Lohse theory than the OB data. I assume that the scaling is significantly influenced by the occurring coherent structures. Other de-

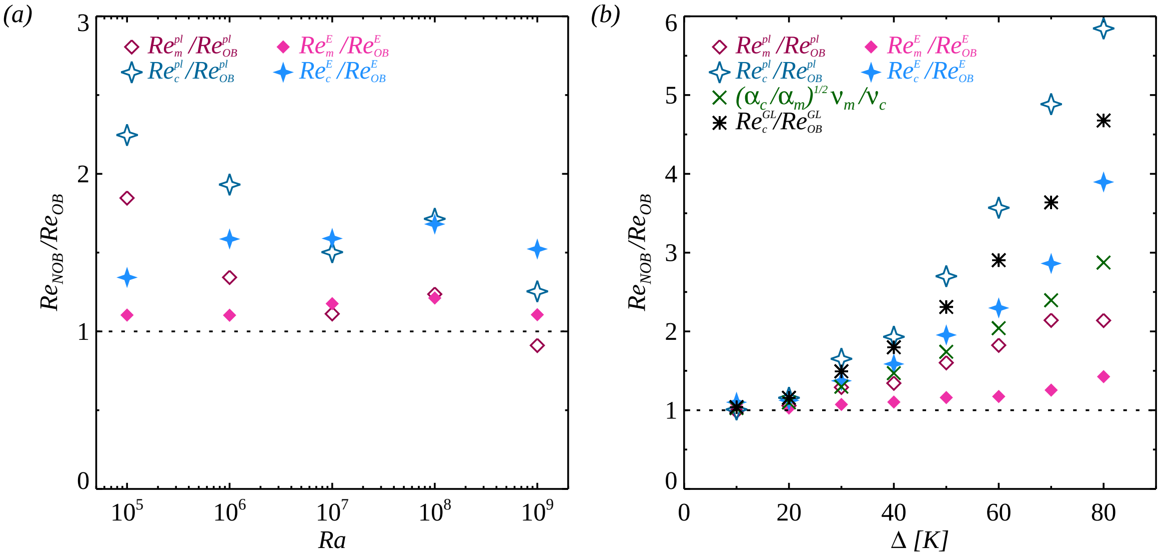

FIGURE 5.15: Ratio Re_{NOB}/Re_{OB} for the Reynolds numbers as defined in figure 5.14. The dashed line marks where $Re_{NOB} = Re_{OB}$. (a) Re_{NOB}/Re_{OB} versus Ra for $\Delta = 40\,K$ (b)Re_{NOB}/Re_{OB} versus Δ for $Ra = 10^6$. The green crosses show the ratio assuming that Re scales with the free-fall velocity, $(\alpha_c/\alpha_m)^{1/2}\nu_m/\nu_c$ as suggested by Sugiyama et al. (2009). The black asterisks shows the ratio based on the Grossmann–Lohse theory, evaluated for Pr_c and Ra_c and for their respective values under OB conditions, Pr_m and Ra_m.

viations might be caused by the fact that the Grossmann–Lohse theory assumes a single wind amplitude originating in the LSC, that furthermore needs to be uniform throughout the Rayleigh–Bénard cell, while for glycerol more complex spatial flow structures occur.

Figure 5.14(b) presents Re as a function of Δ for constant $Ra = 10^6$. Due to the reduced viscosity ν_c in the bulk, the deviation between the two curves for Re_m and Re_c becomes considerably larger with increasing Δ. By evaluating them for the material properties at T_c, equivalent to using Ra_c and Pr_c, a general agreement of Re_c^{GL} with Re_c^{pl} and the principal dependence on Δ can be obtained, especially for higher Δ.

Figure 5.15 shows the dependence of the ratios of the NOB to the OB Reynolds numbers on Ra and Δ. For constant $\Delta = 40\,K$, see figure 5.15(a), the data appear just scattered. However, as seen in figure 5.15(b), for $Ra = 10^6$ and varying Δ, they follow a clear increasing trend. Re_c^{pl} is most sensitive to NOB effects, for $\Delta = 80\,K$ the Reynolds number is 6 times higher than in the OB case; Re_m^E is least sensitive to NOB effects, being only 1.5 times higher in that case. Assuming that U_{tot}^E is similar to the free-fall velocity $\sqrt{\alpha g \Delta H}$, Sugiyama et al. (2009) obtained that the ratio Re_{NOB}^E/Re_{OB}^E should be proportional to $(\alpha_c/\alpha_m)^{1/2}\nu_m/\nu_c$. This is a very rough estimate, being equivalent to a scaling of $Re \propto Ra^{1/2}Pr^{-1/2}$. Nonetheless, the agreement with the obtained DNS data is satisfactory. A refinement of this method would be to use the scaling relations proposed by Grossmann and Lohse (2002). Indeed, this predicts the Δ dependence better, especially for higher Δ.

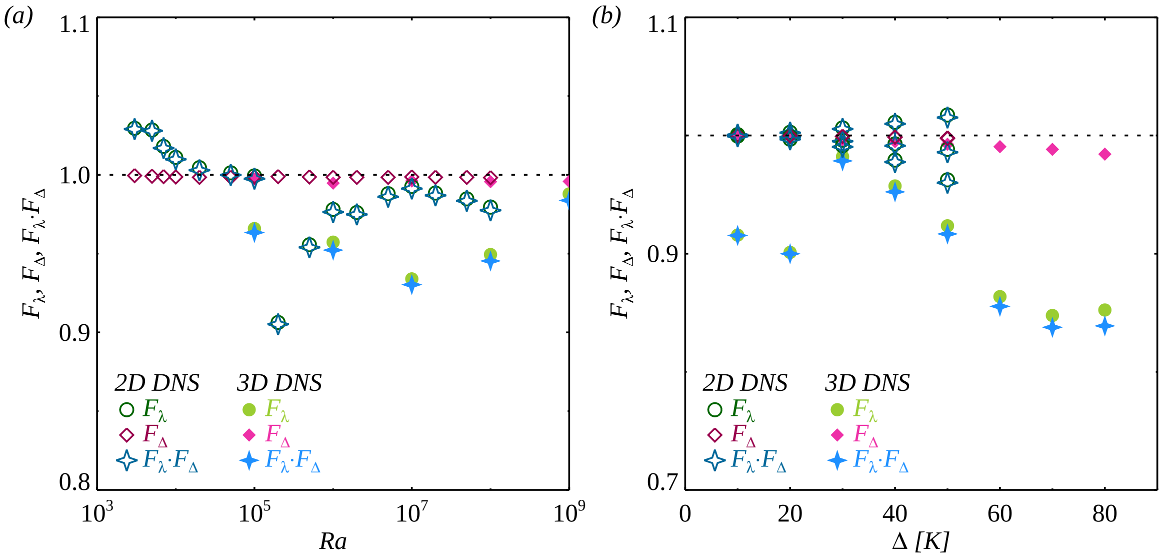

FIGURE 5.16: Nusselt number ratio $Nu_{NOB}/Nu_{OB} = F_\lambda F_\Delta$ and its contributing factors F_λ and F_Δ. Shown are the 3D DNS data as well as the 2D data from Sugiyama et al. (2007). (a) $F_\lambda \cdot F_\Delta$, F_λ and F_Δ versus Ra for $\Delta = 40\,K$. (b)$F_\lambda F_\Delta$, F_λ and F_Δ versus Δ for $Ra = 10^6$. The dashed line corresponds to $F = 1$.

5.2.8 Heat transfer and Nusselt number scaling

The dimensionless heat flux, expressed in terms of the Nusselt number Nu is another important output parameter. High Prandtl number fluids distinguish themselves by a strong convective heat transfer. With the definition of the boundary layers based on the slope criterion, the Nusselt number in the NOB case is given by the exact relation

$$Nu_{NOB} = \frac{H}{\lambda_t^\theta + \lambda_b^\theta} \frac{\kappa_t \Delta_t + \kappa_b \Delta_b}{\kappa_m \Delta}, \tag{5.2.29}$$

as was shown by Ahlers et al. (2006). This equation looks similar to the well-known equation in the OB case,

$$Nu_{OB} = \frac{H}{2\lambda_{OB}}, \tag{5.2.30}$$

and a straightforward calculation then yields for the ratio of the NOB to the OB Nusselt number

$$\frac{Nu_{NOB}}{Nu_{OB}} = \frac{2\lambda_{OB}}{\lambda_t + \lambda_b} \frac{\kappa_t \Delta_t + \kappa_b \Delta_b}{\kappa_m \Delta} = F_\lambda F_\Delta. \tag{5.2.31}$$

The factors F_λ and F_Δ and their product are displayed in figure 5.16. In the case of glycerol, the heat conductivity Λ, or, equivalently the heat diffusivity κ, depends only very weakly on the temperature. Thus $F_\Delta \simeq 1$ for the considered temperature range. The important factor for the deviation of the Nusselt number rather originates from F_λ and not from F_Δ as in the case of water, this was also found by Sugiyama et al. (2007) and was implicitly assumed by Zhang et al. (1997). Since the presented DNS are neither steady nor turbulent, but always plume-dominated or

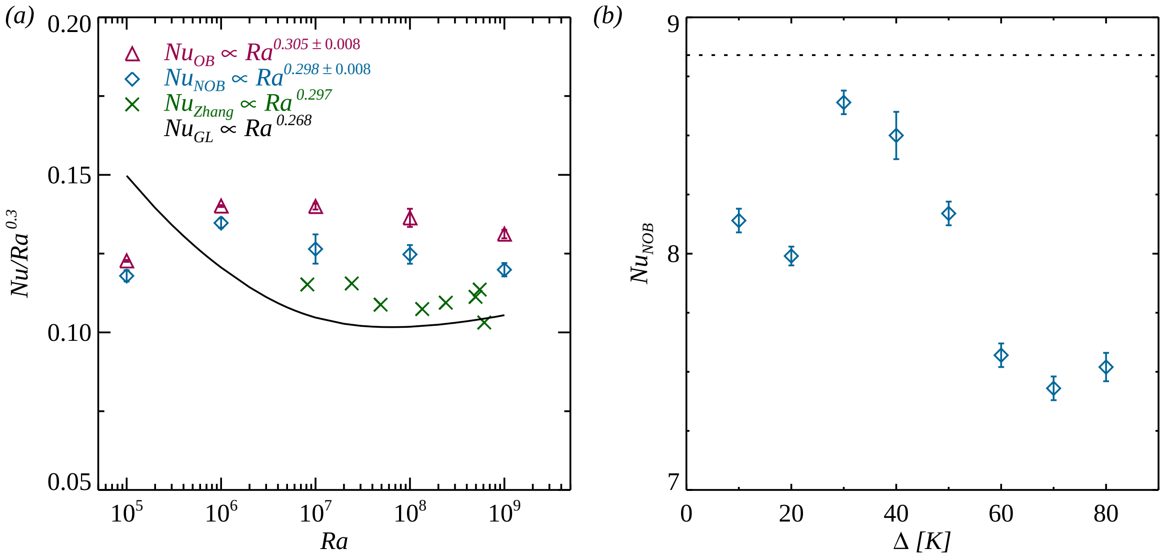

FIGURE 5.17: (a) Reduced Nusselt number $\mathrm{Nu}/\mathrm{Ra}^{0.3}$ as a function of Ra under OB (purple triangles) and NOB conditions with $\Delta = 40\,\mathrm{K}$ (blue diamonds). The Nusselt number is evaluated as a plane average, i.e., the vertical heat flux, and the error bar indicates the standard deviation of the constant Nu profile along z. The experimental data from Zhang et al. (1997) (green crosses) are also shown, however, I would like to point out that first, Pr varied between approximately 600 and 8000, second, their Nusselt number is based on a constant κ, i.e., $\mathrm{Nu} = H/(\lambda_t^\theta + \lambda_b^\theta)$. The black line shows the effective scaling for the OB case, according to the Grossmann–Lohse theory. (b) Nu as a function of Δ under NOB conditions for constant $\mathrm{Ra} = 10^6$ and varying Δ. The dashed line indicates the OB value.

transitional, the Nusselt number depends in a strongly non-linear way on Δ and Ra due to the complex and distinct flow patterns. In the two-dimensional simulations by Sugiyama et al. (2007), this non-linear behaviour of Nu with Δ was found as well. But evidently, the flow patterns are different under these circumstances. For all considered combinations of Rayleigh numbers Ra and temperature differences Δ, the deviations are more pronounced in the three-dimensional case.

Figure 5.17(a) finally also presents Nu as a function of Ra under OB and NOB conditions, including the scaling predicted by Grossmann and Lohse (2000, 2001) and the experimental data by Zhang et al. (1997). The effective exponents can be found in the legend. While the scaling practically does not change under NOB conditions, and the agreement with the experiments is remarkably good considering the different Prandtl numbers, the Grossmann–Lohse theory slightly underestimates the Nusselt number. The reason might be that the available experimental data to fix the constants in this regime are rather sparse, making scaling predictions less accurate.

5.3 Non-Oberbeck–Boussinesq effects in water

This section is devoted to Rayleigh–Bénard convection of water with non-constant thermophysical properties. Several authors have studied NOB effects by means of experimentsAhlers et al. (2006); Brown and Ahlers (2007) and two-dimensional numerical simulations (Sugiyama et al., 2009). While compared to glycerol, the properties of water only posses a rather weak dependence on the temperature, i.e. has the advantages of being computational less expensive, showing developed turbulence already for $\mathrm{Ra} \approx 10^8$ and nonetheless significant NOB effects (Ahlers et al., 2006; Sugiyama et al., 2009).

The simulations were performed under OB and various NOB conditions for the Rayleigh numbers 10^7, 10^8 and 10^9. The temperature differences are chosen to be up to 70 K to guarantee for measurable NOB effects, but being still in a temperature range far enough away from the water density anomaly at around 4 °C. These simulations also serve as reference for the simulations, where the Rayleigh–Bénard cell is additionally rotated, discussed in the following chapter 6. Hence, it is very important to note that by specifying Δ and the temperature-dependencies of the material properties, one also fixes all the other dimensions in the NOB simulations for a constant Ra. The parameters for the performed DNS are presented figure 5.2(a) and in table 5.4.

Ra	Δ[K]	H[cm]	$N_r \times N_\phi \times N_z$
10^7	OB	—	$64 \times 512 \times 128$
10^7	$\{10, 20, 30, 40, 50, 60, 70\}$	$\{3.0, 2.3, 2.1, 1.9, 1.8, 1.6, 1.6\}$	$64 \times 512 \times 128$
10^8	OB	—	$192 \times 512 \times 384$
10^8	$\{10, 20, 30, 40, 50, 60, 70\}$	$\{6.5, 5.1, 4.5, 4.1, 3.8, 3.6, 3.4\}$	$192 \times 512 \times 384$
10^9	OB	—	$384 \times 512 \times 768$
10^9	$\{20, 40, 60\}$	$\{11.0, 8.8, 7.7\}$	$384 \times 512 \times 768$

TABLE 5.4: Simulation parameters, i.e. Rayleigh number Ra, temperature difference Δ, height H and the grid resolution in radial, azimuthal and vertical direction $N_r \times N_\phi \times N_z$. The OB simulations are dimensionless, while NOB simulations always imply dimensions.

5.3.1 Centre temperature T_c

Firstly, I present the results for the centre temperature T_c, since it is probably the most prominent NOB effect. The increase of the temperature within the bulk can clearly be seen in Fig. 5.18 and in the mean temperature profiles in Fig. 5.19(a). The higher the applied temperature difference Δ, the hotter the fluid inside the Rayleigh–Bénard cell. This effect can be evaluated quantitatively by analysing the centre temperature, i.e. the radially, azimuthally and temporally averaged temperature at mid-height,

$$T_c \equiv \langle T\,|_{z=H/2}\rangle_{r,\phi,t}. \tag{5.3.1}$$

Figure 5.19(b) presents T_c as obtained by the DNS for $\mathrm{Ra} \in \{10^7, 10^8, 10^9\}$ for temperature differences Δ between 10 K and 70 K. T_c increases with Δ. For $\Delta = 70\,\mathrm{K}$ T_c is about 5.5 K higher than in the OB case. For comparison, the experimental data by Ahlers et al. (2006) for $10^9 \lesssim \mathrm{Ra} \lesssim 10^{11}$ and the two-dimensional DNS results by

Sugiyama et al. (2009) for $Ra = 10^8$ are also shown. All three data sets are in excellent agreement and, moreover, there is no significant dependence on the Rayleigh number for the cases considered. For lower Ra, i.e. when the bulk is not fully turbulent, T_c as function of Δ might be slightly lower (Sugiyama et al., 2009).

Several models (Ahlers et al., 2006; Manga and Weeraratne, 1999; Wu and Libchaber, 1991; Zhang et al., 1997) have been proposed to predict T_c, however, the suitability of the model strongly depends on the fluid (Chillà and Schumacher, 2012; Horn et al., 2014). In the case of water, an extension of the Prandtl–Blasius boundary

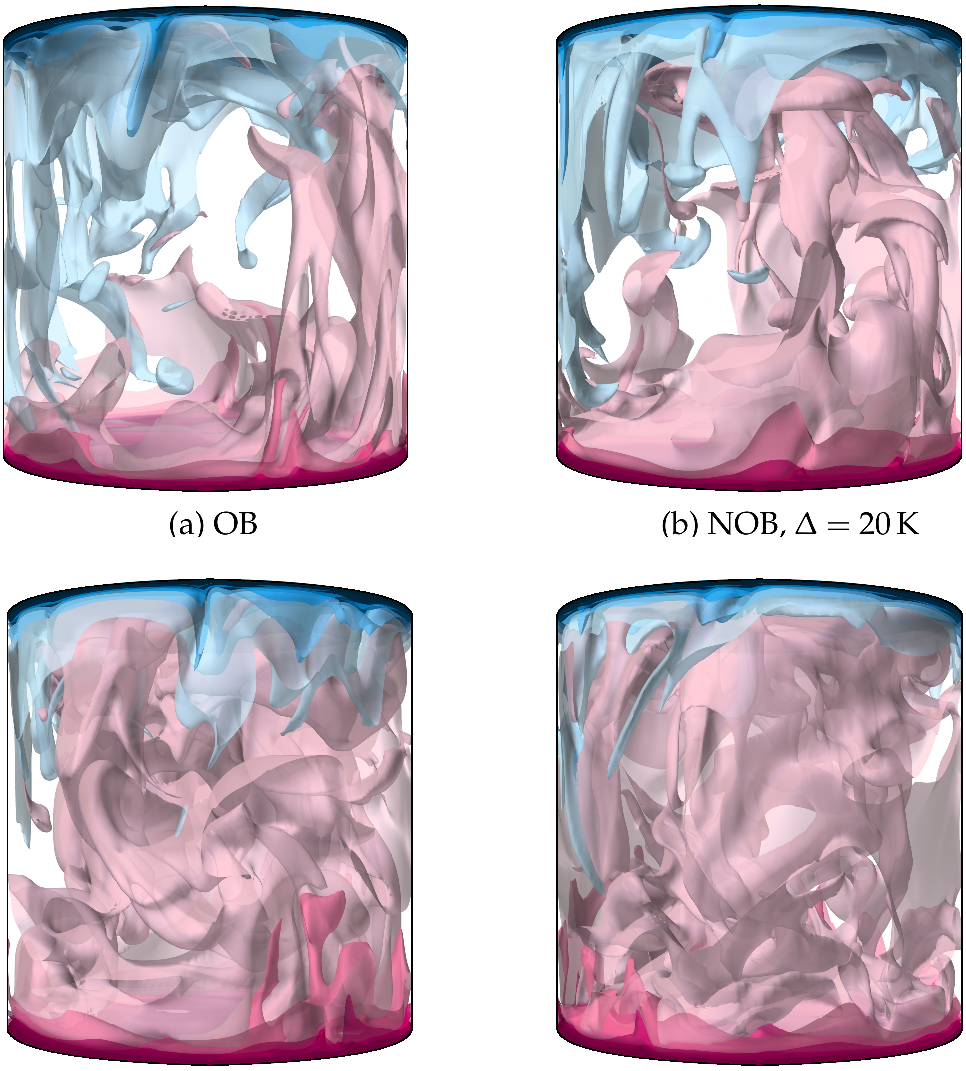

(a) OB

(b) NOB, $\Delta = 20\,\mathrm{K}$

(c) NOB, $\Delta = 40\,\mathrm{K}$

(d) NOB, $\Delta = 60\,\mathrm{K}$

FIGURE 5.18: Instantaneous temperature fields for $Ra = 10^8$ under (a) OB conditions and three different NOB conditions, (b) $\Delta = 20\,\mathrm{K}$, (c)$\Delta = 40\,\mathrm{K}$ and (d) $\Delta = 60\,\mathrm{K}$. Visualized are isosurfaces for ten equidistantly distributed values between the top and bottom temperature, T_t and T_b. Pink corresponds to temperatures above the mean temperature T_m and blue to temperatures below T_m.

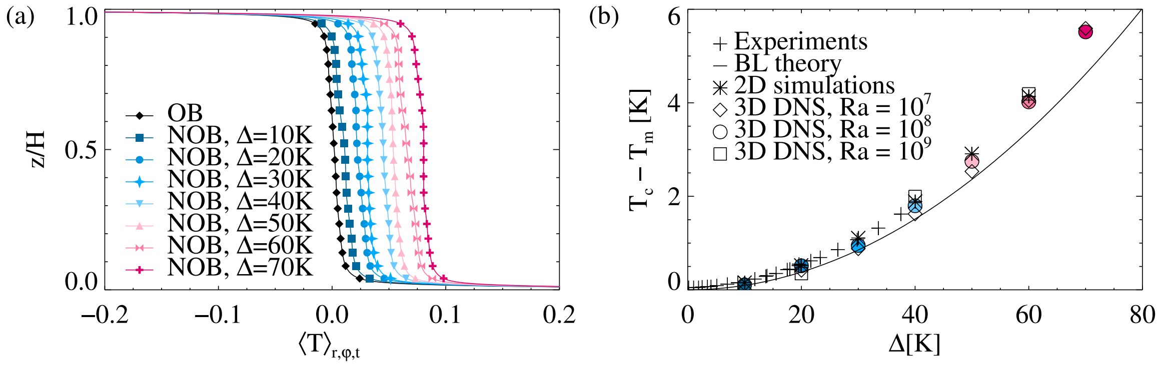

FIGURE 5.19: (a) Mean temperature profiles for $\mathrm{Ra} = 10^8$ under OB and various NOB conditions, $\Delta \in \{10\,\mathrm{K}, 20\,\mathrm{K}, 30\,\mathrm{K}, 40\,\mathrm{K}, 50\,\mathrm{K}, 60\,\mathrm{K}, 70\,\mathrm{K}\}$. Note that not the full temperature range is shown. (b) Deviation of the center temperature T_c from the mean temperature T_m as function of the temperature difference Δ. The pluses show the experimental data by Ahlers et al. (2006), the asterisks represent the two-dimensional numerical data by Sugiyama et al. (2009) for $\mathrm{Ra} = 10^8$, the solid dashed line is the prediction by the extended Prandtl–Blasius boundary layer theoryAhlers et al. (2006). The DNS data obtained for $\mathrm{Ra} = 10^7$, 10^8 and 10^9 are denoted by diamonds, circles and squares, respectively.

layer theory to non-constant viscosity ν and thermal diffusivity κ has been proven to be very successful (Ahlers et al., 2006; Sugiyama et al., 2009). The prediction of this theory is also depicted in Fig. 5.19(b). Since the variation of κ is rather small compared to the variation of ν with temperature, this also supports the hand-wavy explanation of the enhanced T_c: The fluid at the bottom is warmer, thus, in comparison to OB convection, the viscosity is lower and, thus, the fluid and the plumes emerging from the bottom boundary layer are more mobile, i.e. they are able to cross the cell faster. Furthermore, they also spend less time in contact with the ambient fluid and, hence, have less time to cool down. The analogue is true for the cold plumes from the top; their viscosity is higher, they move slower and they have more time to warm up in the bulk. As a consequence, the temperature in the centre of the cell enhances. This suggests, that in the case of water the viscosity is the major reason for an increase of T_c with Δ.

5.3.2 Boundary layers

Another very well-known feature of NOB convection, already discussed for glycerol, are the different boundary layer thicknesses at the top and bottom. They are presented in Fig. 5.20. The boundary layer thicknesses are defined by the slope criterion, i.e. they are determined by the point where the tangent of the profile at the plate intersects with either the center temperature, in the case of thermal boundary layers, or with the maxima of the radial velocity, in the case of viscous boundary layers. Mathematically expressed, the thermal top and bottom boundary layer thicknesses are given by

$$\lambda_t^\theta = \frac{T_t - T_c}{\partial_z \langle T \rangle_{r,\phi,t}|_{z=H}}, \qquad \lambda_b^\theta = \frac{T_c - T_b}{\partial_z \langle T \rangle_{r,\phi,t}|_{z=0}}, \tag{5.3.2}$$

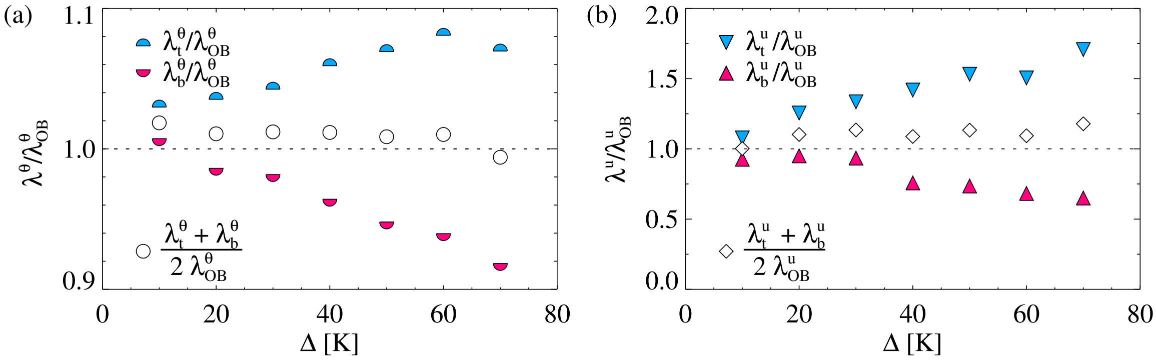

FIGURE 5.20: Boundary layer thicknesses in the NOB case normalized by the boundary layer thickness in the OB case for $Ra = 10^8$. Their calculation is based on the slope criterion, cf. eq.s (5.3.2)–(5.3.3). (a) Thermal boundary layer thicknesses, upper half circles: top thermal boundary layer λ^θ_t, lower half circles: bottom thermal boundary layer λ^θ_b, circles: ratio of the sum of the NOB to the OB boundary layer thicknesses. (b) Viscous boundary layer thicknesses, downward triangles: top viscous boundary layer λ^u_t, upward triangles: bottom viscous boundary layer λ^u_b, diamonds: ratio of the sum of the NOB to the OB boundary layer thicknesses.

and similarly the viscous ones are given by,

$$\lambda^u_t = -\frac{u_r^{\max_t}}{\partial_z \langle u_r \rangle_{r,\phi,t}\big|_{z=H}}, \qquad \lambda^u_b = \frac{u_r^{\max_b}}{\partial_z \langle u_r \rangle_{r,\phi,t}\big|_{z=0}}, \tag{5.3.3}$$

where $u_r^{\max_t}$ and $u_r^{\max_b}$ are the first maxima of the radial velocity profile close to the top and bottom plate, respectively. In the OB case, the top and bottom boundary layers have, of course, the same thickness,

$$\lambda_{OB} = \lambda_t = \lambda_b. \tag{5.3.4}$$

In the NOB case, on the contrary, the top boundary layers are always thicker than the bottom ones. Furthermore, they exhibit the very peculiar behavior, that the sum of their thicknesses approximately equals the sum of the thicknesses in the OB case, i.e.

$$\lambda_t + \lambda_b \approx 2\lambda_{OB}. \tag{5.3.5}$$

This holds for both, the viscous and the thermal boundary layer thicknesses. To be more precise, their ratio $(\lambda_t + \lambda_b)/(2\lambda_{OB})$ equals 1.009 ± 0.007 for the thermal and 1.10 ± 0.06 for the viscous boundary layer thicknesses. Thus, for both types the sum of OB boundary layer thicknesses is slightly greater than the sum of the NOB ones and approximation (5.3.5) works better for the thermal boundary layers. For some time it was suspected that eq. (5.3.5) is a universal NOB behavior (Ahlers et al., 2006), however, for example in the case of glycerol this relation does not hold at all (Horn et al., 2014; Sugiyama et al., 2007).

5.3.3 Nusselt number

Finally, the dimensionless heat flux, the Nusselt number, defined by eq. (5.2.6) is shown in figure 5.21(a) as function of Ra for the OB case and the NOB case with $\Delta = 40\,\mathrm{K}$ and compared to experimental data by Funfschilling et al. (2005) and the predictions by the Grossmann–Lohse (GL) theory (Ahlers et al., 2009; Grossmann and Lohse, 2000, 2001, 2002) using the updated prefactors (Stevens et al., 2013a) $c_1 = 8.685$, $c_2 = 1.441$, $c_3 = 0.462$, $c_4 = 0.013$, $a = 0.482$, $\mathrm{Re}_c = (2a)^2$. The Nusselt number in the DNS presented here is evaluated using the mean value of the r-ϕ plane averaged heat fluxes for all vertical z positions (Shishkina and Wagner, 2007a) and the error bars indicate the standard deviation. There is a good agreement of the experimental data, the OB DNS results and with the GL theory. The Nusselt number in the case of temperature-dependent material properties, $\mathrm{Nu}_{\mathrm{NOB}}$, is always slightly lower than in the pure OB case, $\mathrm{Nu}_{\mathrm{OB}}$. But despite that fact, the deviation and especially its scaling with Ra is only marginal, i.e. $\mathrm{Nu}_{\mathrm{OB}} \propto \mathrm{Ra}^{0.293\pm0.001}$ compared to $\mathrm{Nu}_{\mathrm{NOB}} \propto \mathrm{Ra}^{0.288\pm0.003}$. And even for higher Δ, as depicted in figure 5.21(b), the deviation remains below 5%. The insensitivity of the Nusselt number can be understood by expressing Nu in terms of the temperature gradient at the plates, eq. (5.2.30), in the OB case, and similarly, eq. (5.2.29), in the NOB case, with $\Delta_t = T_c - T_t$ and $\Delta_b = T_b - T_c$ being the top and bottom temperature drop, respectively. Hence, the relation (5.2.31)

$$\frac{\mathrm{Nu}_{\mathrm{NOB}}}{\mathrm{Nu}_{\mathrm{OB}}} = \frac{2\lambda_{\mathrm{OB}}}{\lambda_t^{\theta} + \lambda_b^{\theta}} \frac{\Lambda_t\Delta_t + \Lambda_b\Delta_b}{\Lambda_m\Delta} = F_\lambda F_\Delta \tag{5.3.6}$$

holds (Ahlers et al., 2006). By inserting approximation (5.3.5), the first factor F_λ equals one. By using the exact values obtained from the DNS it is slightly less

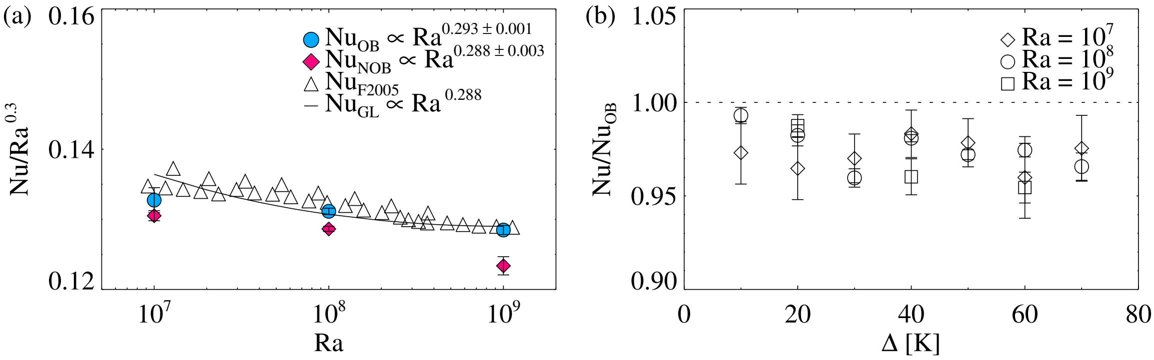

FIGURE 5.21: (a) Reduced Nusselt number $\mathrm{Nu}/\mathrm{Ra}^{0.3}$ as function of Ra under OB (circles) and NOB conditions with $\Delta = 40\,\mathrm{K}$. Additionally, the experimental data by Funfschilling et al. (2005) and the predictions by the Grossmann–Lohse theory (Grossmann and Lohse, 2000) using the updated prefactors (Stevens et al., 2013a) $c_1 = 8.685$, $c_2 = 1.441$, $c_3 = 0.462$, $c_4 = 0.013$, $a = 0.482$, $\mathrm{Re}_c = (2a)^2$ are presented. (b) Nusselt number $\mathrm{Nu}_{\mathrm{NOB}}$ for various NOB conditions normalized by the value under OB conditions $\mathrm{Nu}_{\mathrm{OB}}$ as function of Δ; diamonds: $\mathrm{Ra} = 10^7$, circles: $\mathrm{Ra} = 10^8$, squares: $\mathrm{Ra} = 10^9$. The Nusselt numbers were obtained by the mean value of the r-ϕ plane averaged heat fluxes for all vertical z positions. The error bars indicate the standard deviation.

than one. Since there is also no strong temperature-dependence of Λ, the second factor F_Δ depends only weakly on Δ and is likewise close to one. However, one can even show, that F_Δ is also always less than one, since the center temperature is always higher than the mean temperature. Thus, even though, there is only a weak dependence of Nu on Δ, Nu_{NOB} is necessarily smaller than Nu_{OB}.

5.4 Summary

Rayleigh-Bénard convection of glycerol with $Pr = 2547.9$ and water with $Pr = 4.38$ was investigated in a cylindrical cell of aspect ratio unity. I focused my attention on the influence of NOB effects.

Under ambient conditions the validity range of the OB approximation is severely violated for glycerol. I performed three-dimensional DNS in a range of $10^5 \leqslant Ra \leqslant 10^9$ for OB conditions and NOB conditions between $10\,K \leqslant \Delta \leqslant 80\,K$. The results were compared to the only available experimental data by Zhang et al. (1997, 1998), and numerical (but only two-dimensional) data of Sugiyama et al. (2007). The developing flow patterns in glycerol for lower Ra resemble the behavior of lower Pr and higher Γ, i.e., several cells are observed. The number of cells, moreover, depends on the imposed Δ. However, for large enough Rayleigh numbers, i.e., $Ra \gtrsim 10^8$, a typical LSC as in $\Gamma = 1$ and $Pr = O(1)$ Rayleigh–Bénard convection is found. This behavior could not be reproduced in two-dimensional simulations. While these simulations are useful to investigate qualitatively the properties of the three-dimensional flow, three-dimensional DNS are evidently necessary to resolve its full topology.

Under NOB conditions, the perfect symmetry with respect to the horizontal midplane is broken. One of the most remarkable features then is the higher center temperature. The deviation $T_c - T_m$ is as large as $15\,K$ for $\Delta = 80\,K$. The obtained values of T_c agree perfectly well with the experiments, when only the experimental points for $Pr > 1200$ are considered. For lower Pr, the experimentally obtained center temperatures are lower. The two-dimensional simulations by Sugiyama et al. (2007) yielded a lower T_c than the three-dimensional ones, even though the same Pr was considered in their case. I also compared my results with the predictions of the theoretical and empirical models by Manga and Weeraratne (1999); Wu and Libchaber (1991); Zhang et al. (1997), and Ahlers et al. (2006). While the 2D boundary layer models by Zhang et al. (1997) and Ahlers et al. (2006) overestimate the actual T_c, due to the plume emission all over the plate and the not always existing LSC, the models by Wu and Libchaber (1991), based on the same temperature or velocity scales in the boundary layers, predict T_c very well with a standard deviation of $0.4\,K$.

Furthermore, I analysed the temperature and velocity profiles. Due to the strongly varying viscosity and heat conductivity close to the heating and cooling plates, the temperature profiles bend towards the plate near the cold top plate and farther away from it near the hot bottom plate, whereas the situation for the velocity profiles is the other way round: they bend farther away from the top plate and closer to the bottom plate. This also induces different thermal and viscous boundary layer thicknesses. The top boundary layers are always thicker than the bottom ones. Their ratio is up to 2.5 for the thermal and up to 4.5 for the viscous boundary layers.

The two important output parameters of Rayleigh–Bénard convection, the Reynolds number Re and the Nusselt number Nu, were investigated as well. In the parameter range considered, Re is always higher and Nu is always lower under NOB than under OB conditions. Re was evaluated for different choices of the characteristic velocity, i.e., based on the total volume averaged kinetic energy U^{E}_{tot} and the plume velocity U^{pl}, and for different choices of the characteristic viscosity, i.e., the mean and the centre viscosity ν_m and ν_c. The absolute value of Re is highly sensitive, but the scaling with Ra is only slightly sensitive, to the choice of the characteristic scales. For $Ra = 10^6$ and $\Delta = 80\,K$, the Reynolds number defined with U^{pl} and ν_c is up to 6 times higher than in the OB case. This increase can be described with satisfactory accuracy by the Grossmann–Lohse theory based on Ra_c and Pr_c. The Nusselt number Nu is influenced in a non-linear way by NOB effects, and more strongly than was suggested by the two-dimensional simulations.

The scaling of Nu with Ra shows no significant difference between NOB and OB conditions, i.e., $Nu_{OB} \propto Ra^{0.305}$ and $Nu_{NOB} \propto Ra^{0.298}$. The NOB scaling is in excellent agreement with the experimental data.

For water, the validity range of the OB approximation is much larger. Albeit the fact, that the properties of water only posses a rather weak dependence on the temperature, it shows significant NOB effects. In water, I focused on the most prominent features, namely, the increase of the centre temperature T_c, different boundary layer thicknesses and the modification of the dimensionless heat flux, the Nusselt number Nu. Similar as in glycerol, T_c increases together with the applied temperature difference. For $\Delta = 70\,K$ T_c is about 5.5 K higher than in the OB case. This increase is well predicted by an extension of the Prandtl–Blasius boundary layer theory proposed by Ahlers et al. (2006). This suggests that the temperature dependence of the viscosity is mainly responsible for the enhanced T_c. The top viscous and thermal boundary layers are always thicker than the bottom boundary layers, but their sum equals approximately the sum of the boundary layers under perfect OB conditions. Furthermore, the Nusselt number Nu is lower under NOB conditions, but this deviation remains below 5%, even for temperature differences up to 70 K.

Non-Oberbeck–Boussinesq effects in rotating Rayleigh–Bénard convection of water [*]

Only few systematic studies of the influence of temperature-dependent material properties on rotating Rayleigh–Bénard convection can be found. If, then concerning pattern formation and, thus, with larger aspect ratios (Young et al., 2003). But it is a very fascinating question what happens if NOB and rotational effects are superimposed. Hence, here I discuss simulations of rotating thermal convection in water at $T_m = 40\,^\circ\mathrm{C}$, thus, with $\mathrm{Pr} = 4.38$, considering its actual properties.

6.1 Parameter space

For the simulations with rotation, I set the temperature difference to $\Delta = 40\,\mathrm{K}$ and the Rayleigh number to $\mathrm{Ra} = 10^8$ in the NOB case. The inverse Rossby number range is given by $1/\mathrm{Ro} \in \{0.07, 0.24, 0.35, 0.71, 1.01, 1.41, 2.36, 2.83, 3.54, 4.71, 7.07, 11.31, 14.14\}$. Hence, the smallest Ekman number achieved is $\mathrm{Ek} \approx 3 \times 10^5$, thus, still about one magnitude larger than when asymptotically reduced equations are to be expected to be sufficient, as introduced by Julien et al. (2012). In the OB case, additionally to $\mathrm{Ra} = 10^8$, moreover a series of DNS was conducted for $\mathrm{Ra} = 1.16 \times 10^9$ and $1/\mathrm{Ro} \in \{0.24, 0.71, 1.41, 2.36, 3.54, 7.07, 11.31, 14.14\}$ to compare with available experimental data by Kunnen et al. (2011) with exactly the same Prandtl number of $\mathrm{Pr} = 4.38$.

Since the dimensions are fixed under NOB conditions, it is also possible to estimate the potential importance of centrifugal buoyancy effects by calculating the Froude number,

$$\mathrm{Fr} = \frac{\Omega^2 D}{2g} = \frac{\alpha_m \Delta \Gamma}{8\mathrm{Ro}^2}. \tag{6.1.1}$$

In experiments it is usually attempted to keep Fr as small as possible, i.e. around 0.05 and lowerZhong et al. (2009). For the fastest rotation rates, i.e. $1/\mathrm{Ro} = 14.14$, and $\Delta = 40\,\mathrm{K}$ the Froude number is $\mathrm{Fr} = 0.4$ which suggests that centrifugal buoyancy effects might be observedHart and Ohlsen (1999); Homsy and Hudson (1969); Lopez and Marques (2009); Marques et al. (2007); Rossby (1969) and only for $1/\mathrm{Ro} \lesssim 5$ they are expected to be negligible. Considering $\mathrm{Fr} \neq 0$, however, would lead to an additional source of breaking the symmetry about the mid plane and it

---

[*] Adopted from Horn, S. and Shishkina, O., Rotating non-Oberbeck–Boussinesq Rayleigh–Bénard convection in water, *Phys. Fluids 26(5)* (2014), 055111.

would be hard to decouple centrifugal buoyancy and NOB effects. Thus, I deliberately set $\mathrm{Fr} \equiv 0$.

(a) OB, $1/Ro = 0$ (b) OB, $1/Ro = 0.7$ (c) OB, $1/Ro = 1.4$ (d) OB, $1/Ro = 7.1$ (e) OB, $1/Ro = 14.1$

(f) NOB, $1/Ro = \infty$ (g) NOB, $1/Ro = 0.7$ (h) NOB, $1/Ro = 1.4$ (i) NOB, $1/Ro = 7.1$ (j) NOB, $1/Ro = 14.1$

FIGURE 6.1: Instantaneous temperature fields for $Ra = 10^8$. Visualized are isosurfaces for ten equidistantly distributed values between the top and bottom temperature, T_t and T_b. Pink corresponds to temperatures above the mean temperature T_m and blue to temperatures below T_m. The upper panel, (a)–(e), shows the OB cases, the lower panel, (f)–(j), shows the NOB cases with $\Delta = 40\,K$. The rotation rate increases from left to right. (a), (f) $Ro = 0$; (b), (g) $Ro = 0.7$; (c), (h) $Ro = 1.4$; (d), (i) $Ro = 7.1$ and (e), (j) $Ro = 14.1$.

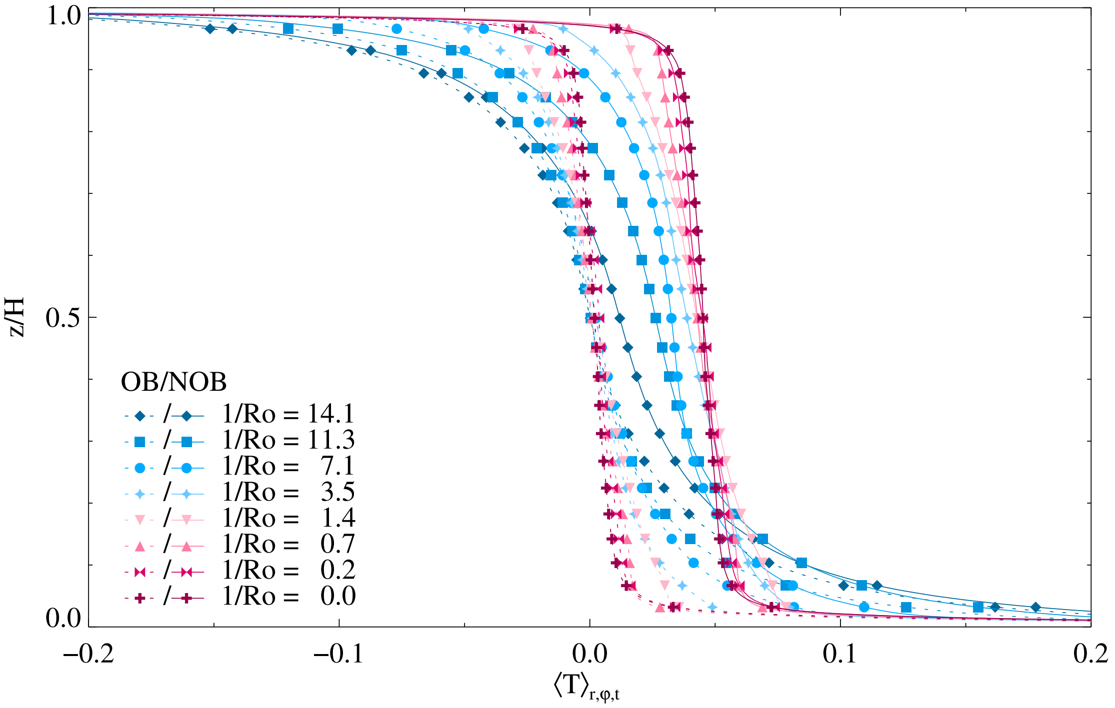

FIGURE 6.2: Mean temperature profiles for $Ra = 10^8$. The dotted lines show the OB profiles, the solid lines the NOB ones with $\Delta = 40\,K$. The color changes from blue to purple with decreasing rotation rate $1/Ro$. Note that not the full temperature range is shown.

6.2 Flow structures and temperature distribution

When a constant rotation rate is applied, the typical plume shape changes. The plumes become more and more elongated with increasing $1/Ro$. For smaller $1/Ro$ a single large-scale circulation (LSC) is the predominant structure, for higher $1/Ro$ the LSC breaks downKunnen et al. (2008) and a regular pattern of columnar vortex structures forms. These columnar vortices are also called Ekman vorticesStevens et al. (2009); Weiss et al. (2010); Zhong and Ahlers (2010) or convective Taylor columns Grooms et al. (2010); King and Aurnou (2012). This change of the flow behavior is visualized by temperature isosurfaces in Fig. 6.1 for $Ra = 10^8$ and four representative inverse Rossby numbers, $1/Ro \in \{0.7, 1.4, 7.1, 14.1\}$ under OB and NOB conditions with $\Delta = 40\,K$.

In the NOB cases for low and moderate rotation rates, $1/Ro \lesssim 1.4$, the bulk of the fluid shows a generally higher temperature, similar as without rotationHorn et al. (2011b). However, for even higher rotation rates, at the point when the columnar vortices become very pronounced, $1/Ro \gtrsim 7.1$, the differences in the temperature fields become less apparent. To investigate this in more detail, I analyze the mean temperature profiles, see Fig. 6.2, the mean temperature gradients, Fig. 6.3(a), and the center temperature T_c as function of $1/Ro$, Fig. 6.3(b).

Both the profiles in Fig. 6.2 in the OB and in the NOB case show a non-zero mean temperature gradient within the bulk. This was found to be a result of vortex-vortex

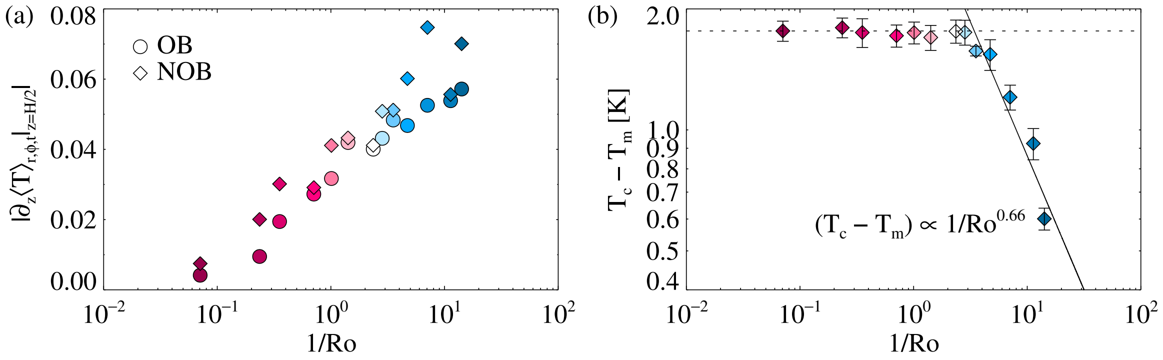

FIGURE 6.3: (a) Absolute value of the mean temperature gradient $|\partial_z \langle T \rangle_{r,\phi,t}|_{z=H/2}|$ for $\mathrm{Ra} = 10^8$, obtained by a linear fit of the mean temperature profiles between $0.4 \leqslant z/H \leqslant 0.6$. The circles denote the OB case, the diamonds the NOB case with $\Delta = 40\,\mathrm{K}$ (b) Deviation of the center temperature T_c from the mean temperature T_m as function of the inverse Rossby number $1/\mathrm{Ro}$ for $\mathrm{Ra} = 10^8$ under NOB conditions with $\Delta = 40\,\mathrm{K}$. The dashed line represents the value in the non-rotating case, $1/\mathrm{Ro} = 0$, the solid line shows a power law fit for $2.8 \leqslant 1/\mathrm{Ro} \leqslant 14.1$.

interactionsJulien et al. (1996); Liu and Ecke (1997). More precisely, at fast enough rotation, when the columnar vortices appear, the flow is nearly two-dimensional and, thus, there is hardly any mixing in vertical direction. The only mixing occurs when vortices merge, which occurs along their lateral extent, i.e. in horizontal direction. Unlike without rotation, there is no fully three-dimensional mixing and consequently, there is a non-zero temperature gradient in the core part of the convection cell. The mean temperature gradient in the center of the cell, $\partial_z \langle T \rangle_{r,\phi,z}|_{z=H/2}$, is determined by making a linear fit on the mean temperature profiles in the range $0.4 \leqslant z/H \leqslant 0.6$ and presented in Fig. 6.3(a). In general, the absolute value of it increases with the rotation rate, and tends to be slightly higher in the NOB cases.

Under NOB conditions the profiles in Fig. 6.2 possess another intriguing feature. With increasing rotation rate, the temperature in the bulk decreases and the OB and NOB profiles for $1/\mathrm{Ro} = 14.1$ approach each other.

Indeed, Fig. 6.3(b), displaying T_c as function of $1/\mathrm{Ro}$, reveals that for high enough rotation rates, $1/\mathrm{Ro} \gtrsim 3.5$, the center temperature shows a sudden drop. Physically, this is readily understood. Under strong rotation the relative magnitude of the viscous term in the Navier–Stokes equations is small and thus, viscous effects in the bulk are less importantGreenspan (1968). But as explained in chaper 5, the increase of the T_c in the case of water is almost solely due to the viscosity. I have performed a power-law fit based on the least squares method. It yielded that $T_c - T_m$ decreases approximately as $1/\mathrm{Ro}^{0.66}$. However, it cannot decrease limitless, but probably reaches at most a value corresponding to the pure conductive state, which is still greater than T_m.

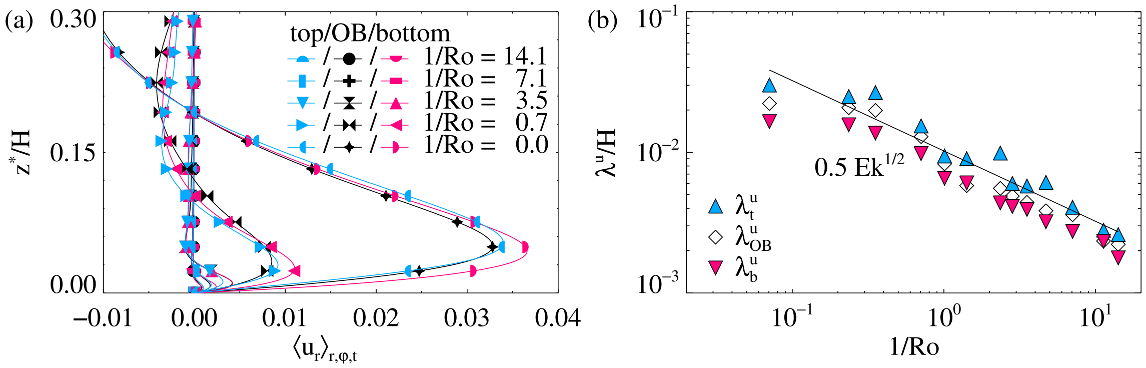

FIGURE 6.4: (a) Mean profiles of the radial velocity, $\langle u_r \rangle_{r,\phi,t}$, for $\mathrm{Ra} = 10^8$ under OB and NOB conditions with $\Delta = 40\,\mathrm{K}$ and various $1/\mathrm{Ro}$. The ordinate shows the distance z^* from the top and bottom plate, respectively, i.e. the profiles under NOB conditions of the upper half of the cell are mirrored along the midplane. The OB profiles were obtained by averaging the upper and lower profiles. Open symbols with solid lines: NOB profiles for the upper half of the cylinder. (b) Viscous boundary layer thicknesses based on the slope criterion (2.5.2) as function of the inverse Rossby number $1/\mathrm{Ro}$; diamonds: OB boundary layer thicknesses λ^u_{OB}, upward triangles: top NOB boundary layer thicknesses λ^u_t, downward triangles: bottom NOB boundary layer thicknesses λ^u_b. The solid line shows the Ekman scaling $0.5\mathrm{Ek}^{1/2}$.

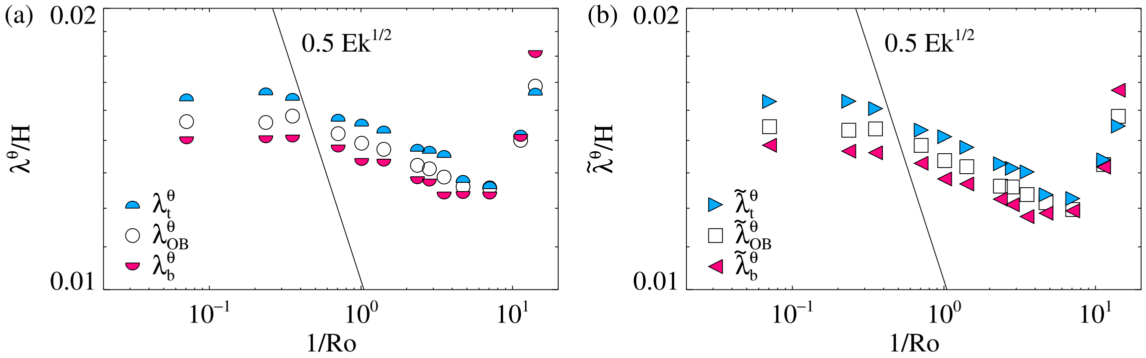

FIGURE 6.5: (a) Thermal boundary layer thicknesses based on the slope criterion (2.5.1) as function of the inverse Rossby number $1/\mathrm{Ro}$; circles: OB boundary layer thicknesses λ^θ_{OB}, upper half circles: top NOB boundary layer thicknesses λ^θ_t, lower half circles: bottom NOB boundary layer thicknesses λ^θ_b. (b) Thermal boundary layer thicknesses based on the slope criterion that considers the mean temperature gradient in the bulk (6.3.1) as function of the inverse Rossby number $1/\mathrm{Ro}$; squares: OB boundary layer thicknesses $\tilde{\lambda}^\theta_{OB}$, right facing triangles: top NOB boundary layer thicknesses $\tilde{\lambda}^\theta_t$, left facing triangles: bottom NOB boundary layer thicknesses $\tilde{\lambda}^\theta_b$. The solid line in both panels shows the Ekman scaling $0.5\mathrm{Ek}^{1/2}$, similar as in Fig. 6.4(b).

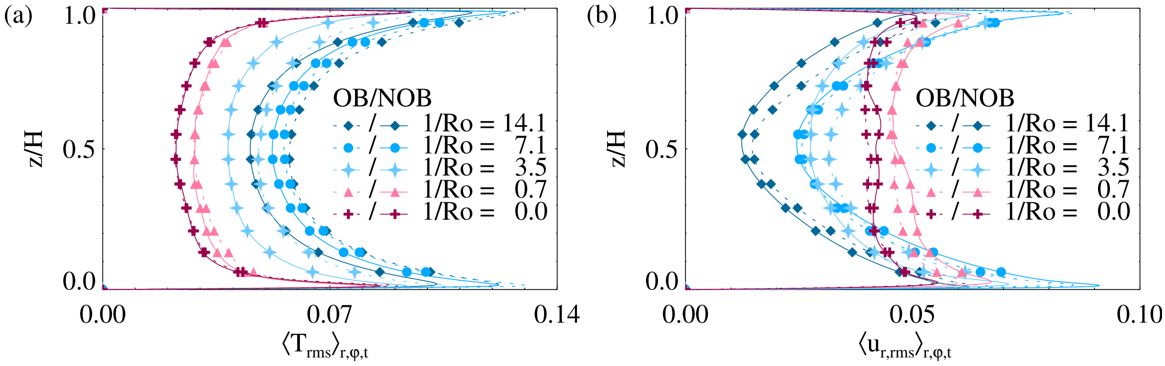

FIGURE 6.6: (a) Mean profiles of the rms temperature for various inverse Rossby numbers $1/Ro$, including no rotation, $1/Ro = 0$. The dotted lines show the OB cases, the solid lines the NOB cases. (b) Mean profiles of the radial rms velocity. Analogous to Fig. (a), the dotted lines show the OB cases, the solid lines the NOB cases.

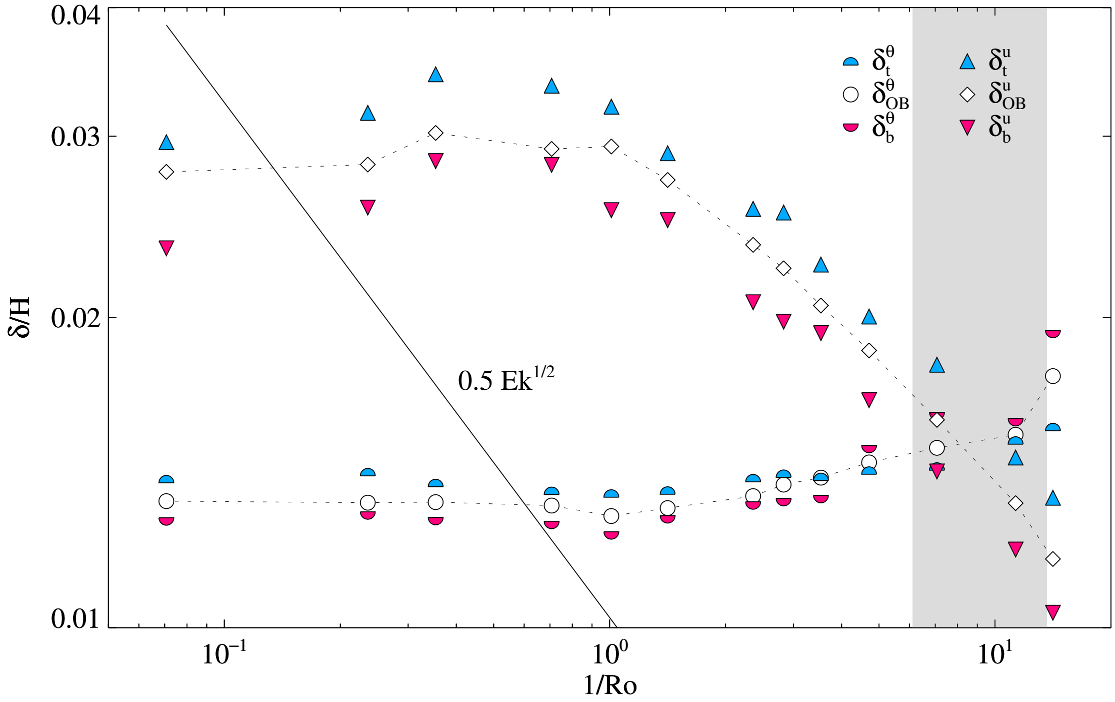

FIGURE 6.7: Thermal and viscous boundary layer thicknesses based on the maxima of the rms temperature and velocity profiles, (6.3.2) and (6.3.3), respectively, as function of the inverse Rossby number $1/Ro$. Circles: OB thermal boundary layer thicknesses δ^{θ}_{OB}, upper half circles: top NOB thermal boundary layer thicknesses δ^{θ}_{t}, lower half circles: bottom thermal NOB boundary layer thicknesses δ^{θ}_{b}. Diamonds: OB viscous boundary layer thicknesses δ^{u}_{OB}, upward triangles: top NOB viscous boundary layer thicknesses δ^{u}_{t}, downward triangles: bottom NOB viscous boundary layer thicknesses δ^{u}_{b}. The solid line shows the Ekman scaling $0.5Ek^{1/2}$, similar as in Fig. 6.4(b). The dashed lines are guides to the eye. The gray shaded area shows the crossover range of the boundary layer thicknesses predicted by King et al. (2012).

6.3 Boundary layers

For rotating convection, the boundary layer thicknesses can also be based on the slope criterion similar to non-rotating convection. This is straight forward in the case of the viscous boundary layers by using eq. (2.5.2). A selection of the radial velocity profiles used for the analysis is presented in Fig. 6.4(a). There is an anticipated asymmetry in the top and bottom NOB profiles. Figure 6.4(a) reveals further that the magnitude of the area-averaged radial velocity near the top and bottom plates decreases with increasing rotation rate, which indicates a breakdown of the large-scale circulation that is essential for non-rotational thermal convection in water for $\mathrm{Ra} = 10^8$.

The maxima for increasing $1/\mathrm{Ro}$ are closer to the top and bottom wall, respectively, a behavior also reflected in the viscous boundary layer thicknesses λ^u presented in Fig. 6.4(b). The viscous boundary layer thickness λ^u decreases with higher rotation rates and it is well-known, that in rapidly rotating flows the viscous boundary layer is an Ekman type boundary layer with a thickness proportional to $\mathrm{Ek}^{1/2}$. In fact, λ^u_{OB} follows $0.5\mathrm{Ek}^{1/2}$ perfectly well for $1/\mathrm{Ro} \gtrsim 0.7$. Under NOB conditions, the drop of λ^u_t occurs at higher $1/\mathrm{Ro}$ than in the OB case and $\lambda^u_t > \lambda^u_{OB}$ for all Ro. On the contrary, the drop of λ^u_b occurs for lower $1/\mathrm{Ro}$ than in the OB case and $\lambda^u_b < \lambda^u_{OB}$ for all $1/\mathrm{Ro}$. The deviation is only small and the scaling exponent of Ek is essentially the same in the OB and the NOB cases. Moreover, the sum of the top and bottom boundary layer thicknesses in the NOB cases still approximately equals their sum in the OB cases. But it is not too surprising, that in opposite to the center temperature T_c, the thicknesses of the viscous boundary layers keep on being non-negligibly influenced by the temperature-dependence of the viscosity. In the Ekman layer, the Coriolis force is balanced by the pressure gradient and the viscous shear.Greenspan (1968) Friction acts to satisfy the no-slip condition at the plates, hence, in the boundary layers the viscous processes are essential, despite the fact that Coriolis force dominates the bulkKing et al. (2012).

The definition of the thermal boundary layer thickness is more trickyStevens et al. (2010a). Instead of using eq. (2.5.1), Stevens et al. (2010a) suggested to use the intersection of the tangent to the mean temperature profile at the plate and of the tangent to the profile at the center of the cell,

$$\tilde{\lambda}^\theta_t = \frac{T_t - T_c - \partial_z \langle T \rangle_{r,\phi,t}\big|_{z=H/2} H/2}{\partial_z \langle T \rangle_{r,\phi,t}\big|_{z=H} - \partial_z \langle T \rangle_{r,\phi,t}\big|_{z=H/2}}, \quad \tilde{\lambda}^\theta_b = \frac{T_c - T_b - \partial_z \langle T \rangle_{r,\phi,t}\big|_{z=H/2} H/2}{\partial_z \langle T \rangle_{r,\phi,t}\big|_{z=0} - \partial_z \langle T \rangle_{r,\phi,t}\big|_{z=H/2}}. \tag{6.3.1}$$

The boundary layer thicknesses based on both definitions are presented in Fig. 6.5. Definition (2.5.1) has the advantage that it allows for some analytical discussion of the Nusselt number, presented in the next section 6.4. Definition (6.3.1) on the other hand, is more physical since it takes the mean temperature gradient into account. But the essential behavior is very similar: λ^θ and $\tilde{\lambda}^\theta$ are almost constant for $1/\mathrm{Ro} \lesssim 0.35$, decrease for $0.35 \lesssim 1/\mathrm{Ro} \lesssim 7.1$, and then sharply increase for $1/\mathrm{Ro} \gtrsim 7.1$. Remarkably, for $1/\mathrm{Ro} > 7.1$ the bottom NOB boundary layers are thicker than the top ones and than the OB boundary layers, whereas the top boundary layers are thinner than the OB boundary layers and consequently, also as the bottom NOB boundary layers. Hence, for fast rotation the situation is reversed to slow and moderate rotation. In addition the line $0.5\mathrm{Ek}^{1/2}$ is also plotted and the point of intersection between λ^u and λ^θ and between λ^u and $\tilde{\lambda}^\theta$ is determined to be at $1/\mathrm{Ro} \approx 1.4$. But this inverse Rossby number does not seem to be crucial for any observed change in a flow feature.

Additionally, the boundary layer thicknesses based on the rms profiles for the temperature and the radial velocityKing et al. (2009); Kunnen et al. (2010) are also evaluated and shown in Fig. 6.6. The thicknesses are then defined by

$$\delta_t^\theta = H - \max\left(z|_{\partial_z\langle u_{r,\mathrm{rms}}\rangle=0}\right), \qquad \delta_b^\theta = \min\left(z|_{\partial_z\langle u_{r,\mathrm{rms}}\rangle=0}\right), \tag{6.3.2}$$

$$\delta_t^u = H - \max\left(z|_{\partial_z\langle T_{\mathrm{rms}}\rangle=0}\right), \qquad \delta_b^u = \min\left(z|_{\partial_z\langle T_{\mathrm{rms}}\rangle=0}\right), \tag{6.3.3}$$

and presented in Fig. 6.7. When the viscous boundary layer thickness is based on the rms criterion, the scaling is still consistent with the Ekman scaling, i.e. $\delta^u \propto \mathrm{Ek}^{1/2}$, however, the absolute value and thus the prefactor is higher. This was also found by Stevens et al. (2009) and Kunnen et al. (2010). According to King et al. (2012) the thermal and viscous Ekman boundary layers should have the same thickness, $\delta^\theta = \delta^u$, somewhere between $6 \lesssim \mathrm{Pr}^{3/4}\mathrm{Ra}^{1/4}\mathrm{Ro}^{3/2} \lesssim 20$, or expressed explicitly in terms of $1/\mathrm{Ro}$ and for $\mathrm{Pr} = 4.38$ and $\mathrm{Ra} = 10^8$, it should be between $6.25 \lesssim 1/\mathrm{Ro} \lesssim 14.3$. The predicted crossover range is marked by a gray shaded area. Indeed, the OB DNS results agree nicely with this prediction. The crossover Rossby number is estimated to be $1/\mathrm{Ro} \approx 7.9$. Under NOB conditions, the crossover of the top boundary layers occurs for higher $1/\mathrm{Ro}$ than the OB crossover, whereas, the crossover of the bottom boundary layers occurs for smaller $1/\mathrm{Ro}$ than the OB crossover. In addition, similar as for the λ^θ and $\tilde{\lambda}^\theta$, the top boundary layers are thicker than the bottom ones for $1/\mathrm{Ro} > 7.1$. Furthermore, the inverse Rossby number $1/\mathrm{Ro}$ where λ^θ and $\tilde{\lambda}^\theta$ show the sudden increase and their respective thicknesses reverses coincides with the inverse Rossby number where $\delta^\theta = \delta^u$, i.e. $1/\mathrm{Ro} \approx 7.9$.

6.4 Heat flux

Finally, I discuss how the Nusselt number is influenced by temperature-dependent material properties in rotating Rayleigh–Bénard convection. The Nusselt number Nu normalized by its value without rotation Nu^∞ as function of the inverse Rossby number $1/\mathrm{Ro}$ is shown in Fig. 6.8.

Under OB conditions the dependence of the heat flux on the rotation rate has been subject to a plethora of experimental and numerical studiesEcke and Niemela (2014); Julien et al. (2012); Kunnen et al. (2006); Liu and Ecke (2009); Schmitz and Tilgner (2009); Stevens et al. (2010b); Weiss and Ahlers (2011a); Zhong et al. (1993); Zhong and Ahlers (2010). It is generally approved, that there are essentially two competing mechanisms that determine how Nu changes with $1/\mathrm{Ro}$ for fluids with $\mathrm{Pr} \gtrsim 1$. On the one hand there is Ekman pumping, leading to an enhancement of the heat transport and on the other hand there is the Taylor–Proudman effectProudman (1916); Taylor (1921), resulting in the suppression of the heat transport. Hence, one often

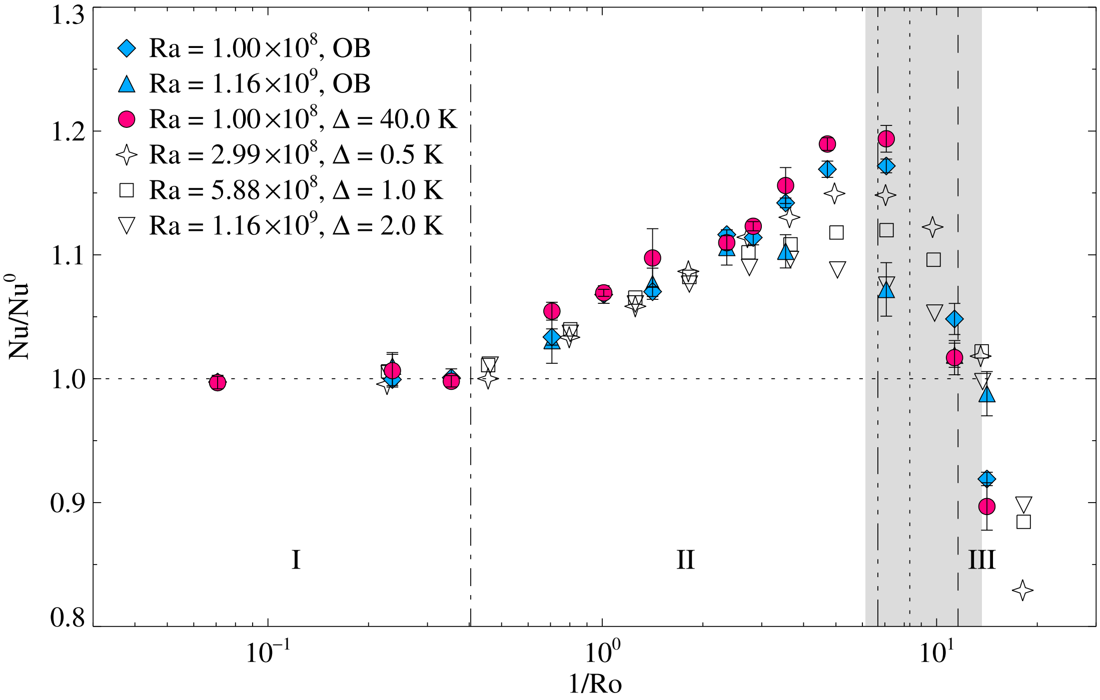

FIGURE 6.8: Nusselt number Nu in the rotating case normalized with the Nusselt number in the non-rotating case Nu^0 as function of the inverse Rossby number 1/Ro. The filled diamonds show the OB DNS data for $\mathrm{Ra} = 10^8$, the filled circles the NOB data for $\Delta = 40\,\mathrm{K}$ and the same Ra, and the filled upward triangles OB data for $\mathrm{Ra} = 1.16 \times 10^9$. For comparison the open stars, squares, and downward triangles show experimental data by Kunnen et al. (2011) for $\mathrm{Ra} = 2.99 \times 10^8$, 5.88×10^8, and 1.16×10^9, respectively, for the same $\mathrm{Pr} = 4.38$. The vertical dot dashed line shows the onset of heat transfer enhancement predicted by Weiss et al. (2010). The other three vertical lines show predictions for the transition to the rotation dominated regime, triple-dot dashed line: Kunnen et al. (2011), dashed line: Ecke and Niemela (2014), dotted line: Julien et al. (2012). The gray shaded area represents the crossover range of the boundary layer thicknesses according to King et al. (2012) as in Fig. 6.7.

distinguishes between three different regimesKunnen et al. (2011); Stevens et al. (2013b); Zhong and Ahlers (2010), indicated by the roman numbers I, II and III in Fig. 6.8.

For low rotation rates, denoted as regime I, the Nusselt numbers in the rotating and in the non-rotating case are virtually the same. Hence, the system is governed by the buoyancy force. For more rapid rotation, regime II, there is a sudden increase of Nu and then, after reaching a maximum which marks the transition to regime III, the heat transport drops rapidly. The transition from regime I to II was found to be a bifurcation and a finite size effect of the Rayleigh–Bénard cellWeiss and Ahlers (2011a); Weiss et al. (2010). The critical inverse Rossby number for this transition was determined to

$$\frac{1}{\mathrm{Ro}_c} = \frac{a}{\Gamma}\left(1 + \frac{b}{\Gamma}\right), \qquad a = 0.381,\ b = 0.061 \tag{6.4.1}$$

which results in $1/\mathrm{Ro}_c = 0.4$ for the case of $\Gamma = 1$.

The enhancement of the heat transport in regime II is commonly understood to be due to the formation of columnar vortex structures. They suck additional heat out of the thermal boundary layerJulien et al. (1996); Kunnen et al. (2010); Liu and Ecke (1997, 2009); Rossby (1969), a process called Ekman pumping. The decrease in regime III is explained with help of the Taylor–Proudman theorem. It states that for very rapid rotation all steady slow motions in an inviscid fluid are two-dimensional, in other words, that all components of the velocity are not allowed to vary in the direction of the rotation axis (Chandrasekhar, 1961). Strictly speaking the Taylor–Proudman theorem is not valid in the time-dependent convective flow considered here. Nonetheless, the tendencies are correctly captured by it. In this regime the system is expected to behave as if it was in geostrophic balance. However, the exact border between the regimes II and III is slightly arbitrary and several combinations of the control parameters have been proposed to determine whether the flow is rotation or buoyancy dominatedEcke and Niemela (2014); Julien et al. (2012); King et al. (2012, 2009); Rossby (1969); Schmitz and Tilgner (2009, 2010). Furthermore, the heat flux is not the only way to characterize this transition but there are also other approaches, e.g. using the helicitySchmitz and Tilgner (2010), the strength of the large-scale circulationStevens et al. (2009) or the toroidal and poloidal energyHorn and Shishkina (2015).

In Fig. 6.8 the DNS results for $\mathrm{Ra} = 10^8$ and $\mathrm{Ra} = 1.19 \times 10^9$ are compared to experimental data and several recent predictions for the regime transitions. As previously the Nusselt number was obtained by the mean value of the r-ϕ plane averaged Nu for all vertical z positions.

The agreement with the experimental data by Kunnen et al. (2011) for $\mathrm{Ra} = 1.19 \times 10^9$ and $\mathrm{Pr} = 4.38$ is excellent. Furthermore, these authors have shown that their measurements also agree with the data by Zhong and Ahlers (2010). Unfortunately, neither group measured for Rayleigh numbers as low or for temperature differences as high as the ones presented here. However, the trend of the Nusselt number to an enhanced heat flux increase and a shift of this maximum to higher $1/\mathrm{Ro}$ with decreasing Ra is captured nicely. The higher maximum for lower Ra is explained by a lower turbulent viscosity Stevens et al. (2013b).

The maximum heat flux for $\mathrm{Ra} = 10^8$ is observed for $1/\mathrm{Ro} \approx 7.1$, which is the same point, where the viscous Ekman and the thermal boundary layers intersect, $\delta^u = \delta^\theta$. This impact of the boundary layer dynamics in rotating Rayleigh–Bénard convection on the global heat transport was first suggested by Rossby (1969) and later on taken up by others, e.g. Julien et al. (1996); King et al. (2012, 2009). According to King et al. (2012) the crossover of the boundary layers is supposed to mark the transition of the heat transport behaving either quasigeostrophic or weakly rotating. Similar as in Fig. 6.7 the proposed transition range for $\mathrm{Ra} = 10^8$ is visualized by a gray-shaded area and fits nicely to the DNS. However, transitions in the scaling behavior of Nu with the rotation rate were also observed in numerical simulations with stress-free boundary conditions by Schmitz and Tilgner (2009) where no Ekman boundary layers are present. It might be worthwhile testing whether a generalization in terms of dissipation layers suggested by Petschel et al. (2013) for

$1/\mathrm{Ro}$	$\mathrm{Nu}_{\mathrm{OB}}$	$\mathrm{Nu}_{\mathrm{NOB}}$	$T_c - T_m [\mathrm{K}]$
0.0	32.94 ± 0.10	32.31 ± 0.08	1.80 ± 0.12
0.07	32.85 ± 0.15	32.21 ± 0.14	1.76 ± 0.10
0.24	32.92 ± 0.13	32.52 ± 0.42	1.80 ± 0.10
0.35	32.97 ± 0.21	32.24 ± 0.13	1.75 ± 0.14
0.71	34.05 ± 0.19	34.07 ± 0.22	1.72 ± 0.11
1.01	35.18 ± 0.21	34.55 ± 0.03	1.75 ± 0.11
1.41	35.26 ± 0.07	35.46 ± 0.76	1.70 ± 0.11
2.36	36.77 ± 0.06	35.86 ± 0.16	1.76 ± 0.12
2.83	37.01 ± 0.07	36.29 ± 0.08	1.75 ± 0.12
3.54	37.62 ± 0.06	37.35 ± 0.46	1.57 ± 0.04
4.71	38.51 ± 0.18	38.43 ± 0.13	1.54 ± 0.13
7.07	38.60 ± 0.14	38.57 ± 0.33	1.21 ± 0.09
11.31	34.53 ± 0.40	32.86 ± 0.44	0.93 ± 0.08
14.14	29.81 ± 0.37	28.63 ± 0.63	0.60 ± 0.04

TABLE 6.1: Nusselt numbers as presented in Fig. 6.8 for the OB and the NOB case with $\Delta = 40\,\mathrm{K}$ and $\mathrm{Ra} = 10^8$. Furthermore the last column shows the deviation of the centre temperature from the mean temperature for this NOB case as presented in Fig. 6.3(b).

non-rotating Rayleigh–Bénard convection can be found.

Other authors proposed transition parameters, that were supposed to be independent of the boundary conditions. Julien et al. (2012) suggested an approach based on an asymptotic state in the limit $\mathrm{Ek} \to 0$ which is expected to be valid for Ekman numbers still about one magnitude lower than the ones investigated here for $\mathrm{Ra} = 10^8$. Nonetheless their prediction of the transitional regime with active Ekman pumping, given by $1 \gtrsim \mathrm{Ro} \gtrsim \mathrm{Pr}^{1/8}\mathrm{Ra}^{-1/8}$, yielding $1 \lesssim 1/\mathrm{Ro} \lesssim 8.3$ for $\mathrm{Ra} = 10^8$, matches the maximum Nu decently. Ecke and Niemela (2014) empirically determined the transition to geostrophic turbulence by measurements in helium with $\mathrm{Pr} = 0.7$. There, the thermal boundary layer is always thicker than the viscous one, thus, the argumentation of a crossover of boundary layers does, of course, not apply. But despite that, their transitional Rossby number $1/\mathrm{Ro}_t = 1.5\mathrm{Pr}^{1/2}\mathrm{Ra}^{1/14}$, which gives 11.7 for $\mathrm{Ra} = 10^8$, also coincides in a good approximation with the Rossby number where the thermal boundary layers based on the slope criterion start to increase, where the rms boundary layer thicknesses intersect and the maximum of the Nusselt number is found.

Now the question arises in which way NOB effects influence the heat transport in rotating convection. Fig. 6.8 shows that $\mathrm{Nu}_{\mathrm{NOB}}$ normalized by its value without rotation $\mathrm{Nu}^{\infty}_{\mathrm{NOB}}$ is virtually the same and agrees within the statistical error with $\mathrm{Nu}_{\mathrm{OB}}/\mathrm{Nu}^{\infty}_{\mathrm{OB}}$ for $1/\mathrm{Ro} \lesssim 3.5$. Thus, the temperature dependence of the material properties influences the Nusselt number in the same way as without rotation. However, in the small range between $3.5 \lesssim 1/\mathrm{Ro} \lesssim 11.3$, the ratio $\mathrm{Nu}_{\mathrm{NOB}}/\mathrm{Nu}^{\infty}_{\mathrm{NOB}}$ is greater than $\mathrm{Nu}_{\mathrm{OB}}/\mathrm{Nu}^{\infty}_{\mathrm{OB}}$. This does not mean that the actual Nusselt number is larger,

Nu_{NOB} is only at most as large as Nu_{OB} within the statistical error. For $1/Ro \gtrsim 11.3$, the situation is reversed, i.e. $Nu_{NOB}/Nu^{\infty}_{NOB} < Nu_{OB}/Nu^{\infty}_{OB}$.
To understand this behavior, it is useful to consider again eq. (5.2.31), i.e. the separation of the ratio Nu_{NOB}/Nu_{OB} into a contribution by the boundary layers, F_{λ}, and a contribution by the temperature drops, F_{Δ}. The factor F_{Δ} is independent of $1/Ro$ for $1/Ro \lesssim 3.5$. For more rapid rotation, the center temperature T_c drops, as discussed before and was shown in Fig. 6.3(b), thus the top temperature drop Δ_t increases and the bottom temperature drop Δ_b decreases. Consequently, F_{Δ} decreases, but only marginally. The factor F_{λ} is also independent of $1/Ro$ for $1/Ro \lesssim 3.5$. Afterwards it increases, which is also the point where the thermal boundary layers in the NOB case intersect, as was presented in Fig. 6.5(a). F_{λ} has its maximum value of 1.03 for $1/Ro = 7.1$. For the highest $1/Ro$, when the top boundary layer thickness λ^{θ}_{t} is thinner than the bottom boundary layer thickness λ^{θ}_{b}, F_{λ} is smaller than in the non-rotating case. Hence, the influence on the boundary layers is crucial for Nu. The drop of T_c is only of minor importance.

6.5 Summary

The influence of non-Oberbeck–Boussinesq effects on rotating thermal convection in water was investigated by means of three-dimensional DNS.
For low and moderate rotation rates, the Rayleigh–Bénard system responds very similar to the temperature dependencies of the material properties as without rotation. That is, T_c has the same value, the top thermal and viscous boundary layers are thicker than the corresponding bottom ones and Nu_{NOB}/Nu_{OB} is the same as in the non-rotational case.
However, for rapid rotation, certain NOB effects, i.e. those caused by the viscosity are suppressed. The reason is that viscous effects in the bulk of the Rayleigh–Bénard cell become negligible for strong rotations rates. This is best reflected by the behaviour of T_c that shows a sharp decrease for $Ro \lesssim 0.2$. Although this might suggest that in experiments many symmetries being inherent in Rayleigh–Bénard convection are restored under NOB conditions if only the rotation rate is high enough, one has to be careful since it will probably be a fallacy. There, not only the centrifugal buoyancy, that was not considered in this study, would be another source of breaking of the top-bottom symmetry, including a higher centre temperatureHart and Ohlsen (1999), but furthermore, the boundary layers keep on being strongly influenced by viscous forces.
Under NOB conditions the crossover of the top (bottom) thermal and viscous boundary layers happens for slightly smaller (larger) Ro than under OB conditions. At this crossover Rossby number the absolute deviation between Nu_{OB} and Nu_{NOB} is minimal and smaller than without rotation. Moreover, at this Ro, the top thermal boundary layers become thinner than the bottom ones, whereas for the viscous boundary layer the situation remains as without rotation and the top viscous boundary layers are thicker than the bottom ones.

CONCLUSIONS AND OUTLOOK

In this thesis different aspects of turbulent Rayleigh–Bénard convection have been studied that go beyond of what the majority of recent investigations focuses on. The two main concerns here, were the influence of rotation and the influence of non-Oberbeck–Boussinesq (NOB) effects, and their combination. In addition also the impact of the Prandtl number was considered. Thus, the objective was to get us closer to the understanding of the turbulent convective flow behaviour in nature. With this in mind, three-dimensional direct numerical simulations (DNS) of turbulent Rayleigh–Bénard convection were performed.

Firstly, rotating Rayleigh–Bénard convection of a fluid with a Prandtl number of $Pr = 0.8$ under perfect Oberbeck–Boussinesq (OB) conditions was discussed. The fluid was confined in a slender cylindrical cell with an aspect ratio of $\Gamma = 1/2$. DNS were performed for the Rayleigh number range $10^5 \leqslant Ra \leqslant 10^9$ and the inverse Rossby number range $0 \leqslant 1/Ro \leqslant 20$. Based on this data, I proposed a new method to universally capture regime transitions using the decomposition of the velocity field into toroidal and poloidal parts. Four different regimes were identified. First, a buoyancy dominated regime occurring as long as the toroidal energy e_{tor} is not affected by rotation and remains equal to that in the non-rotating case, e^0_{tor}. Second, a rotation influenced regime, starting at rotation rates where $e_{tor} > e^0_{tor}$ and ending at a critical inverse Rossby number $1/Ro_{crit}$ that is determined by the balance of the toroidal and poloidal energy, $e_{tor} = e_{pol}$. Third, a rotation dominated regime, where the toroidal energy e_{tor} is larger than both, e_{pol} and e^0_{tor}. Fourth, a geostrophic turbulence regime for high rotation rates where the toroidal energy drops below the value of non-rotating convection. A good agreement with other common methods is found, having, however, several advantages over them: It captures all the transitions. It works independent of the Prandtl number and the aspect ratio. It is based on a global quantity, and thus, is very robust.

Secondly, the influence of temperature-dependent material properties on Rayleigh–Bénard convection was investigated in three different liquids, ranging from a very small Prandtl number for mercury with $Pr = 0.0232$, over a moderate one for water with $Pr = 4.38$, to a very large one for glycerol with $Pr = 2547.9$. A series of three-dimensional DNS was conducted in a cylindrical cell with a unity aspect ratio, $\Gamma = 1$. Simulations were performed under OB conditions for all three liquids and furthermore, various NOB conditions, i.e. temperature differences, were studied on the examples of water and glycerol.

For that purpose, I implemented temperature-dependent material properties into a finite volume DNS code, by prescribing polynomial functions (up to seventh order in the case of glycerol and up to third order in the case of water) for the viscosity, the heat conductivity and the density. The DNS revealed that NOB effects lead to a breakdown of the top-bottom symmetry typical for OB simulations. The observed

NOB effects include, but are not limited to, different thermal and viscous boundary layer thicknesses, asymmetric plume dynamics and an increase of the centre temperature T_c. Their intensity strongly depends on the particular fluid.

In glycerol, simulations were performed within a range of Rayleigh numbers of $10^5 \leqslant Ra \leqslant 10^9$. For the highest temperature differences, $\Delta = 80\,\mathrm{K}$, the viscosity at the top is about 360% times higher than at the bottom, while the differences of the other material properties are less than 15%. The temperature and velocity profiles and the thermal and viscous boundary layer thicknesses were analysed. Under NOB conditions, the temperature in the centre of the cell, T_c, increases with increasing Δ and can be up to 15 K higher than under OB conditions. The comparison of these findings with several theoretical and empirical models showed that 2D boundary layer models overestimate the actual T_c, while models based on the temperature or velocity scales predict T_c very well with a standard deviation of 0.4 K. Furthermore, the obtained temperature profiles bend closer towards the cold top plate and further away from the hot bottom plate. The situation for the velocity profiles is reversed: they bend farther away from the top plate and closer towards to the bottom plate. The top boundary layers are always thicker than the bottom ones. Their ratio is up to 2.5 for the thermal and up to 4.5 for the viscous boundary layers. Additionally, the Reynolds number Re and the Nusselt number Nu were investigated: Re is higher and Nu is lower under NOB conditions. The Nusselt number Nu is influenced in a non-linear way by NOB effects, stronger than it was suggested by 2D simulations. The actual scaling of Nu with Ra in the NOB case is $Nu \propto Ra^{0.298}$ and is in excellent agreement with the experimental data.

In water, the Rayleigh number Ra ranged from 10^7 to 1.16×10^9 and temperature differences Δ up to 70 K were considered. Here, the NOB effects are reflected in an up to 5.5 K enhancement of the center temperature and in an up to 5% reduction of the Nusselt number. The top thermal and viscous boundary layer thicknesses increase and the bottom ones decrease, while the sum of the corresponding top and bottom thicknesses remains as in the classical OB case.

Furthermore, rotating Rayleigh–Bénard convection was studied in water as well, both under OB and under NOB conditions. The inverse Rossby number range $0.07 \leqslant 1/Ro \leqslant 14.1$ was studied for $\Delta = 40\,\mathrm{K}$ with the focus on $Ra = 10^8$. Rotation applied to NOB thermal convection reduces the central temperature enhancement. Under NOB conditions the top (bottom) thermal and viscous boundary layers become equal for a slightly larger (smaller) inverse Rossby number than in the OB case. Moreover, for rapid rotation the thermal bottom boundary layers become thicker than the top ones. The Nusselt number normalized by that in the non-rotating case depends similarly on $1/Ro$ in both, the NOB and the OB cases. The deviation between the Nusselt number under OB and NOB conditions is minimal when the thermal and viscous boundary layers are equal.

The progess in numerical investigations of turbulent thermal convection is very closely connected with the development of supercomputers. So far, the next generation of supercomputers also led to the feasibility of simulations at higher Rayleigh numbers, and therewith to simulations closer to realistic conditions. Even now, simulations are getting close to the so-called ultimate regime and the analysis of the toroidal and poloidal energy might be another possibility to determine where this transition occurs. However, not only achieving higher Ra is desirable. Other questions seeking for an answer, are for example: How do NOB effects influence convection in water at temperatures around the density anomaly? Do the vortex statistics change in rotating NOB convection? How does rotation influence convection in a fluid with a high Prandtl number such as glycerol, in particular also with respect to NOB conditions?

Many more questions can be asked. And once answered they might lead to new ones. Thus, Rayleigh–Benard convection will probably keep on being a challenging topic in fluid dynamics.

LIST OF FIGURES

LIST OF TABLES

List of publications*

Horn, S. and Shishkina, O., Toroidal and poloidal energy in rotating Rayleigh–Bénard convection, *J. Fluid Mech. 762* (2015), 232–255.

Horn, S. and Shishkina, O., Rotating non-Oberbeck–Boussinesq Rayleigh–Bénard convection in water, *Phys. Fluids 26(5)* (2014), 055111.

Shishkina, O., Wagner, S. and **Horn, S.**, Influence of the angle between the wind and the isothermal surfaces on the boundary layer structures in turbulent thermal convection. *Phys. Rev. E 89(3)* (2014), 033014.

Shishkina, O., **Horn, S.** and Wagner, S., Falkner–Skan boundary layer approximation in Rayleigh–Bénard convection, *J. Fluid Mech. 730* (2013), 442–463.

Horn, S., Shishkina, O. and Wagner, C., On non-Oberbeck–Boussinesq effects in three-dimensional Rayleigh–Bénard convection in glycerol, *J. Fluid Mech. 724* (2013), 175–202.

Horn, S. and Wagner, C., Rotating Rayleigh–Bénard convection of SF_6 in a slender cylinder, *Direct and Large-Eddy Simulation IX, Springer* (2015), 353–359.

Horn, S., Shishkina, O. and Wagner, C., Non-Oberbeck–Boussinesq effects in Rayleigh–Bénard convection of liquids, *Turbulence and Interactions, Springer* (2014), 99–105.

Horn, S., Shishkina, O. and Wagner, C., Direct Numerical Simulation of Non-Oberbeck-Boussinesq Effects in Turbulent Rayleigh-Bénard Convection of Water. *New Results in Numerical and Experimental Fluid Mechanics VIII, Springer* (2013), 599–606.

Horn, S., Kaczorowski, M. and Shishkina, O., Direct Numerical Simulations of turbulent Rayleigh–Bénard convection, *inSiDE 10(2)* (2012), 34–37.

Shishkina, O., **Horn, S.** and Kaczorowski, M., Direct Numerical Simulations of turbulent Rayleigh–Bénard convection, *High Performance Computing in Science and Engineering, Verlag der Bayerischen Akademie der Wissenschaften* (2012), 144–146.

Horn, S., Shishkina, O. and Wagner, C., The influence of non-Oberbeck–Boussinesq effects on rotating turbulent Rayleigh–Bénard convection, *J. Phys.: Conf. Ser. 318(8)* (2011), 082005.

Horn, S., Shishkina, O. and Wagner, C., The Influence of Non-Oberbeck–Boussinesq Effects and Rotation on Turbulent Rayleigh–Bénard Convection, *Proceedings of TSFP-7* (2011).

Horn, S., Shishkina, O. and Wagner, C., Non-Oberbeck-Boussinesq effects in three-dimensional Rayleigh–Bénard convection, *Direct and Large-Eddy Simulation VIII, ERCOFTAC Series, 15, Springer*, (2011), 377–382.

---

*which are presented in part or in full in this thesis

Bibliography

Ahlers, G., Brown, E., Fontenele Araujo, F., Funfschilling, D., Grossmann, S. and Lohse, D., Non-Oberbeck–Boussinesq effects in strongly turbulent Rayleigh–Bénard convection, *J. Fluid Mech. 569* (2006), 409–445.

Ahlers, G., Fontenele Araujo, F., Funfschilling, D., Grossmann, S. and Lohse, D., Non-Oberbeck–Boussinesq Effects in Gaseous Rayleigh–Bénard Convection, *Phys. Rev. Lett. 98* (2007), 054501.

Ahlers, G., Grossmann, S. and Lohse, D., Heat transfer and large scale dynamics in turbulent Rayleigh-Bénard convection, *Rev. Mod. Phys. 81* (2009), 503.

Ahlers, G., He, X., Funfschilling, D. and Bodenschatz, E., Heat transport by turbulent Rayleigh–Bénard convection for $\mathrm{Pr} \simeq 0.8$ and $3 \times 10^{12} \lesssim \mathrm{Ra} \lesssim 10^{15}$: aspect ratio $\Gamma = 0.50$, *New J. Phys. 14* (2012), 103012.

Backus, G., Poloidal and toroidal fields in geomagnetic field modeling, *Rev. Geophys. 24* (1986), 75–109.

Batchelor, G. K., *An introduction to fluid dynamics* (Cambridge university press, 1967).

Bénard, H., Les tourbillons cellulaires dans une nappe liquide, *Rev. Gen. Sci. Pures Appl 11* (1900), 1271.

Bobkov, V. et al., Thermophysical Properties of Materials for Nuclear Engineering: a Tutorial and Collection of Data, *IAEA, Vienna* .

Boronski, P. and Tuckerman, L. S., Poloidal-toroidal decomposition in a finite cylinder. I: Influence matrices for the magnetohydrodynamic equations, *J. Comput. Phys. 227* (2007), 1523–1543.

Boubnov, B. and Golitsyn, G., Experimental study of convective structures in rotating fluids, *Journal of Fluid Mechanics 167* (1986), 503–531.

Boussinesq, J. V., *Théorie analytique de la chaleur*, vol. 2 (Gauthier-Villars Paris, 1903).

Breuer, M., Wessling, S., Schmalzl, J. and Hansen, U., Effect of inertia in Rayleigh–Bénard convection, *Phys. Rev. E 69* (2004), 026302.

Brown, E. and Ahlers, G., Rotations and cessations of the large-scale circulation in turbulent Rayleigh–Bénard convection, *J. Fluid Mech. 568* (2006), 351–386.

BROWN, E. AND AHLERS, G., Temperature gradients, and search for non-Boussinesq effects, in the interior of turbulent Rayleigh–Bénard convection, *Europhys. Lett. 80*.

BUELL, J. C. AND CATTON, I., Effect of rotation on the stability of a bounded cylindrical layer of fluid heated from below, *Phys. Fluids 26* (1983), 892.

BURNISHEV, Y., SEGRE, E. AND STEINBERG, V., Strong symmetrical non-Oberbeck–Boussinesq turbulent convection and the role of compressibility, *Phys. Fluids 22* (2010), 035108.

BUSSE, F. H., On the stability of two-dimensional convection in a layer heated from below, *J. Math. & Phys. 46* (1967a), 140–150.

BUSSE, F. H., The stability of finite amplitude cellular convection and its relation to an extremum principle, *J. Fluid Mech. 30* (1967b), 625–649.

BUSSE, F. H., Non-linear properties of thermal convection, *Rep. Prog. Phys. 41* (1978), 1929–1967.

BUSSE, F. H., High Prandtl number convection, *Phys. Earth Planet. Inter. 19* (1979), 149–157.

CASTAING, B., GUNARATNE, G., KADANOFF, L., LIBCHABER, A. AND HESLOT, F., Scaling of hard thermal turbulence in Rayleigh–Bénard convection, *J. Fluid Mech. 204* (1989), 1–30.

CHANDRASEKHAR, S., *Hydrodynamic and Hydromagnetic Stability* (Clarendon Press, Oxford, 1961).

CHAVANNE, X., CHILLA, F., CHABAUD, B., CASTAING, B. AND HEBRAL, B., Turbulent Rayleigh–Bénard convection in gaseous and liquid He, *Physics of Fluids 13* (2001), 1300.

CHILLÀ, F. AND SCHUMACHER, J., New perspectives in turbulent Rayleigh-Bénard convection, *The European Physical Journal E 35* (2012), 1–25.

CHORIN, A. J., A Numerical Method for Solving Incompressible Viscous Flow Problems, *Journal of Computational Physics 2* (1967), 12–26.

CHORIN, A. J. AND MARSDEN, J. E., *A Mathematical Introduction to Fluid Mechanics*, 4th ed. (Springer-Verlag, 2000).

CHRISTENSEN, U. AND HARDER, H., 3-D convection with variable viscosity, *Geophys. J. Int. 104* (1991), 213–226.

CONSTANTIN, P. AND DOERING, C. R., Infinite Prandtl Number Convection, *Journal of Statistical Physics 94* (1999), 159–172.

ECKE, R., ZHONG, F. AND KNOBLOCH, E., Hopf bifurcation with broken reflection symmetry in rotating Rayleigh-Bénard convection, *Europhys. Lett. 19* (1992), 177.

ECKE, R. E., *Handbook of Environmental Fluid Dynamics*, vol. 1, chap. Convection (Rotating Fluids) (CRC Press, 2012), 505–512.

ECKE, R. E. AND NIEMELA, J. J., Heat transport in the geostrophic regime of rotating Rayleigh-Bénard convection, *Phys. Rev. Lett. 113* (2014), 114301.

FALKNER, V. M. AND SKAN, S. W., Some approximate solutions of the boundary layer equations, *Phil. Mag. 12* (1931), 865–896.

FITZJARRALD, D. E., An experimental study of turbulent convection in air, *Journal of Fluid Mechanics 73* (1976), 693–719.

FUNFSCHILLING, D., BROWN, E., NIKOLAENKO, A. AND AHLERS, G., Heat transport by turbulent Rayleigh-Bénard convection in cylindrical samples with aspect ratio one and larger, *J. Fluid Mech. 536* (2005), 145–154.

GETLING, A. V., *Rayleigh–Bénard convection: structures and dynamics* (World Scientific Publishing Co. Pte. Ltd., 1998).

GOLDSTEIN, H., KNOBLOCH, E. AND MERCADER, I., Convection in a rotating cylinder. Part 2. Linear theory for low Prandtl numbers, *J. Fluid Mech 262* (1994), 293–324.

GOLDSTEIN, H., KNOBLOCH, E., MERCADER, I. AND NET, M., Convection in a rotating cylinder. Part 1. Linear theory for moderate Prandtl numbers, *J. Fluid Mech. 248* (1993), 583–583.

GRAY, D. D. AND GIORGINI, A., The validity of the Boussinesq approximation for liquids and gases, *Int. J. Heat Mass Transfer 19* (1976), 545–551.

GREENSPAN, H. P., *The theory of rotating fluids* (Cambridge University Press (London), 1968).

GROOMS, I., JULIEN, K., WEISS, J. B. AND KNOBLOCH, E., Model of Convective Taylor Columns in Rotating Rayleigh-Bénard Convection, *Phys. Rev. Lett. 104* (2010), 224501.

GROSSMANN, S. AND LOHSE, D., Scaling in thermal convection: A unifying theory, *J. Fluid Mech. 407* (2000), 27–56.

GROSSMANN, S. AND LOHSE, D., Thermal convection for large Prandtl numbers, *Phys. Rev. Lett. 86* (2001), 3316–3319.

GROSSMANN, S. AND LOHSE, D., Prandtl and Rayleigh number dependence of the Reynolds number in turbulent thermal convection, *Phys. Rev. E 66* (2002), 16305.

GROSSMANN, S. AND LOHSE, D., On geometry effects in Rayleigh–Bénard convection, *J Fluid Mech. 486* (2003), 105–114.

GROSSMANN, S. AND LOHSE, D., Fluctuations in turbulent Rayleigh–Bénard convection: the role of plumes, *Phys. Fluids 16* (2004), 4462.

GROSSMANN, S. AND LOHSE, D., Multiple scaling in the ultimate regime of thermal convection, *Phys. Fluids 23* (2011), 045108.

HART, J. AND OHLSEN, D., On the thermal offset in turbulent rotating convection, *Phys. Fluids 11* (1999), 2101.

HE, X., FUNFSCHILLING, D., NOBACH, H., BODENSCHATZ, E. AND AHLERS, G., Transition to the Ultimate State of Turbulent Rayleigh-Bénard Convection, *Phys. Rev. Lett. 108* (2012), 024502.

HERRMANN, J. AND BUSSE, F., Asymptotic theory of wall-attached convection in a rotating fluid layer, *J. Fluid Mech. 255* (1993), 183–183.

HOMSY, G. AND HUDSON, J., Centrifugally driven thermal convection in a rotating cylinder, *J. Fluid Mech. 35* (1969), 33–52.

HORN, S., KACZOROWSKI, M. AND SHISHKINA, O., Direct Numerical Simulations of turbulent Rayleigh–Bénard convection, *inSiDE 10(2)* (2012), 34–37.

HORN, S. AND SHISHKINA, O., Rotating non-Oberbeck–Boussinesq Rayleigh–Bénard convection in water, *Phys. Fluids (1994-present) 26* (2014), 055111.

HORN, S. AND SHISHKINA, O., Toroidal and poloidal energy in rotating Rayleigh–Bénard convection, *J. Fluid Mech. 762* (2015), 232–255.

HORN, S., SHISHKINA, O. AND WAGNER, C., Non-Oberbeck-Boussinesq effects in three-dimensional Rayleigh-Bénard convection, *in Direct and Large-Eddy Simulation VIII* (Springer, 2011a), 377–382.

HORN, S., SHISHKINA, O. AND WAGNER, C., The influence of non-Oberbeck-Boussinesq effects on rotating turbulent Rayleigh–Bénard convection, *J. Phys.: Conf. Ser. 318* (2011b), 082005.

HORN, S., SHISHKINA, O. AND WAGNER, C., Direct Numerical Simulation of Non-Oberbeck-Boussinesq Effects in Turbulent Rayleigh-Bénard Convection of Water, *in New Results in Numerical and Experimental Fluid Mechanics VIII* (Springer, 2013a), 599–606.

HORN, S., SHISHKINA, O. AND WAGNER, C., On non-Oberbeck–Boussinesq effects in three-dimensional Rayleigh–Bénard convection in glycerol, *J. Fluid Mech. 724* (2013b), 175–202.

HORN, S., SHISHKINA, O. AND WAGNER, C., Non-Oberbeck-Boussinesq Effects in Rayleigh–Bénard Convection of Liquids, *in Turbulence and Interactions* (Springer, 2014), 99–105.

HORN, S., SHISHKINA, O. AND WAGNER, S., The Influence of Non-Oberbeck–Boussinesq Effects and Rotation on Turbulent Rayleigh–Bénard Convection, *in Proceedings of TSFP-7* (2011c).

HORN, S. AND WAGNER, C., Rotating Rayleigh–Bénard Convection of SF_6 in a Slender Cylinder, *in Direct and Large-Eddy Simulation IX* (Springer, 2015), 353–359.

JULIEN, K., KNOBLOCH, E., RUBIO, A. M. AND VASIL, G. M., Heat transport in low-Rossby-number Rayleigh-Bénard convection, *Phys. Rev. Lett. 109* (2012), 254503.

JULIEN, K., LEGG, S., MCWILLIAMS, J. AND WERNE, J., Hard turbulence in rotating Rayleigh–Bénard convection, *Phys. Rev. E 53* (1996), R5557–R5560.

KING, E. M. AND AURNOU, J. M., Thermal evidence for Taylor columns in turbulent rotating Rayleigh-Bénard convection, *Phys. Rev. E 85* (2012), 016313.

KING, E. M., STELLMACH, S. AND AURNOU, J. M., Heat transfer by rapidly rotating Rayleigh–Bénard convection, *J. Fluid Mech. 691* (2012), 568–582.

KING, E. M., STELLMACH, S., NOIR, J., HANSEN, U. AND AURNOU, J. M., Boundary layer control of rotating convection systems, *Nature 457* (2009), 301–304.

KRISHNAMURTI, R. AND HOWARD, L. N., Large-scale flow generation in turbulent convection, *Proc. Natl. Acad. Sci. USA 78* (1981), 1981–1985.

KUNNEN, R. P. J., CLERCX, H. J. H. AND GEURTS, B. J., Heat flux intensification by vortical flow localization in rotating convection, *Phys. Rev. E 74* (2006), 056306.

KUNNEN, R. P. J., CLERCX, H. J. H. AND GEURTS, B. J., Enhanced Vertical Inhomogeneity in Turbulent Rotating Convection, *Phys. Rev. Lett. 101* (2008), 174501.

KUNNEN, R. P. J., CLERCX, H. J. H. AND GEURTS, B. J., Vortex statistics in turbulent rotating convection, *Phys. Rev. E 82* (2010), 036306.

KUNNEN, R. P. J., CLERCX, H. J. H. AND VAN HEIJST, G. F., The structure of sidewall boundary layers in confined rotating Rayleigh–Bénard convection, *J. Fluid Mech. 727* (2013), 509–532.

KUNNEN, R. P. J., GEURTS, B. J. AND CLERCX, H. J. H., Turbulence statistics and energy budget in rotating Rayleigh–Bénard convection, *Eur. J. Mech. (B/Fluids) 28* (2009), 578–589.

KUNNEN, R. P. J., STEVENS, R. J. A. M., OVERKAMP, J., SUN, C., VAN HEIJST, G. F. AND CLERCX, H. J. H., The role of Stewartson and Ekman layers in turbulent rotating Rayleigh–Bénard convection, *J. Fluid Mech. 688* (2011), 422–442.

KUO, E. AND CROSS, M., Traveling-wave wall states in rotating Rayleigh-Bénard convection, *Phys. Rev. E 47* (1993), R2245–R2248.

LANDAU, L. D. AND LIFSCHITZ, E. M., *Lehrbuch der Theoretischen Physik VI, Hydrodynamik*, 5th ed. (Verlag Harri Deutsch, 2007).

LEONARD, A., Energy cascade in large-eddy simulations of turbulent fluid flows, *Adv. Geophys. 18* (1975), 237–248.

LIU, Y. AND ECKE, R., Heat transport scaling in turbulent Rayleigh–Bénard convection: Effects of Rotation and Prandtl number, *Phys. Rev. Lett. 79* (1997), 2257–2260.

LIU, Y. AND ECKE, R. E., Heat transport measurements in turbulent rotating Rayleigh-Bénard convection, *Phys. Rev. E 80* (2009), 036314.

LOPEZ, J. AND MARQUES, F., Centrifugal effects in rotating convection: nonlinear dynamics, *J. Fluid Mech. 628* (2009), 269–297.

MANGA, M. AND WEERARATNE, D., Experimental study of non-Boussinesq Rayleigh–Bénard convection at high Rayleigh and Prandtl numbers, *Phys. Fluids 11* (1999), 2969–2976.

MARQUES, F., MERCADER, I., BATISTE, O. AND LOPEZ, J. M., Centrifugal effects in rotating convection: axisymmetric states and three-dimensional instabilities, *J. Fluid Mech. 580* (2007), 303.

MARQUES, F., NET, M., MASSAGUER, J. M. AND MERCADER, I., Thermal convection in vertical cylinders. A method based on potentials of velocity, *Comput. Methods Appl. Mech. Engrg. 110* (1993), 157–169.

NAKAGAWA, Y. AND FRENZEN, P., A theoretical and experimental study of cellular convection in rotating fluids, *Tellus 7* (1955), 1–21.

OBERBECK, A., Ueber die Wärmeleitung der Flüssigkeiten bei Berücksichtigung der Strömungen infolge von Temperaturdifferenzen, *Annalen der Physik 243* (1879), 271–292.

OGAWA, M., SCHUBERT, G. AND ZEBIB, A., Numerical simulations of three-dimensional thermal convection in a fluid with strongly temperature-dependent viscosity, *J. Fluid Mech. 233* (1991), 299–328.

OLSON, P. AND BERCOVICI, D., On the equipartition of kinetic energy in plate tectonics, *Geophysical research letters 18* (1991), 1751–1754.

ORESTA, P., STRINGANO, G. AND VERZICCO, R., Transitional regimes and rotation effects in Rayleigh–Bénard convection in a slender cylindrical cell, *Eur. J. Mech. (B/Fluids) 26* (2007), 1–14.

PETSCHEL, K., STELLMACH, S., WILCZEK, M., LÜLFF, J. AND HANSEN, U., Dissipation Layers in Rayleigh-Bénard Convection: A Unifying View, *Phys. Rev. Lett. 110* (2013), 114502.

PROUDMAN, J., On the Motion of Solids in a Liquid Possessing Vorticity, *Proc. Roy. Soc. (London) A 92* (1916), 408–424.

RAYLEIGH, L., LIX. On convection currents in a horizontal layer of fluid, when the higher temperature is on the under side, *The London, Edinburgh, and Dublin Philosophical Magazine and Journal of Science 32* (1916), 529–546.

ROSSBY, H. T., A study of Bénard convection with and without rotation, *J. Fluid Mech. 36* (1969), 309–335.

SCHLICHTING, H. AND GERSTEN, K., *Grenzschicht-Theorie* (Springer, 2006).

SCHMALZL, J., BREUER, M. AND HANSEN, U., On the validity of two-dimensional numerical approaches to time-dependent thermal convection, *Europhys. Lett. 67* (2004), 390–396.

SCHMITT, L. AND FRIEDRICH, R., Large-eddy simulation of turbulent backward facing step flow, *in 7th GAMM-Conference on Numerical Methods in Fluid Mechanics* (Vieweg und Sohn, 1988), 355–362.

SCHMITZ, S. AND TILGNER, A., Heat transport in rotating convection without Ekman layers, *Phys. Rev. E 80* (2009), 015305(R).

SCHMITZ, S. AND TILGNER, A., Transitions in turbulent rotating Rayleigh-Bénard convection, *Geophys. Astrophys. Fluid Dyn. 104* (2010), 481–489.

SCHUMANN, U., Subgrid scale model for finite difference simulations of turbulent flows in plane channels and annuli, *J. Comput. Phys. 18* (1975), 376–404.

SEGUR, J. B. AND OBERSTAR, H. E., Viscosity of Glycerol and Its Aqueous Solutions, *Ind. Eng. Chem. 43* (1951), 2117–2120.

SHI, N., EMRAN, M. S. AND SCHUMACHER, J., Boundary layer structure in turbulent Rayleigh–Bénard convection, *J. Fluid Mech. 706* (2012), 5–33.

SHISHKINA, O., HORN, S. AND KACZOROWSKI, M., Direct Numerical Simulations of turbulent Rayleigh–Bénard convection, *in High Performance Computing in Science and Engineering* (Verlag der Bayrischen Akademie der Wissenschaften, 2012), 144–146.

SHISHKINA, O., HORN, S. AND WAGNER, S., Falkner–Skan boundary layer approximation in Rayleigh–Bénard convection, *J. Fluid Mech. 730* (2013), 442–463.

SHISHKINA, O., STEVENS, R. J. A. M., GROSSMANN, S. AND LOHSE, D., Boundary layer structure in turbulent thermal convection and its consequences for the required numerical resolution, *New J. Phys. 12* (2010), 075022.

SHISHKINA, O. AND WAGNER, C., A fourth order accurate finite volume scheme for numerical simulations of turbulent Rayleigh–Bénard convection in cylindrical containers, *C. R. Mecanique 333* (2005), 17–28.

SHISHKINA, O. AND WAGNER, C., Analysis of thermal dissipation rates in turbulent Rayleigh–Bénard convection, *J. Fluid Mech. 546* (2006), 51–60.

SHISHKINA, O. AND WAGNER, C., Boundary and interior layers in turbulent thermal convection in cylindrical containers, *Int. J. Computing Science and Mathematics 1* (2007a), 360–373.

SHISHKINA, O. AND WAGNER, C., A fourth order finite volume scheme for turbulent flow simulations in cylindrical domains, *Computers & Fluids 36* (2007b), 484–497.

SHISHKINA, O. AND WAGNER, C., Local heat fluxes in turbulent Rayleigh–Bénard, *Phys. Fluids 19* (2007c), 085107.

SHISHKINA, O., WAGNER, S. AND HORN, S., Influence of the angle between the wind and the isothermal surfaces on the boundary layer structures in turbulent thermal convection, *Phys. Rev. E 89* (2014), 033014.

SHISHKINA, O. V., The Neumann stability of high-order symmetric schemes for convection-diffusion problems, *Siberian Mathematical Journal 48* (2007), 1141–1146.

SIGGIA, E. D., High Rayleigh number convection, *Annu. Rev. Fluid Mech. 26* (1994), 137–168.

SILANO, G., SREENIVASAN, K. AND VERZICCO, R., Numerical simulations of Rayleigh–Bénard convection for Prandtl numbers between 10^{-1} and 10^4 and Rayleigh numbers between 10^5 and 10^9, *J. Fluid Mech. 662* (2010), 409–446.

STEVENS, R. J., CLERCX, H. J. AND LOHSE, D., Optimal Prandtl number for heat transfer in rotating Rayleigh–Bénard convection, *New J. Phys. 12* (2010a), 075005.

STEVENS, R. J., VAN DER POEL, E., GROSSMANN, S. AND LOHSE, D., The unifying theory of scaling in thermal convection: the updated prefactors, *J. Fluid Mech. 730* (2013a), 295–308.

STEVENS, R. J. A. M., CLERCX, H. J. H. AND LOHSE, D., Boundary layers in rotating weakly turbulent Rayleigh–Bénard convection, *Phys. Fluids 22* (2010b), 085103.

STEVENS, R. J. A. M., CLERCX, H. J. H. AND LOHSE, D., Breakdown of the large-scale circulation in $\Gamma = 1/2$ rotating Rayleigh-Bénard flow, *Phys. Rev. E 86* (2012), 056311.

STEVENS, R. J. A. M., CLERCX, H. J. H. AND LOHSE, D., Heat transport and flow structure in rotating Rayleigh–Bénard convection, *Eur. J. Mech. (B/Fluids)* .

STEVENS, R. J. A. M., LOHSE, D. AND VERZICCO, R., Prandtl and Rayleigh number dependence of heat transport in high Rayleigh number thermal convection, *J. Fluid Mech. 688* (2011), 31–43.

STEVENS, R. J. A. M., ZHONG, J.-Q., CLERCX, H. J. H., AHLERS, G. AND LOHSE, D., Transitions between Turbulent States in Rotating Rayleigh–Bénard Convection, *Phys. Rev. Lett. 103* (2009), 024503.

SUGIYAMA, K., CALZAVARINI, E., GROSSMANN, S. AND LOHSE, D., Non-Oberbeck–Boussinesq effects in two-dimensional Rayleigh-Bénard convection in glycerol, *Europhys. Lett. 80* (2007), 34002.

SUGIYAMA, K., CALZAVARINI, E., GROSSMANN, S. AND LOHSE, D., Flow organization in two-dimensional non-Oberbeck–Boussinesq Rayleigh-Bénard convection in water, *J. Fluid Mech. 637* (2009), 105–135.

SWARZTRAUBER, P. N. AND SWEET, R., Efficient FORTRAN Subprograms for the Solution of Elliptic Equations. Technical Note IA-109, *National Center for Atmospheric Research, Boulder, CO* .

TAYLOR, G. I., Experiments with rotating fluids, *Proc. Roy. Soc. (London) 100* (1921), 114–121.

WAGNER, S., SHISHKINA, O. AND WAGNER, C., Boundary layers and wind in cylindrical Rayleigh–Bénard cells, *J. Fluid Mech. 697* (2012), 336–363.

WEISS, S. AND AHLERS, G., Heat transport by turbulent rotating Rayleigh–Bénard convection and its dependence on the aspect ratio, *J. Fluid Mech. 684* (2011a), 205.

WEISS, S. AND AHLERS, G., The large-scale flow structure in turbulent rotating Rayleigh–Bénard convection, *J. Fluid Mech. 688* (2011b), 461.

WEISS, S., STEVENS, R. J. A. M., ZHONG, J.-Q., CLERCX, H. J. H., LOHSE, D. AND AHLERS, G., Finite-Size Effects Lead to Supercritical Bifurcations in Turbulent Rotating Rayleigh–Bénard Convection, *Phys. Rev. Lett. 105* (2010), 224501.

WU, X.-Z. AND LIBCHABER, A., Non-Boussinesq effects in free thermal convection, *Phys. Rev. A 43* (1991), 2833–2839.

XIA, K.-Q., LAM, S. AND ZHOU, S.-Q., Heat-Flux Measurement in High-Prandtl-Number Turbulent Rayleigh-Bénard Convection, *Phys. Rev. Lett. 88* (2002), 064501.

YOUNG, Y.-N., RIECKE, H. AND PESCH, W., Whirling hexagons and defect chaos in hexagonal non-Boussinesq convection, *New J. Phys. 5* (2003), 135.

ZHANG, J., CHILDRESS, S. AND LIBCHABER, A., Non-Boussinesq effect: Thermal convection with broken symmetry, *Phys. Fluids 9* (1997), 1034–1042.

ZHANG, J., CHILDRESS, S. AND LIBCHABER, A., Non-Boussinesq effect: Asymmetric velocity profiles in thermal convection, *Phys. Fluids 10* (1998), 1534.

ZHONG, F., ECKE, R. AND STEINBERG, V., Asymmetric modes and the transition to vortex structures in rotating Rayleigh-Bénard convection, *Phys. Rev. Lett. 67* (1991a), 2473.

ZHONG, F., ECKE, R. AND STEINBERG, V., Asymmetric modes and the transition to vortex structures in rotating Rayleigh-Bénard convection, *Phys. Rev. Lett. 67* (1991b), 2473.

ZHONG, F., ECKE, R. AND STEINBERG, V., Rotating Rayleigh-Bénard convection: Küppers-Lortz transition, *Physica D: Nonlinear Phenomena 51* (1991c), 596–607.

ZHONG, F., ECKE, R. AND STEINBERG, V., Rotating Rayleigh–Bénard convection: asymmetric modes and vortex states, *J. Fluid Mech. 249* (1993), 135–159.

ZHONG, J.-Q. AND AHLERS, G., Heat transport and the large-scale circulation in rotating turbulent Rayleigh–Bénard convection, *J. Fluid Mech. 665* (2010), 300–333.

ZHONG, J.-Q., STEVENS, R. J. A. M., CLERCX, H. J. H., VERZICCO, R., LOHSE, D. AND AHLERS, G., Prandtl-, Rayleigh-, and Rossby-Number dependence of heat transport in turbulent rotating Rayleigh–Bénard Convection, *Phys. Rev. Lett. 102* (2009), 044502.